THÈSE POUR OBTENIR LE GRADE DE DOCTEUR DE L'UNIVERSITÉ DE MONTPELLIER

En Chimie et Physico-Chimie des Matériaux

École doctorale Sciences Chimiques Balard (ED 459)

Unité de recherche Institut Européen des Membranes

Engineering of the interlayer space of nanolaminate membranes for molecular sieving

Présentée par Wensen WANG

Le 10 Novembre 2023

Sous la direction de Philippe MIELE du Directeur de thèse
et Damien VOIRY du co-Directeur de thèse

Devant le jury composé de

Sophie CASSAIGNON, Professeure, Sorbonne Université	Rapporteur
Mohamed EI-ROZ, Chargé de recherche, University of Caen Normandy	Rapporteur
Cecilia DE CARVALHO CASTRO E SILVA, Associate Professor, Mackenzie Presbyterian University	Examinateur
Benoit MAHLER, Chargé de recherche, Université Claude Bernard Lyon 1	Examinateur
Philippe MIELE, Professeur, Université de Montpellier	Directeur
Damien VOIRY, Chargé de recherche, Université de Montpellier	Co-Directeur

UNIVERSITÉ DE MONTPELLIER

Acknowledgements

I wish to express my deepest gratitude to the distinguished jury members, whose insightful feedback and valuable critiques have significantly contributed to the refinement and progression of this thesis.

I extend my deepest gratitude to my thesis director, Philippe, for his steadfast support and guidance. His assistance, especially with numerous administrative tasks, enabled me to continue my studies in France without obstacles. Moreover, his meticulous review and invaluable feedback significantly improved the quality and comprehensibility of this research.

My utmost gratitude is extended to my supervisor, Damien, who has been an integral part of this incredible journey, directing all my experiments and providing unflagging companionship. His role in my life goes beyond merely being a mentor in scientific research, guiding me toward insightful and fruitful discoveries. His optimism and continual encouragement have been my beacon of light, particularly during challenging times. I still remember how hard my first year was. Even though I worked hard, it seemed like nothing was working. I felt so sad. But Damien never lost faith in me. He kept telling me that nothing was easy, and he felt the good news was coming. His patience, encouragement, and tireless help in resolving issues ultimately saw me through that difficult period. I consider myself fortunate to have had his unwavering support, which prevented me from succumbing to despair during the darkest hours. Today, as I behold the dawn of victory, I hold the deepest appreciation for Damien in my heart. His support has been instrumental in my journey, and for this, I am eternally grateful.

I also want to give special thanks to Nicolas Onofrio, who did the atomistic calculations, Eddy Petit, who performed the liquid NMR and HPLC for membrane rejection quantification, and Luc Lajaunie, who carried out and analyzed the (S)TEM measurements. I am also grateful to Christel Gervais for her work in conducting the solid ^{13}C NMR spectroscopy measurements. Each of these individuals played a crucial

role in my research journey, and their contributions were essential in reaching the successes I now see. For their tireless efforts and collaboration, I'm deeply appreciative.

I also want to give a heartfelt thank you to my friends Ji, Jiefeng, Huali, Yang, Kun, Bonito, Lucie, Mathilde, and Hippolyte, along with everyone in the Low Dimension Materials Research Group. We worked together as a big family, and their friendship, advice, and help were priceless throughout this journey.

Additionally, I am extremely grateful to the China Scholarship Council (CSC) for funding my PhD. Their support gave me the chance to embark on this amazing adventure. The opportunities and experiences this journey has offered me have been truly transformative.

Lastly, my most profound thanks go to my family and my girlfriend. Their enduring support, encouragement, and love have provided me with the strength to navigate the challenging journey of completing this thesis. I dedicate this work to you all. Thank you.

Résumé

Cette thèse présente une exploration approfondie du potentiel et des défis des membranes en matériaux bidimensionnels (2D) pour diverses applications de séparation, offrant à la fois des aperçus fondamentaux et des approches innovantes pour leur conception et leur application. Elle commence par étudier l'essor des membranes en matériaux 2D, notamment l'oxyde de graphène (GO), les dichalcogénures de métaux de transition (TMD) et les carbures et/ou nitrures de métaux de transition (MXene), en tant qu'alternative prometteuse aux membranes polymères conventionnelles pour diverses applications de séparation. Parallèlement, les défis auxquels sont confrontées les membranes 2D sont également abordés. Enfin, les stratégies d'adaptation des matériaux 2D pour améliorer leurs performances de séparation membranaire sont mises en évidence.

La thèse se penche ensuite sur le développement de membranes laminaires construites à partir de nanofeuillets de MoS_2 en 2D, démontrant la manipulation de l'espace entre les couches pour améliorer les performances de dessalement. Nous révélons une stratégie permettant d'ajuster finement les largeurs capillaires et la structure d'empilement des nanocanaux en fonction de la nature des groupes fonctionnels attachés aux nanofeuillets de MoS_2, ce qui permet d'obtenir des taux impressionnants de perméation de l'eau et de rejet des sels. Ces travaux ouvrent la voie à la conception future de membranes de dessalement et de nanofiltration à haut rendement énergétique.

Enfin, l'accent est mis sur les applications de nanofiltration par solvants organiques (OSN) des membranes d'argile laminées en 2D. En intercalant divers cations mono et multivalents, en particulier le Fe^{3+}, dans la couche intermédiaire des nanofeuillets d'argile, nous améliorons considérablement la stabilité et la capacité de tamisage moléculaire des membranes, démontrant des performances impressionnantes dans la séparation des colorants et la purification des solvants organiques.

Les perspectives de recherche futures sont également explorées, soulignant l'importance d'améliorer la stabilité et l'extensibilité des membranes et de développer

des techniques de fabrication durables. Les perspectives d'étudier davantage les rôles des groupes fonctionnels et des cations dans la modification des propriétés des membranes, de développer des membranes nanolaminées à plus grande échelle et d'exploiter tout le potentiel des membranes d'argile laminées en 2D pour l'OSN sont discutées. Cette thèse offre non seulement un aperçu précieux de l'état actuel et du potentiel des membranes en matériaux 2D, mais pose également des bases solides pour les recherches futures dans ce domaine.

Abstract

This thesis presents an in-depth exploration of the potential and challenges of two-dimensional (2D) material membranes for various separation applications, offering both foundational insights and innovative approaches to their design and application. It begins by investigating the rise of 2D material membranes, notably graphene oxide (GO), transition metal dichalcogenides (TMDs), and transitional metal carbides and/or nitrides (MXene), as a promising alternative to conventional polymer membranes for diverse separation applications. Meanwhile, the challenges faced by 2D membranes are also addressed. In the end, the tailoring strategies for 2D materials to enhance their membrane separation performance are highlighted.

The thesis then delves into the development of laminar membranes constructed from 2D MoS_2 nanosheets, demonstrating the manipulation of interlayer space for enhanced desalination performance. We reveal a strategy to fine-tune the capillary widths and stacking structure of the nanochannels depending on the nature of the functional groups attached to the MoS_2 nanosheets, leading to impressive water permeation and salt rejection rates. This work paves the way for the future design of energy-efficient desalination and nanofiltration membranes.

Lastly, the focus shifts to organic solvent nanofiltration (OSN) applications of 2D laminated clay membranes. By intercalating mono and multivalent cations, particularly Fe^{3+}, into the interlayer of clay nanosheets, we significantly enhance the stability and molecular sieving ability of the membranes, demonstrating impressive performance in dye separation and organic solvent purification.

Future research perspectives are also explored, highlighting the importance of enhancing membrane stability, scalability, and developing sustainable fabrication techniques. The prospects for further investigating the roles of functional groups and cations in modifying membrane properties, developing larger-scale nanolaminated membranes, and exploiting the full potential of 2D laminated clay membranes for OSN are discussed. This thesis not only offers valuable insights into the current state and

potential of 2D material membranes but also sets a strong foundation for future research in the field.

Publications

1. **Wang W.**, Onofrio N., Petit E., Karamoko B., Wu H., Liu J., Li J., Qi K., Zhang Y., Gervais C., Lajaunie L., Salameh C., Miele P., Zeng Z. & Voiry D. *High-surface-area functionalized nanolaminated membranes for energy-efficient nanofiltration and desalination in forward osmosis*. Nature Water, 2023, **1**(2): 187-197.

2. **Wang W.**, Hao X., Sun R., Moderne M., Liu J., Wu H., Li J., Lajaunie L., Salameh C., Miele P., Zeng Z. & Voiry D. *2D laminated clay membranes with superfast solvent transport for molecular separation*. Prepared and going to submit.

3. **Wang W.**, Miele P., Zeng Z. & Voiry D. *The chemical modification of 2D materials for nanofluidics and molecular sieving*. Prepared and going to submit.

Table of Contents

Acknowledgements 1
Résumé 3
Abstract 5
Publications 7
Chapter 1: General introduction and literature review 11
Two-dimensional Membranes for Molecular Transport and Sieving 12
1.1. membrane separation technology 14
1.1.1 Forward Osmosis Technology 14
1.1.2 Reverse Osmosis Technology 16
1.1.3 Nanofiltration Technology 17
1.1.4 Pervaporation Technology 18
1.1.5 Gas separation technology 19
1.2 membranes materials 20
1.2.1 Polymeric Membranes 21
1.2.2 Inorganic Membranes 23
1.2.3 Two-Dimensional Materials Membranes 25
1.3 Tailoring of 2D membranes 54
1.3.1 Tailoring strategies 54
1.3.2 Tailoring methods 59
1.3.3 Tailoring effects 67
1.4 Conclusion 84
1.5 Reference 86
Chapter 2: Functionalized MoS_2 for water purification and desalination 107
High Surface Area Functionalized Nanolaminated Membranes For Energy Efficient Nanofiltration And Desalination In Forward Osmosis 108
2.1 Abstract 108
2.2 Introduction 108
2.3 Material and Methods 110
2.3.1 Materials 110
2.3.2 Synthesis of single-layer MoS_2 nanosheets 111
2.3.3 Functionalization of single-layer MoS_2 nanosheets 111
2.3.4 Preparation of functionalized MoS_2 membranes 111
2.3.5 Water permeation through nanolaminated MoS_2 membranes 112
2.3.6 Ionic permeation through the nanolaminated MoS_2 membranes 112
2.3.7 Water purification and rejection evaluations 113
2.3.8 Water desalination in tangential cross-flow filtration cell 113
2.3.9 Molecular dynamics simulations parameter 114
2.4 Characterization 115
2.4.1 Characterization methodology 115
2.4.2 Zeta potential of MoS_2 nanosheets 115
2.4.3 ATR-FTIR spectra of MoS_2 membranes 116

2.4.4 Raman Spectrum of MoS_2 nanosheets 117
2.4.5 ^{13}C Nuclear Magnetic resonance spectroscopy (NMR) 118
2.4.6 DFT calculations of NMR parameters 118
2.4.7 TGA measurement on MoS_2 nanosheets 119
2.4.8 SEM images of MoS_2 membranes with different thickness 120
2.4.9 Cross-section view of pristine and functionalized MoS_2 membranes 121
2.4.10 XRD patterns of MoS_2 membranes soaking in water 121
2.4.11 FWHM and capillary width variation of functionalized MoS_2 membranes 122
2.4.12 XRD patterns of GO, MXene, and C_3OH-MoS_2 membranes before and after soaking in water 123
2.4.13 XRD patterns of C_2-MoS_2 and C_3OH-MoS_2 membranes soaking in high concentrated salt solution 124
2.4.14 Contact Angle of MoS_2 membrane 125
2.5 Results and discussion 127
2.5.1 Preparation and Characterization of Functionalized MoS_2 Membranes 127
2.5.2 Ionic Transport and Water Permeation in the Functionalized MoS_2 Membranes 131
2.5.3 Mechanical properties of the 2D membranes from MD simulations 140
2.5.4 Water Purification and Desalination by Forward Osmosis 142
2.6 Conclusion 151
2.7 Note 151
2.7.1 Specific energy consumption (SEC) calculation 151
2.7.2 Comparison of the performance of the MoS_2 membranes with state-of-the-art 2D laminar membranes 152
2.7.3 Force field parameters of MD simulation 153
2.8 Reference 158
Chapter 3: Cation intercalated clay membrane for water purification and organic solvent nanofiltration 165
2D Laminated Clay Membranes with Superfast Solvent Transport for Molecular Separation 166
3.1 Abstract 166
3.2 Introduction 166
3.3 Material and Methods 169
3.3.1 Materials 169
3.3.2 Synthesize of single-layer vermiculate nanosheets 169
3.3.3 Preparation of pristine and cation-treated clay membranes 170
3.3.4 Solvent permeation through nanolaminated clay membranes 170
3.3.5 Solvent purifications performance evaluation 171
3.3.6 Membrane stability evaluation in a tangential cross-flow filtration cell 171
3.4 Characterization 171
3.4.1 Characterization methodology 171
3.4.2 Low magnification transmission electron microscopy (TEM) image and the selected area diffraction pattern (SADP) of clay nanosheets 172
3.4.3 EDX mapping on cross-section of pristine and Fe-clay membranes 173
3.4.4 Stability of pristine and Fe-clay membranes in water and DMSO 174

3.4.5 XRD patterns of pristine and Fe-clay membranes in various organic solvent 176
3.4.6 Water/DMSO contact angle of pristine and cation-treated clay membranes 178
3.4.7 Zeta potential of pristine clay nanosheets 179
3.5 Results and discussion 180
3.5.1 Characterization of nanolaminated clay membranes.....180
3.5.2 Solvent permeation through 2D clay membrane.....184
3.5.3 Nanofiltration for solvent purification 187
3.6 Conclusion.....192
3.7 Note.....193
3.7.1 Comparison of the performance of the Fe-clay membranes with state-of-the-art membranes 193
3.8 Reference.....197
Chapter 4: Summary and perspectives.....204
4.1 Summary.....205
4.2 Perspectives.....206

Chapter 1: General introduction and literature review

Two-dimensional Membranes for Molecular Transport and Sieving

As the world's population continues to grow and industrialization accelerates, the environment is under considerable pressure, giving rise to a myriad of challenges. Among these pressing issues, widespread water pollution, greenhouse gas emissions, and organic solvent waste are particularly urgent concerns. To effectively mitigate these problems, it is crucial to identify and develop energy-efficient and sustainable solutions. In this context, separation processes emerge as a promising approach.

Various separation techniques have been explored and implemented in diverse applications, such as distillation, adsorption, and extraction. However, membrane separation stands out as an environmentally friendly and energy-efficient option. This method involves the selective permeation of components in a mixture through a membrane, offering a sustainable and economically viable alternative to traditional separation techniques. One of the key advantages of membrane separation lies in its ability to operate without phase changes or chemical additives, resulting in reduced energy consumption and minimal environmental impact.

In light of these benefits, the investigation and optimization of membrane materials have become essential for maximizing the efficacy and scalability of membrane-based separation processes. The evolution of membrane materials over the past two centuries has led to tremendous advancements in membrane separation technology (Figure 1.1). Initially, natural materials like clay, porcelain, and animal and plant tissues were used, but with the advent of synthetic polymers and ceramics in the 20th century, membranes saw a revolution in their performance and stability. In recent years, a focus on nanotechnology has allowed the creation of membranes with much smaller pore sizes, enabling separation at the molecular scale. This atomic-scale control over pore size allows for highly precise and selective separations (Figure 1.2), thereby increasing efficiency.

Despite the advancements, the field faces significant challenges. One of the main issues is achieving the optimal tradeoff between selectivity and permeability. High selectivity often comes at the cost of lower permeability and vice versa. Additionally,

membrane aging is another major challenge. The development of novel materials like graphene and other 2D materials offers potential solutions to these challenges. These materials have extraordinary mechanical and thermal properties, and their atomic-scale thickness allows for unprecedented selectivity and permeability, opening new opportunities for efficient separation processes.

This chapter will commence with a brief overview of the separation technology concerning molecular-level sieving. Following this, we will traverse the landscape of membrane materials, examining both widely-used commercial membranes prevalent in the separation market, and state-of-the-art 2D material membranes currently under investigation. The final section of this chapter will underscore the importance of tailoring 2D membranes to augment their performance and meet the rising demands for efficient separation processes.

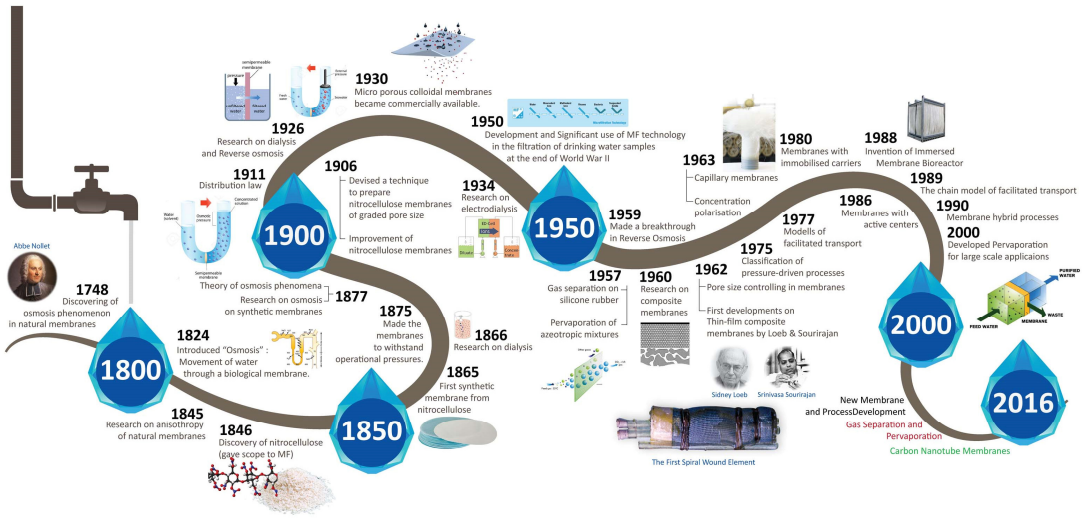

Figure 1.1 Historical development of membranes.

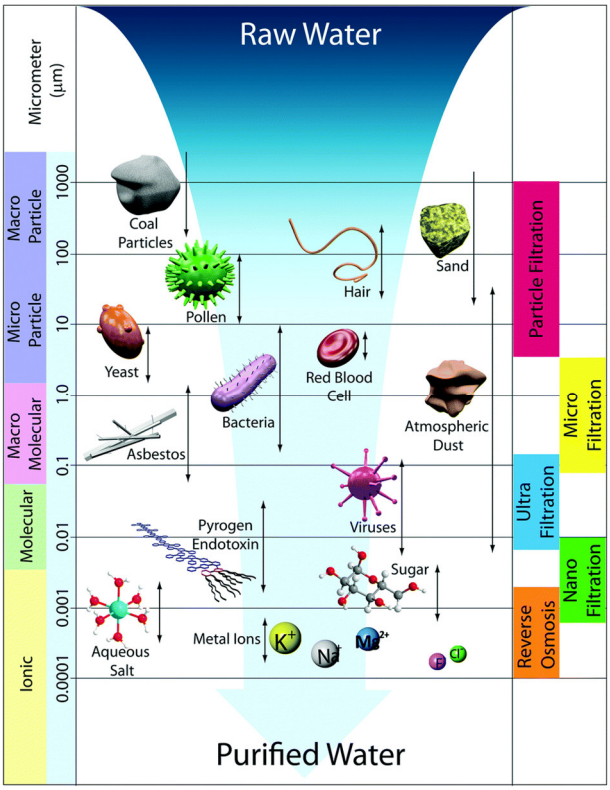

Figure 1.2 Schematic representation of the membrane filtration spectrum. The figure depicts that precise control of membrane pore size and reduction to the nanoscale can enable molecular and atomic scale sieving [1].

1.1. membrane separation technology

Building on the importance of membrane separation techniques, this section will introduce five specific technologies that have garnered significant interest in recent years due to their potential for addressing the molecular-level sieving. These technologies, namely forward osmosis (FO), reverse osmosis (RO), nanofiltration (NF), pervaporation (PV), and gas separation, have distinct characteristics and applications, making them suitable for various separation tasks. The following parts will introduce and discuss each of these membrane-based separation processes in detail, highlighting their principles, advantages, and current applications.

1.1.1 Forward Osmosis Technology

Concept and Principles

Forward osmosis operates on the principle of natural osmosis, where solvent molecules

flow spontaneously across a semipermeable membrane from a region of low solute concentration (feed solution) to a region of high solute concentration (draw solution). The osmotic pressure gradient created by the difference in solute concentrations drives the solvent molecules through the membrane, resulting in the dilution of the draw solution and the concentration of the feed solution. Afterward, the draw solution is typically treated to recover the purified solvent, and the concentrated feed solution can be further processed or disposed of, depending on the application.

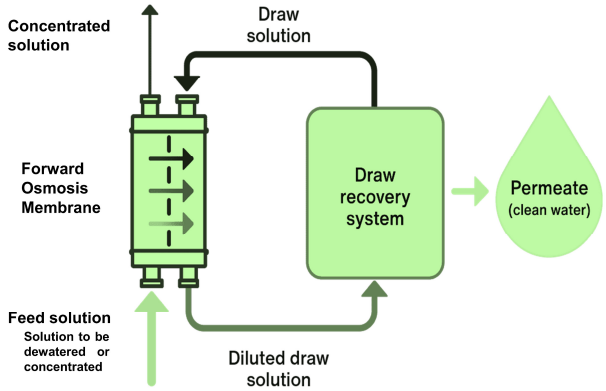

Figure 1.3 Forward osmosis technology.

Advantages of Forward Osmosis Technology

One of the most significant advantages of FO technology is its low energy consumption. Since the process relies on natural osmotic pressure gradients, no external pressure is needed to drive the solvent across the membrane, resulting in energy savings when compared to pressure-driven membrane separation techniques, such as reverse osmosis.

Another notable advantage of FO technology is its reduced propensity for membrane fouling. Since the process does not involve applying external pressure, the fouling particles are less likely to become compacted on the membrane surface, which can extend the membrane's operational life and reduce maintenance requirements.

Furthermore, FO technology can operate with a wide range of feed solution concentrations, making it a versatile option for various applications, including those involving high salinity or high turbidity solutions.

Applications of Forward Osmosis Technology

Forward osmosis technology has been explored for various applications, including water purification, desalination, wastewater treatment, and resource recovery.

1.1.2 Reverse Osmosis Technology

Concept and Principles

At its core, reverse osmosis operates based on the principle of utilizing external pressure to counteract the natural osmotic pressure. This pressure difference drives water molecules through a semipermeable membrane while retaining dissolved salts, organic compounds, and other impurities. The membrane employed in RO systems is designed to selectively permit water molecules to pass through, effectively rejecting a majority of contaminants. Consequently, purified water is obtained on one side of the membrane, with a concentrated solution of impurities left behind on the other.

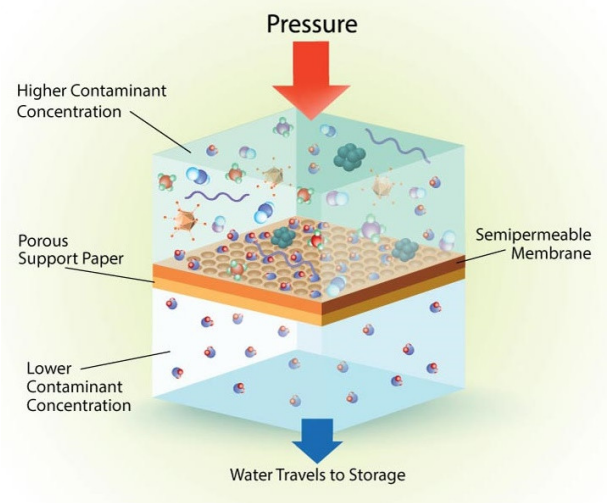

Figure 1.4 Reverse osmosis technology.

Advantages of Reverse Osmosis Technology

One of the main strengths of RO technology lies in its high purification efficiency. RO systems are capable of removing up to 99% of dissolved salts, organic compounds, and particulates, delivering water of exceptional quality.

Another notable advantage of RO technology is its scalability. RO systems can be designed to accommodate a broad range of capacities, from small-scale household units to expansive industrial plants.

Furthermore, reverse osmosis does not rely on the addition of chemicals for water purification. This characteristic reduces the risk of secondary pollution and lowers operating costs.

Current Applications of Reverse Osmosis Technology

One prominent area of application is desalination, where RO is a popular choice for seawater and brackish water desalination. In these contexts, RO provides potable water for municipal and industrial use, addressing water scarcity issues in many regions around the world.

1.1.3 Nanofiltration Technology

Concept and Principles

Nanofiltration is a membrane-based separation process that operates in the range between ultrafiltration and reverse osmosis in terms of pore size, molecular weight cut-off, and operating pressure. NF membranes typically have pore sizes in the range of 1-10 nm and can selectively separate solutes based on their size and charge. The separation process is driven by applying pressure on the feed solution, forcing the solvent and smaller solutes through the membrane while retaining larger solutes and particles.

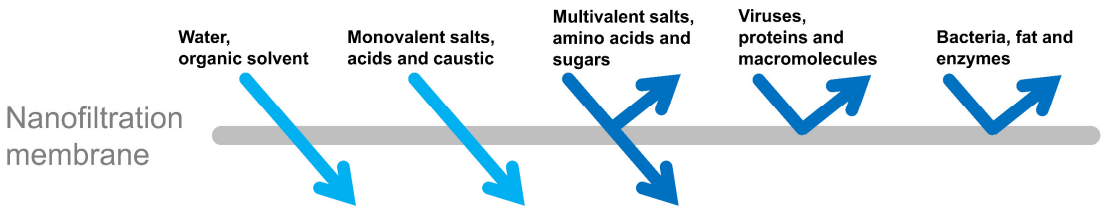

Figure 1.5 Nanofiltration Technology.

Advantages of Nanofiltration Technology

One of the main advantages of NF technology is its ability to selectively separate solutes based on size and charge, which enables the recovery of valuable components and the removal of contaminants in various applications. This selectivity allows for the treatment of complex mixtures and the production of high-quality products.

Another significant advantage of NF is its relatively low energy consumption compared to reverse osmosis, as it operates at lower pressures.

Furthermore, NF technology can be easily scaled up or down, making it suitable for both small-scale and large-scale operations.

Applications of Nanofiltration Technology

In water treatment, NF is used for the removal of hardness ions, organic matter, and micropollutants from drinking water and for the treatment of industrial wastewater. In the food and beverage industry, NF is employed for the concentration and purification of valuable components, such as proteins, sugars, and polyphenols.

In the pharmaceutical industry, NF is utilized for the separation and purification of active pharmaceutical ingredients, as well as the removal of impurities and solvents from drug formulations. The recovered solvents can then be recycled and reused within the production process, reducing costs and promoting sustainable and circular manufacturing practices.

1.1.4 Pervaporation Technology

Concept and Principles

Pervaporation involves the selective transport of one or more components of a liquid mixture through a dense membrane by a combination of permeation and evaporation processes. The feed mixture is typically in contact with the upstream side of the membrane, while the downstream side is kept under vacuum or swept with an inert gas to maintain a low partial pressure of permeating components. The difference in chemical potential across the membrane drives the permeation of the target component(s), which then evaporates on the downstream side, forming a vapor that can be condensed and collected as a purified product.

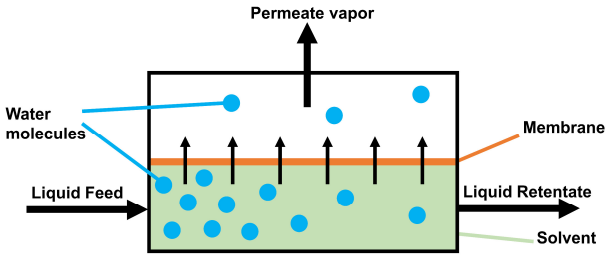

Figure 1.6 Pervaporation technology.

Advantages of Pervaporation Technology

One of the key advantages of pervaporation is its ability to separate components in azeotropic or close-boiling mixtures. Pervaporation can efficiently separate such mixtures without the need for additional chemicals or high operating temperatures.

Another significant advantage of pervaporation is its low energy consumption as the process operates at relatively low temperatures and pressures.

Moreover, pervaporation is a highly selective process, which can be tailored to target specific components in a mixture by adjusting membrane materials and operating conditions.

Applications of Pervaporation Technology

Pervaporation has been successfully applied to various industries and applications, including the separation of organic-organic mixtures and organic-aqueous mixtures. In the chemical and petrochemical industries, pervaporation is used for the separation of azeotropic mixtures, solvent recovery and dehydration.

1.1.5 Gas separation technology

Concept and Principles

Gas separation technology, predominantly based on membrane separation processes, offers a viable approach for selectively isolating and purifying specific gases from a mixed gas stream. The underlying principle involves the differential permeation rates of gases through a membrane material, governed by their molecular size and solubility. This results in the partitioning of gases across the membrane, with the desired gas

collected on the permeate side.

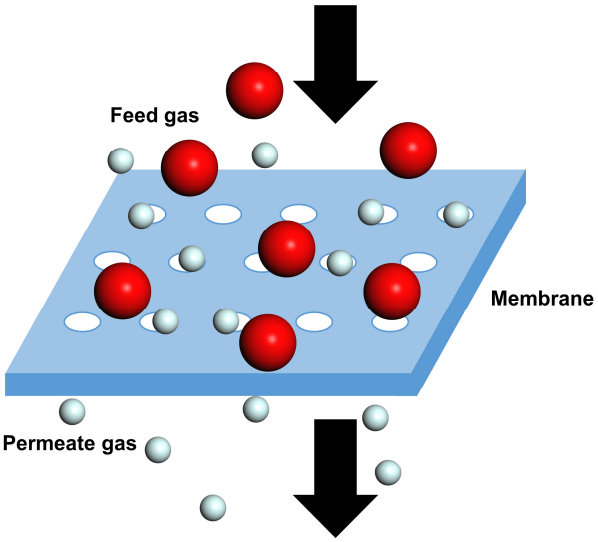

Figure 1.7 Gas separation technology.

Advantages of gas separation technology

One of the main advantages of this technology is its energy efficiency, as it operates at ambient temperature and requires no phase change.

Moreover, it's inherently scalable and flexible, catering to different operational demands.

Applications of gas separation technology

Gas separation technology is extensively employed across industries such as petrochemical, where it aids in the purification of natural gas, and in environmental contexts, such as carbon capture and storage (CCS) for mitigating greenhouse gas emissions. Furthermore, it also plays a significant role in air separation units for producing high-purity oxygen or nitrogen.

1.2 membranes materials

As we move forward in our exploration of membrane separation techniques, it is essential to acknowledge the central role of membrane materials in determining the performance and efficiency of these processes. The properties of the membrane, such

as its selectivity, permeability, and stability, are critical factors influencing the success of the separation process. In light of this, researchers have devoted considerable effort to the development and optimization of membrane materials that exhibit desirable characteristics for various applications.

To provide a comprehensive understanding of the different types of membrane materials and their respective attributes, the following sections will delve into the properties and applications of three primary categories of membrane materials: 2.1 polymeric membranes, 2.2 inorganic membranes, and 2.3 two-dimensional material membranes. Each of these membrane categories exhibits unique properties that make them suitable for specific separation applications. By examining the advantages and limitations of each membrane material, we can gain insights into the current state of the field and the potential directions for future research and development efforts to further enhance the performance and applicability of membrane separation technologies.

1.2.1 Polymeric Membranes

Polymeric membranes are among the most widely utilized membrane materials in various separation processes due to their relatively low cost, ease of fabrication, and versatile properties. This section will provide a brief overview of the different types of polymeric membranes (classified by composition), their primary applications, and inherent advantages and limitations.

Classification of Polymeric Membranes and Their Applications

(i) Cellulose Acetate (CA): CA membranes are known for their outstanding hydrophilic properties and good mechanical strength. They have been widely used in forward osmosis, reverse osmosis, ultrafiltration, and microfiltration processes for water purification, desalination, and wastewater treatment applications [2, 3].

(ii) Polyamide (PA): PA membranes are known for their high chemical resistance, good mechanical strength, and excellent selectivity. They are primarily used in reverse osmosis and nanofiltration processes for seawater desalination, wastewater treatment,

and the removal of organic compounds from various solutions [4, 5]. Polyamide membranes are also employed in the gas separation industry for applications such as hydrogen recovery and the separation of carbon dioxide from natural gas [6].

(iii) Polyimide (PI): Polyimide membranes exhibit superb thermal and chemical stability, making them suitable for high-temperature applications and harsh chemical environments. They are primarily used in gas separation processes, such as air separation, natural gas purification, and carbon capture [7, 8].

(iv) Poly (vinyl alcohol) (PVA): PVA membranes are characterized by their remarkable hydrophilic nature due to the pendant hydroxyl groups. They are often used in pervaporation processes for solvent dehydration [9].

Advantages of Polymeric Membranes

Polymeric membranes offer several benefits that make them a popular choice for various separation processes:

(i) Versatility: The diverse range of polymeric materials available enables the development of membranes with tailored pores sizes to meet the requirements of specific applications.

(ii) Ease of fabrication: Polymeric membranes can be easily fabricated through various techniques, such as phase inversion, interfacial polymerization, and electrospinning, allowing for cost-effective and scalable production.

(iii) Tunability: Polymeric membranes can be modified through various functionalization strategies, such as surface modification, blending, and the incorporation of additives, to improve their separation performance, selectivity, and stability.

Limitations of Polymeric Membranes

Despite their numerous advantages, polymeric membranes also have some inherent drawbacks:

(i) Fouling: Polymeric membranes are susceptible to fouling, which can lead to

reduced permeate flux and separation efficiency. This issue necessitates regular cleaning and maintenance to mitigate its impact.

(ii) Trade-off between permeability and selectivity: Polymeric membranes often face a trade-off between permeability and selectivity, which can be challenging to overcome in the pursuit of high-performance membrane materials.

In conclusion, polymeric membranes represent a versatile and widely used class of membrane materials for various separation applications, owing to their diverse properties, ease of fabrication, and tunability in terms of functionalization and modification. Although some limitations exist, ongoing research is focused on addressing these challenges and developing novel polymeric materials with improved performance and stability for advanced separation processes.

1.2.2 Inorganic Membranes

Inorganic membranes have gained considerable attention in the field of separation technology due to their excellent thermal, chemical, and mechanical stability. This section will briefly introduce the inorganic membranes types, their primary applications, and inherent advantages and limitations.

Classification of Inorganic Membranes and Their Applications

Inorganic membranes can be broadly classified into three main categories based on their composition: (i) ceramic membranes, (ii) metallic membranes, and (iii) zeolite membranes.

(i) Ceramic Membranes: Ceramic membranes are made from materials such as alumina, titania, zirconia, and silica. These membranes exhibit high thermal and chemical stability, making them suitable for applications in harsh operating conditions. Ceramic membranes are commonly employed in microfiltration and ultrafiltration processes for water purification, wastewater treatment, and the separation of particles and macromolecules in various industries, such as food and beverage, pharmaceutical,

and petrochemical sectors [10-13].

(ii) Metallic Membranes: Metallic membranes are composed of metals or metal alloys, such as palladium, silver, stainless steel, and nickel. They are characterized by high mechanical strength and excellent thermal stability. Metallic membranes are predominantly used for hydrogen separation [14, 15]. Additionally, they are employed in the separation of liquid mixtures, such as oil-water separation [16].

(iii) Zeolite Membranes: Zeolite membranes consist of crystalline aluminosilicate materials with well-defined microporous structures. They exhibit high selectivity due to their molecular sieving properties and are resistant to various chemicals. Zeolite membranes are widely used for gas separation processes, such as air separation, carbon capture, and hydrocarbon separations [17, 18].

Advantages of Inorganic Membranes

(i) Stability: Inorganic membranes exhibit excellent thermal, chemical, and mechanical stability, allowing them to withstand harsh operating conditions and aggressive chemical environments.

(ii) Selectivity: Certain inorganic membranes, such as zeolite, offer high selectivity due to their well-defined pore structures and molecular sieving properties.

(iii) Durability: Inorganic membranes generally exhibit a longer operational lifespan compared to polymeric membranes, as they are less susceptible to fouling, degradation, and mechanical failure.

Limitations of Inorganic Membranes

(i) Cost: The fabrication of inorganic membranes is often more complex and expensive compared to polymeric membranes, which may limit their widespread adoption in cost-sensitive applications.

(ii) Brittleness: Ceramic and zeolite membranes are prone to brittleness, making them susceptible to mechanical failure under stress or during handling.

(iii) Complexity: The fabrication and functionalization of certain inorganic

membranes, such as zeolite, can be challenging due to the complexity of their structures and the need for precise control over pore size and distribution.

To sum up, inorganic membranes show great potential as a category of membrane materials suitable for diverse separation applications due to their superior stability, selectivity, and longevity. Despite certain constraints, current investigations are aimed at overcoming these obstacles while devising innovative inorganic materials with enhanced performance and affordability for cutting-edge separation procedures.

1.2.3 Two-Dimensional Materials Membranes

Why 2D Materials

As discussed in the previous sections, polymeric membranes, due to their diverse range of species and ease of processing and scaling up, currently dominate the separation membrane market. However, conventional polymeric membranes have shown limitations in their performance as there exists a trade-off between permeability and rejection [19]. Additionally, issues such as plasticization and fouling can negatively affect their performance and reduce their service life. Inorganic membranes, although possessing superior thermal and chemical stability, often face challenges in terms of fabrication complexity and brittleness [20, 21]. Consequently, there is a growing interest in exploring new materials with high permeability and rejection capabilities, which could serve as next-generation separation membranes.

Two-dimensional (2D) materials, characterized by their atomically thin structure in one direction and large lateral size in the other two directions, have demonstrated immense potential in various fields, including catalysis [22, 23], electronic conduction [24, 25], energy storage and conversion [26, 27], and, most importantly, membrane separation [28, 29]. The unique structure of 2D materials allows for the construction of transport channels with atomically thin barriers, providing unparalleled permeability [30, 31]. Furthermore, their large lateral surfaces, rich in active sites and charge distribution, facilitate targeted chemical functionalization and controllable charge

regulation. Consequently, by utilizing modified 2D materials, it is possible to design channels with ideal chemical and physical selectivity [32].

Over the past few decades, researchers have synthesized hundreds of 2D materials with varying structures [33-35], such as porous and nonporous inner planes. This vast array of materials has significantly expanded the possibilities for selective channel construction. Additionally, the excellent dispersibility of some 2D materials in solution [36] makes it convenient to process them into membranes using well-established methods, such as casting and coating [37].

In contrast to traditional polymeric and inorganic membranes, 2D materials offer a promising avenue for advancing membrane separation technology [38]. Their inherent characteristics, coupled with the diversity of structures available, pave the way for developing next-generation separation membranes with enhanced permeability and selectivity. The integration of 2D materials not only overcomes the limitations of conventional polymer membranes in terms of performance trade-offs but also addresses the fabrication and brittleness challenges associated with inorganic membranes.

As research into the fundamental properties and fabrication processes of 2D materials continues to progress, it is anticipated that they will play a pivotal role in revolutionizing the field of membrane separation. With potential to outperform both polymer and inorganic membranes in terms of permeability, selectivity, and fabrication simplicity, 2D materials hold great promise for a wide range of separation applications, ultimately contributing to the development of sustainable and energy-efficient solutions to meet the increasing demands of various industries.

2D Material Membranes Classification, Application, and Challenges

When employing 2D materials for separation applications, two distinct types of selective channels can be created by assembling these materials into membranes [39]. Both types offer unique advantages and challenges, making them suitable for different separation processes.

The first type comprises 2D nanosheet membranes (Figure 1.8 a), which consist

of a single or a few layers of porous nanosheets supported by a porous substrate. The selectivity of these membranes is achieved through the differing transmission rates of the penetrants via the nanopores present on the 2D nanosheets. Factors such as size confinement, electrostatic interaction, and chemical or physical adsorption play crucial roles in influencing the transmission rates [40]. Due to the ultra-short transmembrane distance, 2D nanosheet membranes are considered as the ultimate separation membranes, offering the potential for unparalleled performance [41-45].

The second type involves 2D laminar membranes, (Figure 1.8 b) which are constructed by stacking 2D nanosheets layer upon layer. The mass transport in these membranes occurs within the confined interlayer nanochannel formed between two adjacent layers and in-plan channels created by intrinsic or perforated nanopores on nanosheets and the intraplanar gaps from the in-plan neighboring nanosheets. As different penetrants navigate the tortuous transmembrane pathway, high selectivity is achieved through size exclusion, electrostatic repulsion, and preferential adsorption within the nanochannel [32]. By optimizing the interstitial nanostructure and the physical and chemical properties of the nanosheet surfaces, laminar membranes can exhibit impressive performance in terms of both permeability and selectivity [46-48].

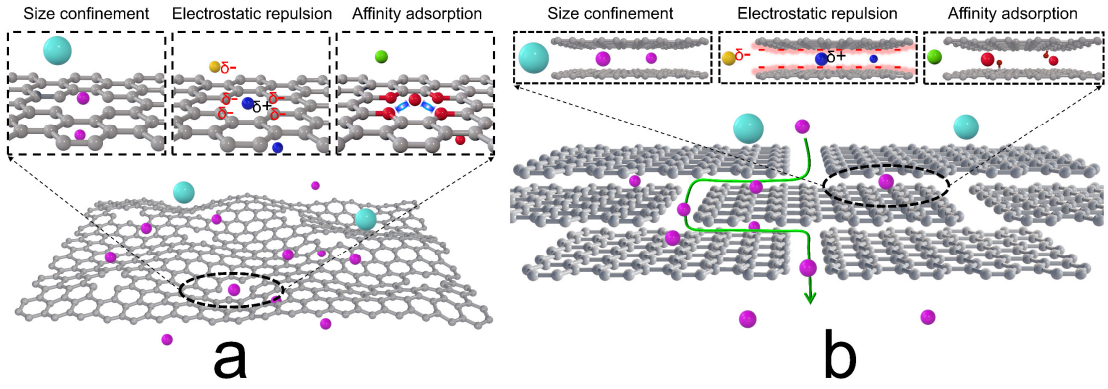

Figure 1.8 Schematic diagram of two types of selective channels constructed by 2D materials and their separation mechanism. a, Single-layer 2D nanosheet membrane. The selectivity originates from the size confinement, electrostatic interaction and chemical or physical adsorption of nanopores for the penetrants. **b**, 2D laminar membrane. The selectivity comes from the sized exclusion, electrostatic repulsion and prior adsorption of nanochannels for the penetrants.

(a) 2D nanosheet membranes

2D nanosheet membranes have attracted significant attention in the field of membrane separation due to their remarkable separation performance. These membranes can be further classified into two categories: i) perforated 2D nanosheets and ii) intrinsically porous 2D nanosheets. In recent years, various studies have been conducted to explore the potential of these membranes in gas and liquid separations, yielding impressive results that have far exceeded the performance of conventional membranes.

i) Perforated 2D nanosheets

Perforated 2D nanosheets are created by introducing nanopores into an otherwise nonporous 2D material. These nanopores can be generated through various methods such as electron beam lithography, reactive ion etching, and chemical etching [49-53]. Graphene, a single layer of carbon atoms arranged in a hexagonal lattice, is one of the most widely studied 2D materials for perforated nanosheet membranes. The introduction of subnanometer-sized pores in graphene has been shown to exhibit exceptional performance both in liquid and gas separation.

Mahurin and his team conducted an experimental analysis of the movement of ions and water through a stable, single-layer graphene membrane with nanometer-scale pores. Their findings suggest the potential use of porous, single-layer graphene as a desalination membrane. The oxygen plasma etching method was employed to produce nanometer-scale pores with tunable pores sizes in the graphene monolayer (Figure 1.9 a). The membranes thus obtained displayed nearly 100% salt rejection and swift water transport. Remarkably, water flow rates of up to 10^6 g m^{-2} s^{-1} at 40 °C were recorded when pressure difference was employed as the driving force, whereas the flow rates are near 70 g m^{-2} s^{-1} atm^{-1} when using osmotic pressure as the driving force [41]. Despite their remarkable filtration abilities, which allow for the blocking of the majority of ions, the practical application of porous graphene sheets has been hindered by their inherent fragility. Yang and his team have countered this drawback by developing a nanoporous graphene membrane, strengthened with a framework of single-walled carbon nanotubes

(SWNTs) (Figure 1.9 b). This construction of a large-scale graphene-nanomesh/single-walled carbon nanotube (GNM/SWNT) hybrid membrane effectively combines the merits of atomically thin membranes with exceptional mechanical strength. The monolayer GNM is designed with an abundance of subnanometer pores, facilitating efficient water molecule transport and offering size-selective separation by blocking solute ions or molecules. The SWNT network serves as a microscopic foundation, isolating the GNM into microsized islands and preserving the structural integrity of the GNM. Impressively, a water permeation rate of 20.6 liters m^{-2} $hour^{-1}$ bar^{-1} was achieved using GNM/SWNT-10s, while a large 97% salt rejection was maintained in a forward osmosis module. Moreover, the GNM/SWNT membrane demonstrated a hydraulic permeability of 97.6 liters m^{-2} $hour^{-1}$ bar^{-1}, with NaCl rejection rates exceeding 86% in a reverse osmosis module [43].

Expanding beyond water-phase ionic and molecular separation, nanoporous graphene has been explored for non-aqueous systems. Karnik and colleagues have crafted a chemically robust nanoporous graphene membrane and investigated organic liquids transport under subnanometer confinement (Figure 1.9 c). Their findings revealed that solvent properties can influence solute diffusion across graphene nanopores and continuum flow breakdown occurs when pore sizes is comparable to the sizes of the solvent. Noteworthy is the hexane permeance across the graphene membrane, which reached at 3.88 L m^{-2} h^{-1} bar^{-1}, markedly surpassing that of its branched isomers, which recorded a permeance of less than 0.1 L m^{-2} h^{-1} bar^{-1}. By comprehensively engineering membrane, nanoporous graphene membranes demonstrated outstanding performances. Specifically, in methanol, a permeance of 16.5 L m^{-2} h^{-1} bar^{-1} was achieved, along with a 95.9% rejection of Rose Bengal (RB) (molecular weight: 1018 g mol^{-1}). Meanwhile, in ethanol, the performance was measured at 4.92 L m^{-2} h^{-1} bar^{-1} with a 97.3% rejection rate [54].

Bunch and colleagues were among the pioneers in using porous graphene membranes for gas separation. Their research demonstrated that ultraviolet-induced oxidative etching could create pores in micrometer-sized graphene membranes, which

subsequently functioned as molecular sieves. They utilized a pressurized blister test and mechanical resonance to gauge the transport of a variety of gases (including H_2, CO_2, Ar, N_2, CH_4, and SF_6) through these pores. Two porous graphene membranes were fabricated, labeled as Bi-3.4 Å and Bi-4.9 Å. These labels reflect their respective capabilities: the Bi-3.4 Å bilayer graphene membrane could sieve molecules with kinetic diameters greater than that of Ar (3.4 Å), while the Bi-4.9 Å membrane could sieve molecules with kinetic diameters smaller than that of SF_6 (4.9 Å) [31]. Subsequently, Park and his team developed physically perforated double-layer graphene, encompassing up to several million pores with narrowly distributed diameters between less than 10 nanometers to 1 micrometer. They reported an H_2/CO_2 selectivity of 4.69, and a hydrogen permeance approaching 10^{-2} mol m^{-2} s^{-1} Pa^{-1} for porous graphene with an average pore size of 7.6 nm, several orders of magnitude better than other gas separation membranes [45]. In addition, Agrawal and his team have innovatively employed a nanoporous-carbon-assisted graphene transfer technique to construct a sizable area (1 mm^2) of single-layer graphene membrane on a macroporous support. Remarkably, despite the ultralow density of intrinsic defects (a porosity of a mere 0.025%), the membrane achieves an impressive H_2 permeance of up to 4.1×10^{-7} mol m^{-2} s^{-1} Pa^{-1}. Moreover, when tested with a mixed gas feed, the membrane yielded an H_2/CH_4 separation factor of up to 18. In a bid to further optimize the membrane, they implemented an ozone functionalization-based etching and pore-modification process. This strategy led to an increase in nanopore density and/or a reduction in effective pore size, resulting in a significant improvement in H_2 permeance (by up to 300%) and H_2/CH_4 selectivity (by up to 150%) [42].

Similarly, MoS_2, another 2D material, has also been studied for its potential in perforated nanosheet membranes. In an initial exploration of the potential of nanoporous MoS_2 and other TMDs for desalination, Heiranian et al. demonstrated over 99% salt rejection through MD simulations. Notably, the predicted permeate flux of monolayer MoS_2 (exceeding 10 L cm^{-2} per day per MPa) was estimated to be 5-fold larger than other desalination membranes and 70% higher than a monolayer graphene

with equivalent pore size and porosity [55]. Ion transport through monolayer MoS_2, achieved by creating 300-1200 pores of 0.5 to 1 nm in size using an ion beam irradiation technique, has also been reported (Figure 1.9 d) [56]. Despite extensive research efforts into the synthesis of MoS_2 via CVD or modified CVD methods, practical realizations have been absent, and investgiations have been primarily focused on MD simulations. This may be due to the difficulty and lack of scalability in synthesizing defect-free MoS_2. Consequently, due to the inherent challenges associated with monolayer MoS_2, lamellar membranes are emerging as a viable and scalable alternative.

Boron nitride (BN) nanosheets have also been manipulated to form nanoporous structures for membrane applications. Cun and colleagues prepared a large, 4-inch single-orientation monolayer of hexagonal boron nitride (h-BN) nanomesh and transferred it onto a substrate. The 2 nm voids in the h-BN layer were created by exposing h-BN/Rh(111) to low-energy Ar ions and then applying an annealing procedure (Figure 1.9 e). Subsequent ion conductance experiments revealed the pivotal role the number of voids in the tested nanoporous BN membrane plays in influencing the characteristics of the current-voltage curve [57]. Keyser and his team fabricated hexagonal boron nitride with inherent defects using the CVD method. They noted a remarkable shift from monovalent cation selectivity to anion selectivity by modulating the concentration of multivalent ions and triggering charge inversion on the 2D membrane. This observation highlights the potential of this membrane for osmotic power generation [58].

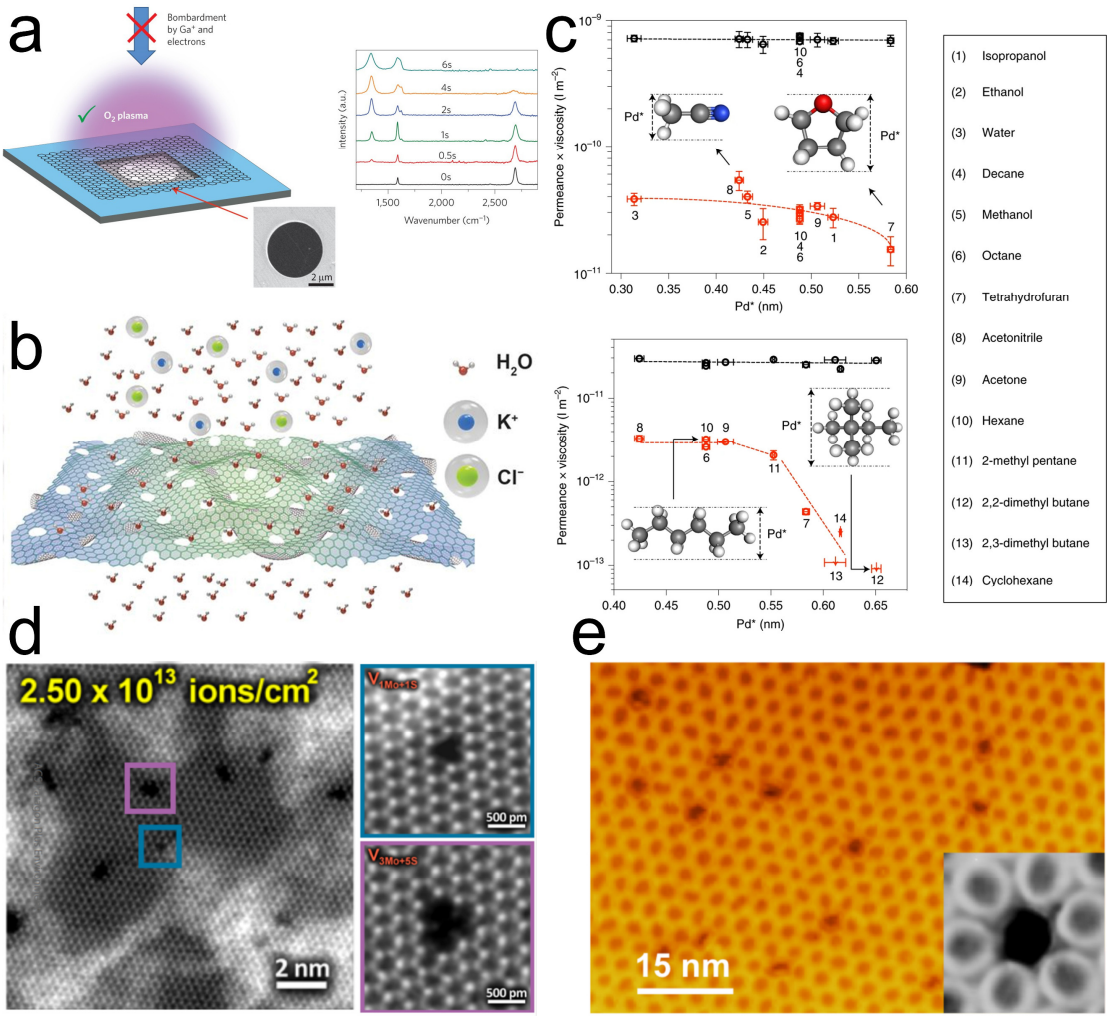

Figure 1.9 Perforated 2D nanosheets membranes. a, Schematic and Scanning Electron Microscopy (SEM) image of a single-layer graphene layer suspended on a 5 μm diameter hole. Various techniques for nanoporous graphene fabrication are illustrated, including ion bombardment, electron bombardment, and O_2 plasma treatment. **b**, Schematic representation of a mechanically robust, large-area Graphene Nanomesh/Single-Walled Carbon Nanotube (GNM/SWNT) hybrid membrane designed for efficient water desalination. **c**, Display of the dependency of the viscosity-permeance product on the smallest permeable solvent diameter (Pd*) for PITEM(50)-(top) and PITEM(20)-supported (bottom) nanoporous graphene membranes, respectively. The dashed lines serve as a visual guide, and permeance is calculated based on the total membrane area. **d**, Characterization of single-layer MoS_2 and high magnification images of atomic vacancies with varying atomic configurations, using Aberration-Corrected Scanning Transmission Electron Microscopy (AC-STEM). **e**, Presentation of multiple 2 nm voids at pore sites, resulting from the "can-opener" effect post annealing of h-BN/Ar/Rh(111) to 900 K, Ut = -1.20 V, It = 0.50 nA. The right-bottom insets provide 9×9 nm^2 close-up views of voidal v-BN.

ii) Intrinsically porous 2D nanosheets

Intrinsically porous 2D nanosheets possess inherent pores or voids within their structure, eliminating the need for further perforation. These materials are of great interest for membrane separation applications due to their natural size-selective characteristics. Examples of such materials include metal-organic frameworks (MOFs) and covalent-organic frameworks (COFs) [59].

For instance, ultrathin MOF nanosheets have been explored for their potential in ion separation applications. A study conducted by Wang and his team used a facilitated interfacial growth strategy to integrate UiO-66-$(COOH)_2$ crystals into a single artificial nanochannel (NC) within polyethylene terephthalate (PET) membranes. These resulting metal–organic framework-based subnanochannels (MOF-SNCs), with their unique asymmetric structures, demonstrated rapid conductivity for monovalent ions such as K^+, Na^+, and Li^+ along the subnanometer-to-nanometer channel direction. Meanwhile, the conductivity of divalent ions such as Ca^{2+} and Mg^{2+} was considerably lower, exhibiting a distinct mono/divalent ion selectivity of 10^3. Interestingly, the ion transport was pH-dependent, with the selectivity capable of being modulated by a factor of 10^2 to 10^4 when the pH was varied from 3 to 8. Binary ion permeation experiments indicated a K^+ permeation rate of 10^5 mol m^{-2} h^{-1} and superior K^+/Mg^{2+} selectivity, surpassing the performance of previously reported membranes [60]. Zhang and colleagues have documented the successful exfoliation of 2D monolayer aluminum tetra-(4-carboxyphenyl) porphyrin frameworks, also known as Al-MOF nanosheets. They then used these exfoliated nanosheets to assemble ultra-thin, water-stable Al-MOF membranes. Remarkably, the 2D Al-MOF membranes have demonstrated water flux rates reaching up to 2.2 mol m^{-2} $hour^{-1}$ bar^{-1}, while maintaining near-total rejection rates of almost 100% for the examined inorganic ions [61]. In addition to ionic sieving [62], MOFs are expanding their potential by exhibiting other separation capabilities [63, 64]. Jin et. al. presented an approach to mitigating lattice defects in MOF membranes, leveraging a high-probability theoretically coordination strategy (Figure 1.10 a). This technique generates adequate chemical potential to circumvent the steric obstruction

experienced when fully linking ligands to metal clusters. The application of this method resulted in the successful preparation of three distinct MOF membranes, namely, Zr-MOF(fumarate), Zr-MOF(BDC), and Zr-MOF[BDC-$(OH)_2$]. This work has resulted in the development of a series of highly interconnected MOF membranes, boasting ångström-sized lattice openings, capable of achieving high and stable separation performance for gases, water desalination, and organic solvent azeotropes. Specifically, the Zr-MOF(fumarate) membrane demonstrated an H_2 permeability of 1175 Barrer (where 1 Barrer = 10^{-10} cm^3(STP) cm^{-2} s^{-1} cm Hg^{-1}) and an H_2/CO_2 selectivity of 69.2. For desalination, the Zr-MOF membranes exhibited an extraordinarily high water/salt selectivity reaching up to 9000. Moreover, the Zr-MOF(fumarate) membrane showed a high flux of 17.71 kg m^{-2} h^{-1} and methanol purity greater than 99.5 wt% when dealing with methanol/DMC azeotrope mixtures [65].

COF nanosheets have shown promise in various separation applications due to their highly ordered porous structures and customizable functionalities [66]. For example, Tang and his team engineered monolayer COF nanosheets and showcased their potential in osmotic energy harvesting (Figure 1.10 b). They supported the metal tetraphenylporphyrin-based COF (MTPP–COF) monolayers, featuring a square nanopore array, on SiNx. These membranes, characterized by an orderly pore configuration and a high pore density of up to 4.5×10^{12} cm^{-2}, achieved remarkably low membrane resistivity and exceptionally high ion conductivity. Owing to the intrinsic positive charge of the COF nanosheets, they displayed superior anion selectivity. When employed as osmotic power generators, these membranes generated an unprecedented output power density exceeding 200 W m^{-2} upon the mixing of artificial seawater and river water [67]. Shinde and colleagues prepared a crystalline TFP-DHF 2D COF membrane, composed of 1,3,5-triformylphloroglucinol (TFP) and 9,9-dihexylfluorene-2,7-diamine (DHF), using the Langmuir-Blodgett (LB) method. This method enables the construction of a single COF layer, approximately four unit cells in thickness, which can be transferred to various support surfaces layer by layer. Supported on an anodic aluminum oxide (AAO) porous surface, the TFP-DHF 2D COF

membrane demonstrated exceptional permeabilities for both polar and nonpolar organic solvents. These permeabilities were about 100 times greater than those of amorphous membranes prepared using the same method, and were comparable to the best-performing polymer membranes. The membrane showcased a sharp molecular sieving property with a molecular weight retention onset (MWRO) around 600 Da and a molecular weight cutoff (MWCO) close to 900 Da [68].

Two-dimensional conjugated-polymer-frameworks (CPFs) have also been considered as intrinsically porous 2D nanosheets for membrane applications [69, 70]. Their high thermal and chemical stability, along with their tunable pore structure, make them suitable for various separation processes. In a study, Han and his team managed to synthesize ultrathin CPF nanosheets with a thickness down to 1 nm through chemical vapor deposition (Figure 1.10 c). Intrinsically, these CPF membranes possess regular, rhombic sub-nanometer (10.3 x 3.7 Å) channels, which allow for efficient water transport while blocking ions. With an ideal thickness of 8 nm, the membranes exhibited an impressive water flux reaching as high as 112 mol m^{-2} h^{-1} bar^{-1} (~2 L m^{-2} h^{-1} bar^{-1}), while maintaining a salt rejection rate of 99.5% under forward osmosis conditions. Notably, these CPF membranes also demonstrated a high-pressure resistance of up to 13 bar for 450 hours and achieved a NaCl rejection rate of 83% and a water flux of >9.5 L m^{-2} h^{-1} bar^{-1} in reverse osmosis conditions [71, 72].

The above examples demonstrate the impressive performance of 2D nanosheet membranes in various separation applications. Their unique properties, such as high permeability, selectivity, and tunable pore structures, have garnered significant interest in the scientific community. However, it is important to note that the fabrication of large-scale, defect-free membranes remains a significant challenge. As research progresses, it is expected that novel strategies for the synthesis, assembly, and functionalization of 2D nanosheets will be developed to overcome these challenges and further improve the performance of 2D nanosheet membranes.

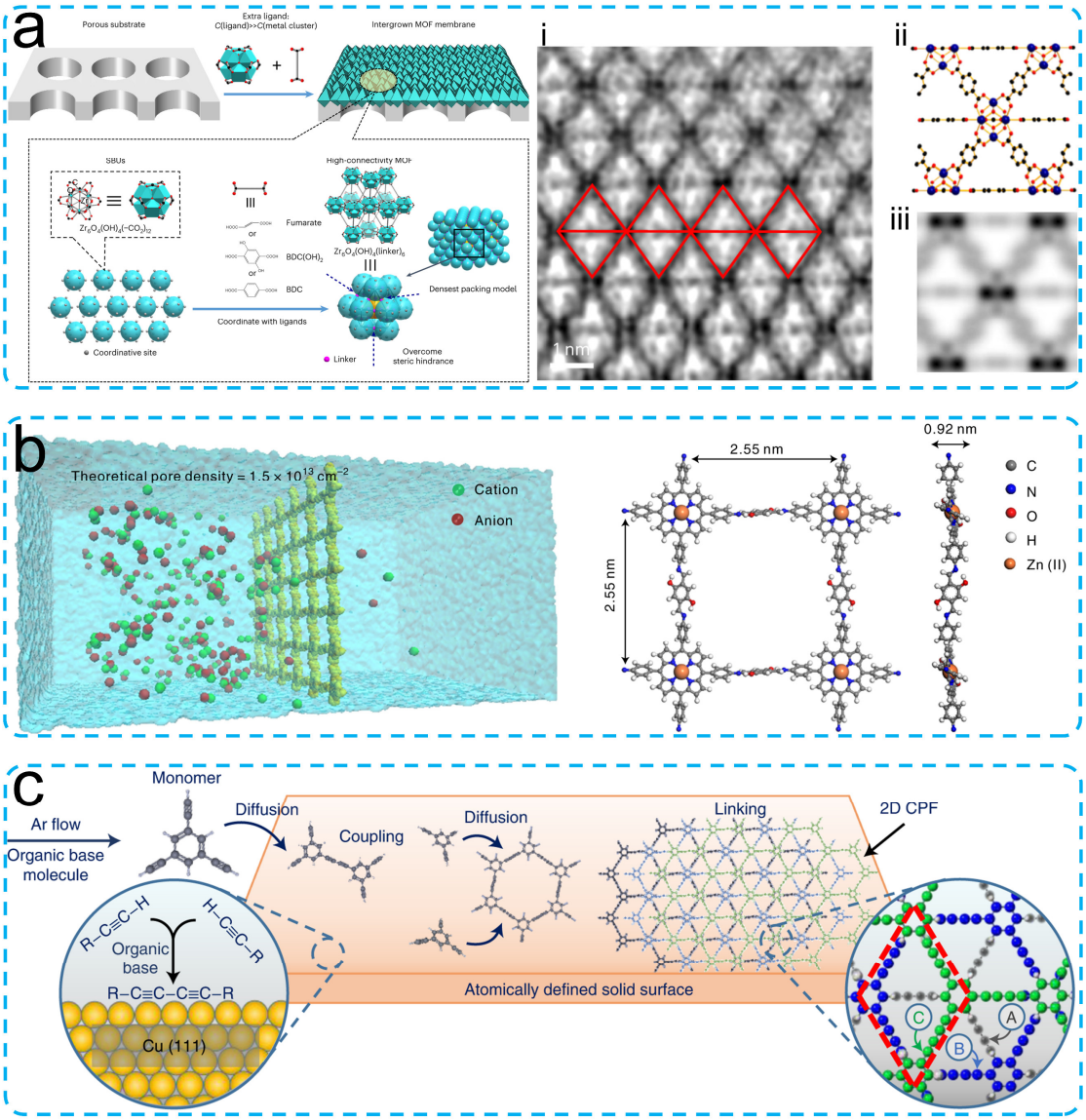

Figure 1.10 Intrinsically porous 2D nanosheets membranes. a, Depiction of MOF membrane formation with perfect lattices. $Zr_6O_4(OH)_4(-CO_2)_{12}$ SBUs coordinate with diacid ligands to generate a 12-connected Zr-MOF intergrown membrane on the surface of a porous substrate (left). High-resolution TEM (HRTEM) images of Zr-MOF(BDC) along the [110] zone axes reveal a perfect lattice (right). (i) Contrast transfer function-corrected image. (ii) Projected structural model. (iii) Simulated projected potential. **b**, Morphology and structure characterization of a COF monolayer membrane. Schematic representation of ion transport through a COF monolayer membrane under a salt gradient (left), and a simulated structure of ZnTPP–COF derived from density functional theory calculations (right). **c**, Synthesis and characterization of sCPF membrane. The figure provides a schematic illustration of the surface-confined CVD growth of ABC-stacked sCPF membrane. The distinct stacking layers (A–C) are represented in grey, blue, and green. The red dashed lines are used to highlight the formed rhombic channel between adjacent layers (B and C).

(b) 2D laminar membranes

Transitioning from 2D nanosheet membranes, another fascinating class of 2D material-based membranes is the 2D laminar membranes. In contrast to nanosheet membranes, laminar membranes are assembled *via* the stacking multiple nanolayers, which considerably reduces defects and increases mechanical strength. These improvements enable their potential use in real-life separation processes and higher-pressure operations. The distinctive structure of 2D laminar membranes, characterized by adjustable interlayer spacing and a large specific surface area, has been employed in various applications such as water desalination, gas separation, and organic solvent recovery. Furthermore, the diverse range of 2D materials enables the design of membranes with tailored properties, addressing specific separation challenges.

In the following sections, we will delve into various types of 2D laminar membranes, exploring their structure, preparation, properties, and applications in membrane separation processes. The focus will be on i) graphene oxide (GO) and its derivative laminar membranes, ii) transition metal dichalcogenides (TMDs) laminar membranes, iii) transitional metal carbides and/or nitrides (MXene) laminar membranes, and iv) clay and 2D LDH laminar membranes

i) Graphene oxide (GO) and reduced graphene oxide (rGO)

Graphene oxide (GO) and reduced graphene oxide (rGO) are derivatives of graphene, which is a single-atom-thick sheet of carbon atoms arranged in a honeycomb lattice. GO is synthesized from graphene through the oxidation process, introducing oxygen-containing functional groups such as hydroxyl, epoxy, and carboxyl on the basal plane and edges. The chemical reduction of GO leads to the formation of rGO, which has fewer oxygen-containing functional groups and improved electrical conductivity compared to GO.

Various methods have been employed for the synthesis of GO, including Hummers' method [73], Brodie's method [74], and Staudenmaier's method [75], with

the Hummers' method being the most widely used due to its efficiency and low risk [76]. For the reduction of GO to rGO, numerous reducing agents such as hydrazine, sodium borohydride, and ascorbic acid have been employed [77].

GO and rGO laminar membranes are typically fabricated by stacking multiple layers of nanosheets through various techniques, such as vacuum filtration, spin-coating, and layer-by-layer assembly. Vacuum filtration is a widely used method due to its simplicity and scalability, allowing for the fabrication of membranes with controllable thickness and interlayer ordering [78].

The applications of GO and rGO laminar membranes in membrane separation processes have been extensively studied, demonstrating promising results in various fields. The first breakthrough in the development of GO laminar membranes was reported by Nair et al., who demonstrated a complete barrier to various states of matter, encompassing liquids, vapors, and gases - even helium (Figure 1.11 a). Remarkably, these membranes permit the rapid permeation of water, with water molecules traversing through the membrane around 10^{10} times faster than helium. The underlying mechanism involves the low-friction movement of a water monolayer within the two-dimensional capillaries shaped by proximate graphene sheets. The hindrance of other molecules' diffusion is attributed to the capillaries' reversible constriction under low humidity conditions and/or due to blockages formed by water [47]. In a subsequent experiment, it was shown that the GO laminar membrane, when applied in an aqueous environment, could function as a molecular sieve (Figure 1.11 b). This membrane effectively blocks any solutes that have hydrated radii exceeding 4.5 angstroms. Interestingly, ions smaller than this size are able to pass through the membrane at rates thousands of times greater than what conventional diffusion would predict [48]. Since then, numerous studies have focused on optimizing the fabrication and performance of GO laminar membranes for different applications.

Water purification: GO and rGO membranes have shown remarkable performance in removing contaminants from water. For example, Zhang and colleagues reported a graphene oxide membrane characterized by a high rejection rate, exceeding

95% for various heavy metal ions, including lead (Pb^{2+}), nickel (Ni^{2+}), and zinc (Zn^{2+}) ions, all the while demonstrating outstanding water permeability measured at 4.7 L m^{-2} h^{-1} bar^{-1}. Furthermore, this membrane showcased impressive long-term performance stability, maintaining its effectiveness throughout a 150-hour nanofiltration examination [79]. Peng and his team revealed the exceptional separation capabilities of GO membranes, including an 85% rejection rate for Evans Blue (EB, 1.2 nm x 3.1 nm), and a water flux of 71 L m^{-2} h^{-1} bar^{-1}. The GO separation performance was found to be influenced by variables such as pH, salt concentration, and applied pressure. For instance, as the pH decreased, the flux also declined, while the rejection rate of EB molecules increased. Specifically, at a pH of 3, the flux dropped to 12.19 L m^{-2} h^{-1} bar^{-1}, and the rejection rate reached 100%. Moreover, as the pressure escalated from 0.3 MPa to 1.3 MPa, the growth rate of water flux noticeably decelerated, while the EB rejection rate rose from 90.2% (at 0.3 MPa) to 98.8% (at 1.3 MPa) [80]. Zhang and colleagues documented their work on a rGO membrane with a thickness of 100 nm. Under forward osmosis conditions, using a 2.0 mol L^{-1} NaCl solution as the draw solution, this membrane exhibited a water flux of 57.0 L m^{-2} h^{-1} (Figure 1.11 c). Notably, the membrane demonstrated superb selectivity towards organic matter and various ions, completely blocking Acid Orange 7 (AO7) and copper ions (Cu^{2+}) over a filtration period of 12 hours [81]. Gao and colleagues highlighted the exceptional separation performance of rGO membranes under nanofiltration. The 22 nm-thick rGO membrane showcased a significant pure water permeability of 21.8 L (m^2 h bar)$^{-1}$. Simultaneously, it maintained an extraordinarily high rejection rate, exceeding 99%, for large organic dyes like methyl blue and direct red 81 [82].

Desalination: Numerous investigations have been undertaken to explore the viability of GO and rGO membranes for desalination purposes. However, these membranes have shown only moderate salt rejection capabilities [37, 83-88]. For example, pure GO membranes exhibited a water flux of 0.6 L/m^2×h and a salt rejection rate of 60% in forward osmosis (FO) experiments [89]. Under 1MPa pressure in reverse osmosis (RO) setups, a lower salt rejection rate of around 25% was observed [90].

Comparatively, rGO membranes demonstrated superior NaCl rejection, attributed to their reduced interlayer spacing. Zhang et al showed that a favorable NaCl rejection of 83% with water permeance of 1.05 LMH/bar was achieved in an air-thermally treated rGO (Air-rGO) membrane (Figure 1.11 d) [88].

Organic solvent nanofiltration (OSN): The application of GO and rGO membranes in OSN has also shown promising results [91, 92]. Nair et al reported a highly laminated graphene oxide (GO) membrane, stacked with large GO flakes, which displayed excellent methanol permeance, approximately 7 $L/m^2 \cdot h \cdot bar$, and an impressive rejection rate exceeding 99.9% for small molecular weight organic dyes (Figure 1.11 e) [93]. Shi and his team developed a solvent-solvated rGO (S-rGO) membrane. The S-rGO membrane with 18 nm exhibited an exceptionally high acetone permeance, reaching up to 215 $L\ m^{-2}\ h^{-1}\ bar^{-1}$. Remarkably, the S-rGO membrane entirely rejected negatively charged Evans blue molecules (EB, 960.8 $g\ mol^{-1}$, 3.4 nm) in a methanol solution, while maintaining an extremely high solvent permeance of 75.3 $L\ m^{-2}\ h^{-1}\ bar^{-1}$ [94].

Gas separation: The gas separation performance of GO and rGO membranes has been widely investigated [95]. Li and colleagues documented that ultrathin GO membranes demonstrated remarkably high separation selectivities, reaching up to 3400 for H_2/CO_2 mixtures and 900 for H_2/N_2 mixtures. Moreover, these membranes exhibited an impressive H_2 permeance surpassing 10^{-7} $mol/m^2 \cdot s \cdot Pa$ (Figure 1.11 f) [46]. In another study, Park and his team noted that ultrathin GO membranes, less than 10 nm in thickness, exhibited a CO_2/N_2 selectivity of approximately 20 and a CO_2 permeance close to 8500 barrer [96]. Joshi et al. reported a Fe intercalated rGO membranes with the highest N_2/CO_2 selectivity of approximately 97 at 110 mbar. When increasing pressure to 330 mbar, these iron-enhanced rGO membranes (Fe-rGOMs) display an N_2/CO_2 selectivity of around 67 and a N_2 permeance of roughly 1317 GPU [97].

Pervaporation: GO membranes have also shown potential in pervaporation applications due to their sub-nanometer interlayer spacing and the hydrophilic nature of the GO sheets, which favor prioritized water permeation [78, 98-100]. A study by

Huang and colleagues utilized a GO membrane with a thickness between 600 and 1600 nm for the separation of ethanol and dimethyl carbonate (DMC)/water using pervaporation, demonstrating exceptional separation performance for DMC/water mixtures with a separation factor of 740 and a total water permeability of 1702 g/(m^2 h) [99]. Another study by Liu and associates discovered that the permeability of water was approximately 80 times faster than that of alcohols. This led to the preferential extraction of water in pervaporation of water/alcohol mixtures, yielding alcohols with a concentration of around 97% [98].

Despite the promising performance of GO and rGO laminar membranes, several challenges need to be addressed to fully realize their potential in real-world applications. First, the long-term stability of these membranes in aqueous environments remains a concern due to the inherent hydrophilicity of GO, which can cause swelling and a subsequent decrease in performance. Second, the fabrication of large-scale, defect-free membranes with uniform interlayer spacing and controlled pore sizes is still a significant challenge. Finally, the improvement of their mechanical strength and resistance to fouling is necessary to extend their service life and applicability in various separation processes.

In conclusion, the development of graphene oxide (GO) and reduced graphene oxide (rGO) laminar membranes has shown great potential in various membrane separation processes. By addressing the current challenges associated with their stability, scalability, and performance, these membranes are expected to play an increasingly important role in the future of membrane technology. As research on GO and rGO laminar membranes continues to advance, their potential for real-world applications becomes increasingly promising.

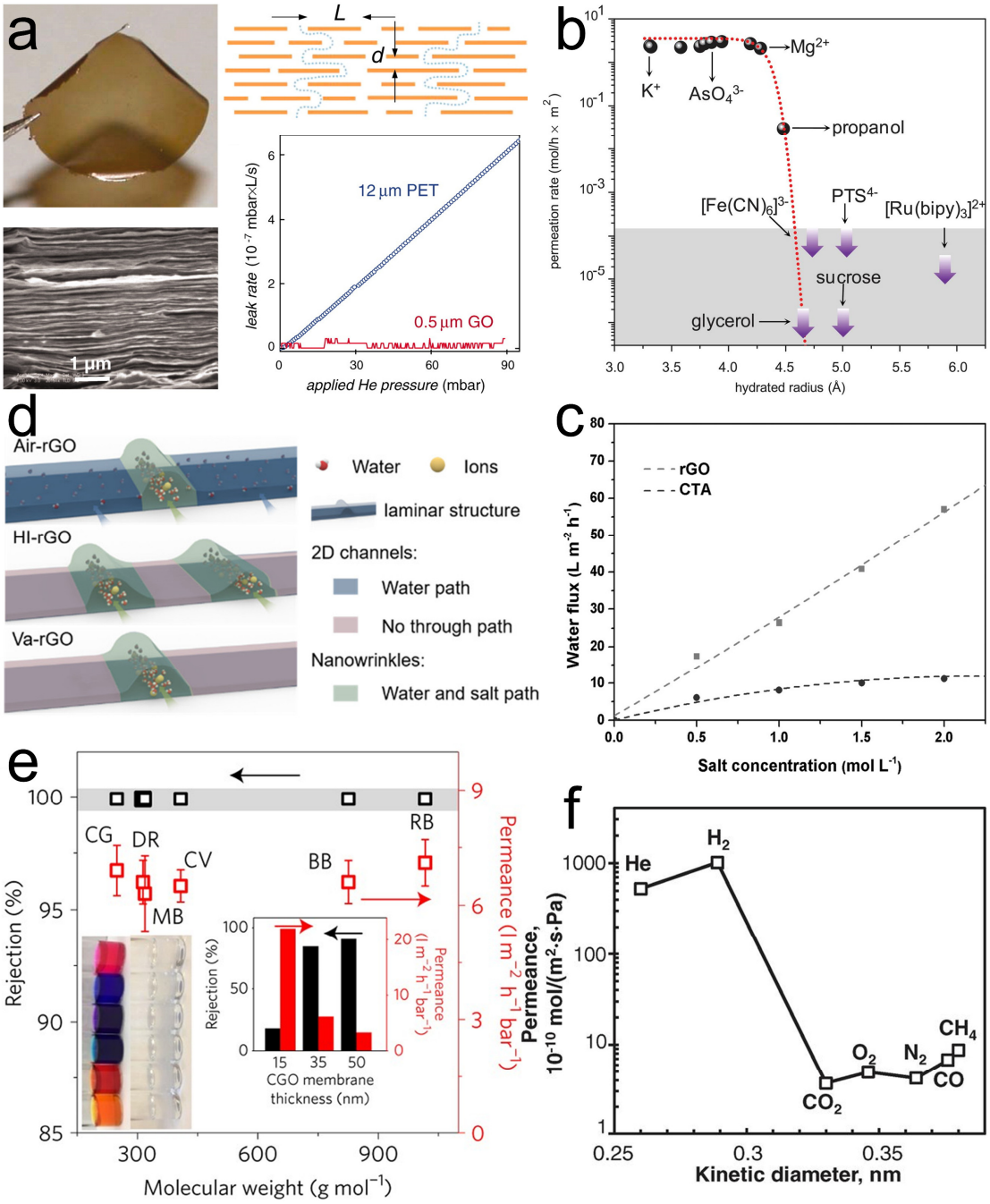

Figure 1.11 GO and rGO laminar membranes. a, Demonstration of the fabrication of helium leak-tight GO membranes. The photograph displays a 1-µm-thick GO film peeled from a Cu foil (top-right). An electron micrograph reveals the cross-section of the membrane (bottom-right). A schematic illustrates potential pathways for permeation through the laminates (top-left), where a typical L/d ratio is ~1000. Examples of He-leak measurements for a freestanding submicrometer-thick GO membrane and a reference PET film (normalized per square centimeter) are shown (bottom-left). **b**, Illustration of the sieving property through GO membranes showing the permeation rates across a 5-µm-thick GO membrane using a 1 M feed solution. No detectable permeation was recorded for solutes within the gray area during tests lasting at least 10

days. The thick arrows indicate detection limits, which vary depending on the solute. The dashed curve serves as a guide, showing an exponentially sharp cutoff at 4.5 Å, with a width of ≈0.1 Å. **c**, Variations of water fluxes across a 100 nm-freestanding rGO membrane as function of the salinity of the draw solution and compared to commercial HTI cellulose triacetate (CTA) membranes. **d**, Diagram illustrating the transport of water and NaCl through the 2D nano-architectures, including nanochannels and nanowrinkles, in the thermally treated GO under air (Air-rGO), thermally treated GO under vacuum (Va-rGO), and HI vapor reduced GO (HI-rGO) membranes. **e**, Demonstration of molecular sieving and organic solvent nanofiltration via HLGO membranes. This figure showcases the rejection and permeance of various dyes in methanol in relation to their molecular weight. The left inset offers a visual comparison of dye solutions in methanol pre- and post-filtration through an 8 nm HLGO membrane. The right inset provides a graphical representation of MB rejection and methanol permeance through a CGO membrane of varying thicknesses. **f**, Single-gas permeation accross GO membranes supported on porous Anodic Aluminum Oxide (AAO) at 20°C, featuring permeances of seven gaseous molecules through a GO membrane with 18 nm thickness.

ii) Transition metal dichalcogenides (TMDs)

Transition metal dichalcogenides (TMDs) are a class of layered materials composed of a transition metal atom (such as Mo, W, Nb, or Ta) and two chalcogen atoms (such as S, Se, or Te). These materials possess unique electronic, optical, and mechanical properties, making them attractive candidates for various applications, including membrane separation. TMDs are typically synthesized through chemical vapor deposition (CVD), physical vapor deposition (PVD), and chemical exfoliation [101].

To fabricate TMD laminar membranes, several methods can be employed, such as vacuum/pressure filtration, layer-by-layer assembly, and solution casting due to the good dispersibility in aqueous phase. These techniques allow for precise control of the membrane thickness, enabling the tailoring of membrane properties for specific separation applications.

TMD laminar membranes have demonstrated promising performance in various membrane separation processes [102]:

Water purification: Sun and colleagues initially reported on a MoS_2 laminar membrane that had an 89% rejection rate for Evans Blue and exhibited a water permeance of 245 LMH/bar, which is 3-5 times greater than that of GO membranes [103]. Mi and his team assessed the dye separation performance of layered MoS_2 membranes (Figure 1.12 a). The membrane with 500 nm thickness achieved 90% removal efficiency for rhodamine-WT. However, the rejection of methylene blue dropped from an initial 100% to approximately 40% since physical adsorption occurred on the membrane surface at the start of the filtration test [104]. Hu et al. reported a MoS_2 laminar membranes stacked by atomic-defect-rich 1T-MoS_2 (S-ADR-MoS_2) nanosheets, which exhibited high water fluxes (181–345 L $m^{-2}h^{-1}$ bar^{-1}) and effective Pb^{2+} separation performance (84.5–99.6%) [105]. In another study, Wang et al., found that the MoS_2 laminar membranes could recover Ag^+ with the 1-day removal capacity of ~ 4000 mg/g, due to a redox reaction between Ag^+ ions and MoS_2 nanosheets [106]. Peng and colleagues reported the size-selective tungsten disulfide (WS_2) separation membranes crafted from chemically exfoliated WS_2 nanosheets through filtration. These laminated WS_2 membranes exhibit a water permeance of 450 L m^{-2} h^{-1} bar^{-1}, with a rejection rate exceeding 90% for Evans Blue molecules [107].

Desalination: The pristine MoS_2 membrane demonstrated superior desalination performance in comparison to the GO membrane. By assembling chemically exfoliated MoS_2 nanosheets using pressure-assisted filtration, a laminated membrane approximately 500 nm thick was produced by Wang et al. This membrane showed a rejection rate of roughly 55-70% for sodium-based ionic species, including acetate, sulfate, and citrate, and a pure water flux of 50 LMH/bar [104]. In another study, Li and his team constructed MoS_2 membranes with a thickness of approximately 7 nm (Figure 1.12 b). They achieved this by transferring Chemical Vapor Deposition (CVD)-grown, centimeter-scale 2D MoS_2 layers onto porous polymeric substrate. These MoS_2 membranes showed high water permeance (>322 L m^{-2} h^{-1} bar^{-1}), due to the ultra-thin membrane thickness, along with impressive ion rejection rates exceeding 99%. This high rejection rate was observed for various seawater salts such as Na^+, K^+, Ca^{2+}, and

Mg^{2+} [108].

Organic solvent nanofiltration (OSN): The application of TMD laminar membranes in OSN has been explored as well. Zhang and his team utilized a few-layer molybdenum disulfide (MoS_2) nanoflakes, fabricated through a hydrothermal method (referred to as hydro-MoS2), to construct the laminar membrane. This method was developed to address the chemical and structural instability of membranes constructed from chemically exfoliated MoS_2 nanosheets, which showed a rapid decline in solute rejection over a short period of time. By combining the hydro-MoS_2 membrane construction with a "supportive" drying process, they achieved a high rejection rate of over 87% against Rose Bengal (size 1.45 nm) while still permitting isopropanol (size 0.58 nm) to pass through at a rate of more than 3 L m^{-2} h^{-1} bar^{-1} during a test spanning 7 days [109]. Ran utilized MoS_2 nanosheets as the structural building blocks to develop ultrathin 2D lamellar membranes for OSN (Figure 1.12 c). A dry MoS_2 (D-MoS_2) membrane, with a thickness of 20 nm and an interlayer distance of 0.62 nm, displayed remarkable water and acetonitrile permeance of 458 and 1371 L m^{-2} h^{-1} bar^{-1}, respectively. Meanwhile, the solvated MoS_2 (S-MoS_2) membrane, featuring wider galleries and a thickness of 36 nm, showed even higher permeance for water and acetonitrile, reaching 1881 and 5207 L m^{-2} h^{-1} bar^{-1} respectively. Importantly, both the D-MoS_2 and S-MoS_2 membranes exhibited optimal rejections for molecules larger than 1.4 nm, with 100% rejection rates for Evans Blue and Methylene Blue [110].

Gas separation: TMD laminar membranes have demonstrated promising results in gas separation applications. Wang and colleagues prepared ultrathin 2D MoS_2 membranes for H_2/CO_2 separation (Figure 1.12 d). The resultant membrane, which was 17 nm thick, demonstrated a significant H_2 permeance of 27440 GPU. However, its H_2/CO_2 selectivity of 3.4 was relatively lower, which is attributed to the fairly large nanochannel interlayer spacings (0.62 nm and 1.0 nm) and the presence of non-selective nanopores [111]. Furthermore, Eswaramoorthy and his team identified that 2H phase MoS_2 membranes, despite having a narrower interlayer spacing of 0.62 nm than the 1.1 nm found in 1T phase MoS_2 membranes, exhibit enhanced gas permeability by 30%,

maintaining similar gas selectivity. The resulting membrane achieved an H_2 permeability of 1175 barrer and an H_2/CO_2 selectivity of 8.29, thus outperforming the established Robeson upper bound limit [112].

TMDs laminated membranes, such as MoS_2, have exhibited exceptional water permeation in reverse osmosis (RO) applications and improved stability (limited swelling) compared to GO membranes, thanks to their strong van der Waals (VdW) forces and the absence of hydrophilic groups. However, several challenges still need to be addressed to fully exploit the potential of TMDs membranes in practical applications:

a) *Molecular cutoff dependence on intercalated water:* The molecular cutoff of MoS_2 membranes relies on the presence of intercalated water molecules within the laminated structure. This could potentially affect the long-term stability and selectivity of the membranes, especially under varying operational conditions.
b) *Scalability:* Although TMDs membranes have shown promising performance on a laboratory scale, their production on an industrial scale remains a challenge. Developing cost-effective, scalable methods for synthesizing and assembling TMDs membranes is crucial for their widespread adoption in various applications.
c) *Stability:* While TMDs membranes demonstrate better stability compared to GO membranes, they still face issues related to their long-term stability under various conditions, such as pH, temperature, and pressure. Further research is needed to enhance the chemical and mechanical stability of TMDs membranes to ensure their reliability in real-world applications.
d) Reproducibility: The reproducibility of TMDs membrane performance is another critical aspect to consider. The fabrication process must be consistent to ensure that the membrane properties remain uniform, allowing for predictable and reliable performance in different applications.

By addressing these challenges, TMD-based laminated membranes could unlock

new opportunities in the field of membrane separation and pave the way for advanced, efficient, and sustainable technologies. Continued research and development efforts are required to overcome these challenges and fully realize the potential of TMDs laminated membranes.

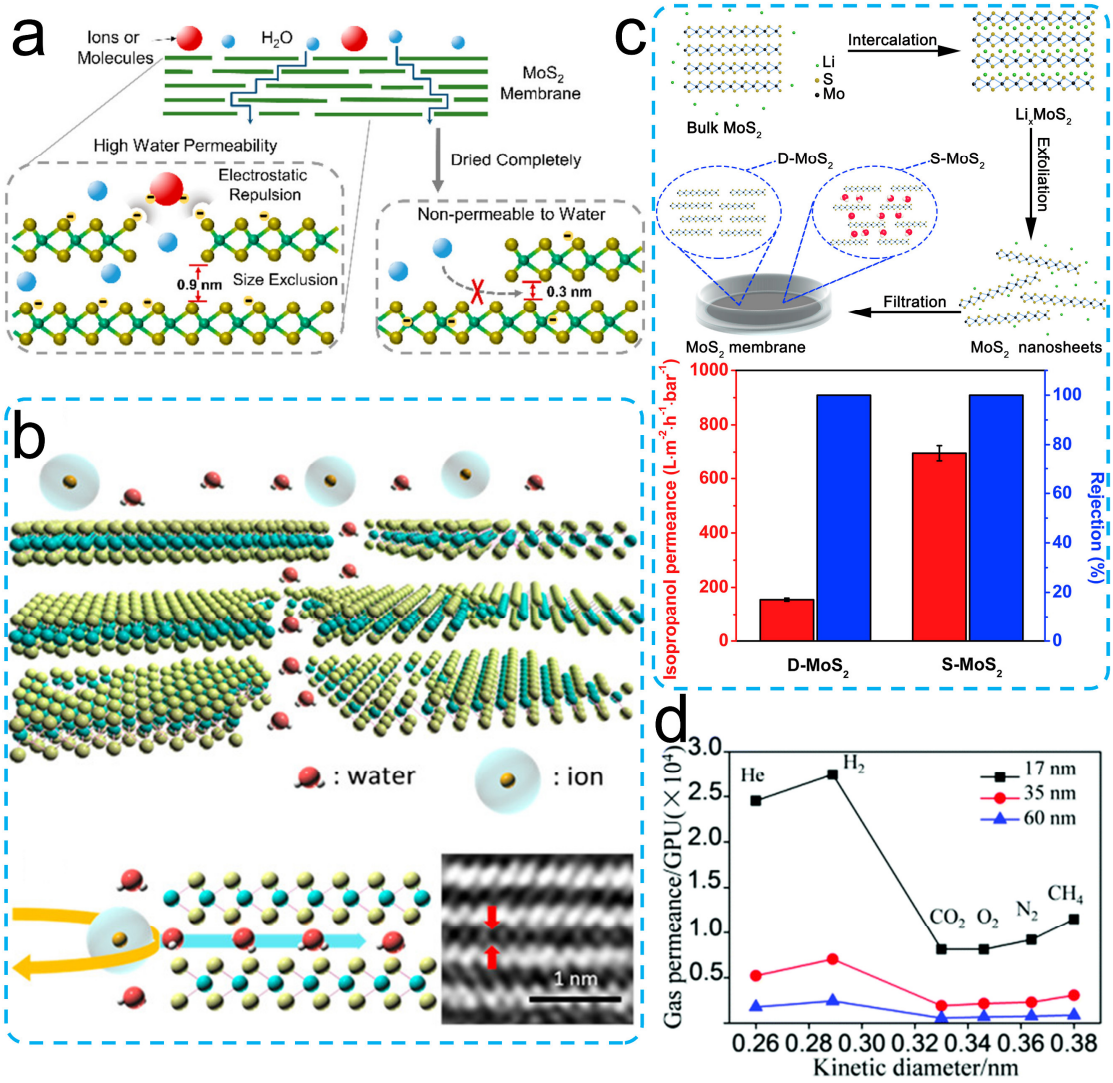

Figure 1.12 TMDs laminar membranes. a, Detailed depiction of the MoS_2 membrane separation mechanisms for ionic and organic dye, incorporating size exclusion and electrostatic repulsion. **b**, A schematic representation to demonstrate the translocation of water molecules through nanopores located within the grain boundaries of the horizontally-arrayed, multilayered 2D MoS_2 (top). It should be noted that the nanopores' dimensions are sufficient to permit water permeation. The side-view graphic indicates how water molecules readily traverse the interlayer vdW gaps, while larger-sized hydrated ions are effectively repelled (bottom). The inset HRTEM image highlights the vdW gap (indicated by red arrows), serving as a conduit for water transportation. **c**, Graphic presentations of D-MoS_2 and S–MoS_2 lamellar membrane preparation processes (top). Data representation of isopropanol permeance and

rejections of D-MoS_2 and S–MoS_2 concerning MB and MLB mixed solutions in isopropanol (bottom). Testing was conducted at 1 bar under cross-flow conditions. **d**, Graphical representation of gas permeance of MoS_2 membranes as a function of gas dynamic diameter.

(iii) MXenes Laminar Membranes

MXenes, a unique family of two-dimensional (2D) transition metal carbides, nitrides, and carbonitrides, have recently emerged as promising materials for membrane separation applications [113]. These materials are typically represented by the general formula $M_{n+1}X_nT_x$, where M represents a transition metal, X stands for carbon and/or nitrogen, and T_x represents the surface terminations, such as -OH, -O, and -F. The synthesis of MXenes primarily involves the selective etching of the A-group element from the parent MAX phase ($M_{n+1}AX_n$), where A is an element from groups 13-16 in the periodic table, followed by intercalation and exfoliation to obtain 2D nanosheets.

MXenes laminar membranes are fabricated by stacking MXene nanosheets into a layered structure, which imparts unique properties such as tunable interlayer spacing, high specific surface area, and excellent mechanical strength. These membranes have shown great potential in various membrane separation applications, including water purification, gas separation, and ion sieving.

Numerous researchers have explored the application of MXene laminar membranes in various membrane separation processes. Here, we present an overview of some of these studies, focusing on their key findings and performance data.

Water purification: Gogotsi and colleagues documented an interesting size- and charge-selective ion sieving effect in 2D $Ti_3C_2T_x$ membranes (Figure 1.13 a). The free-standing MXene membrane, possessing nanochannel height of approximately 6.4 Å, demonstrated an impressive rejection capacity towards the methylthioninium$^+$ (MB+) dye cation, while allowing the diffusion of metal ions at varying permeation rates - the order being $Na^+ > Li^+ > K^+ > Ca^{2+} > Ni^{2+} > Mg^{2+} > Al^{3+}$. Furthermore, a 2D $Ti_3C_2T_x$ membrane, with a thickness of 1.5 μm, displayed an exceptional water permeance of 37.4 L/(Bar·h·m^2), which is nearly six times greater than that of a GO membrane (only

6.5 L/(Bar·h·m^2)) of similar thickness [114]. Wang and his team successfully fabricated a porous and 2D lamellar $Ti_3C_2T_x$ membrane by employing $Fe(OH)_3$ nanoparticles as sacrificial templates. These nanoparticles were bound tightly to the $Ti_3C_2T_x$ nanosheets through electrostatic forces during the membrane deposition process, and were later removed by acid washing, resulting in additional nanochannels in the final membranes. These restructured membranes exhibit a remarkable water permeance of 1084 L m^{-2} h^{-1} bar^{-1}, which is five times greater than that of the untreated membranes. Simultaneously, these membranes effectively barred the passage of molecules larger than 2 nm. This included nearly complete rejection of 5 nm gold nanoparticles, while also displaying 97%, 90% and 85% rejection against cytochrome c (1.7 x 1.7 nm^2), Evans blue (1.2 × 3.1 nm^2), and rhodamine B (1.8 x 1.4 nm^2), respectively [115].

Desalination: The use of pristine MXene for desalination has rarely been reported due to the swelling of MXene membranes caused by the high hydrophilicity of nanosheets. Addressing this issue, Lu and colleagues created self-cross-linked MXene membranes by forming Ti-O-Ti bonds between adjacent nanosheets through a simple heat treatment (Figure 1.13 b). These thermal treated membranes exhibited relative stability and superior anti-swelling property. And the interlayer spacing in water solution decreased from 6.6 Å to 5.4 Å. Furthermore, an impressive enhancement in the NaCl rejection rate from 55.4% to 98.6% was observed under the forward osmosis process, albeit with a slight reduction in water permeance from 0.08 to 0.05 L m^{-2} h^{-1} bar^{-1} [116].

Organic solvent nanofiltration (OSN): Qiao and his team developed a lamellar MXene membrane stacked by double-layered $Ti_3C_2T_x$ nanosheets. The 230-nm-thick membrane presented exceptional transport behavior for organic solvents, including high permeance rates exceeding 5000 L m^{-2} h^{-1} bar^{-1} for both acetone and acetonitrile, and a rate of 3563 L m^{-2} h^{-1} bar^{-1} for methanol. Additionally, the membrane blocked dyes larger than 2 nm, boasting a rejection rate of 96% for reactive black (RB, 2.0 nm) and a complete 100% rejection for acid yellow 79 (AY79, 2.8 nm) (Figure 1.13 c) [117].

Gas separation: Ding and his colleagues developed lamellar MXene membranes

for use in gas separation processes. They found that the MXene membrane displayed high permeabilities of 2164 Barrer for He and 2402 Barrer for H_2 when tested with relatively small gas molecules. However, there was a significant drop in permeance for larger molecules such as O_2, N_2, and CH_4, with CO_2 permeability being as low as 10 Barrer. This resulted in a H_2/CO_2 selectivity ratio exceeding 160, highlighting the potential of this membrane for effective hydrogen purification [118]. Shen et al. revealed that 2D MXene membranes, with a thickness of just 20 nm, exhibited remarkable molecular sieving performance, achieving a H_2/C_3H_8 selectivity of 110 (Figure 1.13 d) [119]. Liu and his team provided evidence that MXene membranes are capable of operating under high temperatures, reaching as high as 320 °C. These membranes displayed a moderate H_2 permeance and a H_2/N_2 selectivity of 41, further testifying to the effectiveness of MXene materials in these applications [120].

Although MXene laminar membranes have demonstrated potential in applications like water purification, gas separation, and OSF, challenges remain [121]. Improvements in separation efficiency, permeability, antifouling properties, and mechanical strength are required. Desalination applications are still in the early stages, with obstacles such as swelling needing further research. Addressing these challenges will help advance MXene laminar membranes for practical separation processes.

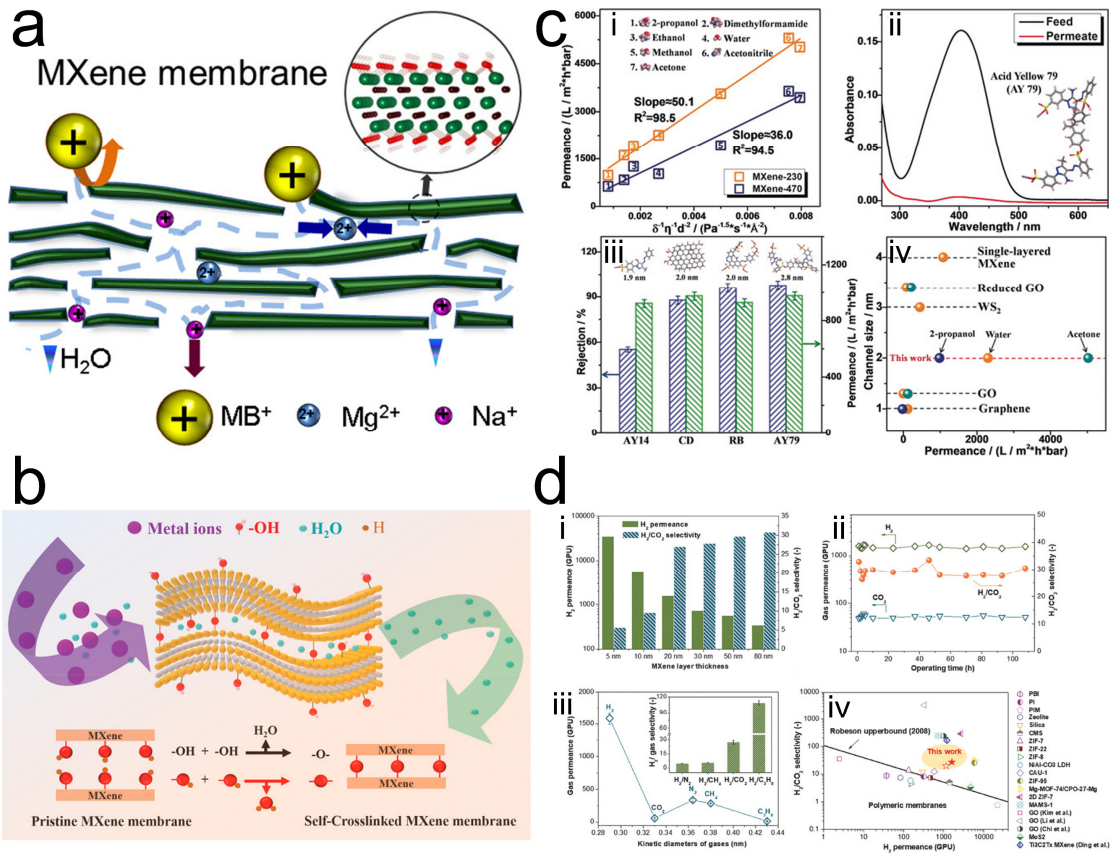

Figure 1.13. MXene laminar membranes. a, Schematic illustrating the selective permeability of cations through a $Ti_3C_2T_x$ membrane, accompanied by a complete rejection of large MB^+. **b**, A depiction of the self-crosslinking mechanism in MXene membranes via an -OH + -OH = -O- + H_2O reaction across adjacent MXene nanosheets, signifying the transition from PMM to SCMM. **c**, Organic solvent nanofiltration through MXene membranes. (i) A plot of solvent permeance versus the combined solvent property for MXene membranes with varying thicknesses. (ii) Ultraviolet/Visible light absorption spectra of AY79 in 2-propanol before and after filtration via MXene-230. (iii) The separation capabilities of MXene-230 for molecules of differing dimensions. (iv) Comparative evaluation of solvent permeance for laminated membranes with distinct channel dimensions (for brevity, the average channel sizes are depicted, and the precise channel dimensions are: Single-layered MXene=2–5 nm; rGO=2–3.4 nm; WS_2=2–4 nm; GO=1.3 nm; graphene approximately 1 nm). **d**, Gas transport characteristics of a H_2-selective MXene membrane. (i) Influence of MXene membrane thickness on H_2/CO_2 separation efficacy. (ii) Long-term operation of 20 nm-thick membrane for H_2/CO_2 separation. (iii) Gas transport behaviors of H_2, CO_2, N_2, CH_4, and C_3H_8 through a 20 nm-thick MXene membrane, along with an insert comparing H_2/gas selectivity. (iv) A comparison of H_2/CO_2 separation performance for different membranes.

(iv) Clay and 2D LDH Laminar Membranes:

Clay laminar membranes:

Clay materials, consisting of naturally occurring hydrated aluminosilicates, have attracted significant attention in the field of membrane separation due to their inherent layered structure, cost-effectiveness, and abundant availability [122]. Clay nanoparticles, such as vermiculate, montmorillonite, kaolinite, and halloysite, can be exfoliated into individual 2D nanosheets using chemical and mechanical treatments.

The fabrication of clay laminar membranes usually involves the assembly of exfoliated clay nanosheets through vacuum filtration, leading to a well-ordered lamellar structure.

Clay laminar membranes have demonstrated potential in ion exchanges and transport [123, 124], hence further served as proton/cation conducting membranes (Figure 1.14 a) [125-127] or energy harvesting membranes (Figure 1.14 b) [128]. The main advantages of clay-based membranes include their natural abundance, cost-effectiveness, and versatile surface chemistry. Despite the promising aspects of clay laminar membranes, their instability in water poses a significant limitation for their utilization in water treatment applications. This instability arises from the rapid swelling and dissolution of clay materials in the presence of water, which leads to the disintegration of the membrane structure, compromising its integrity and separation performance. Although a few studies have reported the use of clay laminar membranes for water treatment (Figure 1.14 c) [129, 130], further research is required to overcome this challenge by developing innovative strategies for enhancing the water stability of clay-based membranes.

2D LDH laminar membranes:

Layered double hydroxides (LDHs) are a class of anionic clay materials composed of stacked positively charged layers and intercalated anions [131]. They typically consist of metal cations, such as Mg, Al, or Zn, in a brucite-like structure. The synthesis of LDHs can be achieved through various methods, including co-precipitation,

hydrothermal synthesis, and sol-gel routes.

The preparation of 2D LDH laminar membranes involves the exfoliation of bulk LDH materials into individual nanosheets, followed by the assembly of these nanosheets into a layered structure using techniques similar to those used for clay laminar membranes.

However, 2D-LDH membranes have not been extensively explored for water purification applications due to their inherent instability in water and especially for low pH. This issue presents a significant challenge for the implementation of 2D-LDH materials in aqueous-based separation processes. To expand the applicability of 2D-LDH membranes, future research should focus on enhancing their water stability and exploring potential strategies for addressing this limitation.

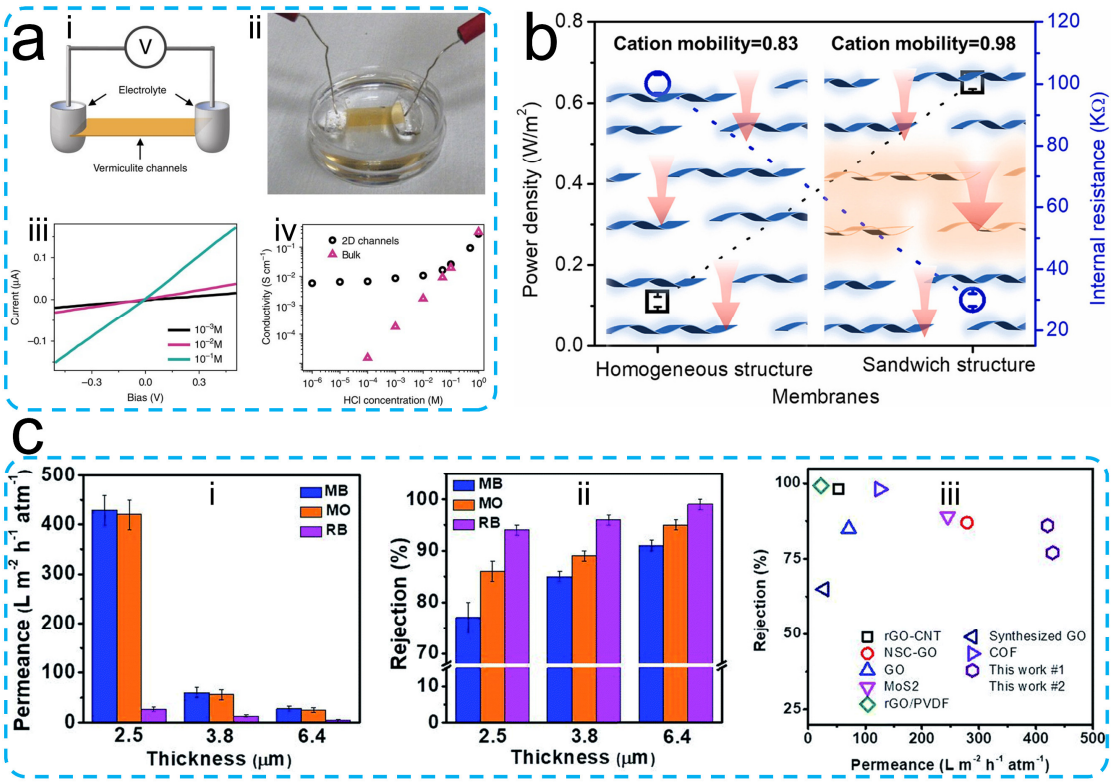

Figure 1.14. Clay laminar membranes. a, Surface charge-controlled proton mobility through vermiculite channels. This is represented by a schematic diagram (top-left) and an image of the actual vermiculite nanofluidic device (top-right). Typical I–V curves within the 2D channels are presented (bottom-left), and the ionic conductivity correlating with electrolyte concentration is plotted (bottom-right). **b**, Ionic transport and osmotic energy harvesting performance exhibited by 2D nanofluidic membranes

with a sandwich layout stacked by arrays of parallel clay nanosheets. **c**, Assessment of the RMMs' separation efficacy. Permeation (i) and rejection (ii) of MB, MO, and RB through RMMs with different thickness. (iii) Comparative analysis of permeance and rejection of the RMM versus other separation membranes documented in the literature.

1.3 Tailoring of 2D membranes

Despite the fascinating performance demonstrated by pristine 2D membranes, several challenges and limitations hinder their practical application in various separation processes. To address these issues and enhance the performance of 2D membranes, researchers have devoted substantial efforts to modify and tailor these materials. Innovative strategies, methods, and effects have been explored to optimize the properties of 2D membranes, pushing the boundaries of their separation capabilities and expanding their range of applicability.

In this section, we will delve into the tailoring of 2D membranes using selected reports from the literature. We will review the following key aspects: *Tailoring strategies* (1.3.1), which will discuss the principles and fundamentals for modifying the membrane properties to achieve desired performance; *Tailoring methods* (1.3.2), which will provide an overview of the techniques used to introduce alterations and modifications to the membrane structure and composition; and *Tailoring effects* (1.3.3), which will examine the impacts of these alterations on the membrane performance, including selectivity, permeability, and stability. By gaining a comprehensive understanding of these aspects, we can better appreciate the potential of tailored 2D laminar membranes in addressing the challenges associated with conventional membrane separation processes.

1.3.1 Tailoring strategies

As mentioned earlier, the mass transfer process in 2D membranes primarily occurs through apertures within the 2D nanosheets (2D nanosheet membranes) or interlayer channels (2D laminar membranes). Any alterations to the solute transport pathways can significantly affect membrane performance. Grossman and colleagues conducted a

study on the desalination performance of porous graphene membranes using simulation methods [132]. They discovered that pore size, pore edge chemistry, and the affinity for water and ions played crucial roles in water transport and ion rejection. For example, hydroxyl-modified pores exhibited better affinity for water than hydrogen-saturated pores, resulting in increased water flux. Additionally, the hydroxyl groups surrounding the pores compensated for the ion dehydration process, weakening ion rejection capabilities. Subsequently, O'Hern and coworkers pioneered a method to generate defects in single-layer graphene (SLG) by bombarding it with gallium ions [133]. By controlling the oxidative etching time, they were able to create pores of different sizes, resulting in membranes exhibiting various sieving behaviors. As the pore size changed, the membranes transitioned from anion-selective (with transport controlled by the pore edge charge) to ion transport membranes (where pore size hindered molecular transport) and finally to membranes without separation capabilities. This experimental study highlights the importance of tailoring pore size and charge to fine-tune the separation properties of 2D membranes for specific applications.

For perforated 2D nanosheet membranes, research continues on achieving high-density, uniform sub-nanometer pore distribution while sealing defects. O'Hern et al. proposed a method involving graphene transfer onto a polycarbonate track etch membrane, followed by hafnia deposition using atomic layer deposition (ALD) and nylon-6,6 formation to seal defects [134]. Decorating pore edges has also gained attention. He et al. reported the covalent functionalization of single-layer graphene with CO_2-philic polymeric chains by etching with O_2 plasma and functionalizing with polyethylenimine (PEI) or poly(ethylene glycol)-bis-amine (PEGBA). The resulting membranes exhibited high CO_2/N_2 separation performances [135].

For intrinsic 2D nanosheet membranes, such as covalent organic frameworks (COFs), the reported intrinsic pore sizes are predominantly in the range of 8-50 Å [136]. To achieve sub-nanometer sieving, such as for ions and gases, researchers have used different functional groups to decorate the pores. For example, Kuehl and his team synthesized 2D COF nanosheets using a pre-modification approach, employing the

same backbone of building units (C_3-symmetric hexamine and C_2-symmetric tetraone). By combining different functional groups, they produced 25 kinds of COFs in gram amounts. These highly ordered and modifiable COF nanosheets featured a stable aromatic backbone and functionalized pores, with adjustable pore sizes ranging from 19 to 28 Å. Introducing hydrophilic ionizable carboxylate groups in 2.8 nm diameter pores greatly enhanced water flux in the COF 9 membrane. Besides, COFs 8 and 9 demonstrated the formation of positively or negatively charged pores, making them suitable for different charge rejections [137]. Another strategy involves stacking nanosheets with different pore sizes in a misaligned manner to shrink the overall pore size. Caro and his colleagues prepared COF-COF bilayer composite membranes by successively regulating the growth of imine-based COF-LZU1 and azine-based ACOF-1 layers using a temperature-swing solvothermal approach. Both COF-LZU1 and ACOF-1 have a hexagonal pore structure with aperture sizes of approximately 18 Å and 9.4 Å, respectively. The interlaced pores of the COF-LZU1-ACOF-1 membrane are within the appropriate size range for the kinetic diameter of gas molecules, enabling size-dependent sieving. The as-prepared bilayer membranes exhibited much better separation selectivity for H_2 over CO_2, N_2, and CH_4 thanks to the formation of small interlaced pores (3-5 Å) at the stacking interface [138].

For 2D laminar membranes, the mass transfer process mainly occurs between the interlayers. Using numerical simulations, Grossman and his coworkers designed a bilayer porous graphene channel and found that the geometric structure of the channel, including the interlayer spacing and pore alignment, significantly impacted water flux and separation performance [139]. Wang and his team experimentally demonstrated that due to the strong van der Waals forces between MoS_2 layers, the interlayer spacing in completed dry MoS_2 laminar membranes is as small as 0.3 nm, which does not allow water permeation. However, when fully hydrated, the MoS_2 membrane can retain a 1.2 nm interlayer spacing (corresponding to 0.9 nm free spacing), endowing to high water permeability and moderate-to-high ionic and molecular rejection [104]. This result confirmed the importance of channel opening for the permeability of laminar

membranes.

On the other hand, graphene oxide (GO) possess many of hydrophilic groups on the nanosheets surface, which cannot resist the hydrating forces against the Van der Waals interlayer interactions, leading to a continuous expansion of the interlayer spacing in aqueous environments. Zhang and his colleagues discovered that as a dry GO membrane was soaked in water, it initially maintains a d-spacing of 0.76 nm. However, as the GO membrane remained in water, its d-spacing increases and reaches 6 to 7 nm at equilibrium [140]. The increased interlayer spacing resulted in a rapid decline in separation performance and a decrease in the structural stability of the membrane itself, even leading to decomposition and complete loss of performance. These studies highlight the importance of stable interlayer spacing in 2D laminar membranes for achieving optimal performance.

Besides, numerous studies on water transport behavior in GO interlayer channels have shown that rapid water transport occurs in hydrophobic graphene-like regions, while oxygen-containing functional groups such as hydroxyl and epoxy groups immobilize water molecules, hindering water transport. Numerical simulations have shown that oxygen-containing functional groups on GO not only disturb the arrangement of water molecules but also considerably impact their movement within the GO channel. The mobility of water molecules was assessed using mean square displacement (MSD) analysis. The results showed that the mobility of water molecules in the graphene channel was nearly identical to that in bulk water, suggesting that the graphene sheet did not provide any resistance during transport. However, the mobility of water molecules in the GO channel was significantly reduced, indicating substantial resistance to water transport due to the existence of oxygenated functional groups [141-145]. Simultaneously, a simple experiment conducted by Xu and colleagues validated this observation. By using vacuum filtration of GO suspension at different rates, GO membranes can be stacked with various interlayer structures. When employing slow filtration, the oxygen-containing functional groups on adjacent SLGO flakes tend to self-assemble with each other, forming a symmetrical structure. In contrast, with fast

deposition, the oxygen-containing functional groups may arrange randomly, creating asymmetrical nanoscale defects. In the asymmetrical structure, the graphene domains of the top flakes may face the oxygen-containing regions of the bottom flakes, leading to increased hydrogen bonding during water transport and subsequently reducing the water transport rate. On the other hand, the symmetrical structure obtained through slow stacking will present more graphene-facing regions, allowing for faster water transport and resulting in a four-fold increase in water flux [146]. These results demonstrate that tailoring the surface chemistry of two-dimensional nanosheets will have a significant impact on their transport properties.

Regarding gas separation, numerous studies have been conducted on the CO_2 separation behavior of GO membrane. Using molecular dynamic simulations, Li and colleagues found that, due to the presence of oxygen-containing groups, the GO nanosheet surface exhibits a stronger adsorption effect on CO_2 molecules than on N_2 and CH_4 molecules. This preferential adsorption causes CO_2 to fill the interlayer channels quickly, enabling efficient CO_2/N_2 or CO_2/CH_4 separation [147].

In an experimental study, Wang et al. demonstrated that by reacting poly(ethylene glycol) diamines (PEGDA) with epoxy groups on the GO surface, they could create CO_2-philic nanodomains, which endowed the membrane with a high sorption capacity for CO_2. In contrast, unreacted GO surfaces formed non-CO_2-philic nanodomains, leading to low-friction diffusion. This hybrid tailored structure, featuring both heterogeneous CO_2-philic domains for CO_2 molecule enrichment and non-CO_2-philic nanodomains for rapid CO_2 transport, results in a GO-PEGDA500 membrane exhibiting a high CO_2 permeance of 175.5 GPU and a CO_2/CH_4 selectivity of 69.5, far surpassing the performance of the original GO membrane [148]. These findings highlight the importance of tailoring membrane affinity, particularly for gas separation applications.

Tailoring strategies for 2D nanosheet membranes mainly focus on modifying pore edges to alter their size, charge, and affinity, thereby regulating the membrane's transport and separation capabilities. On the other hand, tailoring 2D laminar

membranes primarily involves adjusting interlayer spacing, nanosheet surface charge, and channel affinity to achieve desired performance.

1.3.2 Tailoring methods

Nanolaminate membranes are made of stacked 2D nanosheets. Any modification of the 2D nanosheets will inevitably impact the behavior of the final membranes. Nanosheets exhibit a large lateral size and high surface reactivity, with numerous active and defect sites that can easily be modified through various techniques such as grafting and adsorption.

To date, numerous tailoring methods have been developed for modifying 2D nanosheets. The tailoring methods can be broadly categorized into two primary groups: covalent modification and noncovalent modification (Figure 1.15). In the following subsections, we will examine each of these categories to provide an overview of the different methods employed for tailoring 2D nanosheets for membrane applications.

Covalent Modification

Covalent modification serves as a direct approach to alter the chemical characteristics of materials, such as charge distribution and hydrophobicity, by forming chemical bonds between functional groups or other entities and the surface of nanosheets. At present, the main methods for grafting include the following five reactions: i) hydrogenation, fluorination, oxidation, and ammonization, ii) nucleophilic reactivity, iii) substitution reactions, iv) amidation, and v) silane coupling. This modification routes depends on the initial surface chemistry of the pristine nanosheets In the following sections, we will provide an overview of each method and discuss their applications in modifying 2D nanosheets.

(i) hydrogenation, fluorination, oxidation, and ammonization

These methods involve the chemical modification of 2D nanosheets by introducing hydrogen, fluorine, oxygen, or nitrogen-containing functional groups to

their surfaces. Among the various 2D materials, graphene has been extensively studied and can be modified through a range of approaches. For instance, fully hydrogenated graphene, known as "graphane," can be produced using a hydrogen plasma atmosphere [149]. Additionally, chemisorption of hydrogen on the graphene surface has been proven to be a viable method, even though only small subareas of the graphene basal plane are unintentionally hydrogenated [150]. Fluorinated graphene can be prepared through methods such as direct gas-fluorination, plasma treatment, hydrothermal fluorination, and photochemical or electrochemical synthesis fluorination [151]. Oxidation can be achieved through either a one-step or a two-step process. The one-step process involves the direct oxidation of graphene using strong oxidants like concentrated sulfuric acid, concentrated nitric acid, or potassium permanganate [152]. In contrast, the two-step process first oxidizes graphite through Hummers' method or electrochemical oxidation, followed by exfoliating or thermally expanding the graphene oxide obtained [153, 154].

Fluorinated 2H WS_2 can be prepared through hydrothermal reactions [155]. MXenes, when eliminating the A layers from parent MAX phases using HF etching, are decorated with abundant surface-terminating groups, including -H, -O, and -F groups [156]. The concentration of HF influences the amount of F groups on the surface. Black phosphorus (BP) nanosheets can be synchronously fluorinated by BF_4--electrolyzed F^- anions, during a one-pot exfoliation process [157]. Additionally, fluorinated hexagonal boron nitride (h-BN) can be prepared using solvent-thermal reactions [158]. When exfoliating h-BN through ball milling with urea, it can be simultaneously functionalized with the -NH_2 group [159, 160].

(ii) Nucleophilic reactivity

Nucleophilic reactivity, a fundamental concept in organic chemistry involving the interaction between a nucleophile (an electron-rich species) and an electrophile (an electron-deficient species), can be applied to 2D nanosheets to functionalize their surfaces by introducing functional groups such as those formed through diazotization

and alkylation. Hirsch and his team used bulk wet chemical exfoliation of graphite to obtain graphene and in situ covalent functionalization with organic aryldiazonium salts. When electron-accepting moieties like aryl diazonium salts react with graphene, electrons can transfer from the basal plane to the reactant, thus achieving covalent bonding between graphene and the aryl group [161]. Not only exfoliated graphene, but also chemically converted graphene (CCG) and epitaxial graphene (EG) have been demonstrated to be successfully modified with diazonium salts at room temperature [162, 163]. Englert and colleagues utilized a liquid Na/K alloy in 1,2-dimethoxyethane (DME) for the reduction and exfoliation of graphite. Then they employed 1-iodohexane as an electrophile to trap the reduced graphite, obtaining alkylated graphene with hexyl chains attached to the basal planes. The alkylation is largely changed the surface property of graphene [164, 165]. Furthermore, by employing diazotization or alkylation, bis- or multi-functional graphene can be prepared [166, 167].

Voiry et al. presented a straightforward and versatile method for the covalent functionalization of 2D TMDs nanosheets (MoS_2, WS_2, and $MoSe_2$) using organohalide reagents (2-iodo-acetamide and iodomethane) or diazonium salts. This defect-free modification arises from an electron transfer reaction between the electron-rich metallic 1T-TMDs and the reactant, resulting in the covalent attachment of an organic group through the formation of a C-S bond as evidenced by NMR and ATP-FTIR spectroscopy [168]. Subsequently, Benson et al. grafted a series of diazonium salts onto MoS_2 nanosheets, creating organically functionalized MoS_2 with phenyl rings. This significantly expanded the variety of functionalized MoS_2 species available for research and applications [169].

The functionalization of BP nanosheets with diazonium salt was demonstrated by Ryder et al. They prepared few-layer BP nanosheets by mechanically exfoliating bulk black phosphorus and then deposited them onto Si/SiO_2 substrates. By immersing the substrates in aryl diazonium salt solutions, the BP nanosheets were spontaneously functionalized, forming phosphorus-carbon bonds [170]. Sofer et al. employed alkyl halides as electrophile reagents to attack the layered BP, which were prepared by shear

force milling in nonaqueous solvents. They successfully grafted alkyl groups onto BP nanosheets [171].

Moreover, electrophilic reactions have also been used to modify hexagonal boron nitride (h-BN). Marti and his team used alkyl halides to functionalize h-BN under strongly reducing conditions (Billups-Birch conditions). When the ratio of Li to BN was 20, 1-bromododecane achieved the highest degree of grafting onto the BN surface. This alkylated BN exhibited exceptional hydrophobicity [172].

(iii) substitution reactions

In addition to direct functionalization on the surface of nanosheets, the abundant heteroatoms and functional groups, such as -F, -OH, and -COOH, on 2D nanosheets' surfaces provide opportunities for grafting other molecules or groups via substitution reactions. Jia and his colleagues employed various organic acids, such as oxalic acid (OA), propandioic acid (PA), succinic acid (SA), hexanedioic acid (HA), and octanedioic acid (OcA), to esterify the hydroxyl groups on the GO basal plane. Furthermore, they used diols or polyols, including ethylene glycol (EG), 1,2-propylene glycol (PG), butylene glycol (BG), 1,6-hexylene glycol (HG), neopentyl glycol (NPG), glycerol (GL), and pentaerythritol (PER), to crosslink with the carboxyl groups on the edges of GO nanosheets, resulting in functionalized GO with different molecular modifications [173]. Subsequently, Jiang and his team attempted to decorate the GO surface with boron by using $K_2B_4O_7$. They achieved excellent covalent modification results through reactions with the surface hydroxyl groups, demonstrating the feasibility of using inorganic acid modification [174]. Zhang and his colleagues also obtained similar results using sodium tetraborate decahydrate (borax) and boric acid [175]. In addition to GO, Jin and his team extended this modification reaction to MXene nanosheets. By using borate to react with the hydroxyl groups on the MXene surface, they obtained boron-bridged MXenes [119].

(iv) amidation

Amidation involves the formation of amide bonds between the nanosheets and functional groups. This is a widely-used method in which amines reacts with epoxy or carboxylic groups on 2D nanosheets surfaces to achieve further functionalization. Hung and his team successfully functionalized graphene oxide (GO) using three different diamine monomers, including ethylenediamine, butylenediamine, and p-phenylenediamine. The results showed that the amine groups in the diamine molecules reacted with epoxy groups on the basal plane and carboxyl groups at the edges, leading to the formation of amidated GO [176]. Subsequently, this method has been widely employed to further functionalize GO nanosheets, with the reactants ranging from amine monomers to cyclic amine molecules (such as piperazine) [177] and amine-containing polymers (like polyethyleneimine) [178].

(v) silane coupling

Silane coupling involves the reaction between silane coupling agents and the hydroxyl groups of the nanosheets. Silane coupling agents are organosilicon compounds that typically contain hydrolyzable groups (e.g., alkoxy or halogen groups) and an organofunctional group. Following hydrolysis, a reactive silanol group is formed, which can react with the surface active groups of the nanosheets. This reaction enables the grafting of organofunctional groups onto the nanosheets, resulting in the covalently modified 2D material's surface. Wu et al. successfully grafted hydrophilic ($-NH_2$) and hydrophobic ($-C_6H_5$, $-C_{12}H_{25}$) groups onto MXene ($Ti_3C_2T_x$) nanosheets by reacting with aminopropyltriethoxysilane (APTES), dodecyltriethoxysilane (DCTES), and mercaptopropyltriethoxysilane (MPTES) [179]. Wang et al. employed KH570 (3-methacryloxypropyltrimethoxysilane) to graft methacryloxypropyl groups onto hydroxyl-activated hexagonal boron nitride (h-BN) nanosheets [180]. These examples demonstrate the versatility and effectiveness of silane coupling agents in functionalizing a variety of 2D nanomaterials.

Noncovalent Modification

Noncovalent modification is an alternative strategy for tailoring 2D nanomaterials without forming covalent bonds. Due to the rich charge distribution and abundant heteroatoms on 2D nanosheets, various substances such as ions, molecules, nanoparticles, and polymers can be easily adsorbed onto their surfaces through π-stacking, van der Waals attraction, hydrogen bonding, or electrostatic attraction. This method can be categorized into four sub-sections: (i) polymer decoration, (ii) nanoparticle decoration, (iii) molecule decoration, and (iv) ion decoration. Each category offers different ways to modify the properties and functionality of 2D nanosheets without altering their intrinsic structures.

(i) Polymer decoration

Polymers, with their diverse chemical structures, can be used to modify nanosheets and impart various properties to them. In the case of 2D materials, polymers have long been used to alter the surface charge of nanosheets. Anti-charged polymers (have opposite charges with nanosheets) are employed to coordinate the surface charge of nanosheets and achieve surface charge reversal. Co-charged polymers (have same charges with nanosheets), on the other hand, interact with nanosheets through hydrogen bonds, enhancing the surface charge distribution. This type of modification can provide enhanced stability, dispersibility, and functionality to the nanosheets, making them suitable for various applications. Ding et al. prepared positively charged MXene (P-MXene) nanosheets by selectively combining polydiallyl dimethyl ammonium (PDDA) with MXene through electrostatic interactions. Subsequent characterizations showed the successful coverage of PDDA on MXene nanosheets, as evidenced by the uniform distribution of nitrogen elements [181]. While Zhang et al. combined negatively charged aramid nanofiber (ANF) with MXene nanosheets through hydrogen bonding, resulting in an enhanced surface negative charge distribution [182].

(ii) nanoparticle decoration

The combination of nanoparticles with nanosheets can impart different surface

patterns to the nanosheets, affecting their overall behavior and properties. In this context, Dong et al. anchored nano-sized Fe_3O_4 particles onto GO nanosheets to assemble a nanofiltration membrane with enhanced performance [183]. Nunes' team intercalated and cross-linked scattered sub-5 nm silica nanoparticles within the GO interlayers, resulting in 2D-dual-spacing channel membranes with improved separation capabilities [184]. Long et al. anchored positively charged 0D alumina (Al_2O_3) nanoparticles (200 nm) onto MXene nanosheets' surfaces through electrostatic interactions, obtaining a nano-intercalation 2D membrane with enhanced channel stability and outstanding molecular separation performance [185].

(iii) molecule decoration

In contrast to polymers and nanoparticles, which are typically decorated on nanosheets prior to membrane assembly, small molecules and ions are generally decorated after the assembly process. This is due to their small size and easy diffusion characteristics, and additionally this effectively prevents nanosheet colloidal aggregation. Hirunpinyopas et al. immersed MoS_2 membranes in different dye solutions, including cationic dye (crystal violet, CV), anionic dye (sunset yellow, SY), and uncharged dye (neutral red, NR), for extended periods (~21 days) to tune their permeation properties [186]. Peng's team confined the ionic liquid such as [BMIM][BF_4] within 2D laminar membranes, such as GO and TMDs, to fabricate high-performance CO_2-philic membranes with enhanced separation capabilities and selectivity [187, 188].

(iv) ion intercalation

Using counter ions (opposite charge to the membrane surface) to tailor the adjacent nanosheets in laminar membranes by electrostatic attraction or cation-π interactions has become a widely adopted, easy-to-implement, and effective universal method for modifying 2D materials membranes. Park et al. found that by modifying graphene oxide nanosheets with a small amount (less than 1 wt %) of Mg^{2+} and Ca^{2+}, the mechanical stiffness (10–200%) and fracture strength (~50%) of graphene oxide paper were

significantly enhanced, as carboxylate groups on the edges can bond to Mg^{2+} and Ca^{2+} [189]. Yeh et al. observed that the increased stiffness of GO membranes supported by porous anodized aluminium oxide membrane (AAO) arises due to the release of aluminium ions from the substrate during membrane preparation. The corrosion of the substrate causes the release of Al^{3+} ions, which in turn, increases the cation-π interaction with the ionized oxygen-containing groups of GO. This results in Al^{3+}-strengthened films that exhibit improved mechanical properties [190]. Chen et al. found that GO membranes with intercalated cations demonstrate a precise control over the interlayer size, with changes in the range of angstroms. By simply immersing the membrane in salted solutions, they were able to achieve precise cationic-control of GO nanovoids, offering an effective method to modify the properties of these membranes [191]. In addition to GO, other 2D materials such as MoS_2 and MXene can also be modified using this approach. Chu et al. employed different cations (K^+, Na^+, Li^+, or Mg^{2+}) to tailor MoS_2 membranes [192], while Ding et al. proposed using Al^{3+} to coordinate MXene membranes [193]. This demonstrates the versatility of using cations to modify and control the properties of various 2D materials-based membranes.

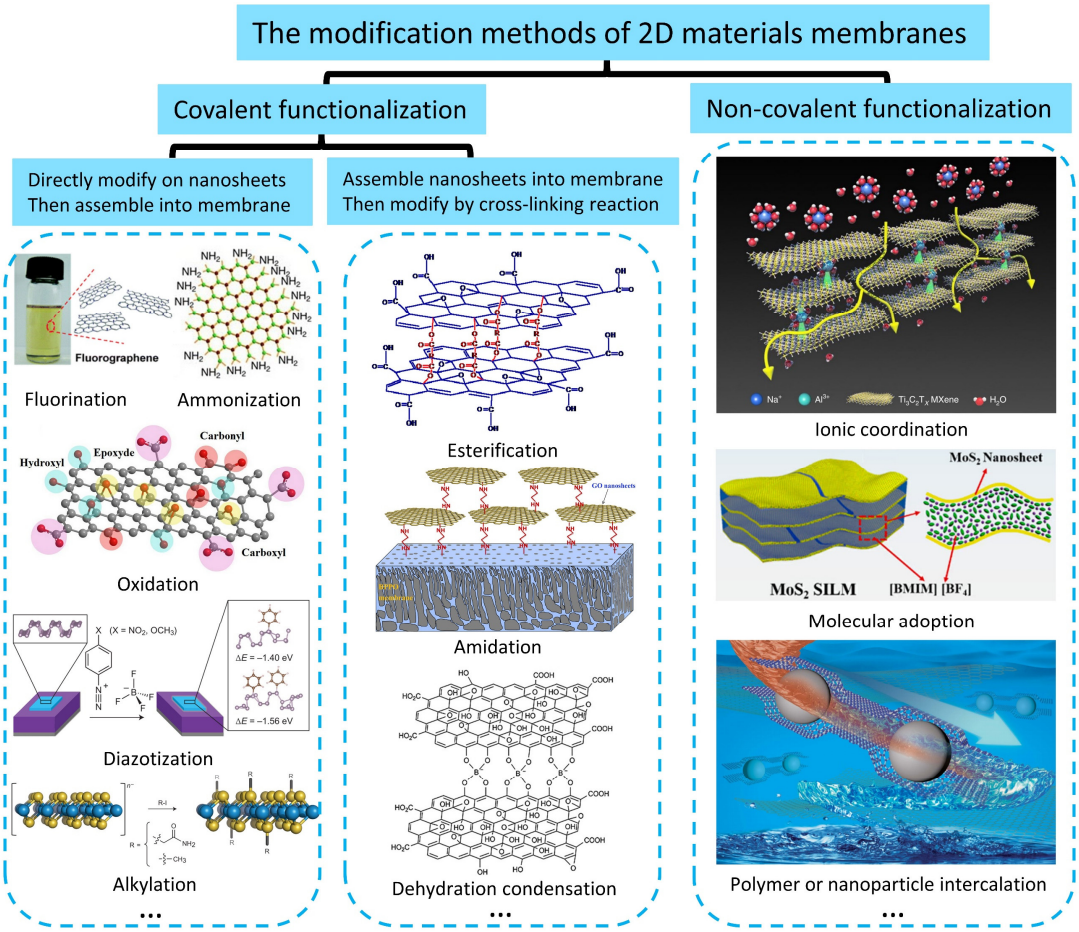

Figure 1.15 The modification strategies of 2D materials membranes. Adapted images showing fluorination, ammonization, oxidation, diazotization, alkylation, esterification, amidation, dehydration condensation, ionic coordination, molecular adoption, polymer or nanoparticle intercalation, respectively.

1.3.3 Tailoring effects

Modified nanosheets acting as the fundamental building blocks of 2D materials membranes, possess diverse surface patterns and physicochemical properties that significantly impact the structure and microenvironments of nanopores/nanochannels. These, in turn, determine the ultimate separation performance of the membranes. Thoughtful modifications of nanosheets can subtly alter the size, charge, affinity, and wettability of selective nanopores/nanochannels. In line with the scope of this thesis, we will pay close attention to the effects of 2D laminar membranes. The subsequent sections will delve into the influence of nanosheets modifications on the architecture and microenvironments of the nanochannels, focusing on (i) interlayer space, (ii)

nanochannel charge, (iii) affinity, and (iv) wettability. Additionally, we will emphasize the impacts of these changes on the overall performance of the membranes.

(i) Interlayer space:

Modifications of nanosheets can impact the interlayer space between the layers, altering the size and accessibility of the nanochannels. By controlling the interlayer distance, the membrane's selectivity and permeability can be tuned to meet the specific separation requirements.

The functional groups grafted onto nanosheets act as pillars for nanochannels, leading to increased interlayer space when nanosheets are assembled into membranes, bringing the opened selective nanochannel. Graphene, the first discovered 2D material to exhibit stable properties, has been used to create laminar membranes. However, its perfect stacking structure with an interlayer space of 0.34 nm does not provide sufficient capillary action for even the transport of small molecules such as hydrogen, helium and water [194]. After oxidation, its variants graphene oxide (GO) is utilized as building units to construct laminar membranes. The oxygenated groups on the GO surface such as hydroxyl, keton and carboxylic serve as pillars (Figure 1.16 a), forming nanochannels between adjacent nanosheets and increasing the interlayer space to 0.8 nm, which allows for the free movement of small molecules like H_2O [47]. MoS_2, one of the most widely studied TMDs, faces a similar challenge. Wang et al. found that the turbo-stacked MoS_2 laminar membranes have a d-space of approximately 0.62 nm in dry conditions, resulting in an interlayer space of less than 0.3 nm [104]. This space is maintained in water due to strong van der Waals forces, rendering the membrane impermeable to water molecules. Voiry et al. first proposed a functionalization strategy that led to covalently functionalized MoS_2 membranes with grafted groups, which show increased interlayer space from 3.9 Å to 5.3 Å, enhancing water permeability and desalination performance, with an 82% NaCl rejection and a water flux of ~33.7 L m^{-2} h^{-1} bar^{-1} was achieved under RO (Figure 1.16 b) [195]. Hoenig et al. provided further evidence that the covalent functional strategy for MoS_2 effectively establishes open

water transport pathways. They discovered that the hydrated ce-MoS_2 membrane initially exhibits a disordered structure with mesoporous scale voids between layers. When partially dried, the large voids close, but parts of the membrane restack and form an interlayer-space close to that of bulk MoS_2, reducing the overall porosity of the membrane. Further, when completely dried, the membrane becomes impermeable. While the functional groups can serve as permanent molecular spacers, allowing fct-MoS_2 membranes to dry without restacking into an impermeable bulk-like structure. This characteristic enables the membrane to rehydrate during testing, resulting in consistent interlayer spacing with fewer voids or impermeable regions, promoting uniform rehydration of the membrane. Hoenig et al. demonstrated that MoS_2 membranes functionalized with acetic acid consistently achieved ~92% rejection of Na_2SO_4 with a flux of ~1.5 L m^{-2} h^{-1} bar^{-1} [196]. MXene laminar membranes exhibit high H_2 permeation over other common gas molecules such as CO_2, N_2, and CH_4, stemming from the small capillary width supported by terminated -F and -OH groups (Figure 1.16 c) [118]. To increase the interlayer space of MXene laminar membranes for solvent transport, silane coupling agents were utilized to react with -OH groups, and the target alkyl groups such as -C_6H_5 and -$C_{12}H_{25}$ were grafted onto the MXene nanosheet surface, leading to increased interlayer space from 1.38 nm to 1.66 nm [179].

Functional groups are beneficial for opening the interlayer space. However, there are potential drawbacks. On one hand, the grafted hydrophilic groups on the nanosheets' surface, such as oxidation groups, can cause swelling when the membranes operate in aqueous solutions. On the other hand, the decreased interaction between nanosheets as a result of penetrants traversing the tortuous transmembrane pathway could lead to delamination. Both factors increase interlayer space and contribute to poor sieving performance. Further nanosheet modifications, such as crosslinking, can provide controllable interlayer spacing.

Crosslinking adjacent nanosheets using exterior molecules reacting with existing surface groups can fix the interlayer space and resist swelling. Hung et al. utilized diamines of different sizes to crosslink GO nanosheets, achieving varying interlayer

spaces from 10.4 to 8.7 Å (Figure 1.16 d). The limited swelling observed in a 90 wt% ethanol-water solution can be attributed to the covalent bonds formed between the layers and diamine, which effectively suppress the swelling of the membrane. The crosslinked GO membranes displayed exceptional pervaporation performance at 80°C, with a permeation flux of 2297 g/(m^2 h) and a water concentration in the permeate of 99.8 wt%. Additionally, the membranes demonstrated long-lasting ethanol dehydration operation at 30°C for 120 hours using the pervaporation process [176]. Similar strategies have been widely applied to GO laminated membranes for various separation applications, including ionic sieving [197], nanofiltration [198, 199], and water desalination [178]. Yuan et al. used thiourea (TU) and m-phenylenediamine (MPD) molecules to cross-link GO nanosheets, resulting in tightly interlocked nanosheets and significantly suppressed swelling in aqueous solutions. The nanochannel size of the TU-GOF and MPD-GOF membranes in water increased only slightly, with swelling ratios of approximately 35% and 29%, respectively. In contrast, the pristine GO membranes exhibited a swelling ratio as high as 156% upon immersion in water. The cross-linking of TU molecules led to improved monovalent salt rejection (95.6% for NaCl) due to the decreased nanochannel size. Meanwhile, the MPD-cross-linked GOF membranes showed simultaneous enhancements in permeability and rejection for both salts and micropollutants, with a 21.0% and 53.3% increase for chloramphenicol (CAP) solution, demonstrating the effectiveness of molecular covalent cross-linking in achieving excellent anti-swelling ability and separation performance [200]. In addition to diamine, organic acids (dicarboxylic acids) and inorganic acids (boric acid) have been used to crosslink GO and MXene nanosheets and fix interlayer space. Xie and his team developed a maleic acid covalent-bridged MXene (MXMA) membrane for pervaporation desalination. The MXene nanosheets were strongly fixed by covalent bonds formed through esterification reactions between the carboxyl groups in maleic acid and hydroxyl groups on the MXene surface. XRD analysis showed that the pristine MX membrane had a d-spacing of 1.37 nm, while the maleic acid cross-linked MXMA membrane had a slightly increased d-spacing of 1.49 nm. The d-spacing of MX

expanded by 31.4% to 1.80 nm in the presence of water, whereas the d-spacing of MXMA only expanded by 2.7%. This indicated that the covalent bridging with maleic acid effectively suppressed interlayer swelling and improved the mechanical strength of the MXMA membrane. During a 50-hour long-term operation, both water flux and salt rejection remained stable, demonstrating the excellent performance and stability of the MXMA membrane in desalination applications [201]. Recently, cysteamine and L-cysteine, both containing -NH_2 and -SH groups, were employed to react with oxygen-containing groups on GO nanosheets. Cheng and colleagues prepared cysteamine or L-cysteine cross-linked GO membranes, referred to as CGO or LCGO. The crosslinking process resulted in a narrower interlayer height, from 0.98 nm down to 0.90 nm, leading to more tightly stacked GO nanosheets and enabling efficient gas sieving. The ultrathin (~50 nm) GO membranes exhibited remarkable gas separation performance with an H_2 permeance of 51.5 GPU, and an H_2/CO_2 selectivity of 21.3, which was more than double that of pristine GO. Due to the covalent interlocking, the membrane maintained its structural stability during continuous mixed gas tests, showing consistent performance over 70 hours of operation [202].

In contrast to covalent modification of nanosheets, a more straightforward approach involves decorating nanosheets with ions, molecules, nanoparticles, and polymers without any chemical reactions. This method allows for the regulation of interlayer space based on the size of the intercalated spacers. Intercalated ions within the nanochannels serve as adhesives, increasing membrane stability and mechanical strength due to strong electrostatic attraction while also resisting swelling.

Chen et al. first utilized various cations (K^+, Na^+, Ca^{2+}, Li^+, and Mg^{2+}) to modify GO laminar membranes, achieving tunable interlayer spaces with angstrom precision, ranging from 11.4 Å to 13.6 Å in water solutions (Figure 1.16 e). The strong cation–π interactions between hydrated cations and aromatic rings in GO nanosheets, along with electrostatic attraction, contribute to the contracted interlayer space. This method allows for efficient and selective exclusion of other ions with larger hydrated volumes. For instance, the Na^+ permeation rate of untreated GOMs is $71.84 \pm 6.75 \times 10^{-2}$ mol

m^{-2} h^{-1}, while that of KCl-treated GOMs is 0.48 ± 0.07 × 10^{-2} mol m^{-2} h^{-1}, with both having a similar thickness of around 280 nm. This represents a decrease of two orders of magnitude, demonstrating the excellent potential for precise ion and molecular sieving in aqueous solutions [191]. The ion modification strategy is also applicable to negatively charged MXene membranes. Al^{3+} and Mn^{2+} have been used to control MXene membrane swelling, resulting in fixed interlayer spaces with limited swelling and highly efficient desalination performance in both forward and reverse osmosis processes. Ding et al. observed that untreated MXMs experienced significant swelling in aqueous solutions, with the d-spacing increasing from 13.5 ± 0.1 Å to 16.5 ± 0.5 Å due to weak interactions between MXene layers. In contrast, Al^{3+}-intercalated MXMs exhibited significantly suppressed swelling when exposed to water or salt solutions, with the d-spacing only increasing from 14.7 ± 0.1 Å to 15.1 ± 0.2 Å, demonstrating their excellent non-swelling property in aqueous solutions. Subsequent ion permeation experiments showed that the rates of monovalent and multivalent ions through Al^{3+}-intercalated MXMs were nearly two orders of magnitude lower than untreated MXMs, indicating greatly enhanced ion rejection performance. In forward osmosis desalination tests, 1.1-μm-thick Al^{3+}-intercalated MXMs rejected over 96% of NaCl with a water flux of around 2.8 L m^{-2} h^{-1}. The intercalated Al^{3+} not only fixed the interlayer distance but also acted as pillars for fast water permeation. When the membrane thickness was reduced to 0.34 μm, the water flux increased to 8.5 L m^{-2} h^{-1}, and NaCl rejection remained as high as 90%, demonstrating the excellent desalination performance of Al^{3+}-intercalated MXMs [193]. Wang and his team developed a method to stabilize the laminar structure of $Ti_3C_2T_x$ membranes using alginate hydrogel pillars. Initially, sodium alginate (SA) molecules were uniformly anchored to the $Ti_3C_2T_x$ nanosheet surface through hydrogen bonding. Following this, the SA-$Ti_3C_2T_x$ membrane was submerged in multivalent cation solutions (Ca^{2+}, Ba^{2+}, Mn^{2+}, and Al^{3+}) to finalize the cross-linking process. This resulted in a uniformly structured, nacre-like membrane that effectively limited swelling. In filtration experiments, the ultrathin Mn-alginate pillared MXene membrane exhibited 100% Na_2SO_4 rejection while maintaining high water

permeance, showcasing exceptional nanofiltration performance [203]. Furthermore, Zhu et al. introduced a method using Keggin Al_{13} polycations as pillars to efficiently stabilize the lamellar structure of a $Ti_3C_2T_x$ membrane. By altering the mass ratio of $Al_{13}/Ti_3C_2T_x$ and adjusting the aging time of the Al_{13} ions, they were able to precisely control the interlayer spacing over a wide range, from 2.7 to 11.2 Å. Membranes with narrower d-spacing displayed improved selectivity for monovalent ions. In a forward osmosis desalination process, such a membrane demonstrated high NaCl rejection (99%) and a fast water flux (0.30 L m^{-2} h^{-1} bar^{-1}). On the other hand, membranes with wider d-spacing exhibited notable selectivity, which was found to depend on cation valence. When used for acid recovery in iron-based industrial wastewater treatment, the membrane showed good H^+/Fe^{2+} selectivity, positioning it as a promising alternative to traditional polymeric membranes [204].

Nanoparticles and polymers, which are larger than ions and molecules, can create a hierarchical nanochannel structure with varied interlayer spacing. SiO_2 nanoparticles have been used to decorate GO nanosheets, forming an hourglass-shaped nanochannel in GO laminar membranes similar to water transport protein structures. The hydrophilic nanoparticles cause the interlayer channels to widen locally, enhancing solvent permeance. In alternating areas without nanoparticles, the GO layers bend, and the π–π interactions maintain the narrow and hydrophobic channels, resulting in high solute rejection. The dual-spacing channel membranes exhibit exceptional performance in organic solvent nanofiltration, with a 10-fold increase in water permeance without compromising solute rejection. The methanol permeance reaches 290 L m^{-2} h^{-1} bar^{-1}, while maintaining more than 90% rejection of dyes larger than 1.5 nm. This heterostructure provides greater permeability for solvent filtration due to the wider interlayer spacing, while still maintaining rejection efficiency because of the numerous narrow slits [184]. Polymers have also been used to modify GO nanosheets, as demonstrated by Andreeva et al., who fabricated a polyamine (PA) intercalated GO membrane (Figure 1.16 f). The polymer, which is pH-responsive, exhibits different morphologies within the nanochannels and imparts the composite membrane with

variable interlayer spacing. This results in an environmentally-responsive function for controlling water transport. For example, membranes prepared at pH 2 show higher water permeability than those prepared at pH 10.2. Furthermore, the permeability of monovalent ions, such as Cs^+, can be altered by the presence of specific ions like K^+, suggesting the adaptability and programmability of this membrane to environmental changes due to the incorporation of the polymer [205].

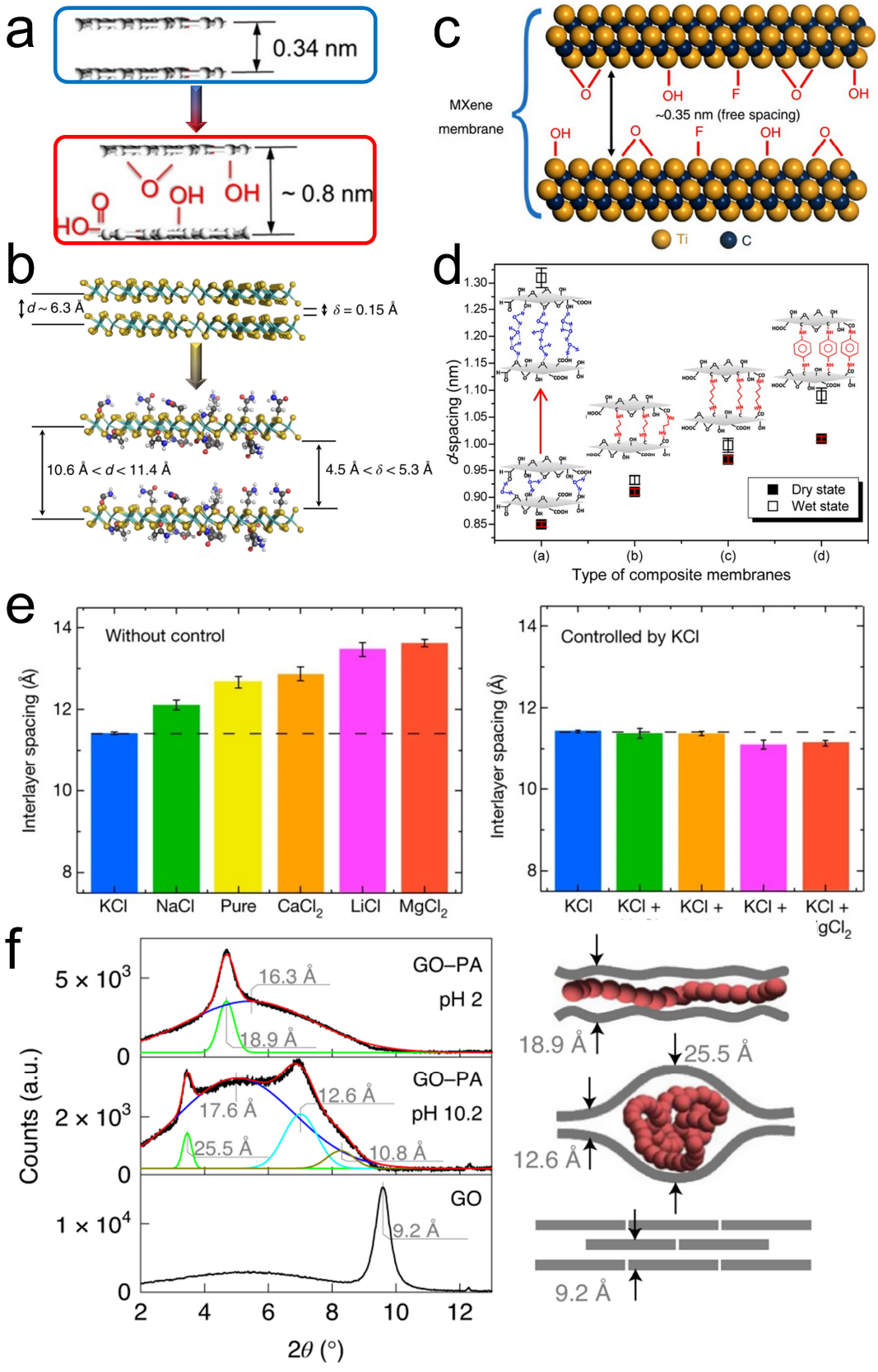

Figure 1.16 The interlayer space changes of 2D laminated membranes aroused by covalent or non-covalent modification. a, Schematic illustration of d-spacings of graphene and GO nanochannel. **b**, Schematics of restacked pristine MoS_2 and

functionalized MoS_2 nanosheets with the interlayer spacing d and the capillary width δ. **c**, Illustration of the spacing between the neighboring MXene nanosheets in the membrane. **d**, Structural diagram and d-spacing of GO and diamine monomer cross-linked GO membrane. **e**, Interlayer spacings for GO membranes immersed in various solutions (left). Interlayer spacings of GO membranes that were soaked in KCl solution, followed by immersion in various salt solutions (right). **f**, X-ray reflection patterns for the GO–PA membranes prepared at different PH solutions with extracted interlayer distances (left) and schematic illustrations for the membranes' structure (right).

(ii) Nanochannel charge:

The majority of pristine nanosheets possess charges, such as the positively charged layered double hydroxide (DLH) and negatively charged GO, TMDs, MXene and clay [206, 207]. The 2D nanochannels with confined space exhibit surface charge governed ion transport behavior. Consequently, laminar membranes composed of negatively charged nanosheets demonstrate preferential transport for cations while blocking anions, and vice versa. As a result, most 2D laminar membranes can serve as cation/anion screening membranes [125]. The sieving type and selectivity ratio are determined by the charge types and quantities on the nanosheets. By modifying the nanosheets, reinforced charge distribution or reversed charge can be achieved, providing novel and highly efficient ion sieving performance for the laminar membrane.

Zhang et al. used 1-(3-Dimethylaminopropyl)-3-ethylcarbodiimide (EDC) to neutralize the negative charge of GO by reacting with the carboxylic group. They then added branched polyethylenimine (PEI) to enrich the surface charge through covalent coupling (Figure 1.17 a) [208]. This process resulted in the synthesis of positively charged GO nanosheets (p-GO). The p-GO membrane exhibited inhibited proton transport behavior compared to the pristine GO membrane. Furthermore, an asymmetric proton transport behavior was observed in a 2D laminar membrane with a heterogeneous structure assembled from p-GO and n-GO nanosheets. Wen et al. used the same method to modify n-GO and p-GO, fabricating a planar GO membrane with heterojunctions (Figure 1.17 b) [209]. An internal electric field formed at the transition zone. In synergy with an external electric field, the transition zone became an ion

depletion area, where the ionic concentration was significantly lower than in the bulk phase. Deionized water could be extracted from the depletion zone, achieving a high rejection rate of 97.0% for NaCl and a water flux of 1529 L m^{-2} h^{-1} bar^{-1} at the outlet.

In addition to covalent modification, noncovalent combinations with polymers can also alter the surface charge of nanosheets. Positively charged MXene nanosheets (p-MXene) were synthesized by adsorbing the positively charged polymer PDDA onto the surface through electrostatic attraction [181]. The p-MXene membrane demonstrated excellent anion selectivity, and when combined with a pristine MXene membrane, which had cation selectivity, the system functioned as a high-performance osmotic power generator (Figure 1.17 c). Under an artificial seawater/river water salinity gradient (0.5 M NaCl / 0.01 M NaCl), an output power density of 4.6 W m^{-2} was achieved, which close to the commercialization benchmark of around 5 W m^{-2}. It is worth noting that the output voltage of 166 mV per unit cell under the artificial seawater and river water salinity gradient was relatively small. To achieve higher voltages, a series of MXene membranes-based nanofluidic reverse electrodialysis device (MXM-RED) stacks were constructed by connecting interleaving MXM pairs in series. As the number of assembled MXM pairs increased from 1 to 10, the output voltages reached up to 1.66 V, which was sufficient to directly power a calculator and perform arithmetic operations. Instead of simply connecting oppositely charged membranes in series, which can lead to excessive counter ion accumulation on the low concentration side of the membrane after prolonged operation, resulting in concentration polarization and weakened ion selectivity and transport capacity, composite membrane with bilayer heterostructure can counteract this issue [210-212]. Due to their structural and/or charge asymmetry, they prevent counter ion accumulation and reduce the effects of concentration polarization. Ding et al. used p-MXene and n-MXene nanosheets to stack a heterostructural MXene membrane. With a 50-fold salinity gradient, the MXene heterostructural membrane achieved an output power density of 8.6 W m^{-2} [213].

Rather than reversing the surface charge, a polymer with the same charge can be used to enrich the surface charge of nanosheets through hydrogen bonding and van der

Waals attraction. Zhang et al. employed negatively charged Kevlar nanofibers to modify MXene nanosheets (Figure 1.17 d) [182]. After assembling into a composite membrane, the enhanced charge density in the nanochannels resulted in increased cation selectivity. Consequently, an outstanding osmotic power density was obtained with this composite membrane when mixing river water and seawater. Subsequently, the intercalation strategy has been widely utilized to prepare various 2D material-based membranes, such as GO/ANF [214], GO/CNF [215], g-C3N4/CNF [216], clay/ANF [217], and COF/SANF [218], with the aim of enhancing the charges of nanochannels for ion selectivity.

In addition to altering nanochannel charges, directly coating polyelectrolytes on membrane surfaces can also modify charge distribution, affecting ionic transport. By coating polycations such as polydiallyl dimethyl ammonium (PDDA), polyethylene imine (PEI), and polyallylamine hydrochloride (PAH) on the GO membrane, it exhibits the ability to exclude AB_2-type salts due to the positively charged surface. This results in a stronger electrostatic repulsion against divalent cations A^{2+} compared to the attraction with monovalent anions B^-. Conversely, coating polyanions such as polystyrene sulfonate (PSS), polyacrylic acid (PAA), and sodium alginate (SA) on the GO membrane leads to the exclusion of A_2B-type salts based on the negatively charged surface, which shows a pronounced electrostatic repulsion towards the divalent anions B^{2-} while attracting monovalent cations A^+. The engineered surface-charged GO membranes demonstrate impressive performance, with a $MgCl_2$ rejection of 93.2% and a water permeance of 51.2 L m^{-2} h^{-1} bar^{-1}, as well as a Na_2SO_4 rejection of 93.9% and a water permeance of 56.8 L m^{-2} h^{-1} bar^{-1}. This significantly exceeds the performance of pristine GO membranes [219].

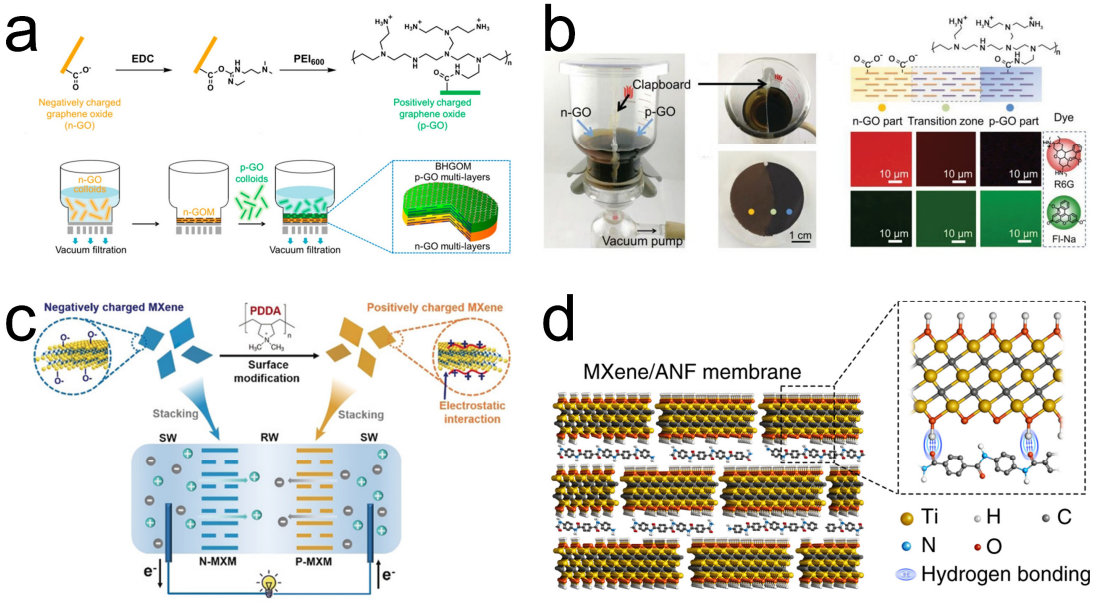

Figure 1.17 The surface charge regulation of 2D laminated membrane based on the chemical modification. a, The preparation of p-GO nanosheets and scheme of the sequential filtration process for the fabrication of heterostructure membrane. **b**, The photographs of the dual-flow filtration setup (left) and planar heterogeneous GO membrane---PHGOM (middle). Fluorescence images on separate parts of the PHGOM (right). **c**, Scheme of nanofluidic energy harvesting device constructed by the cation-selective (negatively charged MXene) and anion-selective (positively charged MXene) MXene membrane pairs. **d,** Schematic of the interior structure of the charged aramid nanofiber (ANF) decorated MXene membrane.

(iii) Affinity:

The affinity of the nanochannel, that is, the interaction between penetrants and the nanosheets, plays a crucial role in the adsorption and diffusion of penetrants within the nanochannel. The addition of groups and molecules to the nanosheets' surfaces can alter the nanochannel's affinity, leading to changes in the membrane's separation performance. In this section, we discuss the changes in affinity resulting from nanosheets modification and their effects on gas separation performance. The impact of the nanochannel's affinity on water transport, referring to wettability, will be addressed in the following section.

Oxygen-containing groups on GO nanosheets not only create unimpeded nanochannels but also provide a strong affinity for polar molecules such as CO_2

compared to N_2 (Figure 1.18 a). This strong adhesion between CO_2 and oxygen groups leads to preferential adsorption, translating to superior CO_2 separation performance. Apart from oxygen groups, amino groups have also been used to modify nanosheets to increase nanochannel affinity. Piperazine, an effective CO_2-philic agent, was grafted onto GO nanosheets by Zhou et al (Figure 1.18 b). These grafted amine-brushes in the GO nanochannels facilitated the transport of CO_2 molecules, resulting in improved CO_2 selectivity and permeance. The GO-piperazine (GOP) hollow fiber membranes exhibited outstanding separation performance under simulated flue gas conditions, achieving a CO_2 permeance of 1020 GPU and a CO_2/N_2 selectivity as high as 680 [177]. Yang et al. developed a gas separation membrane by incorporating an amino-functionalized POSS (POSS-NH_2) nanocage intercalator into GO nanosheets (Fig. 1). The rigid structure and eight amino groups on the side chains of POSS-NH_2 allow for fine regulation of the GO interlayer channel structure, creating favorable physical and chemical microenvironments for CO_2/CH_4 separation. The reduced interlayer free space (ranging from 9.1 to 4.7 Å) due to POSS-NH_2 crosslinking, as well as the steric hindrance of POSS, contributed to enhanced diffusion selectivity for CO_2/CH_4. The amino groups on POSS-NH_2 were able to react reversibly with CO_2, promoting CO_2 transport. By synergistically enhancing diffusion selectivity and facilitated transport mechanisms, the efficient separation of CO_2/CH_4 was successfully achieved and the GO-POSS-NH_2 (5) membrane displayed a CO_2/CH_4 selectivity of 74.5 [220]. Additionally, specific molecules such as borates can create a favorable environment for CO_2 in the nanochannel. Boron-bridged GO and MXene membranes were synthesized and demonstrated highly efficient CO_2 permeance (Figure 1.18 c) [119, 174].

The direct introduction of permeate-philic molecules on the nanosheet via non-covalent binding can also impact the affinity of the nanochannel. Peng et al. suggested filling the nanochannel of 2D laminar membranes with ionic liquid (IL), which would be strongly anchored to the nanosheets surface through electrostatic attraction, forming IL-intercalated GO or TMDs laminar membranes (Figure 1.18 d) [187, 221-223]. The confined IL in the nanochannel exhibited a strong interaction with CO_2, resulting in

enhanced CO_2 adsorption performance for the composite membrane. This led to improved CO_2 selectivity compared to the pristine laminar membrane. Furthermore, their team proposed constructing an ultrafast and highly selective nano Newton's cradle for CO_2 transport by assembling GO nanosheets with positively charged zinc hydroxide nanostrands (ZHNs), and impregnating IL within the nanochannels. The GO laminates form a strong foundation for the entire system. By incorporating IL, the membrane gains the ability to sieve different gases. Meanwhile, ZHNs play a crucial role in boosting selective CO_2 adsorption, leading to remarkable CO_2 separation performance. The resulting nano Newton's cradle demonstrates a significant CO_2 permeance enhancement, over 53 times greater than the GO/IL membrane without ZHNs. Additionally, it exhibits superhigh selectivities for CO_2/light gases (35 for CO_2/H_2, 194 for CO_2/CH_4, and 331 for CO_2/N_2) [224].

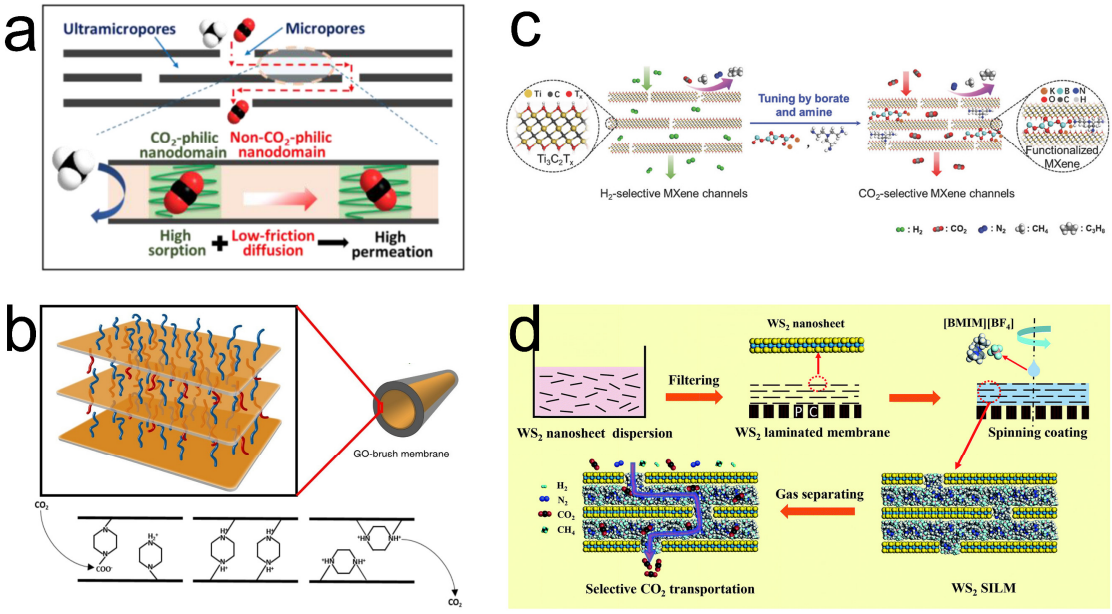

Figure 1.18 The nanochannel affinity adjustment of 2D laminated membrane based on the chemical modification. a, Representation of gas molecules transport in the GO stacking membranes channels containing both CO_2-philic and non-CO_2-philic nanodomains. **b**, The structure diagram of the GO-based hollow fiber membranes with brush-like CO_2-philic agent (top). The CO_2 transport in the GO nanochannel (down). **c**, Structures and gas transport of H_2-selective and CO_2-selective MXene nanofilms. **d**, Schematic diagrams of the synthesis process of the WS_2 supported ionic liquid membrane and selective CO_2 transportation.

(iv) Wettability:

The wettability of membranes has a significant impact on water transport, as evidenced by numerous studies [225-227]. The wettability of 2D laminar membranes is influenced by the surface properties of the nanosheets, which can be easily manipulated by introducing exterior molecules or groups through covalent or noncovalent modification. These molecules reside in the nanochannel, creating either hydrophilic or hydrophobic transport pathways. Hydrophobic nanochannels exhibit weak friction with water molecules due to weak interactions, resulting in high water transport speeds. However, hydrophobic nanochannels are not conducive to the entry of water molecules. Conversely, hydrophilic nanochannels facilitate the entry of water but hinder water transport due to strong adhesion interactions. By delicately tailoring the wettability of nanochannels, different separation applications for membranes can be accommodated, optimizing their performance based on specific needs.

As discussed previously, graphene nanochannels with hydrophobic surfaces exhibit a superhigh water permeation rate due to their low hydraulic resistance [228]. However, after oxidation, the water diffusion rate in GO nanochannels decreases significantly, as grafted oxygenated groups on the nanosheet surface strongly adsorb water molecules and hinder their movement (Figure 1.19 a) [140]. Graphene nanochannels with much longer slip lengths can be considered as 'frictionless' transport pathways for water, while GO nanochannels with an obvious parabolic shape of the velocity profile show increased friction with water. The higher hydraulic resistance of GO suppresses water transport and results in undesired water permeance as confirmed by numerous molecular dynamic simulation studies [104, 145].

To take advantage of graphene nanochannels for super-fast water permeance, Cheng et al. fabricated robust angstrom-channel graphene membranes (ACGMs) by intercalating chitosan into thermally reduced graphene oxide (GO) sheets (Figure 1.19 b) [229]. The hydrophobic ACGMs demonstrated high flux for water and organic solvent permeation in the pervaporation process. Interestingly, the membranes showed

a preference for water permeation over ethanol when the feed solution contained an ethanol and water mixture, due to the prioritized adsorption of water molecules on the membrane surface. The ACGMs exhibit a water flux of 63.8 ± 3.2 kg m^{-2} h^{-1} at 20 °C and 389.1 ± 19.4 kg m^{-2} h^{-1} at 60 °C for a water-ethanol mixture with 90 wt% ethanol, achieving over two orders of magnitude higher performance than conventional pervaporation membranes. This makes them highly promising for ethanol dehydration applications. MoS_2 nanosheets with different grafted groups also exhibit tunable surface wettability [195]. Hydrophobic groups, such as -CH_3 functionalized MoS_2 membranes, have increased slip lengths compared to hydrophilic pristine 1T MoS_2, resulting in higher water flux when they have the same nanochannel size (Figure 1.19 c). The high water flux makes hydrophobic membranes advantageous for water permeation.

In contrast to the high transport efficiency of hydrophobic nanochannels, hydrophilic nanochannels offer advantages in terms of antifouling properties for membranes. Li developed a zwitterionic polymer-brush-modified graphene oxide membrane featuring trimethylamine-N-oxide (TMAO) head groups. This design created a strong surface hydration layer for the membrane. The hydrophilic surface and the disinfection effect provided by the quaternary ammonium groups both contribute to the T-GO membrane's impressive antiadhesion and contact inactivation abilities [230]. Huang et al. discovered that the surface wettability of vermiculite nanosheets could be tuned from superhydrophilic to hydrophobic simply by intercalating hydrated cations into the membrane (Figure 1.19 d). The lithium-intercalated vermiculite laminate (LiV-laminate) exhibited a zero contact angle under wet conditions. The super-hydrophilic surface of LiV-laminate originated from the anomalous hydrated structure of Li at the vermiculite surface. Due to its outstanding antifouling properties, the super-hydrophilic membrane demonstrated excellent oil-water separation performance [231].

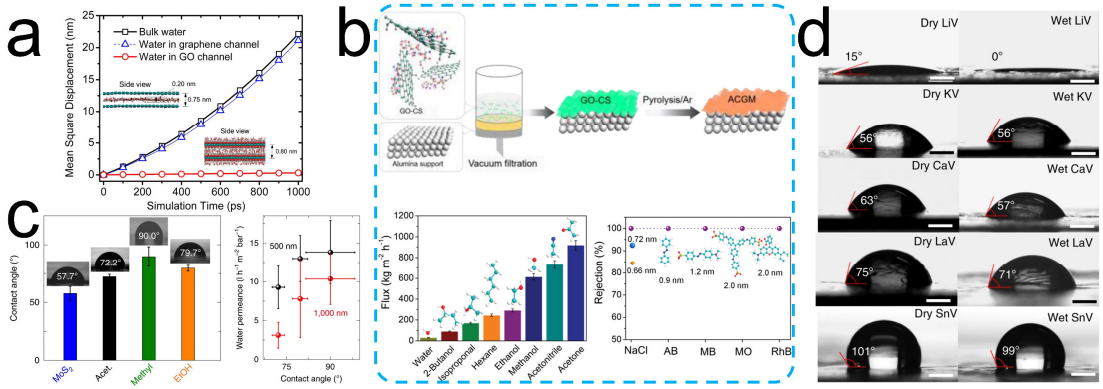

Figure 1.19 The surface wettability control of 2D laminated membrane based on the chemical modification. a, Mean square displacements of water molecules in bulk, the graphene channel, and a GO channel. **b**, Schematic illustrating the preparation of angstrom-channel graphene-based membranes---ACGMs (top). Fluxes of ACGMs and rejection of NaCl and dyes (bottom). **c**, The contact angle of pristine and functionalized MoS_2 membranes (left). Evolution of the water flux with the water contact angle of the functionalized membranes (right). **d**, The water contact angle of cation intercalated vermiculite membrane in dry and wet states.

1.4 Conclusion

The growing environmental concerns have received widespread attention for the development of viable solutions to address these challenges. Membrane separation, as an effective approach, has been extensively applied for various separation application, including gas separation, sewage purification, seawater desalination, and solvent recycling.

Membrane materials, being the core of membrane separation technology, have evolved over time, resulting in the development of various high-performance membranes. In particular, polymer membranes are mature techniques and have found their way to pratical applications in the industrial sector. However, the permeability-selectivity trade-off, aging, and fouling issues have driven researchers to develop a new generation of separation membranes.

Two-dimensional (2D) material membranes have emerged as a promising alternative, endowed with numerous advantages such as ultra-thin thickness, high mechanical strength, and versatile surface chemistry. These properties make 2D

materials, such as graphene oxide (GO), transition metal dichalcogenides (TMDs) and transitional metal carbides and/or nitrides (MXene), interesting candidates for constructing high-performance separation membranes capable of overcoming the limitations of conventional polymer membranes.

With the development of 2D material membranes, researchers have been focusing on strategies to tailor their properties, such as nanopores/nanochannel architecture and microenvironments, to optimize separation performance. These strategies include the introduction of functional groups, cross-linking with adjacent nanosheets, intercalation of molecules, and coordination with ions. As a result, 2D membranes have demonstrated superior performance in various separation applications, including gas and water purification, and molecular and ion sieving.

Despite the remarkable progress in the field of 2D membranes, there remain several challenges that need to be addressed. The long-term stability and scalability of these membranes need to be improved to make them more suitable for realistic applications. Additionally, the development of more efficient and environmentally friendly fabrication methods will be vital to enable sustainable production of 2D membranes.

Overall, 2D membranes hold great potential for a wide range of separation applications, and their performance can be effectively tailored through the manipulation of nanochannel physicochemical properties. As research in this area continues to advance, it is expected that novel materials, fabrication methods, and modification strategies will emerge, enabling the development of next-generation separation membranes with superior performance, stability, and sustainability. In this context, progress in the field of engineering of 2D materials and design of the 2D nanolaminate membrane is therefore requested and served as the main motivation for the present thesis.

1.5 Reference

1. Lee, A., J.W. Elam, and S.B. Darling, *Membrane materials for water purification: design, development, and application.* Environmental Science: Water Research & Technology, 2016. **2**(1): p. 17-42.
2. Vatanpour, V., et al., *Cellulose acetate in fabrication of polymeric membranes: A review.* Chemosphere, 2022. **295**: p. 133914.
3. Li, S., et al., *Recent advances on cellulose-based nanofiltration membranes and their applications in drinking water purification: A review.* Journal of Cleaner Production, 2022. **333**: p. 130171.
4. Yang, Z., H. Guo, and C.Y. Tang, *The upper bound of thin-film composite (TFC) polyamide membranes for desalination.* Journal of Membrane Science, 2019. **590**: p. 117297.
5. Peng, L.E., et al., *A critical review on porous substrates of TFC polyamide membranes: Mechanisms, membrane performances, and future perspectives.* Journal of Membrane Science, 2022. **641**: p. 119871.
6. Bera, D., R. Chatterjee, and S. Banerjee, *Aromatic polyamide nonporous membranes for gas separation application.* e-Polymers, 2021. **21**(1): p. 108-130.
7. Gao, C., et al., *The effect of nanoparticles on gas permeability with polyimide membranes and network hybrid membranes: a review.* Reviews in Inorganic Chemistry, 2021. **41**(1): p. 1-20.
8. Wu, S., et al., *Design of interchain hydrogen bond in polyimide membrane for improved gas selectivity and membrane stability.* Journal of Membrane Science, 2021. **618**: p. 118659.
9. Liu, G. and W. Jin, *Pervaporation membrane materials: Recent trends and perspectives.* Journal of Membrane Science, 2021. **636**: p. 119557.
10. Rani, S.L.S. and R.V. Kumar, *Insights on applications of low-cost ceramic membranes in wastewater treatment: A mini-review.* Case Studies in Chemical and Environmental Engineering, 2021. **4**: p. 100149.
11. Usman, J., et al., *An overview of superhydrophobic ceramic membrane surface*

modification for oil-water separation. Journal of Materials Research and Technology, 2021. **12**: p. 643-667.

12. Arumugham, T., et al., *Recent developments in porous ceramic membranes for wastewater treatment and desalination: A review.* Journal of Environmental Management, 2021. **293**: p. 112925.
13. Asif, M.B. and Z. Zhang, *Ceramic membrane technology for water and wastewater treatment: A critical review of performance, full-scale applications, membrane fouling and prospects.* Chemical Engineering Journal, 2021. **418**: p. 129481.
14. Tanaka, D.P., et al., *Metallic membranes for hydrogen separation*, in *Current trends and future developments on (bio-) membranes*. 2020, Elsevier. p. 1-29.
15. Pal, N., et al., *A review on types, fabrication and support material of hydrogen separation membrane.* Materials Today: Proceedings, 2020. **28**: p. 1386-1391.
16. Shi, Y., et al., *Electro-enhanced separation of microsized oil-in-water emulsions via metallic membranes: performance and mechanistic insights.* Environmental Science & Technology, 2022. **56**(7): p. 4518-4530.
17. Kosinov, N., et al., *Recent developments in zeolite membranes for gas separation.* Journal of Membrane Science, 2016. **499**: p. 65-79.
18. Khulbe, K., et al., *Recent development on the effect of water/moisture on the performance of zeolite membrane and MMMs containing zeolite for gas separation; review.* RSC advances, 2016. **6**(49): p. 42943-42961.
19. Park, H.B., et al., *Maximizing the right stuff: The trade-off between membrane permeability and selectivity.* Science, 2017. **356**(6343): p. eaab0530.
20. Verweij, H., *Inorganic membranes.* Current Opinion in Chemical Engineering, 2012. **1**(2): p. 156-162.
21. Goh, P. and A. Ismail, *A review on inorganic membranes for desalination and wastewater treatment.* Desalination, 2018. **434**: p. 60-80.
22. Fan, F.R., et al., *Emerging beyond-graphene elemental 2D materials for energy and catalysis applications.* Chemical Society Reviews, 2021. **50**(19): p. 10983-11031.

23. Zhao, L., B. Wang, and R. Wang, *A Critical Review on New and Efficient 2D Materials for Catalysis.* Advanced Materials Interfaces, 2022. **9**(29): p. 2200771.
24. Lemme, M.C., et al., *Two-dimensional materials for electronic applications.* Mrs Bulletin, 2014. **39**(8): p. 711-718.
25. Sangwan, V.K. and M.C. Hersam, *Electronic transport in two-dimensional materials.* Annual review of physical chemistry, 2018. **69**: p. 299-325.
26. Zhang, X., et al., *2D materials beyond graphene for high-performance energy storage applications.* Advanced Energy Materials, 2016. **6**(23): p. 1600671.
27. Chen, X., et al., *The marriage of two-dimensional materials and phase change materials for energy storage, conversion and applications.* EnergyChem, 2022. **4**(2): p. 100071.
28. Liu, G., W. Jin, and N. Xu, *Two-dimensional-material membranes: a new family of high-performance separation membranes.* Angewandte Chemie International Edition, 2016. **55**(43): p. 13384-13397.
29. Moghadam, F. and H.B. Park, *Two-dimensional materials: an emerging platform for gas separation membranes.* Current opinion in chemical engineering, 2018. **20**: p. 28-38.
30. Shen, J., et al., *Artificial channels for confined mass transport at the sub-nanometre scale.* Nature Reviews Materials, 2021. **6**(4): p. 294-312.
31. Koenig, S.P., et al., *Selective molecular sieving through porous graphene.* Nature nanotechnology, 2012. **7**(11): p. 728-732.
32. Kang, Y., et al., *2D laminar membranes for selective water and ion transport.* Advanced Functional Materials, 2019. **29**(29): p. 1902014.
33. Tan, C., et al., *Recent advances in ultrathin two-dimensional nanomaterials.* Chemical reviews, 2017. **117**(9): p. 6225-6331.
34. Chang, C., et al., *Recent progress on two-dimensional materials.* Acta Phys. Chim. Sin, 2021. **37**(12): p. 2108017.
35. Zhang, H., *Introduction: 2D materials chemistry*. 2018, ACS Publications. p. 6089-6090.

36. Lin, S., et al., *Understanding the colloidal dispersion stability of 1D and 2D materials: perspectives from molecular simulations and theoretical modeling.* Advances in colloid and interface science, 2017. **244**: p. 36-53.
37. Akbari, A., et al., *Large-area graphene-based nanofiltration membranes by shear alignment of discotic nematic liquid crystals of graphene oxide.* Nature communications, 2016. **7**(1): p. 10891.
38. Zhang, H., et al., *A review of advancing two-dimensional material membranes for ultrafast and highly selective liquid separation.* Nanomaterials, 2022. **12**(12): p. 2103.
39. Liu, P., et al., *Two-dimensional material membranes for critical separations.* Inorganic Chemistry Frontiers, 2020. **7**(13): p. 2560-2581.
40. Xu, G.-R., et al., *Two-dimensional (2D) nanoporous membranes with sub-nanopores in reverse osmosis desalination: Latest developments and future directions.* Desalination, 2019. **451**: p. 18-34.
41. Surwade, S.P., et al., *Water desalination using nanoporous single-layer graphene.* Nature nanotechnology, 2015. **10**(5): p. 459-464.
42. Huang, S., et al., *Single-layer graphene membranes by crack-free transfer for gas mixture separation.* Nature communications, 2018. **9**(1): p. 2632.
43. Yang, Y., et al., *Large-area graphene-nanomesh/carbon-nanotube hybrid membranes for ionic and molecular nanofiltration.* Science, 2019. **364**(6445): p. 1057-1062.
44. Feng, J., et al., *Single-layer MoS_2 nanopores as nanopower generators.* Nature, 2016. **536**(7615): p. 197-200.
45. Celebi, K., et al., *Ultimate permeation across atomically thin porous graphene.* Science, 2014. **344**(6181): p. 289-292.
46. Li, H., et al., *Ultrathin, molecular-sieving graphene oxide membranes for selective hydrogen separation.* Science, 2013. **342**(6154): p. 95-98.
47. Nair, R., et al., *Unimpeded permeation of water through helium-leak–tight graphene-based membranes.* Science, 2012. **335**(6067): p. 442-444.

48. Joshi, R., et al., *Precise and ultrafast molecular sieving through graphene oxide membranes.* science, 2014. **343**(6172): p. 752-754.
49. Lehtinen, O., et al., *Non-invasive transmission electron microscopy of vacancy defects in graphene produced by ion irradiation.* Nanoscale, 2014. **6**(12): p. 6569-6576.
50. Lucchese, M.M., et al., *Quantifying ion-induced defects and Raman relaxation length in graphene.* Carbon, 2010. **48**(5): p. 1592-1597.
51. Russo, C.J. and J.A. Golovchenko, *Atom-by-atom nucleation and growth of graphene nanopores.* Proceedings of the National Academy of Sciences, 2012. **109**(16): p. 5953-5957.
52. Wang, L., et al., *Molecular valves for controlling gas phase transport made from discrete ångström-sized pores in graphene.* Nature nanotechnology, 2015. **10**(9): p. 785-790.
53. Yamada, Y., et al., *Subnanometer vacancy defects introduced on graphene by oxygen gas.* Journal of the American Chemical Society, 2014. **136**(6): p. 2232-2235.
54. Cheng, C., S.A. Iyengar, and R. Karnik, *Molecular size-dependent subcontinuum solvent permeation and ultrafast nanofiltration across nanoporous graphene membranes.* Nature Nanotechnology, 2021. **16**(9): p. 989-995.
55. Heiranian, M., A.B. Farimani, and N.R. Aluru, *Water desalination with a single-layer MoS2 nanopore.* Nature communications, 2015. **6**(1): p. 8616.
56. Thiruraman, J.P., et al., *Angstrom-size defect creation and ionic transport through pores in single-layer MoS_2.* Nano letters, 2018. **18**(3): p. 1651-1659.
57. Cun, H., et al., *Centimeter-sized single-orientation monolayer hexagonal boron nitride with or without nanovoids.* Nano letters, 2018. **18**(2): p. 1205-1212.
58. Caglar, M., et al., *Tunable anion-selective transport through monolayer graphene and hexagonal boron nitride.* ACS nano, 2019. **14**(3): p. 2729-2738.
59. Knebel, A.a. and J. Caro, *Metal–organic frameworks and covalent organic frameworks as disruptive membrane materials for energy-efficient gas separation.* Nature Nanotechnology, 2022. **17**(9): p. 911-923.

60. Lu, J., et al., *Efficient metal ion sieving in rectifying subnanochannels enabled by metal–organic frameworks.* Nature materials, 2020. **19**(7): p. 767-774.
61. Jian, M., et al., *Ultrathin water-stable metal-organic framework membranes for ion separation.* Science advances, 2020. **6**(23): p. eaay3998.
62. Li, X., et al., *Construction of angstrom-scale ion channels with versatile pore configurations and sizes by metal-organic frameworks.* Nature communications, 2023. **14**(1): p. 286.
63. Wang, J., et al., *Ultrathin ZIF-8 Membrane through Inhibited Ostwald Ripening for High-Flux C_3H_6/C_3H_8 Separation.* Advanced Functional Materials, 2022. **32**(47): p. 2208064.
64. Hou, J., et al., *Highly efficient H_2/CO_2 separation via an ultrathin metal-organic framework membrane.* Chemical Engineering Science, 2018. **182**: p. 180-188.
65. Liu, G., et al., *Eliminating lattice defects in metal–organic framework molecular-sieving membranes.* Nature Materials, 2023: p. 1-8.
66. Li, Y., et al., *Laminated self-standing covalent organic framework membrane with uniformly distributed subnanopores for ionic and molecular sieving.* Nature communications, 2020. **11**(1): p. 599.
67. Yang, J., et al., *Advancing osmotic power generation by covalent organic framework monolayer.* Nature nanotechnology, 2022. **17**(6): p. 622-628.
68. Shinde, D.B., et al., *Crystalline 2D covalent organic framework membranes for high-flux organic solvent nanofiltration.* Journal of the American Chemical Society, 2018. **140**(43): p. 14342-14349.
69. Zhuang, X., et al., *A two-dimensional conjugated polymer framework with fully sp 2-bonded carbon skeleton.* Polymer Chemistry, 2016. **7**(25): p. 4176-4181.
70. Liu, K., L. Wang, and R. Dong, *Two-dimensional conjugated polymer films via liquid-interface-assisted synthesis toward organic electronic devices.* Journal of Materials Chemistry C, 2020. **8**(31): p. 10696-10718.
71. Shen, J., et al., *Fast water transport and molecular sieving through ultrathin ordered conjugated-polymer-framework membranes.* Nature Materials, 2022.

21(10): p. 1183-1190.

72. Salameh, C. and D. Voiry, *Sieving in order.* Nature Materials, 2022. **21**(10): p. 1106-1107.
73. Hirata, M., et al., *Thin-film particles of graphite oxide 1:: High-yield synthesis and flexibility of the particles.* Carbon, 2004. **42**(14): p. 2929-2937.
74. Botas, C., et al., *Graphene materials with different structures prepared from the same graphite by the Hummers and Brodie methods.* Carbon, 2013. **65**: p. 156-164.
75. Moo, J.G.S., et al., *Graphene Oxides Prepared by Hummers', Hofmann's, and Staudenmaier's Methods: Dramatic Influences on Heavy-Metal-Ion Adsorption.* ChemPhysChem, 2014. **15**(14): p. 2922-2929.
76. Hummers Jr, W.S. and R.E. Offeman, *Preparation of graphitic oxide.* Journal of the american chemical society, 1958. **80**(6): p. 1339-1339.
77. Agarwal, V. and P.B. Zetterlund, *Strategies for reduction of graphene oxide–A comprehensive review.* Chemical Engineering Journal, 2021. **405**: p. 127018.
78. Tsou, C.-H., et al., *Effect of microstructure of graphene oxide fabricated through different self-assembly techniques on 1-butanol dehydration.* Journal of Membrane Science, 2015. **477**: p. 93-100.
79. Zhang, Y., et al., *Layer-by-layer construction of graphene oxide (GO) framework composite membranes for highly efficient heavy metal removal.* Journal of membrane science, 2016. **515**: p. 230-237.
80. Huang, H., et al., *Salt concentration, pH and pressure controlled separation of small molecules through lamellar graphene oxide membranes.* Chemical Communications, 2013. **49**(53): p. 5963-5965.
81. Liu, H., H. Wang, and X. Zhang, *Facile fabrication of freestanding ultrathin reduced graphene oxide membranes for water purification.* Advanced materials, 2015. **27**(2): p. 249-254.
82. Han, Y., Z. Xu, and C. Gao, *Ultrathin graphene nanofiltration membrane for water purification.* Advanced Functional Materials, 2013. **23**(29): p. 3693-3700.
83. Morelos-Gomez, A., et al., *Effective NaCl and dye rejection of hybrid graphene*

oxide/graphene layered membranes. Nature nanotechnology, 2017. **12**(11): p. 1083-1088.

84. Rashidi, F., et al., *Graphene oxide membranes in extreme operating environments: concentration of kraft black liquor by lignin retention.* ACS Sustainable Chemistry & Engineering, 2017. **5**(1): p. 1002-1009.
85. Wang, Z., et al., *High-performance graphene oxide nanofiltration membranes for black liquor concentration.* ACS Sustainable Chemistry & Engineering, 2019. **7**(17): p. 14915-14923.
86. Wang, Z., et al., *Graphene oxide nanofiltration membranes for desalination under realistic conditions.* Nature Sustainability, 2021. **4**(5): p. 402-408.
87. Li, Y., et al., *Thermally reduced nanoporous graphene oxide membrane for desalination.* Environmental science & technology, 2019. **53**(14): p. 8314-8323.
88. Yuan, S., et al., *Minimizing non-selective nanowrinkles of reduced graphene oxide laminar membranes for enhanced NaCl rejection.* Environmental Science & Technology Letters, 2020. **7**(4): p. 273-279.
89. Abraham, J., et al., *Tunable sieving of ions using graphene oxide membranes.* Nature nanotechnology, 2017. **12**(6): p. 546-550.
90. Wei, Y., et al., *Declining flux and narrowing nanochannels under wrinkles of compacted graphene oxide nanofiltration membranes.* Carbon, 2016. **108**: p. 568-575.
91. Huang, L., et al., *Graphene oxide membranes with tunable semipermeability in organic solvents.* Advanced Materials, 2015. **27**(25): p. 3797-3802.
92. Zheng, S., et al., *Correlating interlayer spacing and separation capability of graphene oxide membranes in organic solvents.* ACS nano, 2020. **14**(5): p. 6013-6023.
93. Yang, Q., et al., *Ultrathin graphene-based membrane with precise molecular sieving and ultrafast solvent permeation.* Nature materials, 2017. **16**(12): p. 1198-1202.
94. Huang, L., et al., *Reduced graphene oxide membranes for ultrafast organic solvent*

nanofiltration. Advanced Materials, 2016. **28**(39): p. 8669-8674.

95. Alen, S.K., S. Nam, and S.A. Dastgheib, *Recent advances in graphene oxide membranes for gas separation applications.* International Journal of Molecular Sciences, 2019. **20**(22): p. 5609.
96. Kim, H.W., et al., *Selective gas transport through few-layered graphene and graphene oxide membranes.* Science, 2013. **342**(6154): p. 91-95.
97. Jin, X., et al., *Effective separation of CO_2 using metal-incorporated rGO membranes.* Advanced Materials, 2020. **32**(17): p. 1907580.
98. Liu, R., et al., *Graphene oxide membrane for liquid phase organic molecular separation.* Carbon, 2014. **77**: p. 933-938.
99. Huang, K., et al., *A graphene oxide membrane with highly selective molecular separation of aqueous organic solution.* Angewandte Chemie, 2014. **126**(27): p. 7049-7052.
100. Chen, X., et al., *Fabrication of graphene oxide composite membranes and their application for pervaporation dehydration of butanol.* Chinese Journal of Chemical Engineering, 2015. **23**(7): p. 1102-1109.
101. Zhao, B., et al., *2D Metallic Transition-metal dichalcogenides: structures, synthesis, properties, and applications.* Advanced Functional Materials, 2021. **31**(48): p. 2105132.
102. Liu, Y., et al., *MoS_2-based membranes in water treatment and purification.* Chemical Engineering Journal, 2021. **422**: p. 130082.
103. Sun, L., H. Huang, and X. Peng, *Laminar MoS_2 membranes for molecule separation.* Chemical communications, 2013. **49**(91): p. 10718-10720.
104. Wang, Z., et al., *Understanding the aqueous stability and filtration capability of MoS_2 membranes.* Nano letters, 2017. **17**(12): p. 7289-7298.
105. Zhang, L., et al., *Fabrication of 1T-MoS_2 nanosheets and the high-efficiency removal of toxic metals in aquatic systems: Performance and mechanisms.* Chemical Engineering Journal, 2020. **386**: p. 123996.
106. Wang, Z., et al., *Removal and recovery of heavy metal ions by two-dimensional*

MoS_2 nanosheets: performance and mechanisms. Environmental science & technology, 2018. **52**(17): p. 9741-9748.

107. Sun, L., et al., *Ultrafast molecule separation through layered WS_2 nanosheet membranes.* ACS nano, 2014. **8**(6): p. 6304-6311.
108. Li, H., et al., *Experimental realization of few layer two-dimensional MoS_2 membranes of near atomic thickness for high efficiency water desalination.* Nano letters, 2019. **19**(8): p. 5194-5204.
109. Guo, B.-Y., et al., *MoS_2 membranes for organic solvent nanofiltration: stability and structural control.* The Journal of Physical Chemistry Letters, 2019. **10**(16): p. 4609-4617.
110. Ran, J., et al., *Ultrathin lamellar MoS_2 membranes for organic solvent nanofiltration.* Journal of Membrane Science, 2020. **602**: p. 117963.
111. Wang, D., et al., *Ultrathin membranes of single-layered MoS_2 nanosheets for high-permeance hydrogen separation.* Nanoscale, 2015. **7**(42): p. 17649-17652.
112. Achari, A., S. Sahana, and M. Eswaramoorthy, *High performance MoS_2 membranes: effects of thermally driven phase transition on CO_2 separation efficiency.* Energy & Environmental Science, 2016. **9**(4): p. 1224-1228.
113. Kumar, J.A., et al., *Methods of synthesis, characteristics, and environmental applications of MXene: A comprehensive review.* Chemosphere, 2022. **286**: p. 131607.
114. Ren, C.E., et al., *Charge-and size-selective ion sieving through $Ti_3C_2T_x$ MXene membranes.* The journal of physical chemistry letters, 2015. **6**(20): p. 4026-4031.
115. Ding, L., et al., *A two-dimensional lamellar membrane: MXene nanosheet stacks.* Angewandte Chemie International Edition, 2017. **56**(7): p. 1825-1829.
116. Lu, Z., et al., *Self-crosslinked MXene ($Ti_3C_2T_x$) membranes with good antiswelling property for monovalent metal ion exclusion.* ACS nano, 2019. **13**(9): p. 10535-10544.
117. Wang, J., et al., *A regularly channeled lamellar membrane for unparalleled water and organics permeation.* Angewandte Chemie International Edition, 2018. **57**(23):

p. 6814-6818.

118. Ding, L., et al., *MXene molecular sieving membranes for highly efficient gas separation.* Nature communications, 2018. **9**(1): p. 155.

119. Shen, J., et al., *2D MXene nanofilms with tunable gas transport channels.* Advanced Functional Materials, 2018. **28**(31): p. 1801511.

120. Fan, Y., et al., *An unprecedented high-temperature-tolerance 2D laminar MXene membrane for ultrafast hydrogen sieving.* Journal of membrane science, 2019. **569**: p. 117-123.

121. Huang, L., L. Ding, and H. Wang, *MXene-Based Membranes for Separation Applications.* Small Science, 2021. **1**(7): p. 2100013.

122. Saha, K., et al., *Applications of lamellar membranes reconstructed from clay mineral-based nanosheets: a review.* ACS Applied Nano Materials, 2022. **5**(11): p. 15972-15999.

123. Zou, Y.-C., et al., *Ion exchange in atomically thin clays and micas.* Nature materials, 2021. **20**(12): p. 1677-1682.

124. Mogg, L., et al., *Atomically thin micas as proton-conducting membranes.* Nature nanotechnology, 2019. **14**(10): p. 962-966.

125. Shao, J.-J., et al., *Self-assembled two-dimensional nanofluidic proton channels with high thermal stability.* Nature communications, 2015. **6**(1): p. 7602.

126. Liu, M.-L., et al., *Two-dimensional nanochannel arrays based on flexible montmorillonite membranes.* ACS applied materials & interfaces, 2018. **10**(51): p. 44915-44923.

127. Xia, Z., et al., *Tunable Ion Transport with Freestanding Vermiculite Membranes.* ACS nano, 2022. **16**(11): p. 18266-18273.

128. Wei, C., et al., *Parallel arrays of clay nanosheets sandwiched in two-dimensional nanofluidic membrane for enhanced ion transport properties.* Journal of Membrane Science, 2023. **680**: p. 121744.

129. Zhou, Y., et al., *Nanofluidic energy conversion and molecular separation through highly stable clay-based membranes.* Journal of Materials Chemistry A, 2019.

7(23): p. 14089-14096.

130. Tian, M., et al., *A two-dimensional lamellar vermiculite membrane for precise molecular separation and ion sieving.* ACS Sustainable Chemistry & Engineering, 2022. **10**(3): p. 1137-1148.
131. Jijoe, P.S., S.R. Yashas, and H.P. Shivaraju, *Fundamentals, synthesis, characterization and environmental applications of layered double hydroxides: a review.* Environmental Chemistry Letters, 2021. **19**(3): p. 2643-2661.
132. Cohen-Tanugi, D. and J.C. Grossman, *Water desalination across nanoporous graphene.* Nano letters, 2012. **12**(7): p. 3602-3608.
133. O'Hern, S.C., et al., *Selective ionic transport through tunable subnanometer pores in single-layer graphene membranes.* Nano letters, 2014. **14**(3): p. 1234-1241.
134. O'Hern, S.C., et al., *Nanofiltration across defect-sealed nanoporous monolayer graphene.* Nano letters, 2015. **15**(5): p. 3254-3260.
135. He, G., et al., *High-permeance polymer-functionalized single-layer graphene membranes that surpass the postcombustion carbon capture target.* Energy & Environmental Science, 2019. **12**(11): p. 3305-3312.
136. Wang, S., et al., *Two-dimensional nanochannel membranes for molecular and ionic separations.* Chemical Society Reviews, 2020. **49**(4): p. 1071-1089.
137. Kuehl, V.A., et al., *A highly ordered nanoporous, two-dimensional covalent organic framework with modifiable pores, and its application in water purification and ion sieving.* Journal of the American Chemical Society, 2018. **140**(51): p. 18200-18207.
138. Fan, H., et al., *Covalent organic framework–covalent organic framework bilayer membranes for highly selective gas separation.* Journal of the American Chemical Society, 2018. **140**(32): p. 10094-10098.
139. Cohen-Tanugi, D., L.-C. Lin, and J.C. Grossman, *Multilayer nanoporous graphene membranes for water desalination.* Nano letters, 2016. **16**(2): p. 1027-1033.
140. Zheng, S., et al., *Swelling of graphene oxide membranes in aqueous solution: characterization of interlayer spacing and insight into water transport*

mechanisms. ACS nano, 2017. **11**(6): p. 6440-6450.

141. Kumar Kannam, S., et al., *Slip length of water on graphene: Limitations of non-equilibrium molecular dynamics simulations.* The Journal of chemical physics, 2012. **136**(2).

142. Cicero, G., et al., *Water confined in nanotubes and between graphene sheets: A first principle study.* Journal of the American Chemical Society, 2008. **130**(6): p. 1871-1878.

143. Gordillo, M. and J. Marti, *Structure of water adsorbed on a single graphene sheet.* Physical Review B, 2008. **78**(7): p. 075432.

144. Gordillo, M. and J. Marti, *Water on graphene surfaces.* Journal of Physics: Condensed Matter, 2010. **22**(28): p. 284111.

145. Wei, N., X. Peng, and Z. Xu, *Understanding water permeation in graphene oxide membranes.* ACS applied materials & interfaces, 2014. **6**(8): p. 5877-5883.

146. Xu, W.L., et al., *Self-assembly: a facile way of forming ultrathin, high-performance graphene oxide membranes for water purification.* Nano letters, 2017. **17**(5): p. 2928-2933.

147. Li, W., et al., *Molecular dynamics simulations of CO_2/N_2 separation through two-dimensional graphene oxide membranes.* The Journal of Physical Chemistry C, 2016. **120**(45): p. 26061-26066.

148. Wang, S., et al., *Graphene oxide membranes with heterogeneous nanodomains for efficient CO_2 separations.* Angewandte Chemie International Edition, 2017. **56**(45): p. 14246-14251.

149. Elias, D.C., et al., *Control of graphene's properties by reversible hydrogenation: evidence for graphane.* Science, 2009. **323**(5914): p. 610-613.

150. Balog, R., et al., *Bandgap opening in graphene induced by patterned hydrogen adsorption.* Nature materials, 2010. **9**(4): p. 315-319.

151. Feng, W., et al., *Two-dimensional fluorinated graphene: synthesis, structures, properties and applications.* Advanced Science, 2016. **3**(7): p. 1500413.

152. Subrahmanyam, K., et al., *A study of graphenes prepared by different methods:*

characterization, properties and solubilization. Journal of Materials Chemistry, 2008. **18**(13): p. 1517-1523.

153. Dong, L., et al., *Synthesis and reduction of large sized graphene oxide sheets.* Chemical Society Reviews, 2017. **46**(23): p. 7306-7316.
154. Ma, J., D. Ping, and X. Dong, *Recent developments of graphene oxide-based membranes: A review.* Membranes, 2017. **7**(3): p. 52.
155. Radhakrishnan, S., et al., *An insight into the phase transformation of WS2 upon fluorination.* Advanced Materials, 2018. **30**(44): p. 1803366.
156. Hu, M., et al., *Surface functional groups and interlayer water determine the electrochemical capacitance of $Ti_3C_2T_x$ MXene.* ACS nano, 2018. **12**(4): p. 3578-3586.
157. Tang, X., et al., *Fluorination-enhanced ambient stability and electronic tolerance of black phosphorus quantum dots.* Advanced Science, 2018. **5**(9): p. 1800420.
158. Radhakrishnan, S., et al., *Fluorinated h-BN as a magnetic semiconductor.* Science advances, 2017. **3**(7): p. e1700842.
159. Chen, C., et al., *Functionalized boron nitride membranes with ultrafast solvent transport performance for molecular separation.* Nature communications, 2018. **9**(1): p. 1902.
160. Wang, Y., et al., *Functionalized boron nitride nanosheets: a thermally rearranged polymer nanocomposite membrane for hydrogen separation.* Angewandte Chemie, 2018. **130**(49): p. 16288-16293.
161. Englert, J.M., et al., *Covalent bulk functionalization of graphene.* Nature Chemistry, 2011. **3**(4): p. 279-286.
162. Lomeda, J.R., et al., *Diazonium functionalization of surfactant-wrapped chemically converted graphene sheets.* Journal of the American Chemical Society, 2008. **130**(48): p. 16201-16206.
163. Bekyarova, E., et al., *Chemical modification of epitaxial graphene: spontaneous grafting of aryl groups.* Journal of the American Chemical Society, 2009. **131**(4): p. 1336-1337.

164. Hidayah, N., et al., *Roles of linear alkyl chain alkylation on reinforcement of graphene based polypropylene nanocomposites.* Materials Today Communications, 2020. **22**: p. 100775.
165. Zhang, L., et al., *In situ alkylated graphene as oil dispersible additive for friction and wear reduction.* Industrial & Engineering Chemistry Research, 2017. **56**(32): p. 9029-9034.
166. Knirsch, K.C., et al., *Mono-and Ditopic Bisfunctionalization of Graphene.* Angewandte Chemie International Edition, 2016. **55**(19): p. 5861-5864.
167. Lucherelli, M.A., et al., *A straightforward approach to multifunctional graphene.* Chemistry–A European Journal, 2019. **25**(57): p. 13218-13223.
168. Voiry, D., et al., *Covalent functionalization of monolayered transition metal dichalcogenides by phase engineering.* Nature chemistry, 2015. **7**(1): p. 45-49.
169. Benson, E.E., et al., *Balancing the hydrogen evolution reaction, surface energetics, and stability of metallic MoS_2 nanosheets via covalent functionalization.* Journal of the American Chemical Society, 2018. **140**(1): p. 441-450.
170. Ryder, C.R., et al., *Covalent functionalization and passivation of exfoliated black phosphorus via aryl diazonium chemistry.* Nature chemistry, 2016. **8**(6): p. 597-602.
171. Sofer, Z., et al., *The covalent functionalization of layered black phosphorus by nucleophilic reagents.* Angewandte Chemie International Edition, 2017. **56**(33): p. 9891-9896.
172. de los Reyes, C.A., et al., *Tunable alkylation of white graphene (hexagonal boron nitride) using reductive conditions.* The Journal of Physical Chemistry C, 2019. **123**(32): p. 19725-19733.
173. Jia, Z. and Y. Wang, *Covalently crosslinked graphene oxide membranes by esterification reactions for ions separation.* Journal of Materials Chemistry A, 2015. **3**(8): p. 4405-4412.
174. Wang, S., et al., *A highly permeable graphene oxide membrane with fast and selective transport nanochannels for efficient carbon capture.* Energy &

Environmental Science, 2016. **9**(10): p. 3107-3112.

175. Zhang, Y., S. Japip, and T.-S. Chung, *Thermally evolved and boron bridged graphene oxide (GO) frameworks constructed on microporous hollow fiber substrates for water and organic matters separation.* Carbon, 2017. **123**: p. 193-204.

176. Hung, W.-S., et al., *Cross-linking with diamine monomers to prepare composite graphene oxide-framework membranes with varying d-spacing.* Chemistry of Materials, 2014. **26**(9): p. 2983-2990.

177. Zhou, F., et al., *Ultrathin graphene oxide-based hollow fiber membranes with brush-like CO_2-philic agent for highly efficient CO_2 capture.* Nature Communications, 2017. **8**(1): p. 2107.

178. Lim, M.-Y., et al., *Cross-linked graphene oxide membrane having high ion selectivity and antibacterial activity prepared using tannic acid-functionalized graphene oxide and polyethyleneimine.* Journal of Membrane Science, 2017. **521**: p. 1-9.

179. Wu, X., et al., *Elucidating ultrafast molecular permeation through well-defined 2D nanochannels of lamellar membranes.* Angewandte Chemie International Edition, 2019. **58**(51): p. 18524-18529.

180. Wang, L., et al., *Tribological performances of hexagonal boron nitride nanosheets via surface modification with silane coupling agent.* SN Applied Sciences, 2021. **3**: p. 1-10.

181. Ding, L., et al., *Oppositely charged $Ti_3C_2T_x$ MXene membranes with 2D nanofluidic channels for osmotic energy harvesting.* Angewandte Chemie, 2020. **132**(22): p. 8798-8804.

182. Zhang, Z., et al., *Mechanically strong MXene/Kevlar nanofiber composite membranes as high-performance nanofluidic osmotic power generators.* Nature communications, 2019. **10**(1): p. 2920.

183. Dong, L., et al., *NH2-Fe3O4-regulated graphene oxide membranes with well-defined laminar nanochannels for desalination of dye solutions.* Desalination,

2020. **476**: p. 114227.

184. Wang, S., et al., *2D-dual-spacing channel membranes for high performance organic solvent nanofiltration.* Journal of Materials Chemistry A, 2019. **7**(19): p. 11673-11682.

185. Long, Q., et al., *Self-assembly enabled nano-intercalation for stable high-performance MXene membranes.* Journal of Membrane Science, 2021. **635**: p. 119464.

186. Hirunpinyopas, W., et al., *Desalination and nanofiltration through functionalized laminar MoS2 membranes.* ACS nano, 2017. **11**(11): p. 11082-11090.

187. Ying, W., et al., *Ionic liquid selectively facilitates CO_2 transport through graphene oxide membrane.* ACS nano, 2018. **12**(6): p. 5385-5393.

188. Chen, D., et al., *Enhanced gas separation through nanoconfined ionic liquid in laminated MoS2 membrane.* ACS applied materials & interfaces, 2017. **9**(50): p. 44251-44257.

189. Park, S., et al., *Graphene oxide papers modified by divalent ions—enhancing mechanical properties via chemical cross-linking.* ACS nano, 2008. **2**(3): p. 572-578.

190. Yeh, C.-N., et al., *On the origin of the stability of graphene oxide membranes in water.* Nature chemistry, 2015. **7**(2): p. 166-170.

191. Chen, L., et al., *Ion sieving in graphene oxide membranes via cationic control of interlayer spacing.* Nature, 2017. **550**(7676): p. 380-383.

192. Chu, C., et al., *Precise ångström controlling the interlayer channel of MoS2 membranes by cation intercalation.* Journal of Membrane Science, 2020. **615**: p. 118520.

193. Ding, L., et al., *Effective ion sieving with Ti3C2T x MXene membranes for production of drinking water from seawater.* Nature Sustainability, 2020. **3**(4): p. 296-302.

194. Su, Y., et al., *Impermeable barrier films and protective coatings based on reduced graphene oxide.* Nature communications, 2014. **5**(1): p. 4843.

195. Ries, L., et al., *Enhanced sieving from exfoliated MoS2 membranes via covalent functionalization.* Nature materials, 2019. **18**(10): p. 1112-1117.
196. Hoenig, E., et al., *Controlling the Structure of MoS_2 Membranes via Covalent Functionalization with Molecular Spacers.* Nano Letters, 2020. **20**(11): p. 7844-7851.
197. Jia, Z. and W. Shi, *Tailoring permeation channels of graphene oxide membranes for precise ion separation.* Carbon, 2016. **101**: p. 290-295.
198. Meng, N., et al., *A low-pressure GO nanofiltration membrane crosslinked via ethylenediamine.* Journal of Membrane Science, 2018. **548**: p. 363-371.
199. Nam, Y.T., et al., *Enhanced stability of laminated graphene oxide membranes for nanofiltration via interstitial amide bonding.* ACS applied materials & interfaces, 2016. **8**(40): p. 27376-27382.
200. Yuan, B., et al., *Cross-linked graphene oxide framework membranes with robust nano-channels for enhanced sieving ability.* Environmental Science & Technology, 2020. **54**(23): p. 15442-15453.
201. Ding, M., et al., *2D laminar maleic acid-crosslinked MXene membrane with tunable nanochannels for efficient and stable pervaporation desalination.* Journal of Membrane Science, 2020. **600**: p. 117871.
202. Cheng, L., et al., *Cysteamine-crosslinked graphene oxide membrane with enhanced hydrogen separation property.* Journal of Membrane Science, 2020. **595**: p. 117568.
203. Wang, J., et al., *Ion sieving by a two-dimensional Ti3C2T x alginate lamellar membrane with stable interlayer spacing.* Nature communications, 2020. **11**(1): p. 3540.
204. Zhu, J., et al., *Precisely tunable ion sieving with an Al13–Ti3C2T x lamellar membrane by controlling interlayer spacing.* ACS nano, 2020. **14**(11): p. 15306-15316.
205. Andreeva, D.V., et al., *Two-dimensional adaptive membranes with programmable water and ionic channels.* Nature Nanotechnology, 2021. **16**(2): p. 174-180.

206. Xie, L., et al., *Surface Charge Modification on 2D Nanofluidic Membrane for Regulating Ion Transport.* Advanced Functional Materials, 2023. **33**(4): p. 2208959.
207. Wu, Y., et al., *Surface charge regulated asymmetric ion transport in nanoconfined space.* Small, 2021. **17**(28): p. 2101099.
208. Zhang, X., et al., *Asymmetric electrokinetic proton transport through 2D nanofluidic heterojunctions.* ACS nano, 2019. **13**(4): p. 4238-4245.
209. Wen, Q., et al., *Electric-field-induced ionic sieving at planar graphene oxide heterojunctions for miniaturized water desalination.* Advanced Materials, 2020. **32**(16): p. 1903954.
210. Wang, W., et al., *Carbon nanofibers membrane bridged with graphene nanosheet and hyperbranched polymer for high-performance osmotic energy harvesting.* Nano Research, 2023. **16**(1): p. 1205-1211.
211. Ai, X., et al., *Recent progress on the smart membranes based on two-dimensional materials.* Chinese Chemical Letters, 2022. **33**(6): p. 2832-2844.
212. Li, C. and L. Gao, *Specific ion selectivity with a reverse-selective mechanism.* Nature Nanotechnology, 2022. **17**(11): p. 1130-1131.
213. Ding, L., et al., *Bioinspired Ti3C2Tx MXene-Based Ionic Diode Membrane for High-Efficient Osmotic Energy Conversion.* Angewandte Chemie International Edition, 2022. **61**(41): p. e202206152.
214. Chen, J., et al., *Biomimetic nanocomposite membranes with ultrahigh ion selectivity for osmotic power conversion.* ACS central science, 2021. **7**(9): p. 1486-1492.
215. Wu, Y., et al., *Enhanced ion transport by graphene oxide/cellulose nanofibers assembled membranes for high-performance osmotic energy harvesting.* Materials Horizons, 2020. **7**(10): p. 2702-2709.
216. Gao, Z., et al., *Increased ion transport and high-efficient osmotic energy conversion through aqueous stable graphitic carbon nitride/cellulose nanofiber composite membrane.* Carbohydrate Polymers, 2022. **280**: p. 119023.

217. Qin, R., et al., *Nanofiber-reinforced clay-based 2D nanofluidics for highly efficient osmotic energy harvesting.* Nano Energy, 2022. **100**: p. 107526.
218. Man, Z., et al., *Serosa-mimetic nanoarchitecture membranes for highly efficient osmotic energy generation.* Journal of the American Chemical Society, 2021. **143**(39): p. 16206-16216.
219. Zhang, M., et al., *Controllable ion transport by surface-charged graphene oxide membrane.* Nature communications, 2019. **10**(1): p. 1253.
220. Yang, L., et al., *Amino-functionalized POSS nanocage intercalated graphene oxide membranes for efficient biogas upgrading.* Journal of Membrane Science, 2020. **596**: p. 117733.
221. Dong, M., et al., *Enhanced molecular transport in two-dimensional nanoconfined ionic liquids.* Applied Materials Today, 2022. **27**: p. 101458.
222. Chen, D., et al., *CO 2-philic WS 2 laminated membranes with a nanoconfined ionic liquid.* Journal of Materials Chemistry A, 2018. **6**(34): p. 16566-16573.
223. Ying, W., et al., *Electrical field facilitates selective transport of CO 2 through a laminated MoS 2 supported ionic liquid membrane.* Journal of Materials Chemistry A, 2019. **7**(16): p. 10041-10046.
224. Wan, X., et al., *Graphene oxide constructed nano Newton's cradle for ultrafast and highly selective CO2 transport.* Journal of Membrane Science, 2022. **652**: p. 120475.
225. Tao, J., et al., *The role of surface wettability on water transport through membranes.* Chemical Engineering Science, 2020. **219**: p. 115602.
226. Zhao, S., et al., *Surface wettability effect on fluid transport in nanoscale slit pores.* AIChE Journal, 2017. **63**(5): p. 1704-1714.
227. Huang, C., et al., *Study of Solid Wall–Liquid Interaction on Pressure-Driven Liquid Transport Through a Nanopore in a Membrane.* Journal of Nanoscience and Nanotechnology, 2009. **9**(2): p. 793-798.
228. Xie, Q., et al., *Fast water transport in graphene nanofluidic channels.* Nature nanotechnology, 2018. **13**(3): p. 238-245.

229. Chen, X., et al., *Selective permeation of water through angstrom-channel graphene membranes for bioethanol concentration.* Advanced Materials, 2020. **32**(33): p. 2002320.
230. Li, M., et al., *Graphene oxide nanofiltration membrane with trimethylamine-N-oxide zwitterions for robust biofouling resistance.* Journal of Membrane Science, 2021. **640**: p. 119855.
231. Huang, K., et al., *Cation-controlled wetting properties of vermiculite membranes and its promise for fouling resistant oil–water separation.* Nature communications, 2020. **11**(1): p. 1097.

Chapter 2: Functionalized MoS_2 for water purification and desalination

*Having established the promising prospects and the associated challenges of 2D material membranes in **Chapter 1**, we delve further into the pursuit of a more practical, scalable, and efficient solution in **Chapter 2**. Here, the attention shifts towards a specific type of 2D material, molybdenum disulfide (MoS_2), with the aim of constructing laminar membranes for enhanced desalination performance. We discuss a novel strategy to address some of the key challenges faced by these 2D membranes, such as their stability and tunability of interlayer space, through the careful modification of nanochannel architectures. We will provide an in-depth exploration of the preparation and application of MoS_2 nanosheets in membrane separation, shedding light on their unique properties and potential in the realm of forward osmosis (FO) filtration. **Chapter 2** will present the results of our investigations and provide a better understanding of 2D materials as nanolaminate building blocks for developing efficient and effective membrane with superior properties.*

High Surface Area Functionalized Nanolaminated Membranes For Energy Efficient Nanofiltration And Desalination In Forward Osmosis

2.1 Abstract

Stacking two-dimensional (2D) nanosheets into laminar membranes to create nanochannels has attracted widespread attention at fundamental and practical levels for separation technology. Constructing space-tunable and long-term stable sub-nanometer channels provide original systems for nanofluidic investigations and accurate molecular sieving. Although proof-of-concept for nanolaminate membranes has recently been demonstrated, uncontrollable swelling and the presence of pinholes prevent the scaling up of these membranes. Here, we report a scalable strategy for the preparation of non-swelling covalently functionalized molybdenum disulfide (MoS_2) membranes with tunable interlayer space and cohesion energy of the laminates. The capillary width of the nanochannels was fine-tuned from 3.5 to 7.7 Å, depending on the nature of the functional groups attached to the MoS_2 nanoplates and has minimal swelling in water. We evaluated the relationship between the capillary width, the surface chemistry, the stacking disorder and the sieving behaviors of the membranes in forwards osmosis (FO). We found that water permeation is strictly controlled by the capillary width of the nanochannels and the stacking disorder of the nanosheets. By combining experimental investigations and numerical simulations, we identified that the functionalization with aryl groups induces the formation of a capillary width of 7.1 Å and interlayer stiffness as low as 5.6 eV $Å^{-2}$, leading to controlled stacking defects. We report the fabrication of membranes up to 45 cm^2, which demonstrate a salt rejection as high as 94.2% for a continuous operating time of 7 days. Our work presents a desalination strategy in FO with a specific energy consumption (SEC) of 4×10^{-3} kWh m^{-3}, which compares favorably with commercial FO membranes. We anticipate that this opens avenues for the development of FO membranes for desalination based on nanolaminated structure.

2.2 Introduction

The construction of selectively permeable membranes with sub-nanometer channels

has gained attention for artificial bionics and molecular sieving by taking advantage of the sub-nanometer size of the pores formed between two successive nanosheets. Two-dimensional nanolaminates are regarded from both fundamental and practical points of view as mimicking systems of the biological protein transport channels and building blocks of nanofiltration membranes [1, 2]. In nanolaminated membranes, mass transport typically occurs within the physical gap between the layers defined as the interlayer space or the capillary width. The fabrication of 2D sub-nanometer channels with controlled dimensionality and chemistry of the interlayer space has therefore emerged as a mature topic in the field of 2D materials [3-5]. The practical demonstration of nanolaminate membranes has not been achieved due to two main bottlenecks, which are (i) the intrinsic instability of the interlayer space and (ii) the difficulty in fabricating pinhole-free membranes on a large scale with controlled thickness [6-8]. Currently, the most widely studied 2D building block of nanolaminate membranes is graphene oxide (GO), which forms free spaces of around 5 Å in dry condition. This allows a narrow molecular sieve size with sharp molecular cut-off for rejecting large molecules and ions at the expense of the water flux [9]. Although the space size can be modulated by encapsulating GO membrane into epoxy under different humidity, the process is rather complex and prevents realistic applications [10]. Other strategies for controlling the pore size of the nanolaminates include ion coordination [11], polymer intercalation [12], crosslinking [13]. Inevitable swelling occurs in pristine GO membrane when it is operated in an aqueous solution, which however dramatically increases the interlayer spacing, leading to a rapid degradation of the sieving performance [14-16]. Besides GO, MoS_2 and MXene nanosheets are alternative building block candidates for the construction of 2D nanochannels [17-20]. MoS_2 laminated membranes have shown outstanding water permeation in reversed osmosis (RO) and the improved stability compared to GO and MXene membranes [21, 22]. Unfortunately, the molecular cutoff of MoS_2 membranes depends on the presence of intercalated water molecules in the laminated structure [23]. We have recently reported a facile strategy to modify the surface chemistry of the MoS_2 nanosheets and tune the

interlayer space [24]. Although the vast majority of the efforts have focused on membranes for RO applications, forward osmosis (FO) is regarded as a strategy to reduce the energy footprint associated with water purification processes. To date, only few studies have however focused on the production and testing membranes with sizes greater than 1 cm^2 due to the difficulty in controlling the integrity of the membrane structures over large area (swelling, delamination, formation of pinholes) [24-26].

Here, using MoS_2 nanosheets as building units, we adopted a chemical functionalization strategy to prepare FO membranes with controlled interlayer space and interlayer stiffness in order to tailor the interlayer space and the stacking disorder in the nanolaminated structure. The membranes are found to be resistant against swelling, while the interlayer space can be adjusted with ångström precision. We demonstrated the fabrication of membranes with thickness from 100 nm up to 1 μm and dimensions as large as 45 cm^2. The membranes achieved a water flux as high as 12 LMH with molecular cutoff of 180 Da and a salt rejection as high as 94.2%. When tested against desalination, the functionalized MoS_2 FO membranes demonstrated superior salt rejection performance for 7 days without significant loss of the water flux compared with GO-based membranes and commercial polymer FO membranes. The nanofluidic behavior in various channels has been studied using physical characterizations and molecular dynamic simulations to unravel the size entanglements of the surface chemistry, the sub-nanometer interlayer space and the disorder of the stacking of the nanosheets in the laminated structure. We finally evaluated the energy consumption of our filtration system and found that the MoS_2 nanolaminate membranes may allow for a lower electrical power consumption compared to commercial FO membranes thus opening avenues for practical applications of nanolaminate FO membranes.

2.3 Material and Methods

2.3.1 Materials

The MoS_2 powder, n-butyllithium, hexane, organohalide, diazonium salt, Nylon filter

paper and organic dye (Nickel(II) phthalocyanine-tetrasulfonic acid tetrasodium salt) were purchased from Sigma Aldrich. The salt, sucrose, organic micropollutant except for dye, and solvent were purchased from Alfa Aesar. The commercial forward osmosis membranes (FTSH2O Flat Sheet Membrane, CTA) were purchased from Sterlitech. All chemicals were used as received.

2.3.2 Synthesis of single-layer MoS_2 nanosheets

The single-layer MoS_2 nanosheets were obtained by exfoliating the bulk MoS_2 powder using the lithium intercalation method. Typically, 400 mg MoS_2 powder and 4 mL n-butyllithium were mixed up in hexane solution and the mixture was stirred at 65°C for 48 h under argon protection. After that, the intercalated powders were collected by vacuum filtration and washed with excessive hexane to remove the unreacted reagent. Then the Li-intercalated powder was added to the water for exfoliation and the process was accelerated by the sonication. After one-hour sonication, the solution was further centrifuged two times at 10,000 g to strip the lithium cations from the nanosheets. In the end, the supernatant containing the single-layer MoS_2 nanosheets was collected after centrifugation twice at 1,400 g for 30 min.

2.3.3 Functionalization of single-layer MoS_2 nanosheets

The single-layer MoS_2 nanosheets were modified in solution by reacting with organohalide reagents and diazonium. First, dimethyl sulfoxide (DMSO) was added to the MoS_2 solution to achieve a volume ratio of 3:2. Then the organohalide reagents or diazonium were directly added to the mixture to react for 48h. The excessive organohalide reagents with ten times fold in molar ratio than MoS_2 was added. While the charged diazonium with the same molar amount as MoS_2 was separately added several times to avoid the electrostatic quench and aggregation. Finally, the functionalized MoS_2 solutions were obtained.

2.3.4 Preparation of functionalized MoS_2 membranes

Vacuum filtration was employed to prepare the laminated membranes using diluted functionalized MoS_2 solution. Briefly, a certain amount of MoS_2 solution was filtered on Nylon filter paper with a pore size of 220 nm. To improve the uniformity of the nanolaminate, polyethersulfone (PES, 50 nm pore size) was used to prepare membranes larger than 10 cm^2. After filtration, the membranes were carefully washed 3 times to remove the unreacted reagents. The prepared membranes were dried at room temperature over 24 h.

2.3.5 Water permeation through nanolaminated MoS_2 membranes

The pure water flux of nanolaminated MoS_2 membranes was measured using the forward osmosis devices, which consist of two compartments filled with equal volumes (40 mL) of salt solution (3 M KCl) and pure water. The MoS_2 membranes were placed in the middle to separate those two compartments. The volume of salt solution as a draw solution would increase due to the passed water. Based on the increased volume (ΔV) with permeation time (Δt), the water flux could be calculated following the equation:

$$J_w = \frac{\Delta V}{A \Delta t} \qquad (2-1)$$

Where the A is the effective membrane area (1.13 cm^2).

2.3.6 Ionic permeation through the nanolaminated MoS_2 membranes

The Na^+/Mg^{2+} permeation through the 400-layer stacked membranes was measured using two Teflon-made compartments, which were filled with the same volume of DI water and 1 M NaCl/$MgCl_2$ or 0.5 M Na_2SO_4 solution, respectively. Magnetic stirring was used all the time to eliminate possible concentration gradients around the membranes. The conductivity of the feed side was recorded as a function of permeation time. According to the measured conductivity, the salt concentration of feed side could be calculated using the following equation:

$$C = \frac{\kappa}{\Lambda_m} \qquad (2-2)$$

where C denotes the salt concentration, κ presents the measured conductivity and Λm is the molar conductivity (NaCl: 126.4 S cm^2 mol^{-1}, $MgCl_2$: 258.6 S cm^2 mol^{-1}, Na_2SO_4:

259.8 S cm^2 mol^{-1}) [27]. The salt permeation rate (J) was calculated by:

$$J = \frac{VC}{At} \qquad (2-3)$$

where V is the solution volume in the feed side (200 mL), C is the calculated concentration from equation (3), A is the surface area of the membrane and t is the permeation time.

2.3.7 Water purification and rejection evaluations

The water purification performances of the membranes were measured using the same apparatus as for the water permeation measurements. However, the draw side and feed side were filled with 2 M sucrose solution and 50 mM micropollutant solution (except for the dye solution, which was 3.3 mM), respectively. The two sides were constantly stirred to avoid the concentration polarization. The draw side solution was collected after 20 h and the concentration of micropollutant in sucrose solution was quantitatively analyzed by High-Performance Liquid Chromatography-Ultraviolet (HPLC-UV). The flux was calculated by equation (2-2) and the rejection was evaluated by the following equation:

$$R\ (\%) = \frac{C_F - C_P}{C_F} \times 100 \qquad (2-4)$$

Where C_F and C_P denote the concentration of the feed and permeate solutions, respectively. Unlike the reverse osmosis experiments, the permeated solution in forward osmosis system was diluted by the draw solution. The real concentration of the permeated solution was calculated using the following equation to eliminate the dilution effects:

$$C_p = \frac{C_D \times V_D}{V_P} \qquad (2-5)$$

Where C_D and V_D are the measured micropollutant concentration in the draw side and the volume of the draw solution. The V_P presents the volume of permeated solution, which is the increased volume in the draw side.

2.3.8 Water desalination in tangential cross-flow filtration cell

We used the tangential cross-flow filtration cell to estimate the water desalination performance of membranes in long-term operation. The membranes with large surfaces prepared on the polyethersulfone (PES) substrates were installed in the middle of the pilot-scale forward filtration unit to separate the flowing draw and feed solution. The draw and feed tank were filled with 2 M sucrose solution and 0.58 wt.% NaCl solution, respectively. A peristaltic pump was utilized to provide a constant flow rate of 3.75 mL min^{-1}. Two balances were used to monitor the mass changes of draw and feed tank and the recorded data was further used to calculate the flux. The solutions in the tank were refreshed every 20 h. At the same time, the sucrose solution was collected and the salt concentration was analyzed by Inductively Coupled Plasma Optical Emission Spectrometry (ICP-OES). According to the increased mass and salt concentration in draw side, the salt rejection could be calculated using equations (2-4) and (2-5).

2.3.9 Molecular dynamics simulations parameter

Molecular dynamics simulations have been performed with the LAMMPS package [28] and the OPLS interatomic potential [29]. To describe Mo-S interactions, we use the potential proposed by Blankschtein [30]. We developed OPLS parameters (harmonic bonds, harmonic angles and dihedrals) for S-C interactions between fixed MoS_2 and various organic functional groups. We used a Monte Carlo procedure (similar to that presented in Ref. [31]) to optimize OPLS parameters against a training set of density functional theory calculations (details in Section 2.7.3). Molecular models consist of 2 layers of T' MoS_2 replicated 8 and 14 times in the x and y directions, starting from the rectangular unit cell. Functionalization was achieved by randomly grafting functional groups to S atoms until the fraction of 20% groups/S was reached. In order to obtain good statistics on the data points corresponding to the potential energy surface, we scanned 4 times successively the interlayer distance (back and forth). One potential energy surface corresponds therefore to 8 times (4 times back and forth) 300 interlayer distances. At each interlayer distance, the functional groups were randomized by performing 10 ps of NVT simulation at 600 K followed by an energy minimization. We

used high temperature MD to provide efficient randomization of the functional groups at each interlayer distances. Although our force field could be used with a larger timestep, we chose a timestep of 0.5 fs in order to properly integrate the equations of motion in the rough conditions of the simulations.

2.4 Characterization

2.4.1 Characterization methodology

Scanning electron microscopy (SEM) images were obtained using Hitachi S4800. The X-ray Diffraction (XRD) was carried out on an Xpert Pro apparatus with filtered Cu Kα radiation (λ = 0.15418 nm) operating at 40 kV and 20 mA. Aberration-corrected high-resolution (scanning) transmission electron microscopy imaging (HR-(S)TEM) and energy-dispersive X-ray spectroscopy (EDS) were performed using a FEI Titan Cubed Themis microscope which was operated at 200 kV. The Themis is equipped with a double Cs aberration corrector, a monochromator, an X-FEG gun, a super EDS detector, and an Ultra High Resolution Energy Filter (Gatan Quantum ERS) which allows for working in Dual-EELS mode. HR-STEM imaging was performed by using HAADF and annular dark-field (ADF) detectors. The Raman spectroscopy was performed on a Renishaw 1000 system using a green laser of 532 nm. Attenuated Total Reflection Fourier Transform Infrared (ATR-FTIR) spectroscopy was conducted on Nicolet Nexus FT-IR spectrometer equipped with Golden Gate Diamond ATR. The solid-state ^{13}C CP MAS NMR experiments were performed on a Bruker 700 MHz (16.4 T) spectrometer at a frequency of 176.05 MHz, using 3.2 and 4 mm Bruker MAS probes spinning at 10 kHz. ^{13}C chemical shifts were referenced to tetramethylsilane, using adamantane as a secondary reference. The ^{13}C solution NMR was conducted for ethyl iodoacetate on a Bruker Avance 300 MHz.

2.4.2 Zeta potential of MoS_2 nanosheets

The zeta potential of pristine and functionalized MoS_2 nanosheets was measured using an Anton Paar Litesizer 500 Particle Analyzer at neutral pH (in DMSO and water

mixture). The exfoliated pristine MoS_2 nanosheets showed a zeta potential of -48.7, suggesting a negatively charged nature, which agreed well with previous reports [32]. The zeta potential was decreased after nanosheets functionalization since the partial charges on nanosheets' surfaces were quenched by electrophiles, as seen in Table 2.1.

Table 2.1 Zeta potential of pristine and functionalized MoS_2

Samples	**Zeta potential (ξ, mV)**
Pristine	-48.7 ± 0.6
C_2	-40.5 ± 1.6
C_3	-39.5 ± 1.5
Ace	-42.9 ± 1.8
Ben	-38.5 ± 1.8
C_3OH	-40.2 ± 1.0
Aryl	-32.6 ± 1.3

2.4.3 ATR-FTIR spectra of MoS_2 membranes

ATR-FTIR spectroscopy was carried out on MoS_2 membranes. To avoid possible residual DMSO to affect the detection of S-C bond, we functionalized the nanosheets in water: isopropanol (2:3 in volume) mixture. An obvious absorption on ~680 cm^{-1} for all functionalized membranes was observed, showing the existence of the S-C bond [33], confirming the covalent grafting of the functional groups.

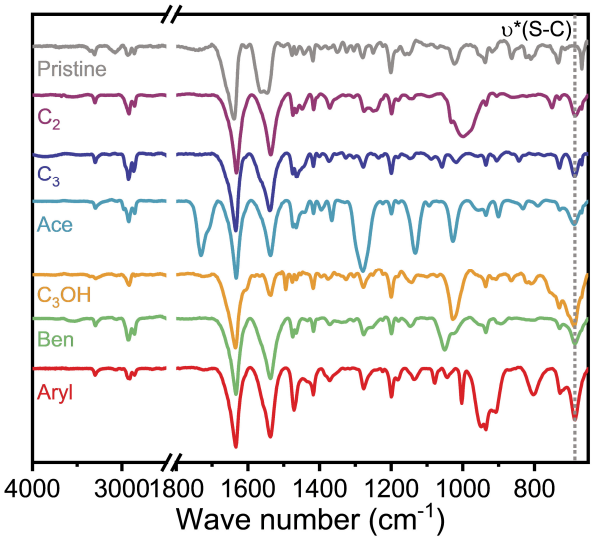

Figure 2.1 Attenuated total reflectance FTIR (ATR-FTIR) spectrum of pristine and functionalized MoS_2. The S-C stretching is highlighted by the dotted gray line.

2.4.4 Raman Spectrum of MoS_2 nanosheets

The Raman spectroscopy was performed on MoS_2 nanosheets to see the changes of vibration modes after functionalization. The pristine MoS_2 nanosheets clearly showed four vibrational modes presented by the A_{1g}, J_1, J_2 and J_3 peaks. Among those, the J_1 and J_3 peaks are highly correlated with electron-phonon coupling [34]. After functionalization, the out-of-plane A_{1g} mode was less affected. While the J_1 and J_3 peaks broadened and exhibited a blueshift. The J_2 peak became significantly stronger and showed a redshift. The changes in vibration modes originated from the modification of functional groups as the covalent bonding with MoS_2 nanosheets would change the original electron structure of MoS_2 nanosheet and induce a new electron-phonon coupling mode.

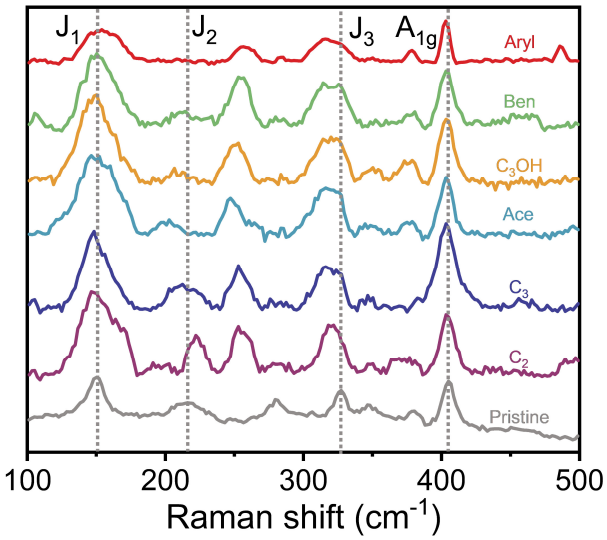

Figure 2.2 Raman spectrum of pristine and functionalized MoS_2 nanosheets. The dotted gray lines represent J_1, J_2, J_3 and A_{1g} peaks of pristine MoS_2 nanosheets, respectively.

2.4.5 ^{13}C Nuclear Magnetic resonance spectroscopy (NMR)

The solid-state ^{13}C CP MAS NMR experiments were carried out on Ace- and Ary-functionalized nanosheets to compare the chemical shift of the aliphatic carbon (α-C) of the functional groups before and after the reaction (see Section 2.5.1, Figure 2.14). The chemical shift of α-C from I-C in ethyl iodoacetate appeared at -3.7 ppm in agreement with previously reported results, which moved to higher ppm value after covalently grafting on MoS_2 nanosheets. While the chemical shift of the other C in ethyl iodoacetate only slightly changed after functionalization. The chemical shift of diazonium salt showed similar changes with ethyl iodoacetate before and after the reaction. Briefly, the chemical shifts of C from N≡N-C in diazonium salt appeared at 115.3 ppm and the peak largely moved around 126 ppm ppm after grafting on MoS_2 nanosheets. The chemical shift of the other C in the diazonium salt did not change significantly after reaction. This ^{13}C shift at higher ppm values from N≡N-C and I-C to S-C environments was confirmed by NMR calculations on simple models (Figure 2.3)

2.4.6 DFT calculations of NMR parameters

Simple models of ethyl-acetate and phenyl groups grafted on an MoS_2 surface were

DFT-relaxed with the VASP code (see Section 2.3.9 and Figure 2.3). ^{13}C NMR chemical shift calculations were then performed within the DFT formalism using the QUANTUM-ESPRESSO (QE) software [35]. The PBE generalized gradient approximation [36] was used and the valence electrons were described by norm conserving pseudopotentials [37] in the Kleinman-Bylander form [38]. The wave functions were expanded on a plane wave basis set with a kinetic energy cut-off of 80 Ry. The shielding tensor was computed using the Gauge Including Projector Augmented Wave (GIPAW) [39] approach, which permits the reproduction of the results of a fully converged all-electron calculation.

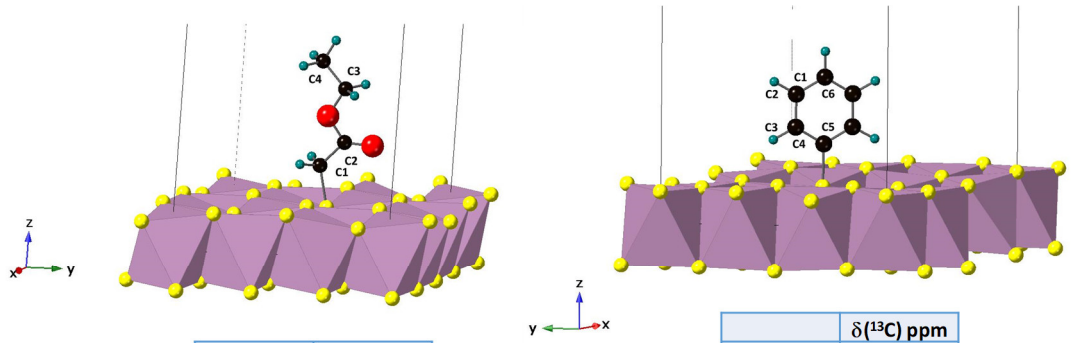

	δ(^{13}C) ppm
C1	59,9
C2	167,7
C3	69,7
C4	6,6

	δ(^{13}C) ppm
C1	139,4
C2	134,3
C3	132,7
C4	142,2
C5	131,9
C6	135,4

Figure 2.3 Calculated ^{13}C NMR chemical shifts in simple models of ethyl-acetate and phenyl groups grafted on an MoS_2 surface Atom color codes: Mo, violet; S, yellow; C, black; H, green; O, red.

2.4.7 TGA measurement on MoS_2 nanosheets

Thermogravimetric analysis (TGA) was carried out on MoS_2 membranes using TGA Q500 Thermogravimetric Analyzer equipped with Thermal Analysis Controller. First, we stabilized the system for 30 min at 100 °C. Then the samples were heated at 10 °C min^{-1} from 100 °C up to 600 °C under N_2 protection. The weight loss was recorded as a function of increased temperature, seen in Figure 2.4. The weight of pristine MoS_2 nanosheets was kept stable in the whole heating process. While the weight of functionalized MoS_2 nanosheets dropped sharply around 230 °C due to the degradation

of functional groups. The extent of functionalization could be estimated by the weight loss from 100 °C to 500 °C as we assumed all of the weight loss comes from the degradation of the grafted groups. The evaluated functionalization degrees per sulfur were ~24 at.%, ~27 at.%, ~24 at.%, ~16 at.%, ~18 at.%, ~22 at.%, for C_2, C_3, Ace, Ben, C_3OH and Aryl-grafted nanosheets, respectively.

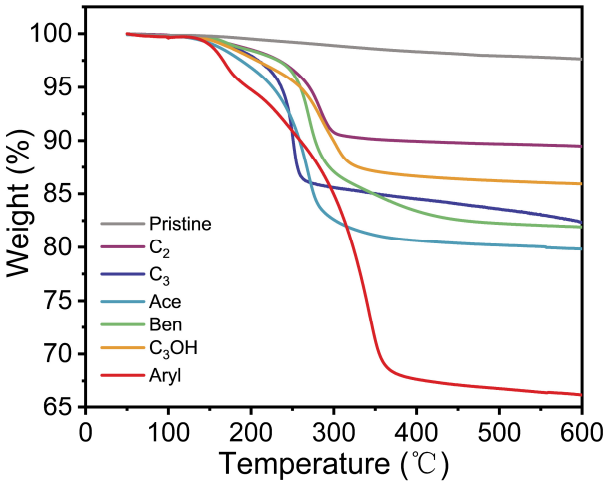

Figure 2.4 TGA traces of pristine and functionalized MoS_2 nanosheets heated to 600°C under nitrogen protection.

2.4.8 SEM images of MoS_2 membranes with different thickness

By adjusting the filtration amount of MoS_2 solution, the membrane thickness can be previously controlled from 1 μm down to 100 nm (Figure 2.5a and 2.5b). From the SEM images, we can clearly see that the porous surface of the substrate can be completely covered by the dense MoS_2 layer formed by the stacking of MoS_2 nanosheets, even with a membrane thickness as low as 100 nm (Figure 2.5c). The dense MoS_2 layer acting as the active layer would give the membrane the desired sieving performance.

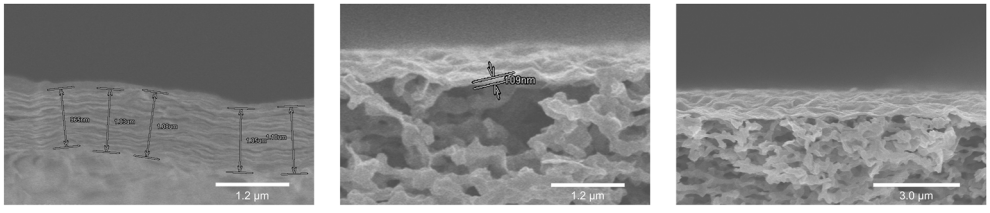

(a) (b) (c)

Figure 2.5 The SEM cross-section view of MoS_2 membranes with thickness of 1 um (**a**), 100 nm (**b**) and 100 nm (**c**). The **b** and **c** have different magnifications. Scale bar represents 1.2 um in (**a**, **b**) and 3 um in (**c**).

2.4.9 Cross-section view of pristine and functionalized MoS_2 membranes

We measured the thickness of MoS_2 membranes before and after functionalization using SEM. Before measurements, all membranes were dried under vacuum for 24 hours to completely remove the water molecules between the interlayers. The thickness of membranes becomes larger after functionalization due to the increased interlayer space.

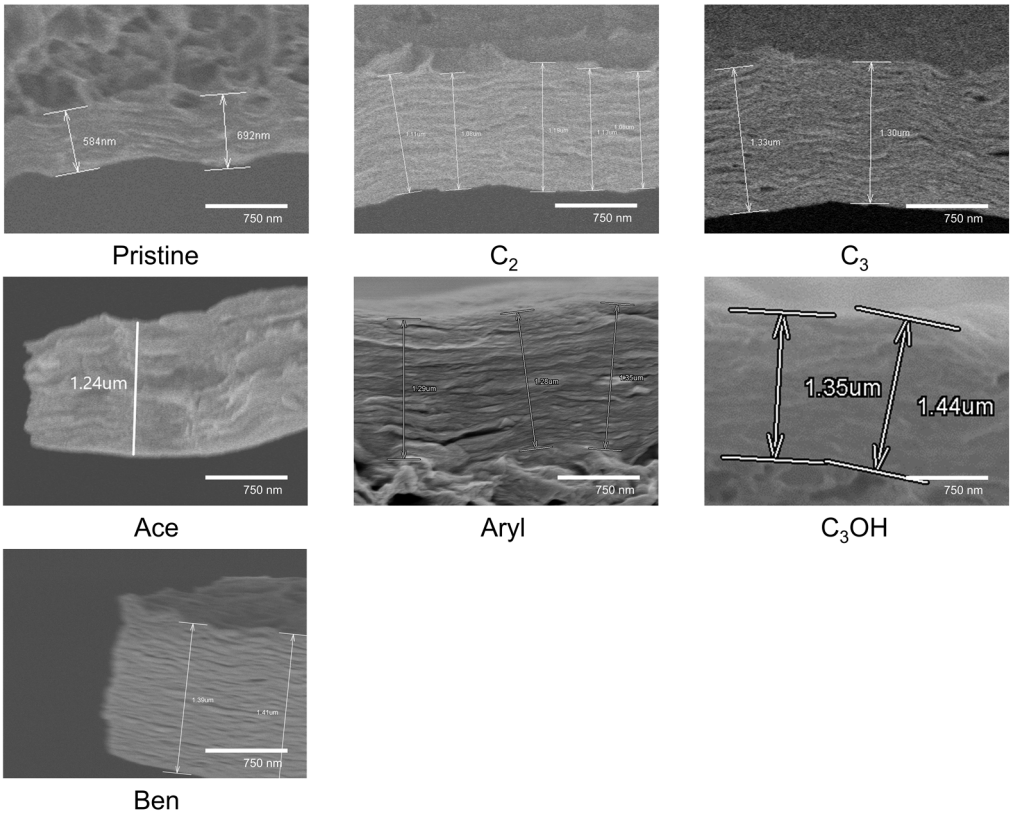

Figure 2.6 Cross-section SEM images of MoS_2 membranes before and after functionalization, scale bar, 750 nm.

2.4.10 XRD patterns of MoS_2 membranes soaking in water

To probe the stability of nanochannels in aqueous solution, XRD was employed to detect the interlayer space after soaking the functionalized MoS_2 membranes in water. We recorded the XRD patterns of membranes with different immersion times. Due to the different detection positions each time and the influence of residual water on the membranes' surface, the peak intensity varied sometimes. However, the peak can always be detected, demonstrating the intact nanochannel. From the graph, we can see that the peak position, which presents the interlayer space, did not shift significantly

during long-term immersion for more than 100 hours, showing the robust nanochannels stacked by functionalized MoS_2 nanosheets.

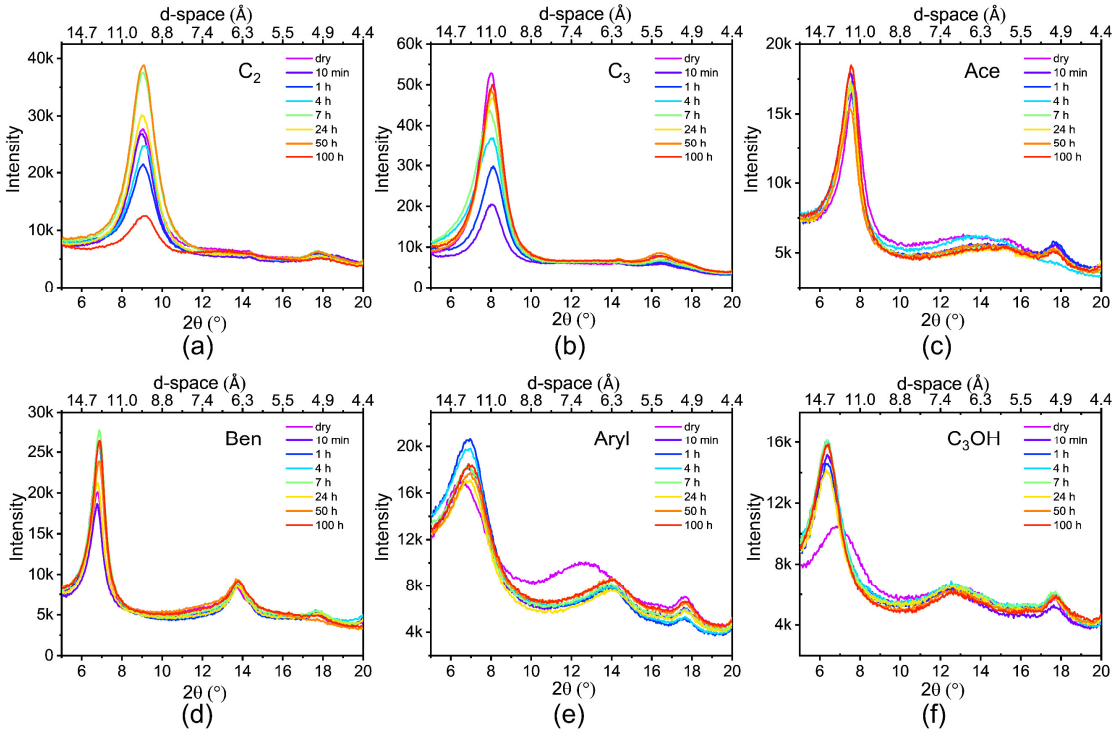

Figure 2.7 XRD patterns of functionalized MoS_2 membranes immersed in water for different times. The dry membranes were obtained by placing them in a vacuum for 24 hours.

2.4.11 FWHM and capillary width variation of functionalized MoS_2 membranes

We analyzed the full-width at half-maximum (FWHM) of XRD patterns measured by immersing the membranes in an aqueous solution for different times. The FWHM of functionalized membranes is different and it maintains stability during the long-term soaking process of more than 100 h, indicating that each functionalized membrane has a unique stack structure and it could keep steady in aqueous solution. According to Bragg's law, we can calculate the capillary width variation by inverting the FWHM, which can qualitatively characterize the degree of order of the laminar membrane stack. A larger variation range suggests a more disordered stack. Among all the functionalized membranes, the Aryl-functionalized membrane has the worst stack order while the Ben-functionalized membranes possess the best alignment.

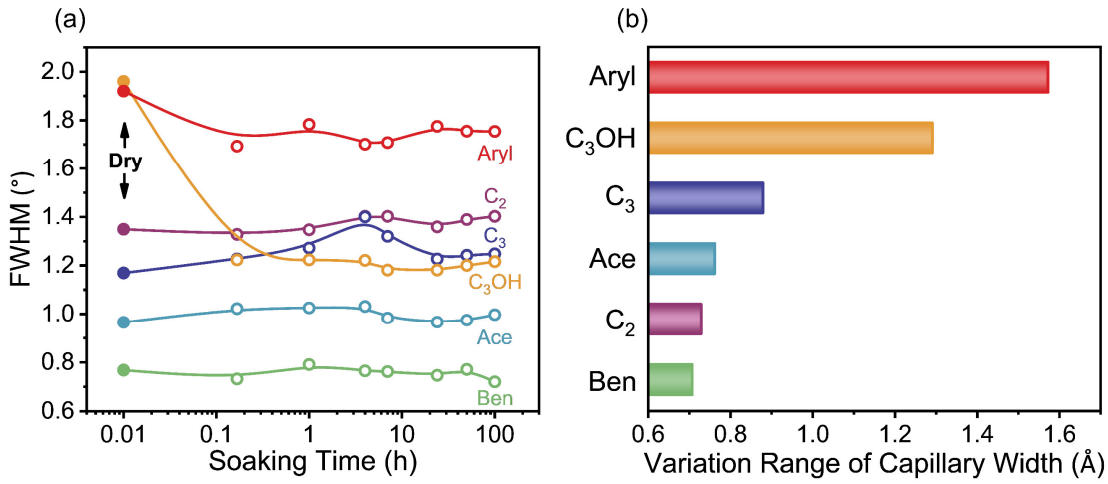

Figure 2.8 a, The full-width at half maximum (FWHM) of XRD peaks measured after immersing the functionalized membranes in water for a different time. All membranes exhibited stable FWHM under soaking conditions. **b**, The calculated variation range of capillary width based on the average FWHM of the immersed membranes. The capillary width variation presents the degree of order of the laminar membrane stack. A more disordered stack would give a larger variation range. The Aryl-functionalized membrane showed the most disordered stack structure while the Ben-functionalized had the most ordered laminated structure among all functionalized MoS_2 membranes.

2.4.12 XRD patterns of GO, MXene, and C_3OH-MoS_2 membranes before and after soaking in water

We measured the swelling ability of the GO, MXene and C_3OH-MoS_2 membranes to compare the stability in water. From Figure 2.9, we can see the d-space of GO and MXene membranes expands from 8.35 Å and 13.38 Å to 16.24 Å and 16.36 Å after soaking in DI water for 100 h, producing an increase of 94.5 % and 22.3%, respectively. This is consistent with previous reports confirming the instability of GO and MXene membranes in aqueous solution [14, 40]. In contrast, the d-space of our C_3OH-MoS_2 membrane increases by only 1.1 Å, from 12.66 Å to 13.75 Å, showing a limited swelling of 8.6 %.

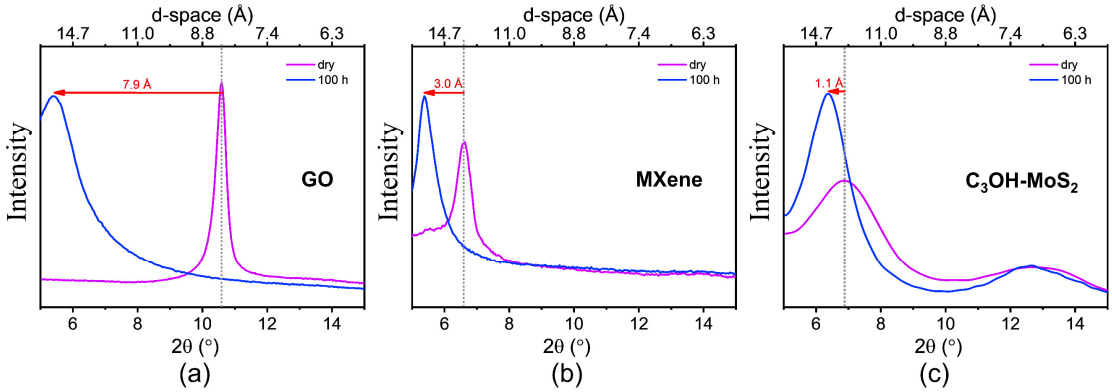

Figure 2.9 XRD patterns of GO (**a**), MXene (**b**) and C_3OH-MoS_2 (**c**) membranes after drying in vacuum for 24h and soaking in DI water for 100 h.

2.4.13 XRD patterns of C_2-MoS_2 and C_3OH-MoS_2 membranes soaking in high concentrated salt solution

We selected two membranes, which show the largest and smallest capillary width in water: C_3OH-MoS_2 and C_2-MoS_2 and soaked them in 1M NaCl and $MgCl_2$ aqueous solution for 100 h to evaluate the stability of MoS_2 in salt solution. The interlayer layer distance was determined based on our XRD investigations and the position of the (002) peak was compared with that measured in pure water. As seen in Figure 2.10, the changes of the capillary width of C_2-MoS_2 and C_3OH-MoS_2 membranes in salt solutions are close to those measure in water. We estimated the swelling to be 7.7% and 0.8% in NaCl and 7.5% and 0.3% in $MgCl_2$ for C_3OH-MoS_2 and C_2-MoS_2 membranes, respectively. Overall these results demonstrate strong stability and excellent anti-swelling properties of the functionalized MoS_2 membranes.

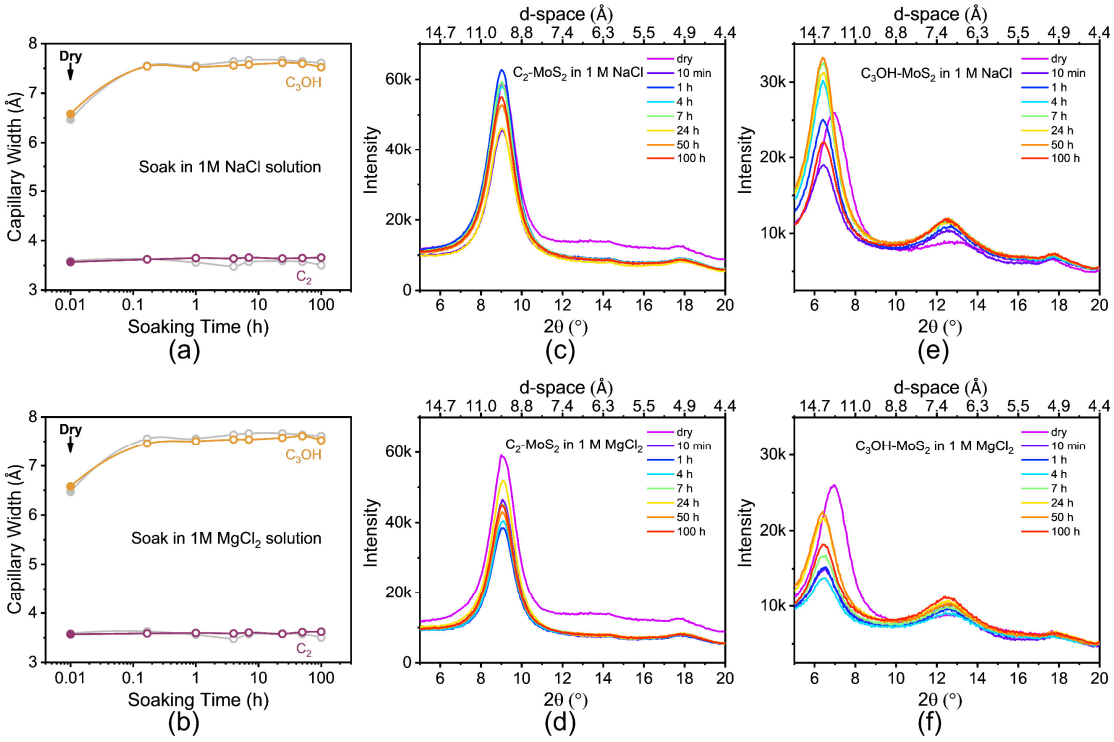

Figure 2.10 Evolution of the capillary width of C_3OH- and C_2-MoS_2 membranes in 1M NaCl (a) and 1M $MgCl_2$ (b) solution over time. The gay symbols represent the capillary width of membranes soaking in pure water. c-f, XRD patterns of C_2- and C_3OH-MoS_2 membranes immersed in 1M NaCl/$MgCl_2$ solution for different times. The dry membranes were obtained by placing them in a vacuum for 24 hours.

2.4.14 Contact Angle of MoS_2 membrane

The contact angle measurements were performed on the pristine and functionalized MoS_2 membranes to observe the changes in the surface nature of nanosheets. Here, we used the air-dried membranes for measurements to best know the wettability of nanochannels experienced by water in permeation experiments. As expected, hydrophobic groups grafted MoS_2 membranes showed an increased contact angle while the hydrophilic group grafted MoS_2 membrane exhibited a decreased angle compared with pristine membrane.

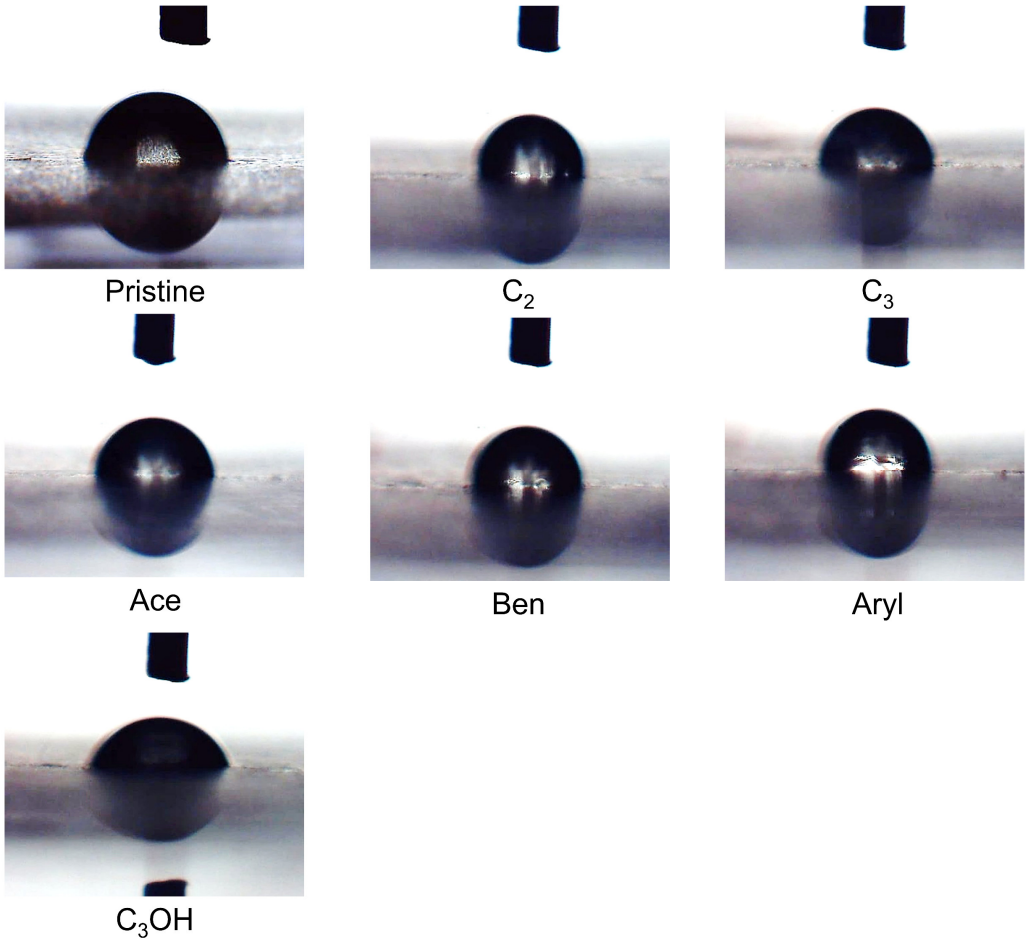

Figure 2.11 Optical photos of a water droplet on the pristine and functionalized MoS_2 membranes prepared by using the DMSO/H_2O (2:1) mixture as solvent.

In addition, we also measured the contact angle of functionalized MoS_2 membranes prepared by using the IPA/H_2O (2:1) mixture as solvent to elucidate the effect of solvent residues since the DMSO has high polarity and slow evaporation. From Figure 2.12, we can see that all the membranes except C_3-functionalized membrane show the same contact angle, indicating that the DMSO has been completely removed from the membrane's surface after washing. While the C_3-functionalized membrane prepared by DMSO/H_2O mixture showed a lower contact angle than that prepared by IPA/H_2O mixture, demonstrating a slight residue of DMSO on C_3-functionalized membrane, resulting from the capture by C_3 groups with the highest grafting degree on nanosheets.

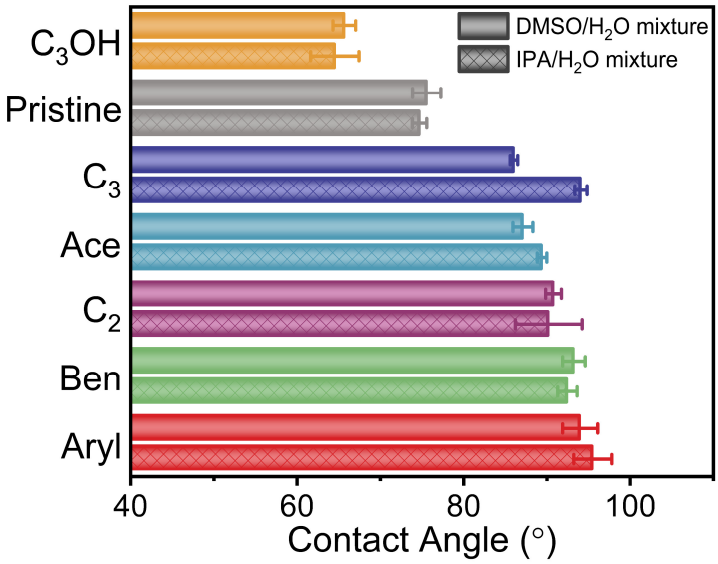

Figure 2.12 Contact angle of pristine and functionalized MoS_2 membranes prepared by using DMSO/H_2O (2:1) mixtures or IPA/H2O (2:1) mixtures as solvent.

2.5 Results and discussion

2.5.1 Preparation and Characterization of Functionalized MoS_2 Membranes

Molybdenum disulfide nanosheets were exfoliated in water from a bulk crystal using the traditional lithium intercalation method [41]. To prevent leaching of the functional groups when operating the membranes, covalent functionalization is preferable. The nanosheets were functionalized using alternatively organohalides or diazonium salts in order to covalently attach alkyl and aryl functional groups, respectively. Six types of molecules were selected: iodoethane, 1-iodopropane, ethyl iodoacetate, (2-iodoethyl) benzene, 3-iodo-1-propanol, and 4-bromobenzenediazonium, offering different sizes and polarities, to tune the surface chemistry of the nanosheets. Figure 2.13a shows the images of High-angle annular dark-field imaging Scanning Transmission Electron Microscopy (HAADF-STEM) of 4-bromobenzenediazonium functionalized MoS_2 nanosheets. We performed Energy Dispersive X-ray Spectroscopy (EDX) elemental mapping of bromine to unambiguously confirm the presence of attached functional groups to the nanosheets. The homogeneous contrast suggests a uniform attachment of the aryl groups on MoS_2. High-resolution transmission electron microscopy (HRTEM) images show that the functionalized nanosheets are still crystalline (Figure 2.13b). The functionalized nanosheets were then characterized by performing Attenuated total

reflectance Fourier-transformed infrared (ATR-FTIR), Raman and ^{13}C nuclear magnetic resonance (^{13}C NMR) spectroscopies. ATR-FTIR and Raman spectroscopies revealed the presence of additional signals or peak splitting after functionalization (Figure 2.1 & 2.2). ^{13}C cross-polarization magic angle spinning Nuclear Magnetic Resonance (CP MAS NMR) has been shown to be a powerful tool to probe the nature of the binding on the nanosheets [24]. ^{13}C NMR was carried out on MoS_2 functionalized with ethyl iodoacetate and 4-bromobenzenediazonium salt to confirm the successful covalent attachment of alkyl and aryl groups respectively. Figures 2.14a, b show the chemical shifts of functionalized MoS_2 nanosheets compared with those of the pristine organohalide or diazonium salt reagents. The ^{13}C signals of the aliphatic carbon (α-C) at -3.7 ppm [42] and 115.3 ppm [43] for ethyl iodoacetate and 4-bromobenzenediazonium respectively disappear after functionalization and are shifted around 46 ppm and 126 ppm. The significant perturbation of the α-C chemical shifts suggests a new chemical environment, which is attributed to the formation of S-C bonds. The observed chemical shifts of the α-C are also in line with our numerical predictions (Figure 2.3). The degree of grafting of functional groups on the nanosheets was estimated using thermogravimetric analysis (TGA) and the averaged density of functional groups reached ~20 at.% per sulfur (Figure 2.4).

The membranes were fabricated by vacuum filtering of the suspension of MoS_2 nanosheets on a nylon porous support. Upon the filtration, the nanosheets vertically stack to form a laminated structure. The obtained MoS_2 membranes will be referred to here as C_2-, C_3-, Ace-, Ben-, C_3OH- and Aryl-functionalized MoS_2 membranes corresponding to iodoethane, 1-iodopropane, ethyl iodoacetate, (2-iodoethyl) benzene, 3-iodo-1-propanol, and 4-bromobenzenediazonium salt treated MoS_2 nanosheets (Figure 2.14c). The ordered interstitial structure was confirmed by the cross-section view of one typical functionalized membrane using scanning electron microscopy (SEM) and X-ray diffraction (XRD) (Figure 2.13c and Figure 2.14d). By adjusting the amount of MoS_2 used for the filtration, the membrane thickness was controlled between 100 nm and 1 μm (Figure 2.5).

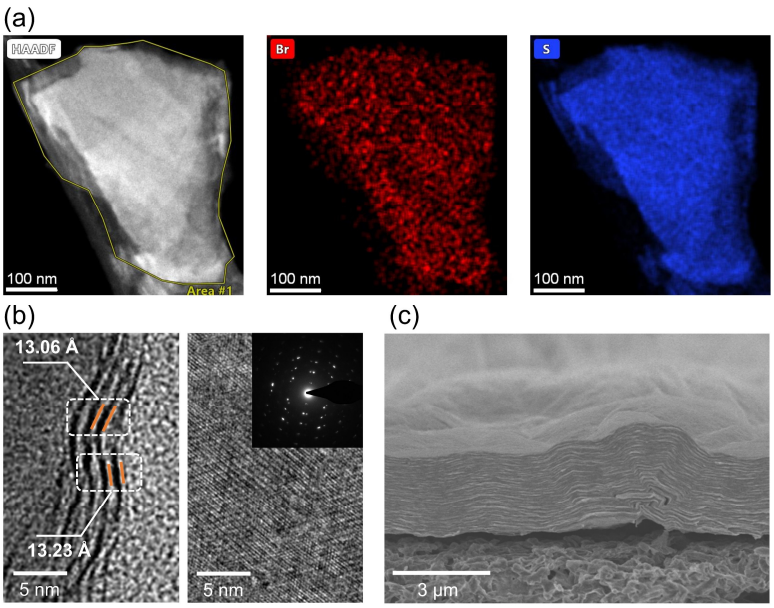

Figure 2.13 Characterizations of the functionalized MoS_2 nanosheets. a, High-angle annular dark-field (HAADF) STEM image of 4-bromobenzenediazonium salt functionalized MoS_2 nanosheets and the corresponding EDX mapping for elements Br (in red) and S (in blue). The elemental mapping of Br in the functionalized MoS_2 nanosheets shows that the aryl groups are homogeneously grafted on the nanosheets surface. **b**, HRTEM images of MoS_2 nanosheets functionalized with aryl groups. The vertically aligned nanosheets form an interlayer spacing of ~13.2 Å, in line with the XRD measurements. Meanwhile, the crystalline nature of the basal plane of Aryl-MoS_2 nanosheets is confirmed by the diffraction pattern (inset). **c**, The SEM cross-section view of laminated membrane prepared by vacuum filtration of Aryl-MoS_2 nanosheets suspension. The highly aligned nanosheets in the vertical direction form 2D capillaries.

We then employed XRD to investigate the structure of the nanolaminated MoS_2 membranes (Figure 2.14d). The XRD pattern from pristine MoS_2 nanolaminates displays an intense (002) peak at ~14.2° corresponding to an interlayer space (d-space) – equivalent to a Mo-to-Mo distance – of ~6.2 Å. After functionalization, this peak shifts to lower angles corresponding to an increased interlayer space between the nanosheets. The capillary width was estimated by subtracting 6.15 Å corresponding to the Mo-Mo distance between two successive layers of MoS_2 in a bulk crystal. We obtained capillary width of 3.6 Å, 4.8 Å, 5.3 Å, 6.9 Å, 6.5 Å, and 7.1 Å for C_2-, C_3-, Ace-, Ben-, C_3OH- and Aryl-functionalized MoS_2, respectively. We attribute the increased height of the nanocapillaries to the presence of the grafted functional groups

on the surface of the nanosheets acting as nanospacers. Our XRD analyses therefore suggest that the interlayer spacing can be fine-tuned to ångström accuracy by employing different sizes of functional groups. To visually observe the increase of the interlayer space, we measured the evolution of the membrane thickness before and after functionalization (Figure 2.14e and Figure 2.6). The thickness determined from our SEM cross-section analyses increases linearly with the d-space distance measured from XRD.

The structural stability of MoS_2 nanolaminates in aqueous solution was examined by successive *ex-situ* XRD measurement at increased soaking time (Figure 2.7). As shown in Figure 2.14f, the space of hydrophobic nanochannel is found virtually stable in water for over 100 hours. We note that the interlayer space of hydrophilic groups such as (-C_3OH) modified nanochannel experienced a slight increase suggesting some water uptake, which is attributed to the more polar nature of the alkyl chains due to the presence of hydroxyl groups. The swelling is however considerably limited at 8.6% compared to graphene oxide or MXene membranes which showed 94.5% and 22.3% swelling respectively after 100 hours (Figure 2.9). We also monitored the evolution of interlayer space by immersing the selected membranes into 1 M NaCl and $MgCl_2$ saline solutions and found minimal difference compared to pure water (Figure 2.10). Our results indicate that stacking functionalized MoS_2 nanosheets into membranes forms stable nanochannels with finely tunable interlayer space and long-term stability. The changes of surface wettability after MoS_2 functionalization were also examined by water contact angle (WCA) measurements (Figure 2.14g and Figure 2.11 & 2.12). Compared to pristine membranes, increased WCA values were obtained in the case of hydrophobic groups grafted on the MoS_2, whereas hydrophilic groups caused a decrease in the WCA. The measurements of the WCA brings direct evidence of the role of the surface chemistry to change the physical and chemical behavior of the membranes.

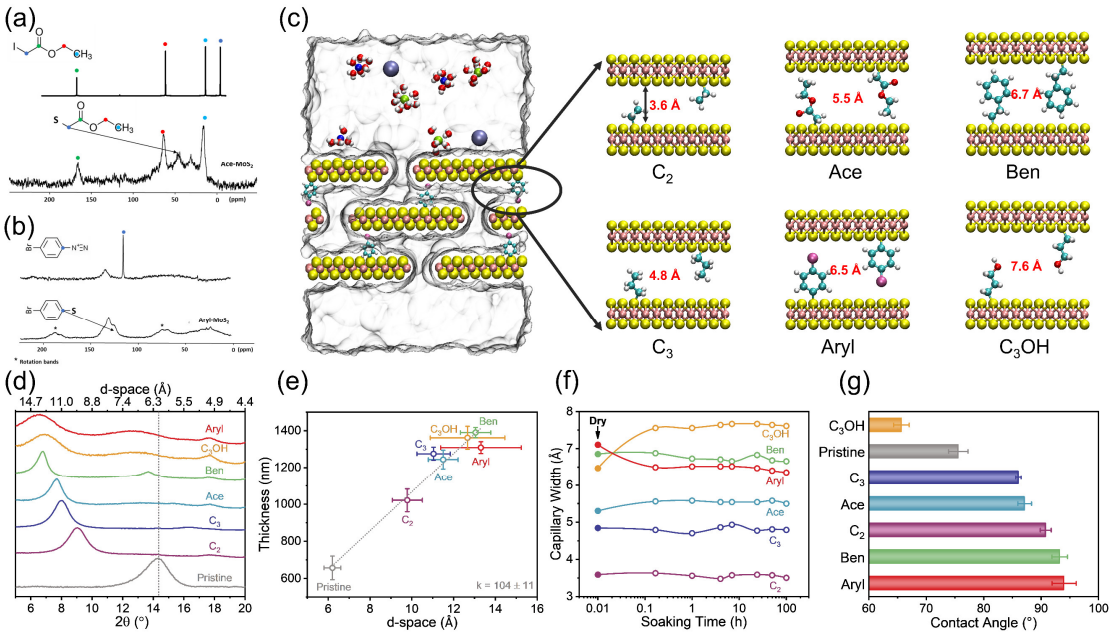

Figure 2.14 Characterization of the functionalized MoS_2 membranes. a and **b**, ^{13}C CP MAS NMR spectra of the Ace-functionalized (**a**, bottom) and Aryl-functionalized (**b**, bottom) MoS_2 nanosheets. ^{13}C NMR spectra of pure chemical reagents namely ethyl iodoacetate (**a**, top, solution) and 4-bromobenzenediazonium (**b**, top, solid-state) were also recorded for comparison. The color dots are used to point out the positions of carbon atoms in different chemical environments. **c**, Schematic illustration of the separation process of stacked functionalized MoS_2 membranes with varied capillary width for water purification and desalination. The values marked in the nanochannels represent the effective layer space in aqueous solution through which water molecules can shuttle. Atom color codes: Mo, pink; S, yellow; C, cyan; H, white; O, red; Br, magenta; Na^+, blue; Cl^-, green; Micropollutant, ice-blue; water, transparent gray. **d**, X-ray diffraction pattern of pristine and functionalized MoS_2 membranes after vacuum drying for 24 h. **e**, Measured thickness of MoS_2 membranes before and after functionalization as a function of d-space. The slope k multiplied by 10 represents the number of stacked layers. **f**, Evolution of the capillary width of functionalized MoS_2 membranes in pure water over the soaking time. **g**, The contact angle of pristine and functionalized MoS_2 membranes. Error bars correspond to standard deviations (s.d.) based on three independent measurements.

2.5.2 Ionic Transport and Water Permeation in the Functionalized MoS_2 Membranes

We first sought to evaluate the transport of the Na^+ ions across the functionalized MoS_2 membranes using a custom-made U-shape cell, where the two-compartments are filled

with an electrolyte solution and DI water, used as permeate and feed solutions, respectively. We found that compared to water, the transport of Na^+ is more sensitive to the height of the 2D capillary, and shows an exponential dependence with the capillary width (Figure 2.15a). The inhibition of Na^+ transport with decreasing channel size arises from steric hindrance of the pore. The permeation rate for Na^+ decreased by 20 folds as the capillary width decreased from 7.6 Å to 3.6 Å compared to 3 folds for water. In aqueous solution, Na^+, Cl^- and SO_4^{2-} have hydration shells with diameters of 7.16 Å, 6.64 Å and 7.58 Å, respectively [44] . This suggests that to enter inside a narrower channel, the ions will necessarily strip more water molecules, which requires additional energy. It is worth noting that the evolution of the permeation rates of Na^+ with the capillary width, *i.e.* the slopes in the middle and right panels of Figure 2.15a, is independent from the nature of the counter ions (Cl^- or SO_4^{2-}). While the faster permeance of Na^+ (about 3 times) in the case of NaCl compared to Na_2SO_4 is attributed to the larger value of hydration energy for SO_4^{2-}: -1330 $kJ.mol^{-1}$ compared to -420 $kJ.mol^{-1}$ and -350 $kJ.mol^{-1}$ for Na^+ and Cl^-, respectively [45]. We also measured the permeation rate of other monovalent ions: Li^+ and K^+ and observed the same trends as that of Na^+. The sensitivity of ion permeation to capillary width follows the hydration energy of the cations: $Li^+ > Na^+ > K^+$ (Figure 2.16). We also found slightly higher permeance rates for Mg^{2+} compared to Na^+ despite larger ionic radius. This is attributed to the Gibbs-Donnan effect due to the presence of remaining excess of charges on the functionalized MoS_2 nanolaminates, as confirmed by our zeta potential measurements (Table 2.1). Remarkably, our results also indicated a stricter dependence of the permeance with the capillary width, which is attributed to the larger hydrated radius and hydration energy of the Mg ions.

The application of hydrostatic pressure in reverse osmosis conditions is known to affect the structure of the capillaries in the nanolaminated structure [46, 47]. Conversely, by operating in FO, we were able to precisely examine the influence of nanochannel structure and surface chemistry on water permeation. We first evaluated the water permeation across the functionalized MoS_2 membranes with different interlayer spaces

under forward osmosis (FO) operation. Concentrated KCl (3M) and deionized (DI) water were used as draw and feed solutions, respectively. Figure 2.15b shows the water flux across the functionalized membranes with increasing stacking sequence from 160 layers up to 1600 layers in forward osmosis conditions. The pristine – *i.e.* non-functionalized – MoS_2 membranes did not allow water molecules to diffuse due to the narrow capillary width of ~0.05 Å (Figure 2.17). Similar water impermeability behavior has been previously reported for MoS_2 membranes tested under reverse osmosis (RO) [23, 48] and highlights to the absence of nanocavities or defects in the laminate structure. In contrast, water permeated through all the functionalized MoS_2 membranes, demonstrating the benefit of functionalization for the diffusion of water. The water flux quickly increased with the decrease of stacking layers due to the shortened pathway for water molecules. We found the highest flux of ~12 L h^{-1} m^{-2} (LHM) in the case of Aryl-functionalized membrane with a stacking of 160 layers. This flux is higher than the typical flux for forward osmosis, which is 5~10 LHM [10, 49] .

We then sought to discriminate the contribution of the capillary width and the surface chemistry of the nanosheets on the water flux. For a fixed number of MoS_2 nanosheets in the nanolaminate, the water flux showed a nearly linear relationship with the capillary width with a ≈3-fold increase when the capillary width increased from 3.6 Å to 7.6 Å. This confirms a size-dependent mass transfer process (Figure 2.18). We then extracted the different slopes values for the functionalized membranes when increasing the number of MoS_2 nanosheets from 160 to 1600. The evolution of the water flux in LMH.$Å^{-1}$ with the number of MoS_2 nanosheets revealed an exponential decrease tendency (Figure 2.15b, inset). According to the curve fitting, our results predict a flux larger than 100 LMH from a nanolaminate membrane with a capillary width of 7 Å and a stacking sequence of 8 layers of MoS_2, corresponding to a thickness of ≈ 10 nm. This finding highlights the potential of nanolaminate functionalized MoS_2 membranes for FO filtration. A final evidence of the role of the surface chemistry was brought by plotting the water permeance as a function of the WCA. The absence of correlation suggests a rather modest contribution of the surface chemistry and the permeation

mechanism is controlled by the structure of the membranes and the interlayer space between the nanosheets in the nanolaminate (Figure 2.19).

To better understand the mechanism of water permeation through the size-varied nanochannel, we conducted permeation experiments at different temperatures. As shown in Figure 2.15c, the permeate flux showed an exponential dependence with temperature in agreement with the Arrhenius law connecting flux and temperature [50]:

$$J = J_0 \, exp\left(-\frac{E_a}{RT}\right) \qquad (2-6)$$

where J and J_0 represent the water fluxes, R (8.314 J mol^{-1} K^{-1}) is the gas constant and T (K) is the temperature. E_a represents the activation energy associated with the water permeation, that is, the energy barriers for water to cross the FO membrane. As can be seen from Figure 2.15d, the activation energy of water permeation decreased linearly with capillary width. Hydrophobic ethyl-functionalized membrane with the narrowest channel demonstrated the highest transmembrane energy barriers for water permeation in line with the fact that the membrane exhibits the lowest water flux. With the increase of capillary width, the energy barriers rapidly and continuously decrease, leading to improved water flux. Remarkably, we note that the activation energy of water permeation is less affected by the nature of the functional groups (Figure 2.20). The results clearly point out the role of the sub-nanometer interlayer distance for controlling the energy barriers and the water permeance under FO filtration. It is also worth noting that the Aryl-functionalized membranes showed the highest flux for all thicknesses, while it had moderate energy barriers suggesting that the energy barrier is not the only parameter governing water diffusion in nanolaminates.

To elucidate the origin of the apparent high-water flux in Aryl-functionalized MoS_2 membranes, we examined the structure of the nanolaminates by comparing the full-height at half-maximum (FWHM) of (002) XRD peaks. The FHWM of the diffraction peaks is known to be a good indicator of the degree of disorder of a crystal and has been used by extension to qualitatively assess the disorder in 2D nanolaminates [24, 51]. The FO membranes made of Aryl-functionalized MoS_2 exhibit the largest FWHM at 1.74° ± 0.03°, indicating a large variation of capillary width of 1.57 Å (Figure 2.8). For

comparison, the variation of the capillary width of the corresponding pristine MoS_2 membranes is of only 0.40 Å. The XRD analyses thus suggest a less ordered stacking compared to the other functionalized membranes. A less ordered structure is therefore likely to bring minor tortuosity, leading to a reduced effective path length for water transport, thereby facilitating the water permeation [51]. To further gauge the influence of the stacking disorder on the water diffusion in the nanolaminate, we plotted the water permeance as a function of capillary width and width variation for nanolaminates with 400 and 1600 nanosheets (Figure 2.15e & 2.15f). We observed that for the thinnest membranes corresponding to a stacking number of 400, the water permeance is controlled by the capillary width, while for thicker laminates the permeance is mainly controlled by the variation in the capillary width. The reduction of the diffusion pathway caused by the decrease of membrane tortuosity is negligible for the thinnest laminates. As the transport pathway increases for thicker membranes, the effect of the tortuosity on the diffusion becomes significant. In light of these results, we identify different behaviors of the nanolaminate FO membranes as the number of two dimensional capillaries increases, which is characterized by a transition from a size-controlled diffusion for the thinnest membranes to disorder-controlled diffusion of the water molecules. Our investigations suggest that the control of both the interlayer space and the stacking disorder in Aryl-functionalized MoS_2 nanolaminates is responsible for the superior water flux in FO, making this membrane a relevant candidate for the realization of practical FO filtration.

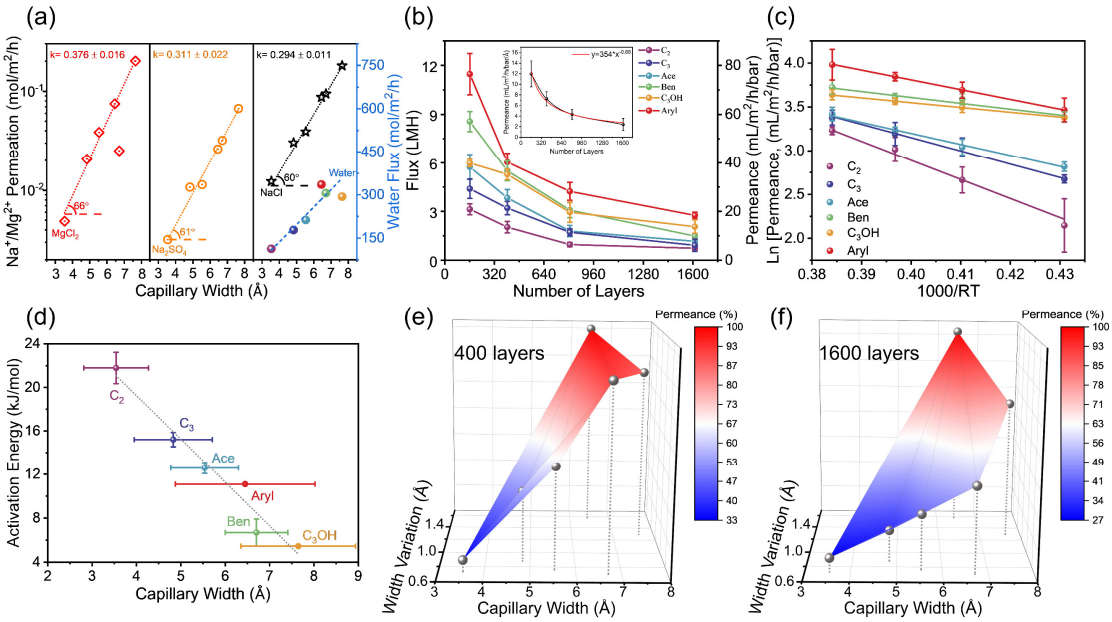

Figure 2.15 Water permeation and ionic transport. a, The Na^+/Mg^{2+} permeation rates and water flux measured by using 400-layer stacked membranes at room temperature. 1 M $NaCl/MgCl_2$ or 0.5 M Na_2SO_4 were employed to provide the high ionic strengths (1 M Na^+/Mg^{2+}) for diffusion. The Na^+/Mg^{2+} permeation rate depends exponentially on the capillary width while the water flux varies linearly. Error bars are omitted for clarity. The dotted lines are best fits. **b**, Water flux of functionalized MoS_2 membranes with different stacking layers measured at room temperature under forward osmosis, where 3M KCl and DI water were used as the draw and feed solution, respectively. Inset: the water permeance as a function of membrane thickness. The red curve is the best fit. **c**, Temperature dependence of water permeation of 400-layer stacked membranes. Solid lines are best fits to Arrhenius activation energies. **d**, Activation energy of water permeation for the functionalized MoS_2 membranes as a function of capillary width. The activation energy varied linearly with capillary width. The dotted line is the best fit. Vertical error bars correspond to the standard deviation of the measurements. The horizontal error bars represent the average half-height of the XRD peaks measured after immersing the membranes in water for a long time (Figure 2.7). **e-f**, The plotted water permeance of membranes with different stacking numbers (400 layers in **e** and 1600 layers in **f**) as a function of capillary width and width variation (Figure 2.8). The permeation rates were normalized by the permeance of Aryl-functionalized MoS_2 membranes. All the vertical error bars are based on at least five independent measurements.

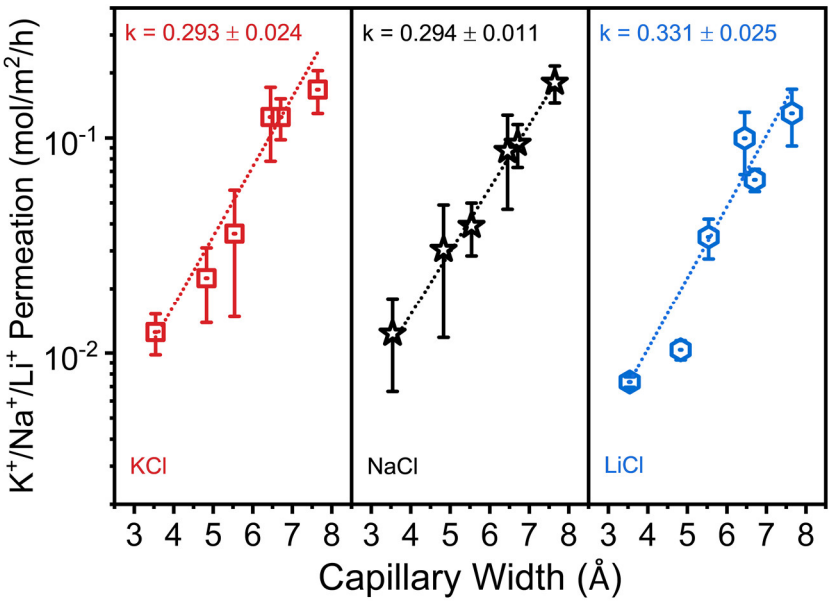

Figure 2.16 Ionic transport across the MoS_2 nanolaminate membranes. The K^+, Na^+ and Li^+ permeation rates were measured by using 400-layer stacked membranes at room temperature. The concentration of the saline solutions was fixed to 1 M. The dotted lines are best fits. The permeation rate of Li^+ and K^+ show the same trends as that of Na^+, characterized by an exponential dependence on the capillary width. Remarkably, the slopes, representing the sensitivity of ion permeation to capillary width, show the following trend in relation to nature of the electrolytes: Li^+> Na^+> K^+, in agreement with the order of hydration energy of monovalent cations. (Li^+: -590 kJ.mol^{-1}, Na^+: -420 kJ.mol^{-1}, K^+: -390 kJ.mol^{-1}) [45].

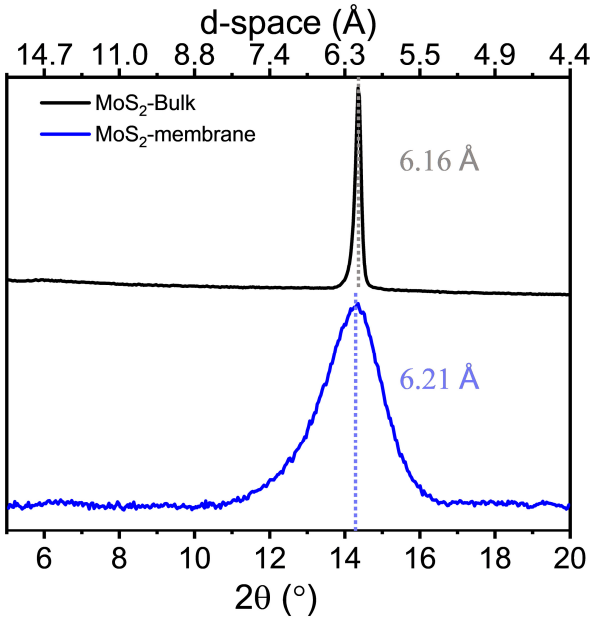

Figure 2.17 XRD patterns of bulk MoS_2 crystal (black) and pristine non-functionalized MoS_2 membrane (blue). As we can see, the pristine membrane has only 0.05 Å free

space between two successive nanosheets, which cannot allow water molecules diffuse into the interlayer.

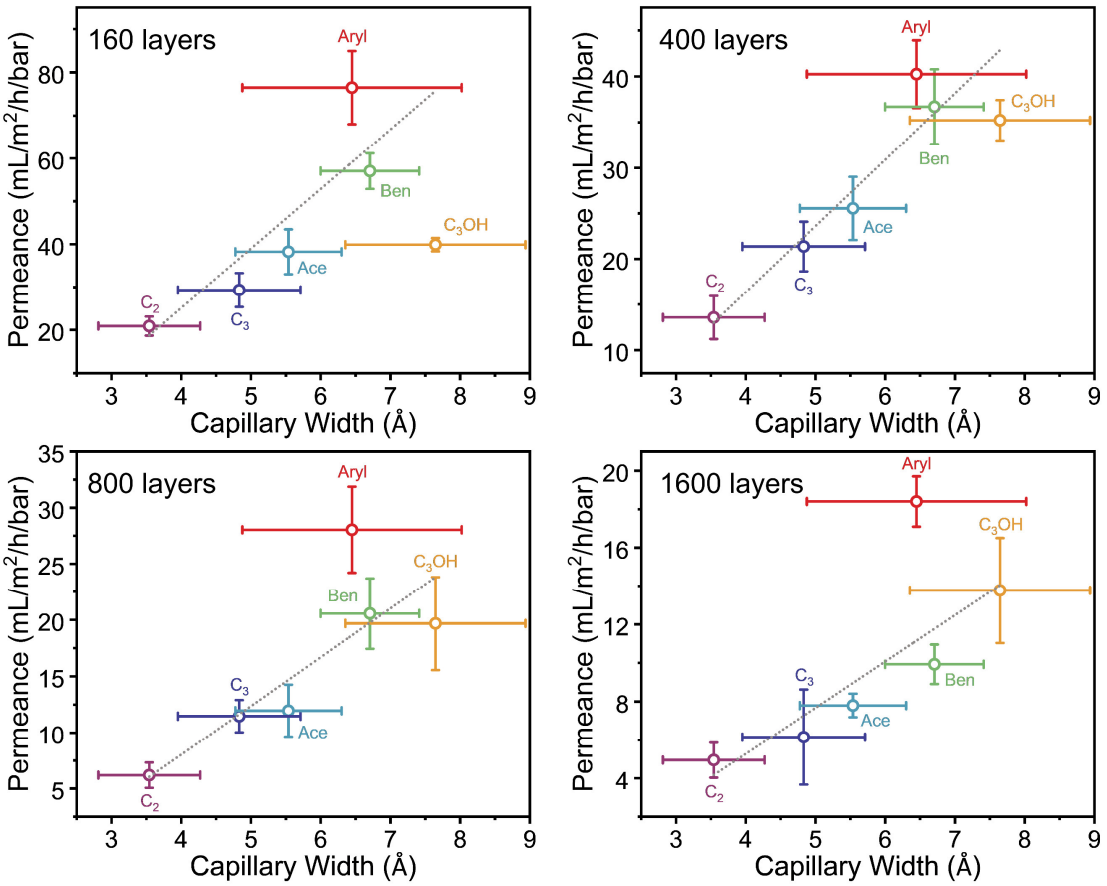

Figure 2.18 The water permeance of functionalized MoS_2 membranes with different thickness and plotted as a function of capillary width. The water permeance shows a nearly linear relationship with capillary width. The dotted lines are the best fits. The vertical error bars corresponding to the standard deviation. The horizontal error bars represent the average half-width of the XRD peaks measured after immersing the membranes in water for a long time (Figure 2.7).

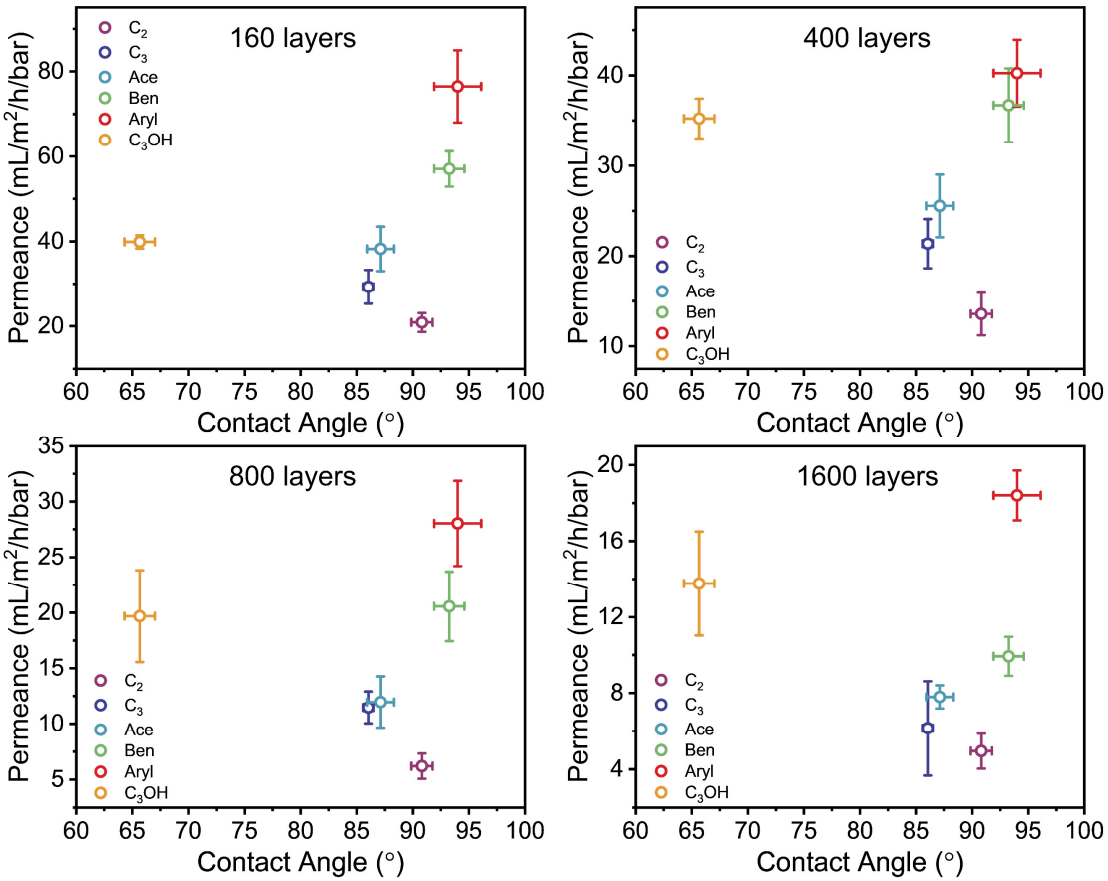

Figure 2.19 The water permeance of functionalized MoS_2 membranes with different thickness and plotted as a function of contact angle. The error bars corresponding to the standard deviation. The water permeance is less affected by the nanochannel wettability. No obvious trends between permeance and contact angle are discovered in our system, suggesting a mass transfer process regulated by structure rather than the surface nature of nanochannels. This may be attributed to the screening effect of high concentrated salt on chemical surface nature as we used 3M KCl as a draw solution. It has been reported that the cation intercalated into the nanochannels would change the surface wettability of 2D laminated membranes [52]. In our system, the KCl would enter the nanochannel through the reverse flow and reside in the interlayer due to the electrostatic attraction from the negatively charged MoS_2 nanosheets. These interactions and the resulting effects are complex and need to be investigated systematically in the future.

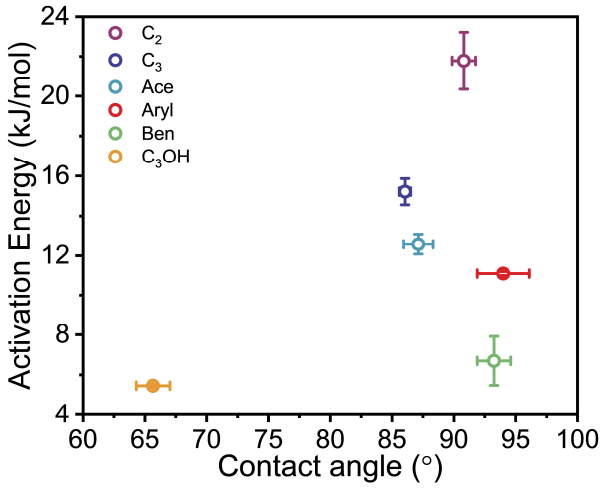

Figure 2.20 The activation energy of water permeation vs contact angle. There is no obvious correlation between activation energy and contact angle.

2.5.3 Mechanical properties of the 2D membranes from MD simulations

The stacking order of the nanolaminate membranes is directly related to the mechanical properties of the layers. Therefore, to get further insight on the atomic origin of the superior water flux of Aryl-functionalized membranes observed above, we performed classical MD simulations of the interaction between functionalized layers (details in the Methods section). Mechanical properties including surface energy and interlayer stiffness can be evaluated by fitting the potential energy of two functionalized layers as a function of interlayer distance, as depicted in Figure 2.21a. Here we use a simple 3-parameters Morse function to fit the potential energy. Our calculations predict surface energies (D_e) of 24, 9 and 6 meV/ Å^2, and interlayer stiffnesses (k_e) of 113.7, 11.1 and 5.6 eV/ Å^2 for pristine, Ben- and Aryl-functionalized MoS_2, respectively (see Figure 2.21b & 2.21c). We obtained capillary width ($\delta=d_0$-6.15, Figure 2.21d) of 0.3, 7.4 and 7.8 Å for pristine, Ben- and Aryl-functionalized MoS_2, respectively, in good agreements with those measured from experiment (0.05, 6.9 and 7.1 Å, Figure 2.14d). As expected, functionalization leads to larger interlayer spacing, smaller surface energy as well as smaller interlayer stiffness. Interestingly, we found that for Aryl-functionalized MoS_2, both the surface energy and the interlayer stiffness are about 50 % smaller than for Ben-MoS_2. The small surface energy and the softness of Aryl-MoS_2 layers can be appreciated by the small depth and the flat bottom of the potential well,

respectively (Figure 2.21a). The combination of small surface energy and interlayer stiffness leads to an increase of stacking defects, which contributes to the broadening of the diffraction peaks measured experimentally. We also performed simulations with a lower extent of functional groups and found that the mechanical properties were only slightly affected, while the capillary width decreased significantly (Table 2.2). Our molecular analysis suggests a direct connection between surface chemistry of the nanosheets and the macroscopic nanofluidic properties of the membranes and it provides a framework for future screening of efficient functional groups for water filtration and desalination.

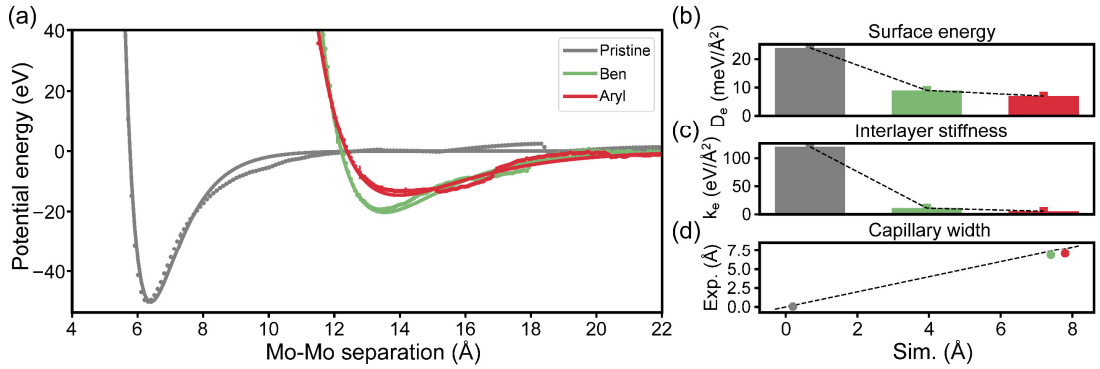

Figure 2.21 Mechanical properties of functionalized MoS_2 nanosheets. a, Potential energy as a function of interlayer separation. To obtain reliable data and statistics, the potential energy surface was scanned 4 times back and forth, as described in the Methods section. Dots correspond to averaged data points and some error bars are displayed (one error bar every 10 averaged data points). Lines correspond to Morse fits as defined by the equation $U(d) = D_e(1-\exp(-\alpha(d-d_0)))^2$. **b**, Surface energy (D_e). **c**, Interlayer stiffness ($k_e = 2D_e\alpha^2$). **d**, Experimental capillary width as a function of those (d_0-6.15) extracted from the Morse fit.

Table 2.2 Mechanical properties of functionalized MoS_2 nanosheets with different grafting degrees from simulation. Notably, the capillary width significantly decreases at 10% functionalization content compare to that of 20%, whereas the simulated capillary width using 20% show a better agreement with the experimental results.

	D_e (meV/Å²)		**k_e (eV/Å²)**		**Capillary width (Å)**		
	10%	**20%**	**10%**	**20%**	**10%**	**20%**	**Experimental**
Ben-	10	9	11.4	11.1	4.8	7.4	6.9
Aryl-	6	6	4.6	5.6	6.1	7.8	7.1

2.5.4 Water Purification and Desalination by Forward Osmosis

To demonstrate the potential of the functionalized MoS_2 membranes, the molecular sieving performance for micropollutants and salt were further evaluated. Four typical micropollutants, a preservative (benzoic acid, BA), a psychoactive drug (caffeine), a common drug (diclofenac sodium, DF) and an organic dye (phthalocyanine), with varied Stoke diameter from ~5.64 Å up to ~14 Å (Table 2.3), were selected and the rejection was measured using high performance liquid chromatography. Rejections of over 90% for all the micropollutants in functionalized membranes were measured, suggesting excellent separation performance in FO. Particularly, the C_2-functionalized membrane with the narrowest channel presented the perfect repulsion of ≈ 100% for the four selected micropollutants. Figure 2.22a shows that the membrane rejection improves with the increase of the molecular weight of the micropollutants in line with the size-limited diffusion as the primary sieving mechanism. To clarify the sieving mechanism, we calculate the ionization degree of the different micropollutants (Table 2.4). Depending on the degree of ionization, we propose that the rejection of functionalized MoS_2 laminated membranes for neutral BA and caffeine molecules stems from a size-limited diffusion mechanism, while for larger weight DF and dye molecules, the rejection is due not only to steric confinement but also to electrostatic interactions between the charges of the molecules and the remaining presence of negative charges on the functionalized MoS_2 nanolaminates. When comparing the evolution of the rejection of the micropollutant with the capillary width, we observe a sharp molecular cut-off of the FO MoS_2 membranes (Figure 2.22b & 2.22c). This behavior highlights the importance of controlling the interlayer space and further evidences the absence of pinholes. To benchmark the performance of the functionalized MoS_2 membranes, we also estimated the separation performance of the graphene oxide (GO) nanolaminates and a commercial polymeric FO membrane (Cellulose Triacetate, CTA) under the same conditions. As shown in Figure 2.22d, the CTA membrane exhibited both a reduced flux and rejection for the smaller contaminants. We determined a rejection of less than 80% for benzoic acid (BA) in agreement with

previous reports from the literature [53]. Both the rejection and the water permeance rapidly increase when filtering large molecules. This behavior is surprisingly the opposite to those of both GO and MoS_2 FO membranes, which showed a decreased rejection and an increased flux for the smaller micropollutants. The decreased performance for sieving out the smallest molecules hints for a rapid fouling due to the blocking of the one-dimensional nanopores of the polymer membranes. Conversely, nanolaminates exhibit a fouling for the largest molecules due to the deposition of the rejected molecules on the surface of the membranes, while the 2D capillaries are not obstructed (Figure 2.23). The surface fouling of the nanolaminate can however be mitigated by operating under tangential crossflow filtration (as described later). GO membranes also exhibited a poor rejection of 65% for the smallest molecules of BA which is attributed to the large capillary width due to swelling. Overall, owing to the tailored and stable interlayer space, the Aryl-functionalized MoS_2 membranes exhibited superior performance both in rejection and flux than GO and commercial polymer membranes.

Table 2.3 Physicochemical properties of Micropollutants [54-57]. The stoke radius of the contaminant, which can represent the effective hydrodynamic radius of molecules in water, was calculated by: $R_H = \frac{k_B T}{6\pi\eta D}$. Where k_B denotes Boltzmann's constant, T presents the temperature, η is the liquid's viscosity and D is the diffusion coefficient of the micropollutant molecules. Stoke radius of NiPc was assessed according to the Stoke radius of porphyrin [57].

Containment	Structure	Molecular weight (g mol^{-1})	Solute charge	Stokes radius (Å)	Ref.
Benzoic Acid	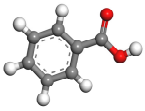	122.1	Neutral	2.82	[54]
Caffeine	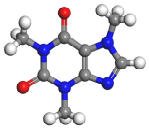	194.2	Neutral	3.18	[55]
Diclofenac sodium	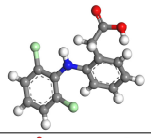	318.1	Negative	4.27	[56]
NiPc	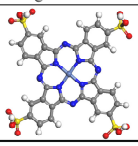	979.4	Negative	≈ 7-10	[57]

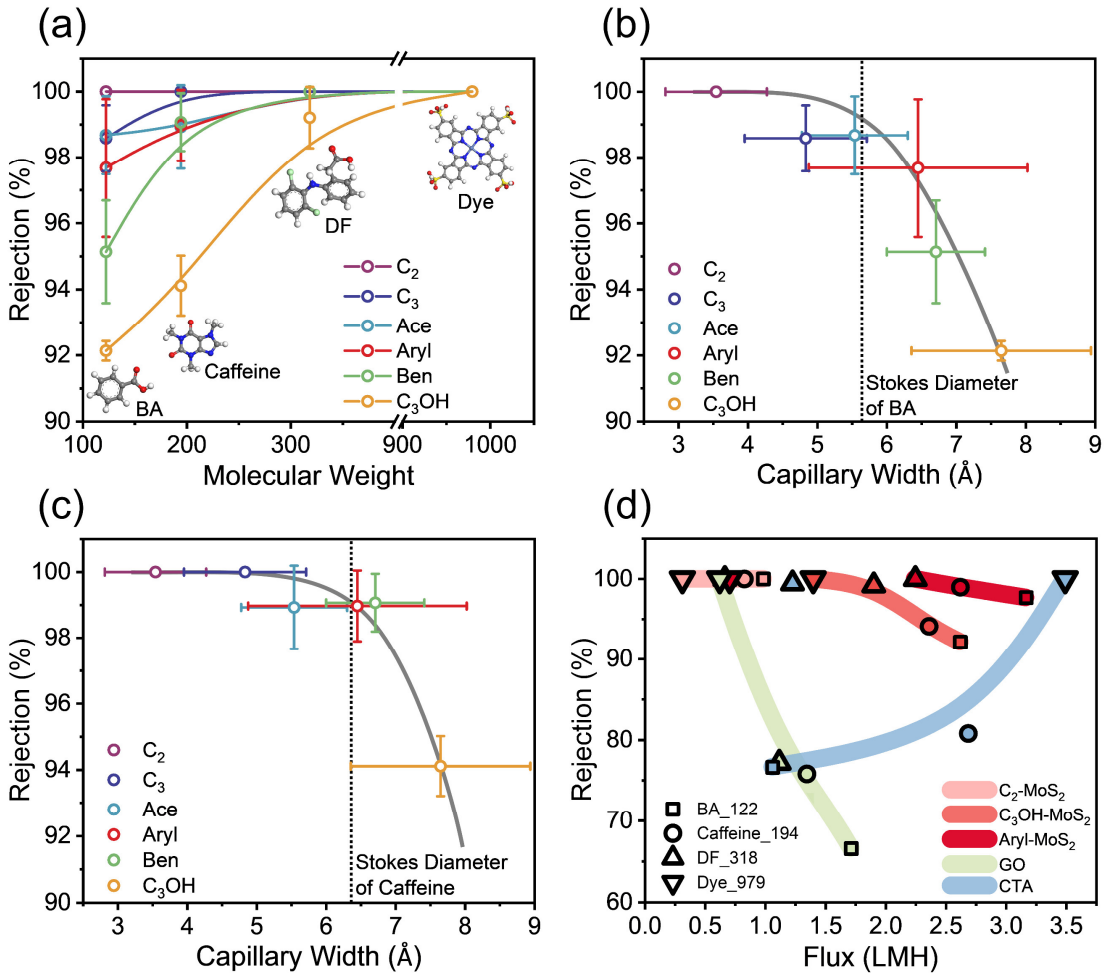

Figure 2.22 Water purification performance of the functionalized MoS_2 membranes. a, Trace organic contaminants rejection measured with 400-layer stacked functionalized MoS_2 membranes at 30°C under forward osmosis, where the 2 M sucrose and 50 mM contaminants (3.3 mM for dye) were used as draw and feed solution. The rejection is plotted as a function of the molecular weight of contaminants. The insets show the molecular structure of contaminants and the gray, white, red, blue, green and yellow balls denote C, H, O, N, Cl and S, respectively. **b** and **c**, Evolution of the rejection for the benzoic acid (**b**) and caffeine (**c**) with the capillary width of membranes. The dotted lines represent the effective hydrodynamic diameter of contaminant molecules (Stokes diameter). The rejection sharply decreases after the capillary width of membranes are larger than the effective diameter of the micropollutants, showing size-selective sieving. The solid gray lines are guides to the eyes. **d**, Comparison of the water purification performance from the functionalized MoS_2 membranes with GO and commercial FO membrane (CTA). Each symbol represents the average flux and rejection calculated from at least five independent measurements and the error bars are omitted for clarity. The complete test data of all functionalized MoS_2 membranes are shown in Figure 2.23.

Table 2.4 The ionization degree of micropollutants in our solution. BA has an ionization equilibrium constant of 6.4×10^{-5} (K_a) at room temperature, giving an ionization degree of 3.6% in a concentration of 50 mM. Therefore, BA can be considered as a neutral molecule in our solution. Caffeine is a methylxanthine alkaloid and a weak base with a K_b of 2.5×10^{-4}, presenting an ionization degree of 7.1%. Most of the caffeine molecules in the solution are still neutral and caffeine is therefore considered as a neutral molecule. The DF and dye however are negatively charged with sodium acting as counter ions.

Containment	Ionization Equilibrium Constant	Ionization Degree
Benzoic Acid	6.4×10^{-5} (K_a)	3.6%
Caffeine	2.5×10^{-4} (K_b)	7.1%

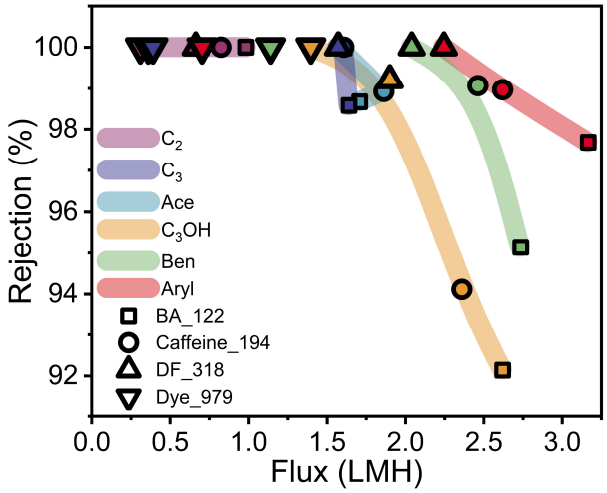

Figure 2.23 The water purification performance of the functionalized MoS_2 membranes. The measurements were performed on the 400-layer functionalized MoS_2 membranes at 30°C under forward osmosis. Only the average flux and rejection based on at least five independent measurements are plotted and the error bars are omitted for clarity.

To properly estimate the molecular weight cutoff (MWCO) of the MoS_2 membranes, we evaluated the rejection performance of the nanolaminates for small neutral compounds: PEG 200 and D-Glucose. As show in Figure 2.24a-c, all the functionalized MoS_2 membranes exhibited high separation performance with rejection greater than 92%, demonstrating excellent cutoff for PEGs and sugar molecules. We observed that the rejection quickly increased with the reduction of the capillary highlighting a size-

limited diffusion in the nanochannels. Interestingly PEG 200 consists in two types of molecules with two molecular weight: PEG-238 and PEG-282 and all of the MoS_2 membranes show greater rejection for PEG-282 in line with a size-dominated sieving mechanism. The rejection of PEG-238 is also slightly lower – especially at the smallest capillary width – than that of D-Glucose despite the two molecules having similar Stokes diameters. This is attributed to different "flexibility" of the molecules. Compared with the planar ring molecule of D-glucose, the alkyl chain of PEG-238 is flexible and can rotate or fold when diffusing in the 2D slits. From a practical point of view, these results highlight the potential of the nanolaminate architecture for the removal of micropollutants as many micropollutants such as biphenyl or aromatic hydrocarbons have a benzene ring.

We then examined the performance of the Aryl-functionalized MoS_2 membranes towards desalination under realistic conditions. FO nanolaminated membranes were prepared by vacuum filtration with sizes up to 45 cm^2 and a stacking of 400 layers, corresponding to a thickness of ≈ 550 nm. We studied the pure water permeance of the planar 45 cm^2 Aryl-functionalized membranes by employing a 2M sucrose as draw solution. A stable water flux of 1.3 LMH was achieved under constant flow conditions at room temperature for a period of 7 days (Figure 2.25). The desalination performance of the functionalized MoS_2 membranes was further evaluated on a pilot-scale tangential flow filtration cell under the forward osmosis operation using 0.1 M NaCl as the feed solution (Figure 2.24d). A water flux greater than 1.6 LMH was achieved and was largely stable over a 7-day period, whereas salt rejection was maintained at greater than ≈ 94.2% and peaked at 96%. These robust desalination properties are attributed to the control of the interlayer distance from the grafted functional groups and the low interlayer stiffness. Remarkably, the interlayer space after 7 days of continuous operation was almost identical to that of the as-prepared membranes (Figure 2.26). We note that the performance is slightly lower than those obtained using smaller membranes, which demonstrated a water flux of 4.37 LMH with a NaCl rejection of 93.9% suggesting that further improvements can be achieved. We also evaluated the

performance of GO membranes and obtained a poor salt rejection of less than 50 % due to the large capillary width of 12.8 Å in line with the literature (Figure 2.9) [10]. Importantly, the GO membrane could only run for one day and then rapidly delaminated upon the application of the tangential flow which highlights their intrinsic instability in water [58]. Besides, commercial CTA polymer membranes exhibited a rejection of around 89.1% with an average flux of 1.25 LMH when tested under the same conditions– consistent with previous reports [59, 60]. Compared with other 2D laminar membranes, the functionalized MoS_2 membranes exhibit a higher water flux and superior salt rejection, exceeding the latest upper bound of state-of-the-art 2D laminar membranes (Figure 2.24e). Importantly the desalination performance is not significantly affected by the upscaling process and the Aryl-functionalized MoS_2 membranes clearly outperform the best desalination performance from the literature under forward osmosis operation (Figure 2.24f). We finally evaluated the specific energy consumption (SEC) of our FO system (see Section 2.7 Note). Under a flow rate of 3.75 mL min^{-1} (1.65 cm s^{-1}), the FO system recovered 148 mL of water in 20 h, corresponding to a SEC of 0.004 kWh m^{-3}. This value is lower than previous reports for flat-sheet CTA membranes, which exhibit SECs of 0.008 kWh m^{-3} and 0.02 KWh m^{-3}, respectively [61, 62]. Although additional processing of the draw solution is requested to obtain potable water, the present FO system shows a clear reduction of the energy footprint compared to the other water recovery approaches such as traditional RO filtration (1.5-2.5 kWh m^{-3}) [63, 64], thermal distillation technology (16.3-27.3 kWh m^{-3})[63], and self-supplied FO with thermolytic ammonium bicarbonate (0.1 kWh m^{-3}) [65].

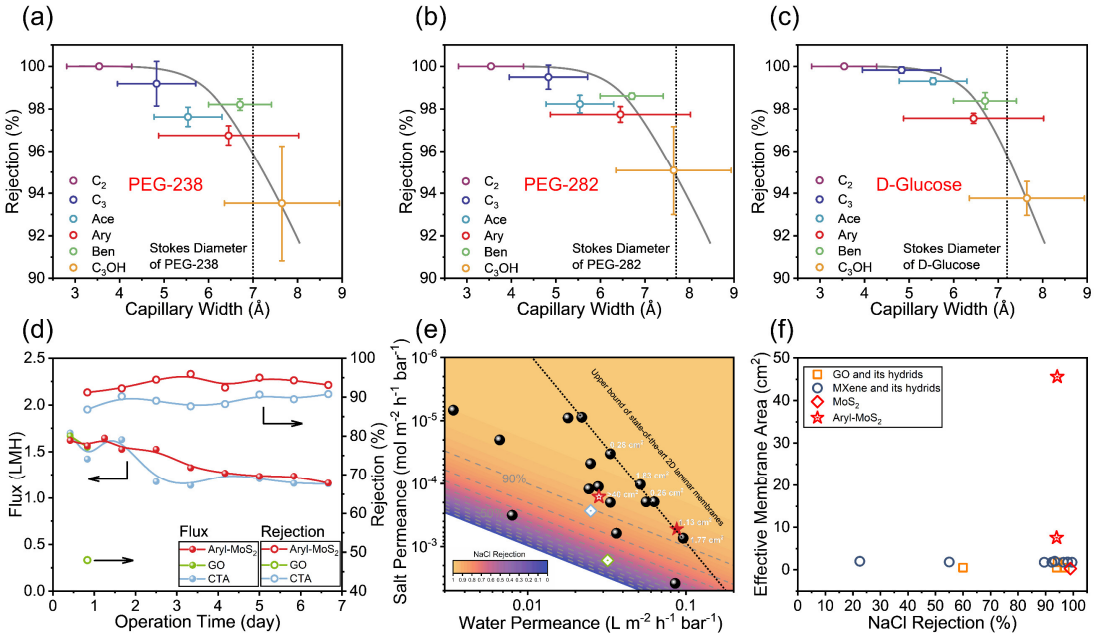

Figure 2.24 Molecular weight cut-off and water desalination performance of the functionalized MoS_2 membranes. Evolution of the rejection for the PEG-238 (**a**), PEG-282 (**b**) and D-Glucose (**c**) with the capillary width of membranes. The rejection was measured with 400-layer stacked functionalized MoS_2 membranes at 30 °C under forward osmosis, where the 2 M sucrose/50 mM PEG 200 and 0.92 M Na_2SO_4/50 mM D-Glucose were used as draw/feed solution, respectively. The dotted lines represent the effective hydrodynamic diameter of PEG and D-Glucose (Stokes diameter). And the solid gray lines are guides to the eyes. **d**, The desalination performance of Aryl-functionalized MoS_2 membrane and the comparison with GO and commercial FO membrane. The measurements were conducted in a tangential cross-flow cell using 2 M sucrose and 0.1 M NaCl as draw and feed solution. The GO membrane could only be run for one day and then decomposed. **e**, Comparison of the desalination performance of Aryl-functionalized MoS_2 (red stars) with other 2D laminar membranes made of GO, MXene and their hybrids. All the data listed in the figure were measured under separation models in forward osmosis cells using sucrose and 0.1 M NaCl as draw and feed solution. Our Aryl-functionalized MoS_2 membranes test data are marked with red stars, while CTA and GO data are denoted by light-blue and green hollow diamonds. The effective membrane area is labeled in white. The black line represents the upper bound of state-of-the-art 2D laminar membranes due to the trade-off between membrane permeability and selectivity. A comprehensive comparison of desalination performance of 2D membranes estimated under diffusion or separation models can be found in Table 2.5 (in Section 2.7 Note). **f**, Comparison of effective membrane area measured in our work with previously reported membranes.

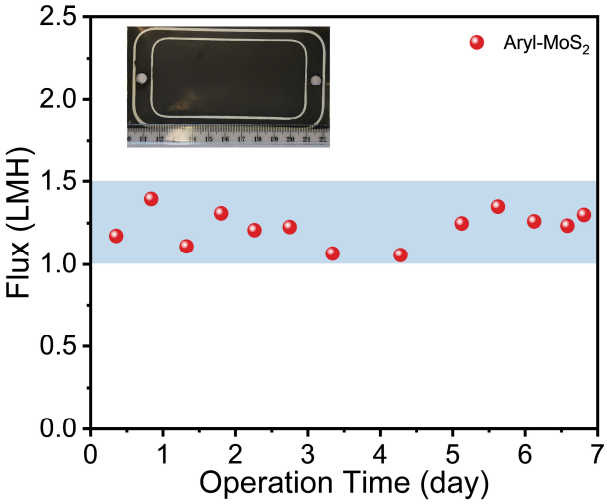

Figure 2.25 Evolution of water flux through a large-scale Aryl-functionalized MoS_2 membrane with operation time. The flux was measured in tangential cross-flow filtration cell at room temperature using 2 M sucrose and DI water as draw and feed solution. The inset image is the optical photo of the tested membrane.

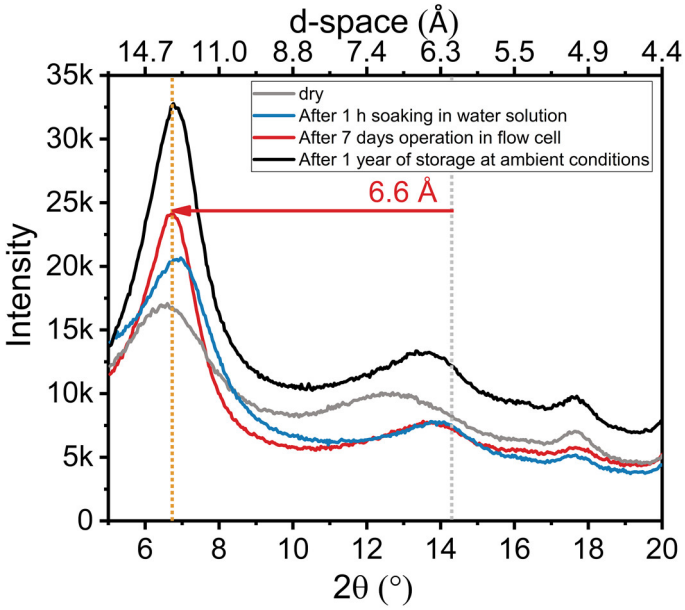

Figure 2.26 The XRD pattern of Aryl-functionalized MoS_2 membrane after 7 days of desalination in a tangential cross flow configuration. The diffraction pattern is compared to that of the same membrane after 1 year of storage at ambient conditions, as well as to that of dried and pristine MoS_2 membranes, and after 1 hour of immersion in water. As shown in Figure, after a long-term operation, the intensity of the (002) peak remains virtually unaffected and exhibits similar FWHM. The peak position does not shift demonstrating that the nanochannels of the functionalized MoS_2 membranes are robust. The rejection stability and the XRD analyses demonstrate that MoS_2 membranes can also sustain the cross-flow shear even for prolonged utilization. Besides, the

capillary width of the tested membrane after 1 year of storage at ambient conditions was also measured. Notably, the (002) peak of the membrane is not modified, which further suggests that functionalized MoS_2 membranes are structurally stable.

2.6 Conclusion

Overall this work presents a robust and scalable method to prepare stable nanolaminated membranes with tunable sieving performance and high water permeance in FO filtration. The structure of the functionalized MoS_2 membranes can be precisely adjusted over a large range of interlayer spaces using alkyl and aryl groups which offers ångström-precision for the 2D nanochannels. Using this approach, we elucidated the contributions from the surface chemistry, the interlayer space and the stacking tortuosity on the behavior of FO nanolaminate membranes. Due to the constant interlayer space in aqueous solution, our functionalized membranes exhibit excellent water purification performance compared with the GO and commercial membranes. In particular, we identified Aryl-functionalized MoS_2 membranes as promising candidates for FO application and demonstrated its scalability up to 45 cm^2. We believe this is a promising strategy for the design of novel energy-efficient nanofiltration and desalination FO membranes.

2.7 Note

2.7.1 Specific energy consumption (SEC) calculation

In FO system, the major energy consumption is attributed to the recirculating pump. Thus, the power consumption from the pump is assumed to equal to the power consumption of the FO system. The SEC was calculated using Eq. (2-7) (2-8):

$$SEC_{FO} = \frac{P_{system}}{Q_P} = \frac{P_{pump}}{Q_p} \qquad (2-7)$$

$$P_{pump} = \frac{p_{FW} \times Q_{FW-in} + p_{DS} \times Q_{DS-in}}{3.6 \times 10^6 \times \eta} \qquad (2-8)$$

where P_{pump} is the power of pump (kW), Q_p is the recovered water flow rate in $m^3.h^{-1}$, η is the pump efficiency, Q_{FW-in} and Q_{DS-in} are feed water and draw solution flow rates in $m^3.h^{-1}$, p_{FW} and p_{DS} are the feed hydraulic pressure (Pa) in feed and draw

side, which is estimated using Eq. (2-9):

$$p = \rho \times g \times h \qquad (2-9)$$

where ρ is density of fluid (kg/m^3), g is acceleration of gravity (9.81 m/s^2), h is head increase across the pump (m), which includes the total head loss and the height at which the solution is pumped. The height of the solution pumped is determined by the installation of equipment. While the head loss is affected by the fluid velocity and viscosity, tube diameter, pipe length and the pipe absolute roughness.

Here, we assumed an 80% efficiency to estimate the power of the pump and a 1 meter long silicone hose with a diameter of 0.22 cm was used for delivering the solutions. After calculations, we estimate an energy consumption as low as 0.004 kWh.m^{-3}.

2.7.2 Comparison of the performance of the MoS_2 membranes with state-of-the-art 2D laminar membranes

The FO desalination performances of the functionalized MoS_2 membranes have been compared with the literature (Figure 2.24e) and the corresponding data are detailed in Table 2.5. There are two models used in FO desalination. The NaCl solution acts as permeate solution in diffusion configuration while as feed solution in separation configuration. The salt permeance under diffusion configuration is measured by the reverse solute flux, while the salt permeance (P_s) under separation model can be estimated from the equations (2-10) and (2-11):

$$J_s = J_w \times C_F \times (1 - R) \qquad (2-10)$$

$$P_s = \frac{J_s}{\Pi} \qquad (2-11)$$

where Π is osmotic pressure in bar, J_s is forward salt flux in mol m^{-2} h^{-1} (molMH), J_w is forward water flux in L m^{-2} h^{-1} (LMH), C_F is feed NaCl concentration in mol L^{-1} (M), and R is the percent salt rejection.

Table 2.5 Comparison of the desalination performance of 2D laminar membranes measured in forward osmosis cells under diffusion or separation models [11] [9] [10] [66] [67] [40] [68] [26] [69] [70] [71] [59] [72].

Type	Membrane configuration	Effective membrane area (cm^2)	Draw solution	Feed solution	Osmotic pressure (bar)	Water flux (LMH)	Water permeance (LMHB)	Salt permeance under separation model (molMHB)	Salt permeance under diffusion model (molMHB)	Salt rejection	Ref
GO	GO-280 nm	1.13	0.25 M NaCl	H_2O	12	0.85	0.0708	-	0.058	n/a	[11]
	KCl-GO-280 nm	1.13	0.25 M NaCl+0.25 M KCl	H_2O+0.25 M KCl	12	0.36	0.03	-	$4.2*10^{-4}$	n/a	
GO	GO-1 μm	0.785	1 M Sucrose	H_2O	25	0.2	0.008	-	-	-	[9]
	GO-5 μm	0.785	1 M NaCl	H_2O	48	n/a	n/a	-	0.052	n/a	
GO/Graphene	GO/G-5 μm	0.5	3 M Sucrose	0.1 M NaCl	75	0.5	0.0067	0.00002	-	97%	[10]
	GO-5 μm	0.5	3 M Sucrose	0.1 M NaCl	75	0.6	0.008	0.00032	-	60%	
	GO/G-1 μm	0.5	3 M Sucrose	0.1 M NaCl	75	2.5	0.0333	0.0002	-	94%	
rGO	rGO-KCl-280 nm	1.13	0.25 M NaCl + 0.25 M KCl	H_2O + 0.25 M KCl	12	0.22	0.0183	-	0.00524	n/a	[11]
	rGO-280 nm	1.13	0.25 M NaCl	H_2O	12	0.57	0.0475	-	0.025	n/a	
Graphene	*l*GP-3 μm	0.264	3 M Sucrose	0.1 M NaCl	75	4.725	0.063	0.0001953	-	96.9%	[66]
	*m*GP-3 μm	0.264	3 M Sucrose	0.1 M NaCl	75	1.875	0.025	0.0000475	-	98.1%	
	*s*GP-3 μm	0.264	3 M Sucrose	0.1 M NaCl	75	1.35	0.018	$9.0*10^{-6}$	-	99.5%	
MXene	Pristine-500 nm	1.83	0.2 M Sucrose	0.1 M NaCl	5	0.427	0.0854	0.003843	-	55%	[67]
	MXene-180 °C-500 nm	1.83	0.2 M Sucrose	0.1 M NaCl	5	0.2575	0.0515	0.000103	-	98%	
MXene	Al-MXene-340 nm	1.77	2 M Sucrose	0.1 M NaCl	50	8.5	0.17	0.001785	-	89.5%	[40]
	Al-MXene-580 nm	1.77	2 M Sucrose	0.1 M NaCl	50	4.8	0.096	0.0007392	-	92.3%	
	Al-MXene-1100 nm	1.77	2 M Sucrose	0.1 M NaCl	50	2.8	0.056	0.000196	-	96.5%	
	Al-MXene-2700 nm	1.77	2 M Sucrose	0.1 M NaCl	50	1.1	0.022	$8.8*10^{-6}$	-	99.6%	
GLGM	GO/LDH-1250 nm	1.77	1 M sucrose	0.01 M NaCl	25	2.25	0.09	0.0000513	-	94.3%	[68]
MoS_2	Pri-MoS_2-330 nm	n/a	2 M Sucrose	0.1 M NaCl	50	0.17	0.0034	$6.8*10^{-6}$	-	98%	[26]
	MoS_2-K^+-330 nm	n/a	2 M Sucrose	0.1 M NaCl	50	1.22	0.0244	0.000122	-	95%	
	MoS_2-Na^+-330 nm	n/a	2 M Sucrose	0.1 M NaCl	50	1.39	0.0278	0.0001112	-	96%	
	MoS_2-Li^+-330 nm	n/a	2 M Sucrose	0.1 M NaCl	50	1.4	0.0280	0.000112	-	96%	
	MoS_2-Mg^{2+}-330 nm	n/a	2 M Sucrose	0.1 M NaCl	50	1.82	0.0364	0.0006188	-	83%	
fGraphene	4 μm	-	10 wt% NaCl	H_2O	85	13.9	0.1635	-	n/a	n/a	[69]
MXene	Nb_2CTx MXene-5 μm	2	0.25 M NaCl	H_2O	12	4.3	0.3583	-	0.525	22.5%	[70]
	NbSA-5 μm	2	0.25 M NaCl	H_2O	12	2.1	0.175	-	0.0083	93.3%	
MoS_2	MoS_2/SY-5 μm	0.28	3 M Sucrose	0.1 M NaCl	75	2.5	0.0333	$3.33*10^{-5}$	-	99%	[71]
CAT		40000	300 g/L Sucrose	H_2O	25	0.8	0.032	-	-	-	[59]

MOF	Al-MOF-100 nm	0.07	0.5 M NaCl	H_2O	24	0.043	0.0018	-	$6.25*10^{-6}$	n/a	[72]
	Al-MOF-100 nm	0.07	0.5 M $CoCl_2$	H_2O	36	0.640	0.0178	-	$4.17*10^{-6}$	n/a	
	Al-MOF-20 nm	0.07	0.5 M $CoCl_2$	H_2O	36	1.44	0.04	-	$4.44*10^{-6}$	n/a	
MoS_2	C_2-MoS_2	1.13	2 M Sucrose	50 mM Benzoic acid	50	0.98	0.0196	-	-	100%	This work
	C_3-MoS_2	1.13	2 M Sucrose	50 mM Benzoic acid	50	1.64	0.0328	-	-	98.6%	
	Acc-MoS_2	1.13	2 M Sucrose	50 mM Benzoic acid	50	1.71	0.0342	-	-	98.7%	
	Ben-MoS_2	1.13	2 M Sucrose	50 mM Benzoic acid	50	2.74	0.0548	-	-	95.2%	
	C_3OH-MoS_2	1.13	2 M Sucrose	50 mM Benzoic acid	50	2.62	0.0524	-	-	92.2%	
	Aryl-MoS_2	1.13	2 M Sucrose	50 mM Benzoic acid	50	3.17	0.0634	-	-	97.7%	
	Aryl-MoS_2 (small membrane)	1.13	2 M Sucrose	0.1 M NaCl	50	4.37	0.0874	0.00053314	-	93.9%	
	Aryl-MoS_2 in tangential cross-flow filtration cell	7.54	2 M Sucrose	0.1 M NaCl	50	1.70	0.034	0.000204	-	94.0%	
	Aryl-MoS_2 (big membrane) in tangential cross-flow filtration cell	45.6	2 M Sucrose	0.1 M NaCl	50	1.41	0.0282	0.00016356	-	94.2%	

2.7.3 Force field parameters of MD simulation

We developed an extension of OPLS force field to describe bromobenzene- and ethylbenzene-functionalized MoS_2. We used a Monte Carlo algorithm, to minimize the error between OPLS and density functional theory energies of various potential energy surfaces corresponding to bond dissociation, angle bend and dihedral twist. DFT calculations were performed with VASP [73, 74] at the PBE level [36] as well as with D3 vdW correction [75]. We performed relaxed surface scans of the PES with VASP by performing multiple geometry relaxations while constraining the bond/angle/dihedral positions and scanning their internal positions. For each bond dissociation scan, there is no other internal degree of freedom than the bond distance itself and this can be obtained straightforwardly. For an angle, for example the angle defined by the 3 atoms A-B-C, for each value of the angle, we performed a geometry relaxation for an ensemble of distances A-B and B-C, and finally selected the lowest energy structure as the reference. We proceeded similarly for dihedrals. We show Figure 2.27, DFT and the optimized OPLS energies over the training set. We can see that our final force field properly describes interactions between MoS_2 and functional groups including C atom from alkane chains (as in MoS_2-ethylbenzene) and C atom from an aromatic group (as in MoS_2-bromobenzene).

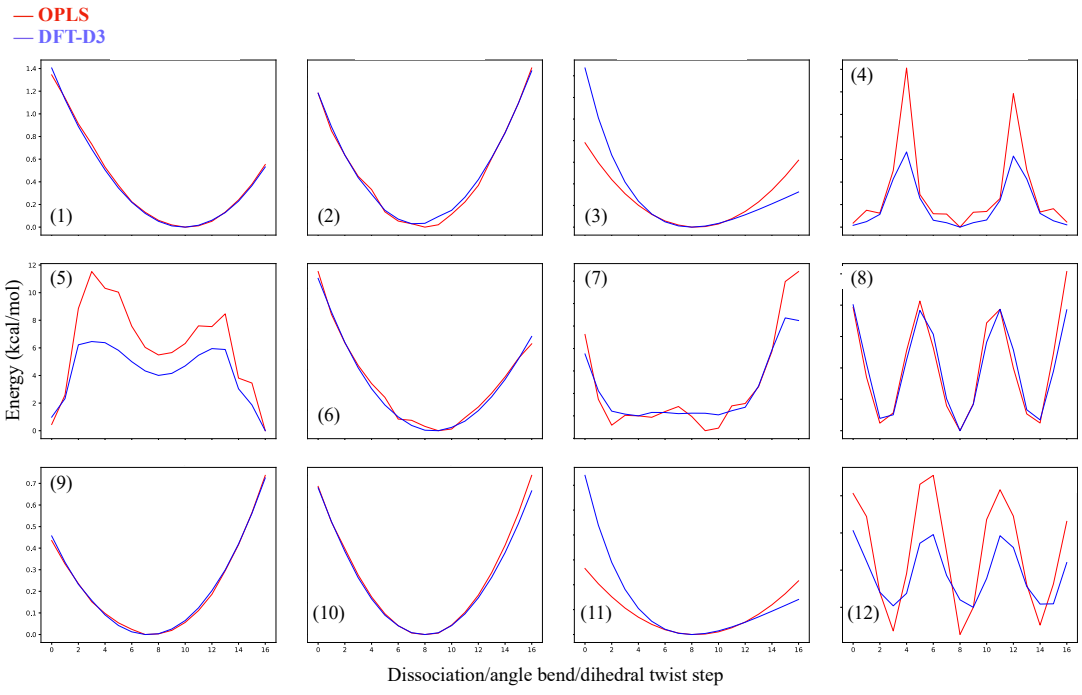

Figure 2.27 Potential energy surfaces corresponding to dissociation, bend and twist of bond/angle/dihedral in various functionalized MoS_2 as a function of steps. Steps were selected as 0.1 Å, 1° and approximately 20° for bond, angle, dihedral, respectively. The blue lines correspond to DFT-D3 reference energies while red lines correspond to the optimized OPLS force field. We provide in Table 2.6 details on each subplot.

Table 2.6 Details on the subplots presented Figure 2.27. The column *system* gives the actual system used as reference for the PES, the column *PES-type* gives the type of PES (bond dissociation/angle bend/dihedral twist), and the column *atoms* gives the ordered atom list corresponding to the bond/angle/dihedral.

PES index	System	PES-type	Atoms
(1)	MoS_2-brbenzene	angle	Mo-S-C
(2)	MoS_2-brbenzene	angle	S-C-C
(3)	MoS_2-brbenzene	bond	S-C
(4)	MoS_2-brbenzene	dihedral	Mo-S-C-C
(5)	MoS_2-ebenzene	dihedral	S-C-C-C
(6)	MoS_2-ethane	angle	S-C-C
(7)	MoS_2-ethane	dihedral	Mo-S-C-C
(8)	MoS_2-ethane	dihedral	S-C-C-H
(9)	MoS_2-methane	angle	Mo-S-C
(10)	MoS_2-methane	angle	S-C-H
(11)	MoS_2-methane	bond	S-C
(12)	MoS_2-methane	dihedral	Mo-S-C-H

Table 2.7 OPLS parameters of the optimized force field. We added the elements Mo and S as OPLS types 907 and 908, respectively with OPLS bond, angle and dihedral types of 111 and 112, respectively (i.e. 907_b111_a111_d111 and 908_b112_a112_d112). Columns "Atom 1-Atom 4" correspond to the OPLS type of the atoms involved in the bond/angle/dihedral. Columns "P1-P4" give the parameters of the bond/angle/dihedral in OPLS force field units (Å and kcal/mol).

Atom 1	Atom 2	Atom 3	Atom 4	P1	P2	P3	P4
13	112			129.49	1.82		
48	112			193.63	1.78		
46	13	112		44.16	104.76		
13	112	111		12.57	134.94		
13	13	112		32.29	111.27		
48	48	112		36.89	112.77		

48	112	111		9.11	147.77		
46	13	112	111	0.05	0.11	0.02	0.82
46	13	13	112	0.64	0.41	-0.24	-0.34
13	13	112	111	0.09	-0.77	0.19	0.03
48	13	13	112	0.50	-0.33	-0.48	0.03
48	48	112	111	0.03	-0.14	0.39	0.05

2.8 Reference

1. Shen, J., et al., *Artificial channels for confined mass transport at the sub-nanometre scale.* Nature Reviews Materials, 2021. **6**(4): p. 294-312.
2. Werber, J.R., C.O. Osuji, and M. Elimelech, *Materials for next-generation desalination and water purification membranes.* Nature Reviews Materials, 2016. **1**(5): p. 1-15.
3. Wang, S., et al., *Two-dimensional nanochannel membranes for molecular and ionic separations.* Chemical Society Reviews, 2020. **49**(4): p. 1071-1089.
4. Kang, Y., et al., *2D laminar membranes for selective water and ion transport.* Advanced Functional Materials, 2019. **29**(29): p. 1902014.
5. Cheng, L., et al., *Two-dimensional-material membranes: Manipulating the transport pathway for molecular separation.* Accounts of Materials Research, 2021. **2**(2): p. 114-128.
6. Safaei, J., P. Xiong, and G. Wang, *Progress and prospects of two-dimensional materials for membrane-based water desalination.* Materials Today Advances, 2020. **8**: p. 100108.
7. Liu, P., et al., *Two-dimensional material membranes for critical separations.* Inorganic Chemistry Frontiers, 2020. **7**(13): p. 2560-2581.
8. Cheng, Y., Y. Pu, and D. Zhao, *Two-Dimensional Membranes: New Paradigms for High-Performance Separation Membranes.* Chemistry–An Asian Journal, 2020. **15**(15): p. 2241-2270.
9. Joshi, R., et al., *Precise and ultrafast molecular sieving through graphene oxide membranes.* science, 2014. **343**(6172): p. 752-754.
10. Abraham, J., et al., *Tunable sieving of ions using graphene oxide membranes.* Nature nanotechnology, 2017. **12**(6): p. 546-550.
11. Chen, L., et al., *Ion sieving in graphene oxide membranes via cationic control of interlayer spacing.* Nature, 2017. **550**(7676): p. 380-383.
12. Shen, J., et al., *Subnanometer two-dimensional graphene oxide channels for*

ultrafast gas sieving. ACS nano, 2016. **10**(3): p. 3398-3409.

13. Hung, W.-S., et al., *Cross-linking with diamine monomers to prepare composite graphene oxide-framework membranes with varying d-spacing.* Chemistry of Materials, 2014. **26**(9): p. 2983-2990.
14. Zheng, S., et al., *Swelling of graphene oxide membranes in aqueous solution: characterization of interlayer spacing and insight into water transport mechanisms.* ACS nano, 2017. **11**(6): p. 6440-6450.
15. Su, P., et al., *Graphene oxide membranes: controlling their transport pathways.* Journal of Materials Chemistry A, 2020. **8**(31): p. 15319-15340.
16. Han, Z.-y., et al., *A review of performance improvement strategies for graphene oxide-based and graphene-based membranes in water treatment.* Journal of Materials Science, 2021: p. 1-30.
17. Sun, L., H. Huang, and X. Peng, *Laminar MoS 2 membranes for molecule separation.* Chemical communications, 2013. **49**(91): p. 10718-10720.
18. Guo, B.-Y., et al., *MoS2 membranes for organic solvent nanofiltration: stability and structural control.* The Journal of Physical Chemistry Letters, 2019. **10**(16): p. 4609-4617.
19. Ren, C.E., et al., *Charge-and size-selective ion sieving through Ti3C2T x MXene membranes.* The journal of physical chemistry letters, 2015. **6**(20): p. 4026-4031.
20. Ding, L., et al., *A two-dimensional lamellar membrane: MXene nanosheet stacks.* Angewandte Chemie International Edition, 2017. **56**(7): p. 1825-1829.
21. Wang, J., et al., *Ion sieving by a two-dimensional Ti3C2Tx alginate lamellar membrane with stable interlayer spacing.* Nature communications, 2020. **11**(1): p. 1-10.
22. Kim, S., H. Wang, and Y.M. Lee, *2D nanosheets and their composite membranes for water, gas, and ion separation.* Angewandte Chemie, 2019. **131**(49): p. 17674-17689.
23. Wang, Z., et al., *Understanding the aqueous stability and filtration capability of MoS2 membranes.* Nano letters, 2017. **17**(12): p. 7289-7298.

24. Ries, L., et al., *Enhanced sieving from exfoliated MoS 2 membranes via covalent functionalization.* Nature materials, 2019. **18**(10): p. 1112-1117.
25. Mei, L., et al., *Simultaneous Electrochemical Exfoliation and Covalent Functionalization of MoS2 Membrane for Ion Sieving.* Advanced Materials, 2022: p. 2201416.
26. Chu, C., et al., *Precise ångström controlling the interlayer channel of MoS2 membranes by cation intercalation.* Journal of Membrane Science, 2020. **615**: p. 118520.
27. Horvath, A.L., *Handbook of aqueous electrolyte solutions*. 1985: Halsted Press.
28. Plimpton, S., *Fast parallel algorithms for short-range molecular dynamics.* Journal of computational physics, 1995. **117**(1): p. 1-19.
29. Jorgensen, W.L., D.S. Maxwell, and J. Tirado-Rives, *Development and testing of the OPLS all-atom force field on conformational energetics and properties of organic liquids.* Journal of the American Chemical Society, 1996. **118**(45): p. 11225-11236.
30. Sresht, V., et al., *Quantitative modeling of MoS2–solvent interfaces: predicting contact angles and exfoliation performance using molecular dynamics.* The Journal of Physical Chemistry C, 2017. **121**(16): p. 9022-9031.
31. Onofrio, N. and T.W. Ko, *Exploring the Compositional Ternary Diagram of Ge/S/Cu Glasses for Resistance Switching Memories.* The Journal of Physical Chemistry C, 2019. **123**(14): p. 9486-9495.
32. Heising, J. and M.G. Kanatzidis, *Structure of restacked MoS2 and WS2 elucidated by electron crystallography.* Journal of the American Chemical Society, 1999. **121**(4): p. 638-643.
33. Socrates, G., *Infrared and Raman characteristic group frequencies: tables and charts*. 2004: John Wiley & Sons.
34. Tan, S.J.R., et al., *Temperature-and phase-dependent phonon renormalization in 1T′-MoS2.* ACS nano, 2018. **12**(5): p. 5051-5058.
35. Giannozzi, P., et al., *QUANTUM ESPRESSO: a modular and open-source*

software project for quantum simulations of materials. Journal of physics: Condensed matter, 2009. **21**(39): p. 395502.

36. Perdew, J.P., K. Burke, and M. Ernzerhof, *Generalized gradient approximation made simple.* Physical review letters, 1996. **77**(18): p. 3865.
37. Troullier, N. and J.L. Martins, *Efficient pseudopotentials for plane-wave calculations.* Physical review B, 1991. **43**(3): p. 1993.
38. Kleinman, L. and D. Bylander, *Efficacious form for model pseudopotentials.* Physical Review Letters, 1982. **48**(20): p. 1425.
39. Pickard, C.J. and F. Mauri, *All-electron magnetic response with pseudopotentials: NMR chemical shifts.* Physical Review B, 2001. **63**(24): p. 245101.
40. Ding, L., et al., *Effective ion sieving with Ti 3 C 2 T x MXene membranes for production of drinking water from seawater.* Nature Sustainability, 2020. **3**(4): p. 296-302.
41. Eda, G., et al., *Photoluminescence from chemically exfoliated MoS2.* Nano letters, 2011. **11**(12): p. 5111-5116.
42. Creemers, A.F. and J. Lugtenburg, *The preparation of all-trans uniformly 13C-labeled retinal via a modular total organic synthetic strategy. Emerging central contribution of organic synthesis toward the structure and function study with atomic resolution in protein research.* Journal of the American Chemical Society, 2002. **124**(22): p. 6324-6334.
43. Duthaler, R.O., H. Förster, and J.D. Roberts, *Nitrogen-15 and carbon-13 nuclear magnetic resonance spectra of diazo and diazonium compounds.* Journal of the American Chemical Society, 1978. **100**(16): p. 4974-4979.
44. Nightingale Jr, E., *Phenomenological theory of ion solvation. Effective radii of hydrated ions.* The Journal of Physical Chemistry, 1959. **63**(9): p. 1381-1387.
45. Teychené, J., et al., *Investigation of ions hydration using molecular modeling.* Journal of Molecular Liquids, 2019. **294**: p. 111394.
46. Wei, Y., et al., *Declining flux and narrowing nanochannels under wrinkles of compacted graphene oxide nanofiltration membranes.* Carbon, 2016. **108**: p. 568-

575.

47. Morelos-Gomez, A., et al., *Effective NaCl and dye rejection of hybrid graphene oxide/graphene layered membranes.* Nature nanotechnology, 2017. **12**(11): p. 1083-1088.
48. Hoenig, E., et al., *Controlling the Structure of MoS2 Membranes via Covalent Functionalization with Molecular Spacers.* Nano Letters, 2020. **20**(11): p. 7844-7851.
49. Chekli, L., et al., *A comprehensive review of hybrid forward osmosis systems: Performance, applications and future prospects.* Journal of Membrane Science, 2016. **497**: p. 430-449.
50. Wang, K.Y., T.-S. Chung, and J.-J. Qin, *Polybenzimidazole (PBI) nanofiltration hollow fiber membranes applied in forward osmosis process.* Journal of Membrane Science, 2007. **300**(1-2): p. 6-12.
51. Lu, X., et al., *Relating selectivity and separation performance of lamellar two-dimensional molybdenum disulfide (MoS2) membranes to nanosheet stacking behavior.* Environmental science & technology, 2020. **54**(15): p. 9640-9651.
52. Huang, K., et al., *Cation-controlled wetting properties of vermiculite membranes and its promise for fouling resistant oil–water separation.* Nature communications, 2020. **11**(1): p. 1-10.
53. Alturki, A., et al., *Performance of a novel osmotic membrane bioreactor (OMBR) system: flux stability and removal of trace organics.* Bioresource technology, 2012. **113**: p. 201-206.
54. Stańczyk, M., A. Boruń, and M. Jóźwiak, *Conductance studies of aqueous solutions of sodium salts of selected benzoic acid derivatives at temperatures from (288.15 to 318.15) K.* Journal of Molecular Liquids, 2019. **278**: p. 247-252.
55. Wang, X.-m., et al., *Performance of nanofiltration membrane in rejecting trace organic compounds: Experiment and model prediction.* Desalination, 2015. **370**: p. 7-16.
56. Maitani, Y., et al., *Ionic size and behavior of diclofenac salts in water and*

ethanol/water mixtures by conductivity at 25° C. Journal of pharmaceutical sciences, 1993. **82**(12): p. 1245-1249.

57. Kang, B., et al., *Catalytically active supramolecular porphyrin boxes: acceleration of the methanolysis of phosphate triesters via a combination of increased local nucleophilicity and reactant encapsulation.* Chemical Science, 2012. **3**(6): p. 1938-1944.
58. Andreeva, D.V., et al., *Two-dimensional adaptive membranes with programmable water and ionic channels.* Nature Nanotechnology, 2021. **16**(2): p. 174-180.
59. Al-aibi, S., et al., *Evaluation of draw solution effectiveness in a forward osmosis process.* Desalination and Water Treatment, 2016. **57**(29): p. 13425-13432.
60. Li, G., et al., *Cellulose triacetate forward osmosis membranes: preparation and characterization.* Desalination and water treatment, 2013. **51**(13-15): p. 2656-2665.
61. Zou, S. and Z. He, *Enhancing wastewater reuse by forward osmosis with self-diluted commercial fertilizers as draw solutes.* Water research, 2016. **99**: p. 235-243.
62. Lambrechts, R. and M. Sheldon, *Performance and energy consumption evaluation of a fertiliser drawn forward osmosis (FDFO) system for water recovery from brackish water.* Desalination, 2019. **456**: p. 64-73.
63. Al-Karaghouli, A. and L.L. Kazmerski, *Energy consumption and water production cost of conventional and renewable-energy-powered desalination processes.* Renewable and Sustainable Energy Reviews, 2013. **24**: p. 343-356.
64. Shannon, M.A., et al., *Science and technology for water purification in the coming decades.* Nanoscience and technology: a collection of reviews from nature Journals, 2010: p. 337-346.
65. Qin, M. and Z. He, *Self-supplied ammonium bicarbonate draw solute for achieving wastewater treatment and recovery in a microbial electrolysis cell-forward osmosis-coupled system.* Environmental Science & Technology Letters, 2014. **1**(10): p. 437-441.
66. Hirunpinyopas, W., et al., *Tunable charge/size selective ion sieving with ultrahigh*

water permeance through laminar graphene membranes. Carbon, 2020. **156**: p. 119-129.

67. Lu, Z., et al., *Self-crosslinked MXene (Ti3C2T x) membranes with good antiswelling property for monovalent metal ion exclusion.* ACS nano, 2019. **13**(9): p. 10535-10544.
68. Wang, L., et al., *Sandwich layered double hydroxides with graphene oxide for enhanced water desalination.* Science China Materials, 2022. **65**(3): p. 803-810.
69. Gong, D., et al., *Interfacial Ions Sieving for Ultrafast and Complete Desalination through 2D Nanochannel Defined Graphene Composite Membranes.* ACS nano, 2021. **15**(6): p. 9871-9881.
70. Hu, W., L. Xie, and H. Zeng, *Novel sodium alginate-assisted MXene nanosheets for ultrahigh rejection of multiple cations and dyes.* Journal of Colloid and Interface Science, 2020. **568**: p. 36-45.
71. Hirunpinyopas, W., et al., *Desalination and nanofiltration through functionalized laminar MoS2 membranes.* ACS nano, 2017. **11**(11): p. 11082-11090.
72. Jian, M., et al., *Ultrathin water-stable metal-organic framework membranes for ion separation.* Science advances, 2020. **6**(23): p. eaay3998.
73. Kresse, G. and J. Furthmüller, *Efficiency of ab-initio total energy calculations for metals and semiconductors using a plane-wave basis set.* Computational materials science, 1996. **6**(1): p. 15-50.
74. Kresse, G. and J. Furthmüller, *Efficient iterative schemes for ab initio total-energy calculations using a plane-wave basis set.* Physical review B, 1996. **54**(16): p. 11169.
75. Grimme, S., et al., *A consistent and accurate ab initio parametrization of density functional dispersion correction (DFT-D) for the 94 elements H-Pu.* The Journal of chemical physics, 2010. **132**(15): p. 154104.

Chapter 3: Cation intercalated clay membrane for water purification and organic solvent nanofiltration

*Upon delving into the intricacies of 2D MoS_2 nanosheets in **Chapter 2**, the focus now transitions to another versatile, cost-effective, and eco-friendly 2D material: clay. Despite the significant strides made with MoS_2 nanosheets, their preparation processes are complex and involve the use of n-butyllithium, a flammable substance with an explosion hazard upon contact with water. In contrast, clay, a natural mineral widely dispersed on earth, offers a safer and more economical alternative for membrane synthesis. The production of 2D clay nanosheets avoids the use of harmful reagents, offering advantages in terms of environmental impact and sustainability.*

***Chapter 3** dives deeper into the exploration of 2D clay nanosheets, particularly focusing on their potential for organic solvent nanofiltration (OSN). By adopting a range of innovative strategies, such as intercalating cations into the interlayer of clay nanosheets, we aim to enhance the structural stability and molecular sieving ability of clay membranes. The transition to clay membranes marks an exciting step towards safer, more sustainable, and cost-effective approaches in the design and application of 2D material membranes, further expanding the breadth of this research in the field of separation technologies.*

2D Laminated Clay Membranes with Superfast Solvent Transport for Molecular Separation

3.1 Abstract

Membrane separation technology, recognized for its high efficiency and environmental compatibility, has been extensively applied in the domain of substance purification, particularly achieving considerable success in water treatment. Nevertheless, its application in organic solvent nanofiltration (OSN) has been stymied by the limited permeation rates of existing membranes. In this study, we engineered two-dimensional (2D) clay nanolaminated membranes, derived from the stacking of exfoliated vermiculite nanosheets, as a potential solution for OSN. The as-synthesized clay membrane displayed limited stability in both water and solvents, necessitating further enhancements. To enhance the membrane's stability and sieving capabilities, cations of various valences (K^+, Na^+, Mg^{2+}, Ca^{2+}, Fe^{3+}) were intercalated into the interlayer of the clay nanosheets. The resulting cation-treated clay membranes displayed considerable enhancement in structural stability in both aqueous and organic phases. Subsequently, the solvent transport behavior and separation performance of these clay membranes were evaluated. Notably, the Fe-clay variant demonstrated superior fixation properties, resulting in enhanced sieving performance, including a rejection rate of over 95% for Methyl Orange (MO, 327.33 Da) and a methanol permeation rate of approximately 165 LMHB. Impressively, these membranes demonstrated enduring operational stability over 100 hours under tangential cross-flow filtration conditions. The findings of this study pave the way for the practical applications of 2D laminated clay membranes in OSN.

3.2 Introduction

Membrane separation technology has emerged as an environmentally friendly, performance-effective, energy-efficient, and easy-to-operate method, finding widespread use in water treatment applications such as sewage purification and seawater desalination [1, 2]. Ingenious design of advanced materials, such as thin-film

composite membranes, has facilitated their extensive use in the industry for aqueous separation [3, 4]. Despite these advances, the application of membrane technology for organic solvent separation remains limited, primarily due to the limited chemical stability (swelling) exhibited by most polymer membranes in organic solvents. Furthermore, low permeation rates and aging issues also hinder the widespread adoption of this technology [5-9]. Simultaneously, the rapidly expanding pharmaceutical and petrochemical industries are driving a strong demand for organic solvent treatment [10-12]. Consequently, there is an urgent need to develop novel membranes that can address this technological gap and enhance the performance of membrane separation processes in organic solvents.

Two-dimensional (2D) materials, characterized by atomic thickness in one direction and vast lateral dimensions in the other two, have garnered significant interest due to their exceptional properties and potential applications in various fields such as catalysis [13], electronic conduction [14], energy storage and conversion [15], and, most importantly, membrane separation [16, 17]. Nanolaminated membranes, created by stacking 2D nanosheets, form slit-type nanochannels between adjacent nanosheets, facilitating the superfast transport of molecules with unexpected nanofluidic behavior [18, 19]. Under nanoscale spatial confinement, desired separation performance can be achieved through size sieving. Widely researched graphene oxide (GO) laminated membranes have shown great promise for separation applications [20-22]; however, they exhibit impermeability for organic solvents [23, 24]. With the rapid development of 2D materials, an increasing number of 2D nanosheets have become available and are utilized as building blocks for the construction of the nanolaminates [25]. MXene and transition metal dichalcogenides (TMDs) laminar membranes demonstrate unparalleled flux for organic solvents and moderate rejection for larger dye molecules, suggesting some potential of 2D laminar membranes for organic solvent nanofiltration (OSN) [26-29]. Nevertheless, the production of these 2D nanosheets is complex, costly, and involves the use of hazardous reagents and strong acids, which limit membrane applications and are unsustainable [30, 31]. Therefore, there is an urgent need to explore

alternative 2D nanosheets that are low-cost, easy to produce, and suitable for OSN applications.

Vermiculite clays, a natural mineral with a layered structure, can be easily exfoliated into 2D nanosheets using a simple ion exchange method [32-34]. Owing to the strong chemical and mechanical stability of 2D clay nanosheets, they have garnered significant research interest as building blocks for 2D laminar membranes. Seminal work by Tian et al. demonstrated the suitability of 2D laminated clay membranes for OSN, opening a path towards low-cost 2D membrane construction for highly efficient separation applications [35]. However, similarly to other 2D laminar membranes based on GO and Mxenes, the high affinity of clay nanosheets for polar molecules can lead to increased interlayer spacing due to swelling, which results in the degradation of sieving performance. A simple method proposed by Fang's team consists in coordinating adjacent GO nanosheets by employing cations using electrostatic attractions and specific adhesion interactions [36]. This strategy was also proven to be suitable for MXene membranes [37]. Despite these advances, our understanding of 2D clay membrane regulation has remained limited. This motivated us to leverage the advantages of 2D clay membranes while enhancing their structural stability to extend their sieving performance in organic phases.

In this work, we exfoliated vermiculite bulk into single layers and reassembled them into 2D nanolaminated membranes. We investigated the organic solvent transport behavior and separation performance for dye molecules. The rejection results of pristine clay membranes indicated poor retention of dye molecules due to increased interlayer spacing, suggesting that these membranes may not be suitable for organic solvent purification. To enhance the stability of interlayer space and confer effective molecular sieving ability to the nanolaminates, different valence cations (K^+, Na^+, Mg^{2+}, Ca^{2+}, and Fe^{3+}) were employed to intercalate into the interlayer of clay nanosheets. We identified that cation-treated clay membranes, termed cation-clay, exhibited limited swelling and increased membrane structural stability in both aqueous and organic phases. Among these, Fe-clay displayed the strongest resistance against swelling, resulting in superior

sieving performance with a rejection rate of over 95% for Methyl Orange (MO, 327.33 Da) and a methanol permeation rate of approximately 165 LMHB. Furthermore, we demonstrated over 100 hours of constant operation under tangential cross-flow filtration conditions with a membrane size of 10 cm^2, paving the way for practical applications of nanolaminated organic solvent nanofiltration membranes.

3.3 Material and Methods

3.3.1 Materials

The vermiculite clay bulk used in this study was sourced from the Agasthyapura area, without any thermal expansion treatment. The Nylon support, chloride salts, and organic dyes, with the exception of 5,10,15,20-(tetra-N-methyl-4-pyridyl) porphyrin tetrachloride (PP), were procured from Sigma Aldrich. PP was purchased from PorphyChem, a specialized provider of porphyrin-based compounds. The organic solvents utilized in the research were obtained from Alfa Aesar. All chemicals were used as received, without any further purification or modification.

3.3.2 Synthesize of single-layer vermiculate nanosheets

The monolayer clay nanosheets were prepared through a series of exfoliation and ion-exchange processes. Firstly, 1g of bulk vermiculite clay crystals were added to 200 mL of saturated NaCl solution, refluxing for 24 hours under vigorous stirring to obtain Na-exchanged clay. The Na-exchanged clay was then collected by filtration and washed extensively with deionized water (DI) to remove residual NaCl. Subsequently, the collected clay was dispersed in a 2 M LiCl solution for Na^+ to Li^+ ion exchange, refluxing and stirring for 24 hours. The solution was filtered, and the collected Li-intercalated clay was washed thoroughly with DI water to eliminate any remaining Li ions. The filtered product was then dispersed in water and stirred at 1000 rpm for 24 hours to enable hydraulic shear peeling. After that, this solution was sonicated for 30 minutes to facilitate the exfoliation process. Finally, the single-layer clay nanosheets were collected from the supernatant after mild centrifugation at 3000 rpm for 30

minutes.

3.3.3 Preparation of pristine and cation-treated clay membranes

The pristine clay membranes were fabricated by pressure-assisted filtration of diluted single-layer nanosheet solutions. Specifically, a certain volume of clay solution was filtered onto a 220 nm pore-sized Nylon support using 1 bar of pressure. To prepare cation-treated clay membranes, 10 mL of different chloride salts (KCl, NaCl, $CaCl_2$, $MgCl_2$, and $FeCl_3$) at a concentration of 0.25 M were added to the pristine membranes. After waiting for 3 hours to allow for ion diffusion and cross-linking, a 1-bar pressure was applied to force the salt solution through the membrane, promoting ion traversal and achieving complete cation cross-linked nanochannels. Next, 50 mL of DI water was added and the membranes was subjected to a pressure of 1 bar to wash away the excess of ions. This process resulted in the formation of cation-treated clay membranes.

3.3.4 Solvent permeation through nanolaminated clay membranes

Nine types of organic solvents, including Hexane, Toluene, Isopropanol (IPA), Dimethyl sulfoxide (DMSO), Ethanol, Tetrahydrofuran (THF), Acetone, Methanol, and Acetonitrile, were used to examine the permeation behavior through 1-µm-thick pristine and Fe-clay membranes using a reverse osmosis filtration cell. In this setup, the organic solvent was added, and a pressure of 1 bar was applied as a driving force for the solvent to cross the membranes. The weight of the passed solvent was automatically recorded by a balance and used to evaluate the flux. The solvent permeance (liter m^{-2} $hour^{-1}$ bar^{-1}) was calculated using the following equation:

$$P_s = \frac{W}{\Delta p\ A\ t\ \rho} \qquad (3-1)$$

where W represents the collected solvent mass (kg), Δp denotes the hydraulic pressure (bar), A is the effective membrane area (m^2), t stands for the permeation time (h), and ρ refers to the solvent density (kg/L). In our dead-end configuration, membranes with an effective area of 13.8 cm^2 were used in for measurements. Additionally, the water permeance was evaluated only for Fe-Clay membranes, as obtaining this measurement

for pristine membranes is challenging due to their rapid redispersion in water.

3.3.5 Solvent purifications performance evaluation

The rejection capacity of clay membranes was evaluated using a high-pressure stirred cell under a dead-end configuration. Eight different organic dyes were dissolved in water or methanol to form feed solutions with a concentration of 25 ppm, which were then filtered through a 500-nm-thick clay membrane at 1-bar pressure. Due to the poor solubility of NP and GX in methanol, only six of dyes were measured using methanol feed solutions. The rejection rates of clay membranes for the dyes, R (%), were calculated using the following equation:

$$\mathrm{R}(\%) = \left(1 - \frac{C_p}{C_f}\right) \times 100 \qquad (3-2)$$

where C_p and C_f represent the concentration of the organic dyes in the permeate and feed solution, respectively. The concentrations of dyes in the collected solutions were quantitatively analyzed by HPLC coupled with mass spectrometry.

3.3.6 Membrane stability evaluation in a tangential cross-flow filtration cell

We utilized a tangential cross-flow filtration cell to evaluate the long-term stability of the Fe-Clay membranes under solvent permeation. Pure water or methanol solution was circulated in the system, with the Fe-Clay membranes positioned between the feed and permeate sides of the cell. A peristaltic pump ensured a consistent flow rate of 8.54 ml min^{-1} while maintaining a pressure of 1 bar. The permeated solvent was collected and weighed using balances, allowing for the calculation of flux throughout the experiment.

3.4 Characterization

3.4.1 Characterization methodology

In order to thoroughly characterize the 2D clay nanosheets and nanolaminated clay membranes, various techniques were employed. Atomic force microscopy (AFM) images were acquired using a Digital Instruments Nanoscope IV, operating in tapping

mode. Standard cantilevers were employed, featuring a spring constant of 40 N/m and a tip curvature of less than 10 nm. The Hitachi S4800 was employed to obtain scanning electron microscopy (SEM) images of nanosheets and cross-sections of membranes. To further study the atomic structure of the clay nanosheets, FEI Titan Cubed Themis microscope was used to capture aberration-corrected high-resolution (scanning) transmission electron microscopy images (HR-(S)TEM). Due to the highly sensitive nature of the flakes when exposed to the electron beam, images were done in low dose (1e/pixel) with a direct detection camera. The structural properties of the membranes were investigated using X-ray Diffraction (XRD), which was carried out on an Xpert Pro apparatus, utilizing filtered Cu Kα radiation (λ = 0.15418 nm) while operating at 40 kV and 20 mA.

3.4.2 Low magnification transmission electron microscopy (TEM) image and the selected area diffraction pattern (SADP) of clay nanosheets

To obverse the morphology and lattice structure of clay nanosheets, the low magnification TEM image and the selected area diffraction pattern (SADP) were taken. As shown in below, the size of the flakes is around 1 × 3 μm, in line with the AFM observations. The SADP, characterized by discrete white spots, demonstrates the single-crystalline nature of the clay nanosheets' basal plane. Notably, these diffraction patterns can be indexed in accordance with the vermiculite structure as reported by Mathieson A. M. and Walker G. F. (Figure 3.1c) [38], thereby confirming the congruency of the unit cell structure. Besides, the following element composition analysis further verified that.

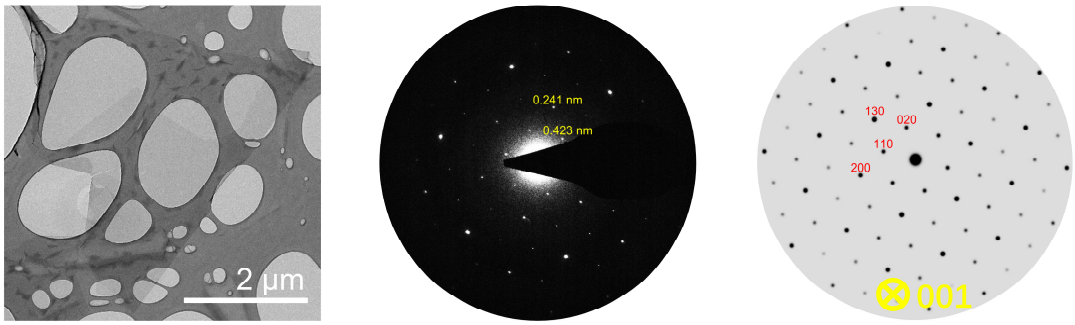

Figure 3.1 Low magnification TEM image of clay nanosheets (**a**) and the SADP (**b**) taken from the area in (**a**). Simulated electron diffraction pattern (**c**) based on the vermiculate structure reported by Mathieson A. M. and Walker G. F.

3.4.3 EDX mapping on cross-section of pristine and Fe-clay membranes

In order to confirm the successful intercalation of Fe^{3+} ions into the interlayer, energy-dispersive X-ray (EDX) mapping was conducted on the cross-section of the pristine and Fe-clay membrane for elemental analysis. These samples were prepared by Au/Pt encapsulation and further cutting by focused ion beam (FIB). As depicted below, the Fe element in the Fe-clay membranes shows even distribution, demonstrating a complete traversal of Fe throughout the membrane. As the clay nanosheets contain Fe, we performed quantitative analyses of the atom concentration of different elements. After Fe intercalation, the atomic fraction of Fe increased by a factor of 2 compared to the pristine membrane. We also noticed that the elemental composition of the pristine clay closely aligns with the data reported by Mathieson [38], exhibiting atomic fractions of 36.57 : 19.70 : 37.17 : 6.56 for Mg : Al : Si : Fe, respectively.

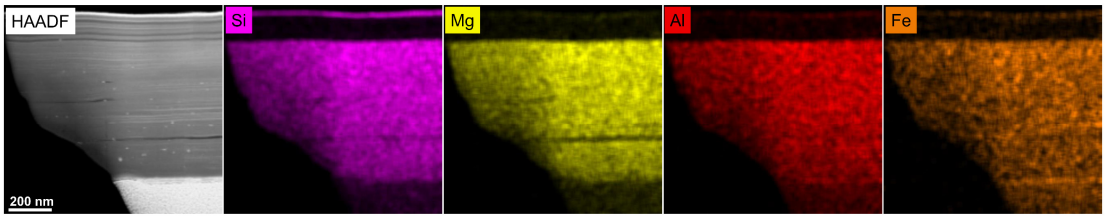

(a) Pristine clay

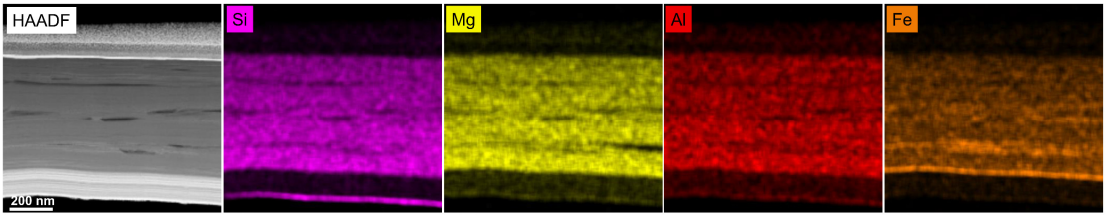

(b) Fe-clay

Figure 3.2 High-angle annular dark-field (HAADF) scanning transmission electron microscopy image of cross-sectional pristine (**a**) and Fe-clay (**b**) membrane and corresponding EDX mapping images for the elements Si, Mg, Al and Fe.

Table 3.1 Elemental distributions of pristine membrane cross-sections

Z	Element	Family	Atomic Fraction (%)	Atomic Error (%)	Mass Fraction (%)	Mass Error (%)	Fit Error (%)
12	Mg	K	35.75	3.12	30.84	2.70	0.04
13	Al	K	18.05	3.25	17.28	3.15	0.10
14	Si	K	40.30	4.96	40.18	4.96	0.05
26	Fe	K	5.90	0.90	11.69	1.70	0.13

Table 3.2 Elemental distributions of Fe-clay membrane cross-sections

Z	Element	Family	Atomic Fraction (%)	Atomic Error (%)	Mass Fraction (%)	Mass Error (%)	Fit Error (%)
12	Mg	K	32.95	2.74	26.54	2.17	0.50
13	Al	K	16.39	2.99	14.66	2.71	0.99
14	Si	K	38.01	4.84	35.38	4.74	0.55
26	Fe	K	12.65	1.80	23.42	2.97	0.28

3.4.4 Stability of pristine and Fe-clay membranes in water and DMSO

The stability of both pristine and Fe-clay membranes was tested by soaking them in water and dimethyl sulfoxide (DMSO) respectively. Free-standing pieces of each membrane (pristine an Fe-intercalated) were immersed in the respective solvents, and

the changes in membrane morphology were documented through photographs taken at different times. In the case of pristine membranes, when immersed in water, we quickly observed rifling and cracks followed by breaking into numerous small pieces, eventually disappearing completely due to the redispersion of the nanosheets. This entire process took place within a span of 20 minutes. On the other hand, the Fe-clay membrane demonstrated robust stability in water, maintaining its structural integrity for over a year. When immersed in DMSO, both the pristine and the Fe-clay membranes maintained their original aspect for a duration of 1 month.

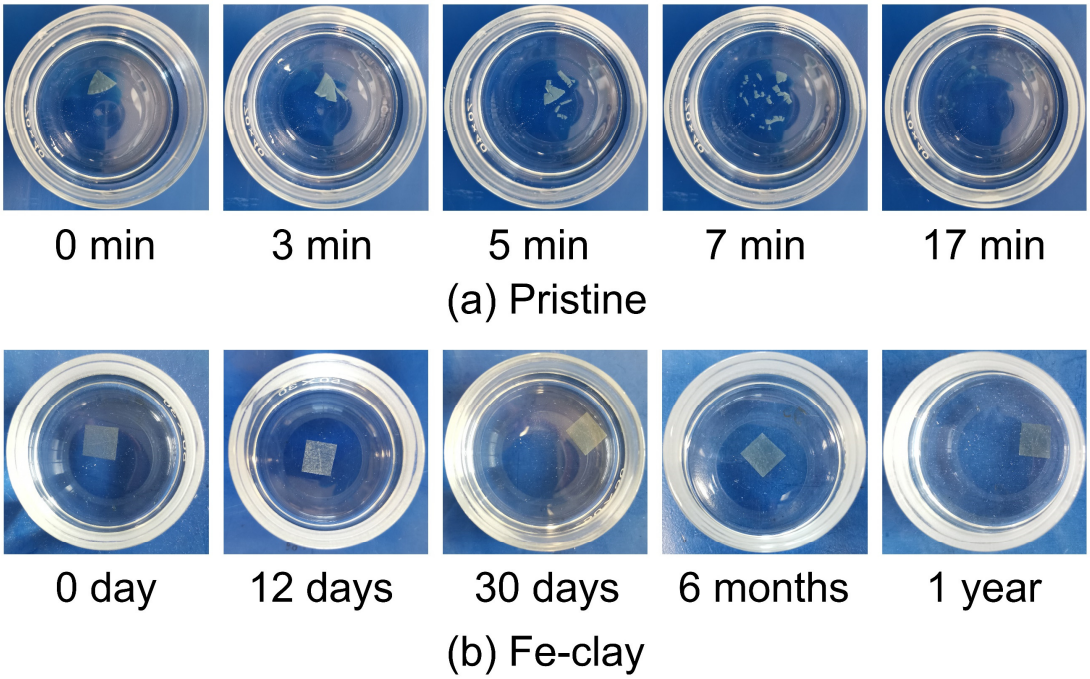

Figure 3.3 Time-dependent optical images of free-standing pristine (**a**) and Fe-clay (**b**) membranes immersed in water.

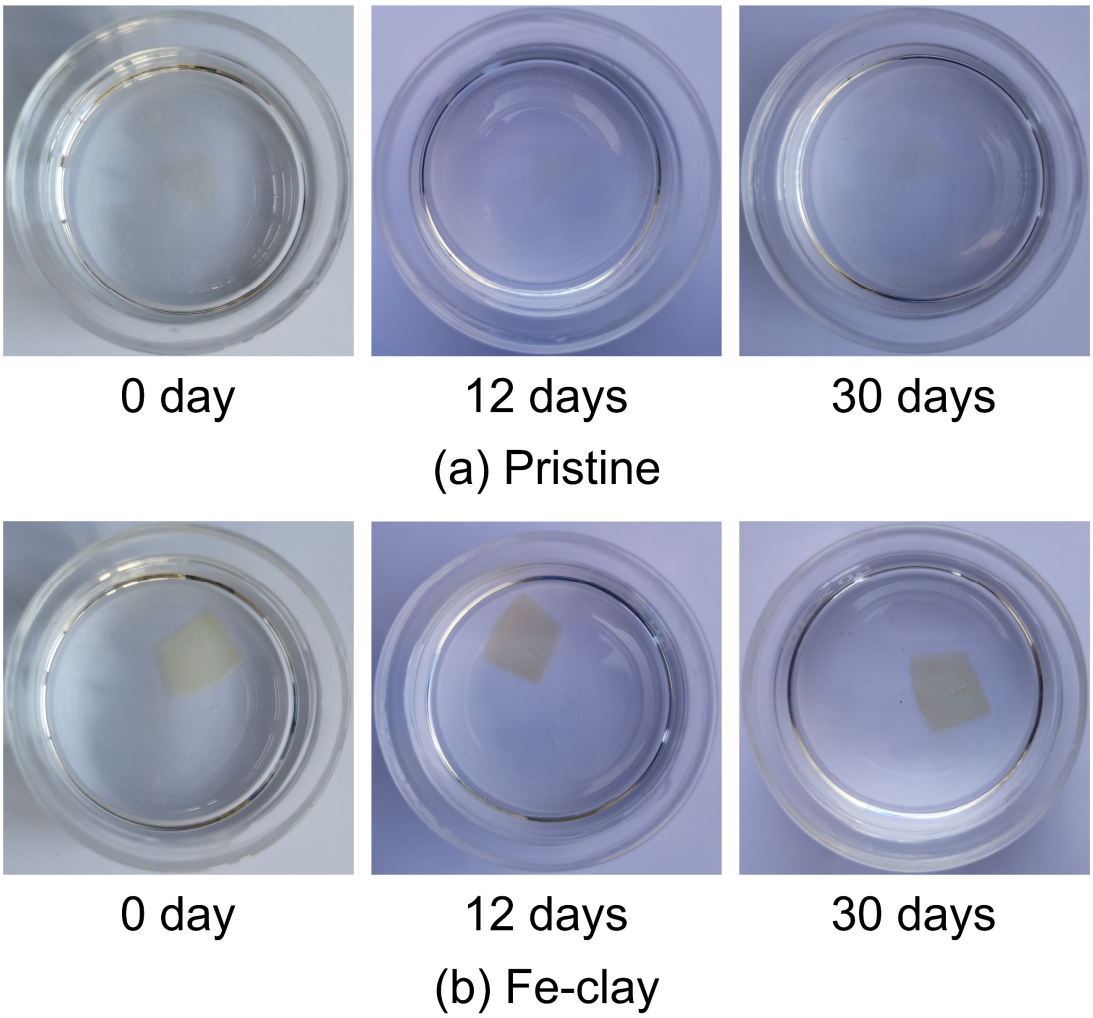

Figure 3.4 Time-dependent optical images of free-standing pristine (**a**) and Fe-clay (**b**) membranes immersed in DMSO.

3.4.5 XRD patterns of pristine and Fe-clay membranes in various organic solvent

Ex-situ XRD measurements were conducted to observe the variations in interlayer spacing and stacking order of pristine and Fe-clay membranes after immersion in different organic solvents. We recorded XRD patterns of the membranes at varying soaking durations. The capillary height and the full width at half maximum (FWHM) were plotted as a function of immersion time. The fluctuations in capillary height between adjacent nanosheets serve as an indicator of the nanochannel stability of the membrane, while the FWHM of XRD peaks can be interpreted as a reflection of the stacking order within nanolaminated membranes [39-41]. In this context, substantial changes in capillary height suggest instability in the nanochannels, while a wider

FWHM corresponds to a more disordered stacking. As evident from the XRD patterns, the capillary height of the pristine membrane increases due to swelling, and the FWHM exhibits considerable fluctuations, indicating that the nanochannels within the pristine clay membrane undergo dramatic changes, and the stacking order of the nanosheets becomes chaotic, thus reflecting poor microstructural stability. In stark contrast, swelling is markedly inhibited when the clay membranes are modified with Fe^{3+}. We found that the stacking order within the Fe-clay remains consistent during solvent soaking, indicating a significant enhancement in structural stability. For a clear comparison, we also calculated the swelling percentage, which is determined by dividing the increase in capillary height by the original capillary height (measured in dry conditions). The results are presented in Figure 3.10d (Section 3.5).

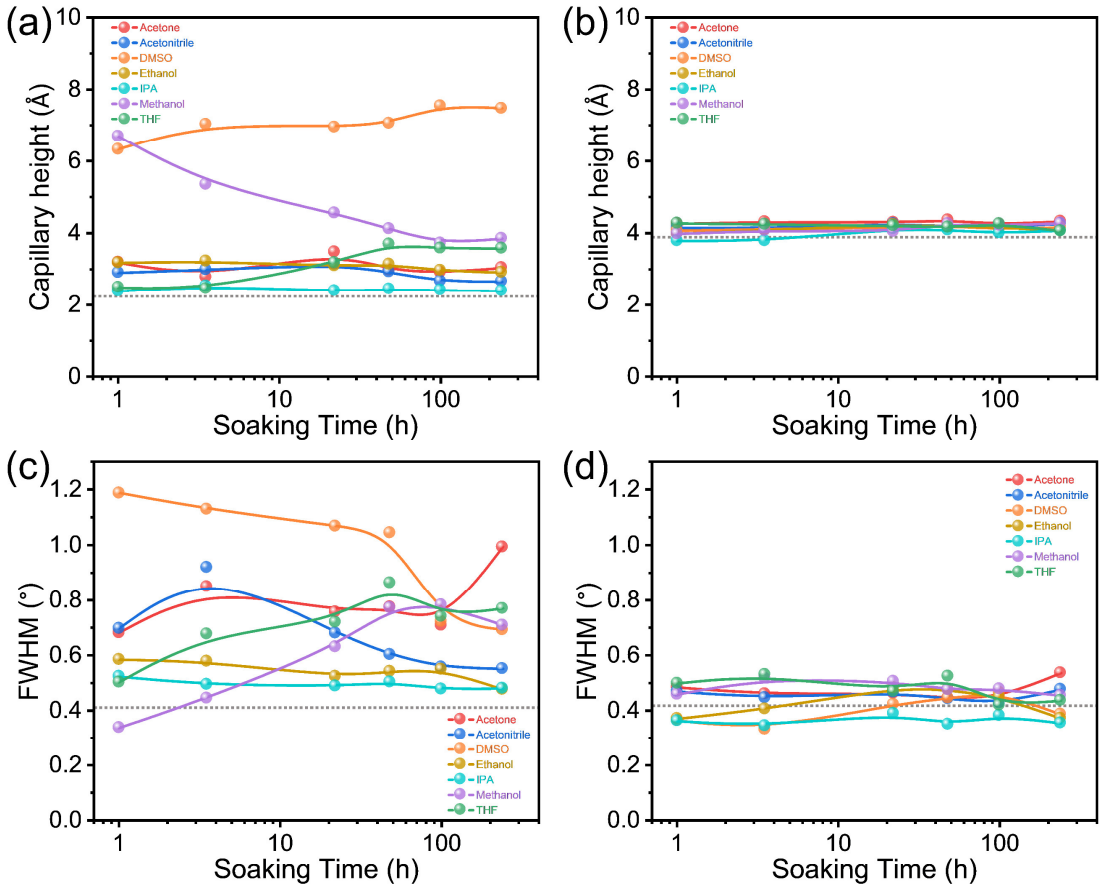

Figure 3.5 Evolution of the capillary height and FWHM of the pristine (**a** and **c**) and Fe-clay (**b** and **d**) membranes in various organic solvents with soaking time. The dotted grey line represents the values measured in dry conditions.

3.4.6 Water/DMSO contact angle of pristine and cation-treated clay membranes

To evaluate the surface wettability of the membranes, water and DMSO contact angle measurements were further evaluated. Six microliters of water or DMSO were dropped onto the membrane surface, and the morphology of the droplets was captured by a camera, as seen below. After cation intercalation, the membranes displayed more hydrophobic properties, as evidenced by an increased water contact angle (WCA). Remarkably, the Fe-clay membrane exhibited a WCA larger than 90°, presenting a reversal in surface wettability compared to the pristine membrane. While the effect on the DMSO contact angle (DCA) after cation intercalation was less pronounced. But the membrane surface still experienced a significant transition from superhydrophilicity to a measurable DCA value. As observed, DMSO quickly spreads out on the pristine membrane surface, resulting in a near-zero contact angle.

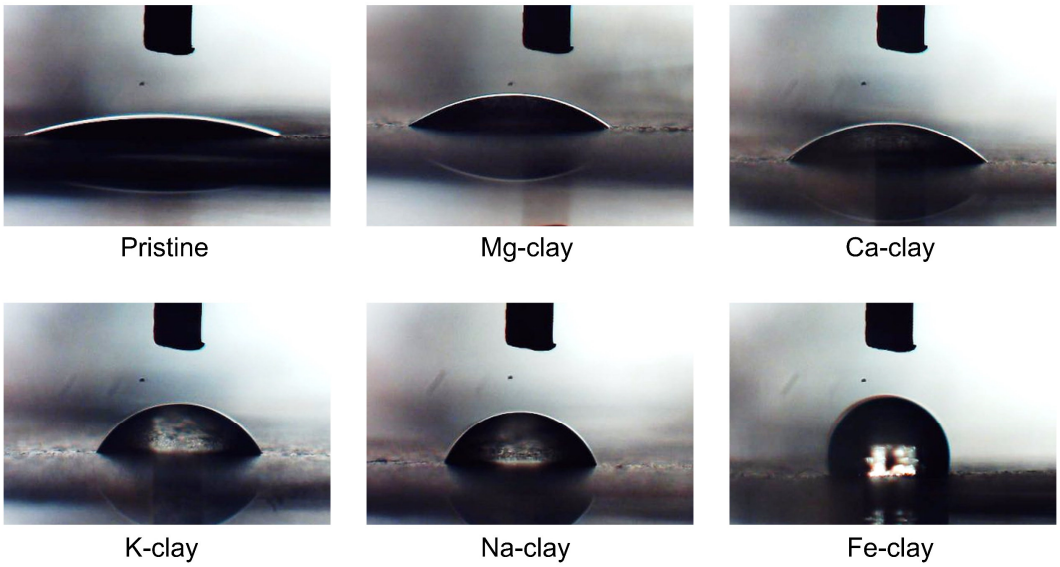

Figure 3.6 Optical photos of a water droplet on the pristine and cation-treated clay membranes in dry condition.

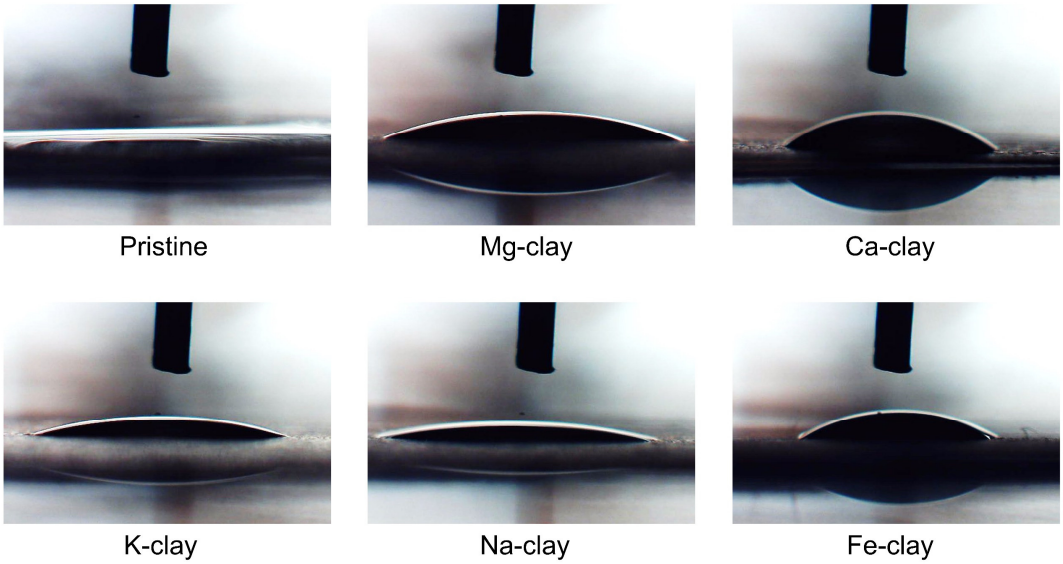

Figure 3.7 Optical photos of a DMSO droplet on the pristine and cation-treated clay membranes in dry condition.

3.4.7 Zeta potential of pristine clay nanosheets

To further characterize the pristine clay nanosheets, we evaluated their zeta potential using a Particle Size Analyzer model Litesizer 500 (Anton Paar). This device operates based on the principle of electrophoretic light scattering (ELS). Performed at neutral pH, the vermiculite suspension demonstrated a zeta potential of -57.7 ± 2.6 mV. This value indicates that the single-layer clay nanosheets possess a negatively charged nature.

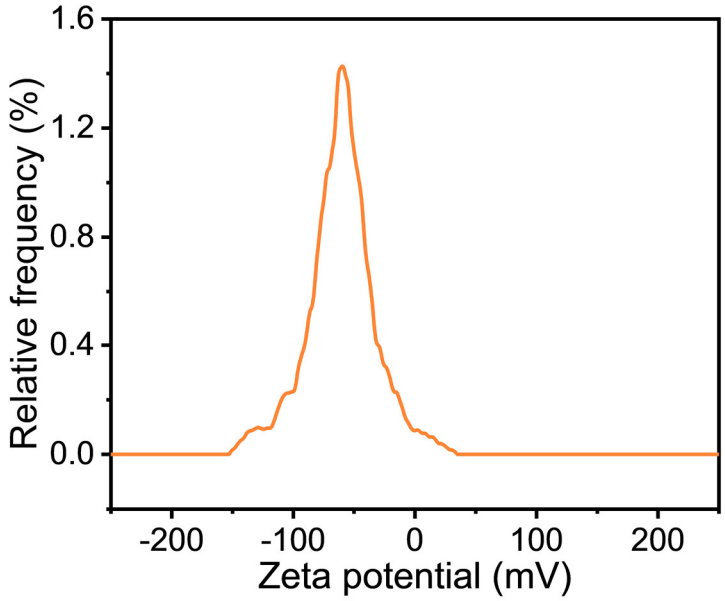

Figure 3.8 Zeta potential of pristine clay nanosheets measured under neutral pH.

3.5 Results and discussion

3.5.1 Characterization of nanolaminated clay membranes

Single-layer vermiculite nanosheets was first obtained through exfoliation of bulk vermiculite using Na^+ and Li^+ exchange methods and subsequent collection via centrifugation. The single-layer nature of clay nanosheets was demonstrated by atomic force microscopy (AFM) with a thickness of nearly 2 nm (Figure 3.9a, height profile), attributable to the strong water adsorbent layer. The obtained nanosheets exhibited a micrometer-sized lateral surface (Figure 3.9a). High-resolution transmission electron microscopy (HRTEM) was employed to characterize the nanosheets, revealing a lattice length of ~0.52 nm as determined by fast Fourier transform (FFT) calculation, indicating excellent crystallinity of the nanosheets (Figure 3.9b). Using a simple pressure-assisted filtration process, the clay nanosheets were stacked into nanolaminate membranes (called hereafter pristine membranes) on porous substrates. The ordered laminar stacking of clay membranes was confirmed by a clear interstitial structure observed in scanning electron microscopy (SEM) cross-sectional views (Figure 3.9c). Cation-treated clay membranes were prepared by further adding cation solutions to the pristine membrane, allowing cations to diffuse transmembrane. Some cations resided in the interlayer due to electrostatic attraction, acting as cross-linking agents to fix the interlayer space. The excess of free cations was removed through extensive washing with water. The cation-treated membranes exhibited strong mechanical properties, as evidenced by their ability to be casually bent (Figure 3.9d & 3.9e). X-ray diffraction (XRD), which is a powerful tool for characterizing 2D laminar membranes [39, 42], was employed to evaluate the interlayer spacing of 2D clay membranes. As shown in Figure 3.9f, pristine membranes exhibited an interlayer space of 1.21 nm. After cation intercalation, all interlayer spaces expanded due to the volume of the ions themselves, except for K-clay, which showed a slight shrinkage in interlayer space, which could be attributed to the intercalation of K ions in the atomic vacancies of the nanosheets. Furthermore, HRTEM cross-sectional views of pristine and Fe-clay membranes were captured (Figure 3.9g & h). The average interlayer space of the pristine membrane was

approximately 1.09 nm, while Fe-clay displayed an increased interlayer space with an average of 0.16 nm, consistent with the XRD results.

The structural stability of 2D clay membranes in both aqueous and organic phases was systematically investigated. We found that the pristine membrane quickly redispersed within 20 minutes when immersed in water, indicating extreme instability for aqueous applications. In contrast, the Fe-clay membrane remained stable when soaked in water for one year, with no visible changes, demonstrating enhanced aqueous stability (Figure 3.3). Both the pristine and Fe-clay membranes maintained structural integrity in dimethyl sulfoxide (DMSO) without dispersion (Figure 3.4). For quantitative comparison, XRD was employed to record changes in the inner interlayer space. As shown in Figure 3.10a, the interlayer space of the wet pristine membrane reaches 1.5 nm due to the existence of the hydration layer. Although the pristine membrane maintained structural integrity in DMSO, the interlayer space exhibited a larger increment to 1.69 nm as DMSO molecules have a greater volume than water molecules. In stark contrast, the Fe-clay membrane shows a constant interlayer space in both water and DMSO, highlighting the crucial role of ions and their valence in improving membrane stability.

To get a better understanding of the effect of intercalated ions on membrane structures, we monitored the changes of the interlayer space for different intercalated clay membranes after immersing in water (Figure 3.10b) and DMSO (Figure 3.10c). These investigations were carried out using ex-situ XRD. Multivalent cation-treated clay membranes demonstrated excellent retention of the interlayer space, highlighting their resistance against swelling in water. We found that monovalent cations exhibited a weaker role in space fixation as evidenced by the larger increase of the interlayer space. Compared to the rapidly increasing interlayer space of Na-clay membranes, K-clay maintained a stable space for over 50 hours, indicating better stability than Na^+ in water. However, all intercalated membranes, with the exception of ferrous clay, experienced a significant increase in interlayer space within a short time, suggesting a low capacity for interlayer space regulation in DMSO. Notably, Fe-clay maintained a

robust interlayer space for over two months, implying durable applications in organic phases. Consequently, we primarily focused on investigating Fe-clay membranes for separation applications in the following sections, as they exhibited lasting stability in both aqueous and organic phases. Additionally, we observed that cation intercalation in clay membranes altered surface wettability (Figure 3.6 & 3.7), indicating potential for extension to other applications, such as oil/water separation as previously reported by Nair's group [33].

We further explored the structural changes of pristine and Fe-clay membranes in various organic solvents. As shown in Figure 3.10d, pristine membranes underwent dramatic swelling, with the interlayer space expanding by 8% to 215% compared to dry membranes. Among these solvents, IPA induced the mildest increase. In contrast, Fe-clay membranes exhibited limited swelling in all selected solvents. Even for harsh conditions, such as using acetone, the maximum swelling was only 10%, emphasizing the remarkably robust nanochannel formation when Fe^{3+} resided in the clay interlayer space. These findings evoke significant interest for separation operations.

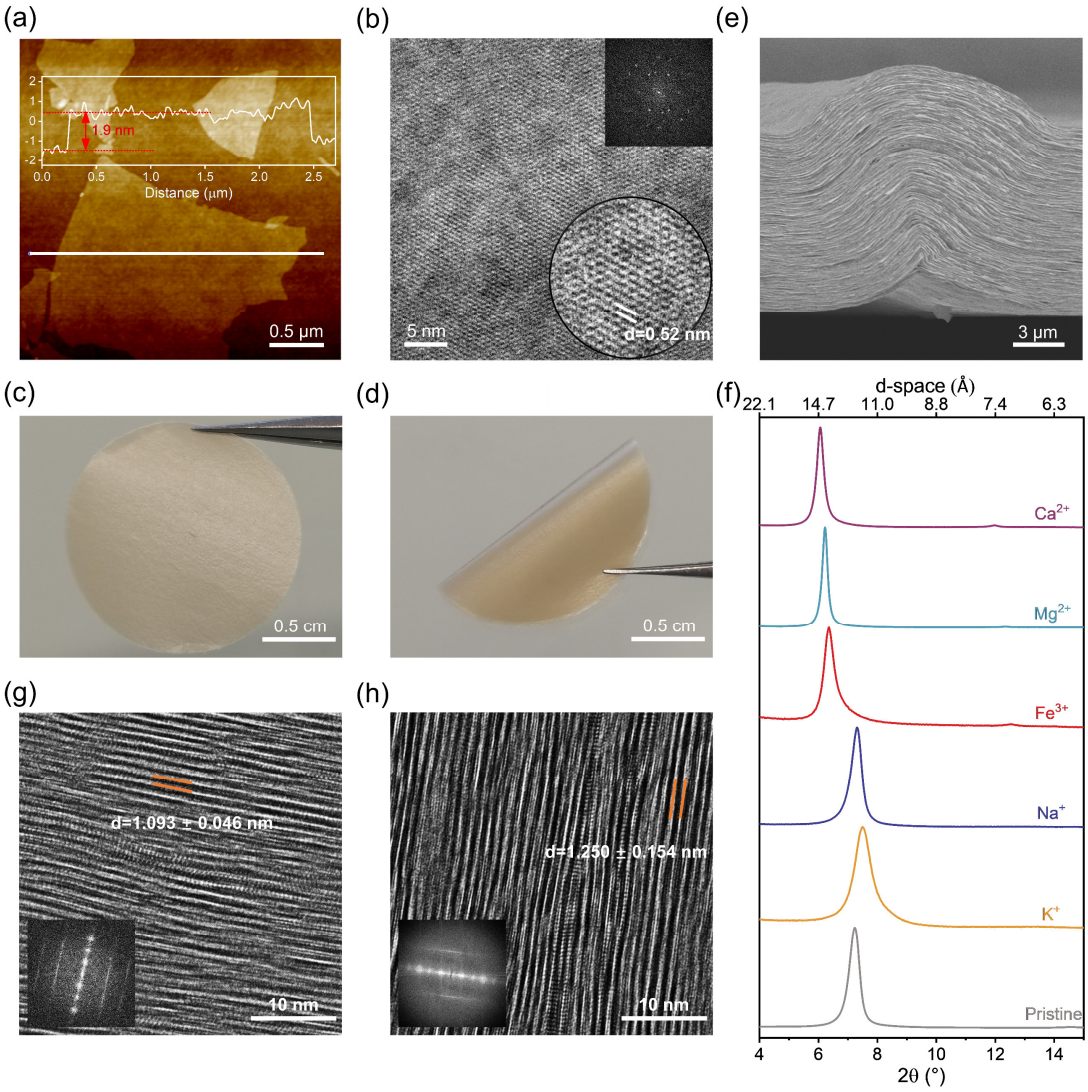

Figure 3.9 Characterization of vermiculite clay nanosheets and their laminar membranes. a, AFM image of exfoliated clay nanosheets. The inset shows the height profiles taken along the white solid line. **b**, HRTEM image of a single-layer clay nanosheets. The top inset presents the Fast Fourier Transform (FFT) pattern of the image, while the bottom inset magnifies the lattice fringes. **c**, SEM cross-sectional view of the laminated clay membrane. **d**, An optical photograph of a free-standing K-clay membrane with a thickness of 5 μm. **e**, Photograph of the K-clay membrane bent with tweezers, demonstrating its resilience and flexibility. **f**, XRD patterns of pristine and ion-treated clay membranes with a thickness of 1 μm. The membranes were vacuum dried for 24 h before measurement. **g**, HRTEM images of the cross-sections of pristine (g) and Fe-clay (h) membranes. The bright regions represent the single-layer clay nanosheets. Inset: the FFT pattern of the image. The d value is calculated from the FFT.

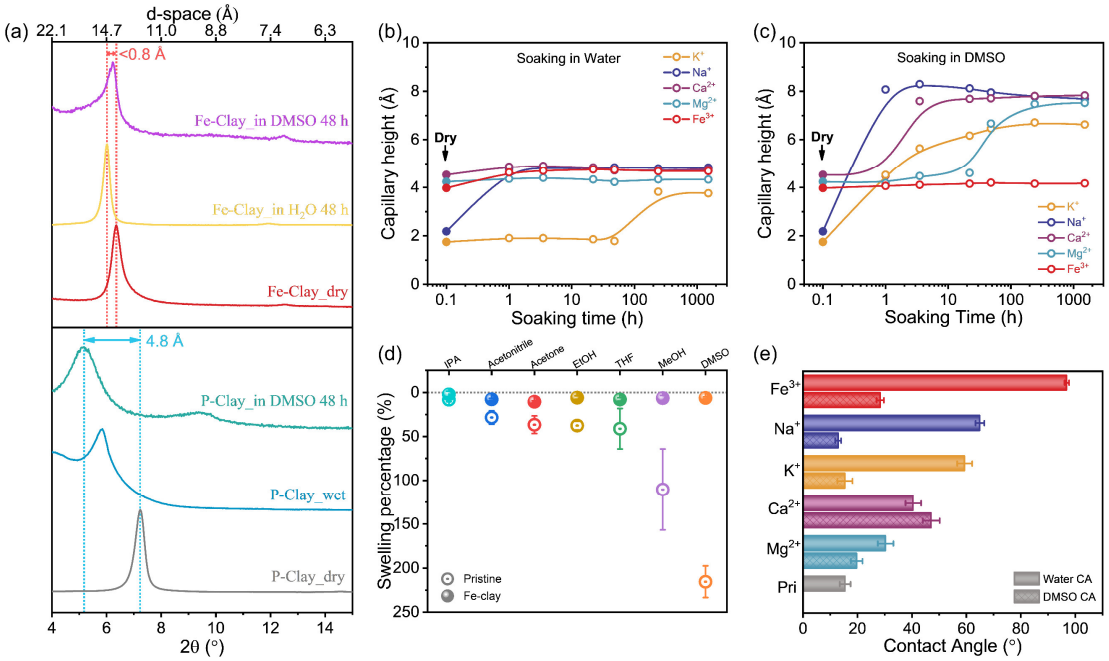

Figure 3.10 Physicochemical properties of laminar clay membranes with a thickness of 1 µm. a, XRD patterns of pristine and Fe-clay membranes before and after immersion in both aqueous and organic solvents. The as-prepared wet pristine membrane was measured instead of water-soaked membrane, as the latter rapidly deteriorates upon contact with water. **b-c**, Evolution of capillary height of different ion treated clay membranes in water (**b**) and DMSO (**c**) with soaking time. The solid dots correspond to the capillary height measured under dry conditions. **d**, Swelling percentage of pristine (hollow circles) and Fe-clay (solid spheres) membrane in various organic solvents under soaking 240 hours. **e**, Water and DMSO contact angles of pristine and ion-treated clay membranes. The DMSO droplets immediately spread out on the pristine membrane surface, resulting in a value close to 0°. The data are expressed as mean values, with error bars representing standard deviations (SD) based on three independent measurements.

3.5.2 Solvent permeation through 2D clay membrane

The permeation behavior of solvents through the nanolaminated clay membranes was initially investigated using a variety of solvents characterized by varying polarities and molecular sizes (Table 3.3). As shown in Figure 3.11a, non-polar solvents like toluene and hexane do not permeate pristine clay membranes. In contrast, polar solvents quickly permeated under pressure, exhibiting outstanding flux. In particular, acetonitrile displayed the highest permeation rate, exceeding 650 LMHB. Similarly, Fe-clay membranes were also impermeable to non-polar molecules (Figure 3.11b).

Notably, Fe-clay membranes with the same thickness as for pristine membranes (1 μm) exhibited a reduced solvent permeance by ~ 75%. The reasons for the decreased flux stem from two aspects: 1) Due to swelling, the interlayer space in pristine membranes is larger than in Fe-clay membranes. The enlarged space facilitates solvent diffusion due to the looser size constraints of the nanochannel walls. 2) Besides interlayer space, another important factor is the stacking order of the laminated membranes [39, 40]. This parameter is often overlooked but turns out to be vital for transport regulation. To evidence this phenomenon, we recorded the XRD patterns of pristine and Fe-clay membranes after solvent permeation. The nanosheets' arrangement in pristine membranes suffered from dramatic adjustment due to weak interactions between adjacent nanosheets as demonstrated by the enlarged FWHM (Figure 3.5). A larger FWHM represents a more disordered stacking structure, creating more shortcuts for solvent permeation and leading to higher flux. After undergoing the tortuous transport of solvent molecules, the nanochannels of the pristine membrane expanded and could not return to their original size, even in dry conditions (Figure 3.11c). In contrast, Fe-clay not only maintained its interlayer space but also preserved its stacking order during solvent permeation. The robust nanochannels of Fe-clay membranes would not only benefit solvent transport but more importantly enhance sieving performance.

Moreover, we discovered that the organic polar molecules' permeance follows a phenomenological transport model, which is observed in porous inorganic membranes [43]. The permeance (Ps) is correlated to its physical parameters: $P_s = \frac{A}{\eta \times d_{kin}^2}$, where A is a proportionality constant determined by membrane structural parameters, η denotes the solvent viscosity (Pa·s), and d_{kin} is the solvent kinetic diameter (m). Pristine membranes show a larger proportionality constant than the Fe-clay membrane, as it possesses a wider interlayer space and weaker stacking structure (Figure 3.5). We prepared Fe-clay membranes with increased thicknesses up to 1250 nm to explore the transmembrane behavior of water, methanol, and acetonitrile molecules. As seen in Figure 3.11d, as membrane thickness increases, the permeance of all tested solvents decreases rapidly due to the extended transmembrane pathway. Notably, the decline in

water permeance is slower, presenting a reverse proportional relationship with membrane thickness. In contrast, organic solvents like methanol and acetonitrile exhibit exponential declines, revealing unfavorable transport in thicker membranes. A similar phenomenon was observed by Nair's team on ultra-thin GO membranes, attributing it to the transition from gradually disappearing pin-hole transmembrane transport to interlayer transport [23]. However, all our stacked membranes are quite thick and far from pin-hole formation. The entire transmembrane process would be strongly related to the movement of solvent molecules in nanochannels under confined conditions, which has been shown to produce unexpected nanofluidic behavior [44, 45]. A detailed understanding of this may be achieved by conducting transport experiments under a device with atomic precision. In this work, we emphasize more on the structural regulation and membrane separation application.

Table 3.3 Various parameters of the organic solvents used in this study.

Solvent	Viscosity [43, 46]	Relative Polarity [47, 48]	Kinetic diameter [49]	Total Hansen solubility parameter [50-52]
	mPa*s		nm	$MPa^{1/2}$
Hexane	0.3	0.009	0.51	14.9
Toluene	0.55	0.099	0.55	18.2
Dimethyl sulfoxide (DMSO)	2	0.444	0.5	26.7
Isopropanol (IPA)	2.038	0.546	0.47	24.6
Ethanol	1.074	0.654	0.44	26.6
Tetrahydrofuran (THF)	0.456	0.207	0.48	19.4
Methanol	0.544	0.762	0.38	29.7
Acetone	0.306	0.355	0.47	20.1
Acetonitrile	0.369	0.46	0.34	24.4
Water	0.89	1	0.265	47.8

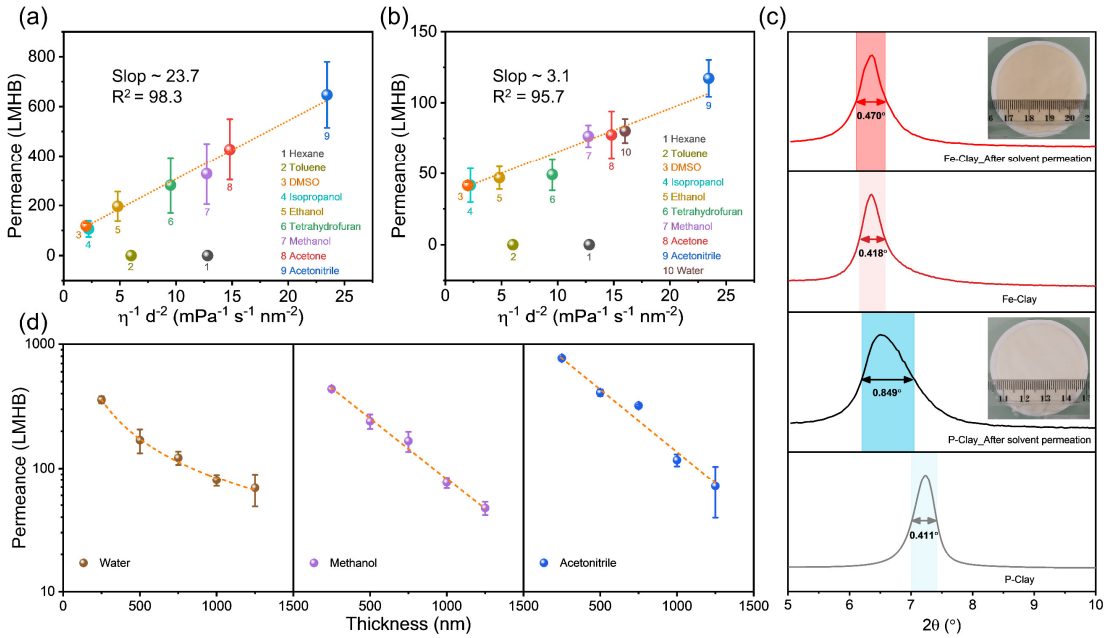

Figure 3.11 Solvent permeation through the laminar clay membranes. a-b, Permeance of pure polar organic solvents through pristine (**a**) and Fe-clay (**b**) membrane, plotted as a function of the inverse product of their viscosity and kinetic dimeter squared. Both pristine and Fe-clay membranes are impermeable to non-polar solvents. The orange dotted lines are best linear fits. **c**, Comparison of XRD patterns of pristine and Fe-clay membrane before and after solvent permeation. The FWHM of the XRD peaks is marked and highlighted by the color pillars. Inset: the photographs of the after-measurement membranes. **d**, Thickness dependence of permeance for water, methanol and acetonitrile through Fe-clay membranes. Water permeance shows an inverse proportionality with membrane thickness, while the permeance of organic solvents exhibits exponential changes. The orange dotted lines represent the best fits. All error bars represent SD derived from at least three independent measurements conducted on distinct samples.

3.5.3 Nanofiltration for solvent purification

To further validate our membranes' defect-free property, we performed separation experiments using organic dyes with negative or positive charges. Eight dyes with different sizes were selected (Table 3.4). The rejection of clay membranes was evaluated by measuring the residual dye concentration in the permeated solution using high-performance liquid chromatography (HPLC). The separation performance of Fe-clay membranes was evaluated in both water (Figure 3.12a & 3.12b) and methanol (Figure 3.12d & 3.12e). As we can see, with increasing molecular weight, which

corresponds to an enlarged molecular size, the membranes exhibited improved rejection in both water and methanol, suggesting that size exclusion is the primary sieving mechanism. Meanwhile, negatively charged dyes were better rejected than positively charged dyes by Fe-clay when they had similar molecular weights, illustrating the importance of electrostatic interaction in molecular sieving. The 2D clay nanosheets are highly negatively charged due to isomorphism, resulting from the positive charge loss after $Al^{3+} \rightarrow Si^{4+}$ replacement in the tetrahedral sheet [53]. Although the intercalated Fe^{3+} ions quench some negative charges, the nanochannel still exhibits a net negative charge, attracting positively charged molecules and repelling negatively charged molecules. We also noticed that higher rejection for the same dye molecules was obtained in water than in methanol. Additionally, reduced solvent permeance was observed under dye feeding compared to pure solvent filtration, originating from a driven force drop due to concentration polarization (CP) [54]. Furthermore, we investigated the dye separation performance of pristine membranes in methanol for comparison. The strong electric attraction between positive dye molecules and 2D nanosheets, coupled with the weak combination of the nanosheets themselves, caused the pristine membrane to quickly become jelly-like under stirring and lose its function. Only the separation performance for negatively charged dyes could be evaluated (Figure 3.13). The pristine membrane showed poor rejection of 25% for methyl orange (MO), while it was larger than 95% in Fe-Clay membranes, highlighting the importance of interlayer space robustness for highly efficient sieving performance. In summary, by combining size confinement and electrostatic interaction, Fe-Clay membranes exhibit outstanding molecular sieving ability with unparalleled solvent permeance. Their performance outperforms the current state-of-the-art membranes (Figure 3.12c & 3.12f), making these Fe-Clay membranes as promising candidates for organic solvent purification.

To further establish the applicability of Fe-clay in the membrane field, we incorporated them into a tangential cross-flow filtration cell for constant permeation operation. The solvent flux of the Fe-clay membrane was recorded to examine its

stability under more realistic conditions. As seen in Figure 3.12g, the Fe-clay demonstrates stable water permeation over 100 hours, verifying the feasibility of long-term operation for membrane applications. Although the methanol permeance exhibited a slight decrease during filtration (Figure 3.12h), the Fe-clay membranes still possess ultrafast methanol transport ability with a flow rate of over 100 LMHB after four days. This exceptional stability of Fe-Clay surpasses the state-of-the-art 2D laminar membranes, which typically exhibit a short operation time of less than 24 hours under pressure [27, 35, 55].

Table 3.4 Physicochemical properties of the organic dyes. Molecular structure presented as a ball and stick model. Color code: C, grey; N, blue; O, red; S, yellow; H, white; Ni, sky-blue; Cu, pink.

Organic dye	Molecular weight (g mol^{-1})	Net charge	Chemical structure
Chrysoidine G (CG)	248.71	+1	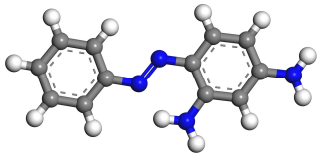
Methyl orange (MO)	327.33	-1	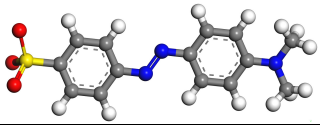
Crystal Violet (CV)	407.98	+1	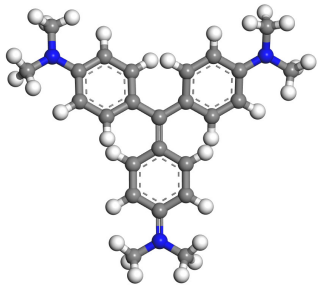
Acid Fuchsin sodium salt (AF)	585.53	-2	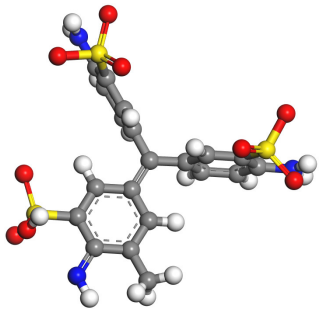

Methyl blue (MB)	799.80	-2	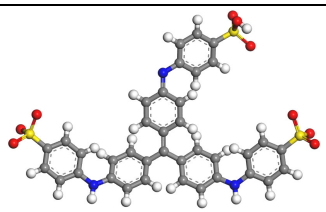
5,10,15,20-(tetra-N-methyl-4-pyridyl) porphyrin tetrachloride (PP)	820.64	+4	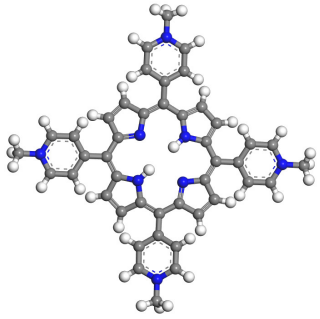
Nickel(II) phthalocyanine-tetrasulfonic acid tetrasodium salt (NP)	979.40	-4	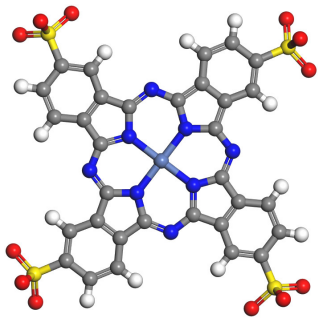
Alcian Blue 8GX (AB)	1298.88	+4	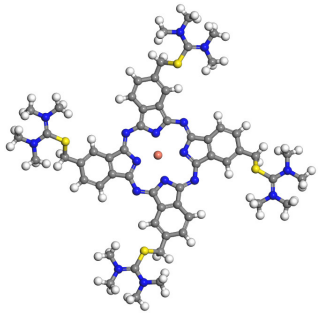

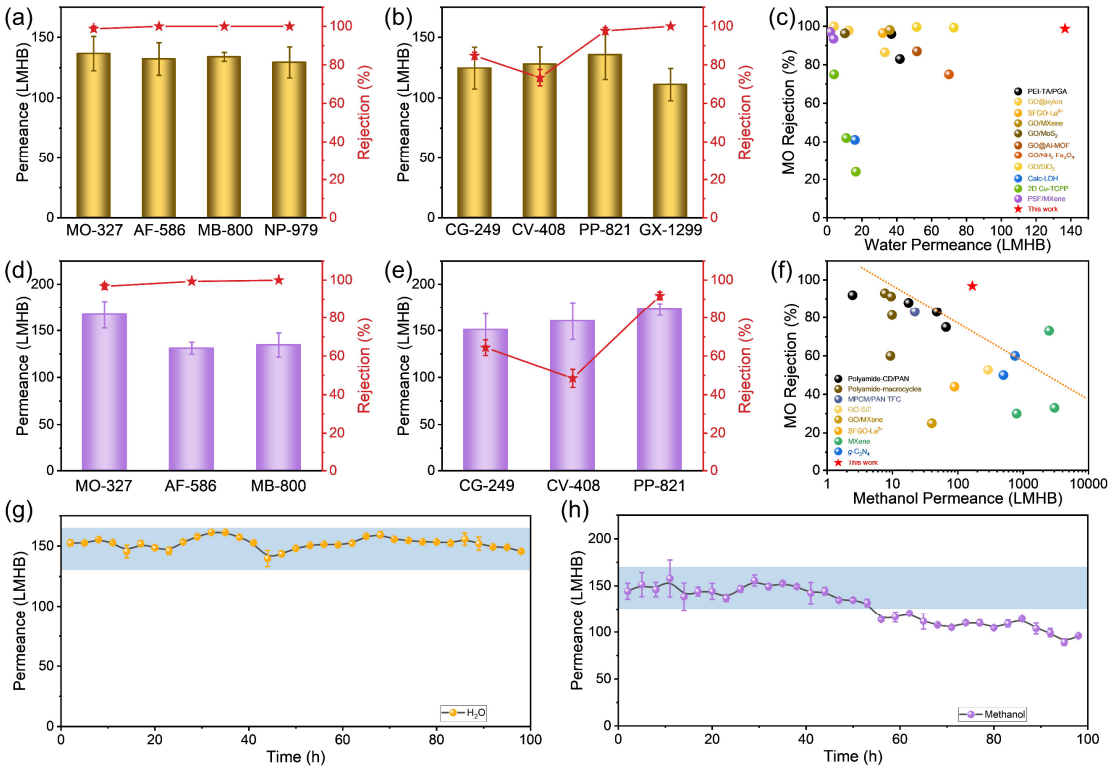

Figure 3.12 Nanofiltration performance of the 500-nm-thick Fe-clay membranes. **a-b**, Negatively (**a**) and positively (**b**) charged dyes rejection and water permeance of Fe-clay membranes. The dyes' abbreviations along with their corresponding molecular weights are indicated on the abscissa. **c**, Comparison of the MO separation performance of Fe-clay membrane in water with that of other 2D materials membranes and their hybrids. A direct comparison can be found in Table 3.5 (Section 3.7 Note). **d-e**, Negatively (**d**) and positively (**e**) charged dyes rejection and methanol permeance of Fe-clay membrane. **f**, Comparison of the MO separation performance in methanol of Fe-clay membrane against state-of-the-art membranes. The orange dotted line in the figure serves as a visual aid, indicating the upper-performance boundary of state-of-the-art membranes. Detailed data are included in Table 3.6 (Section 3.7 Note). **g-h**, Water (**g**) and methanol (**h**) permeance measured under a tangential cross-flow filtration cell for constant operation over 100 hours. All error bars denote SD.

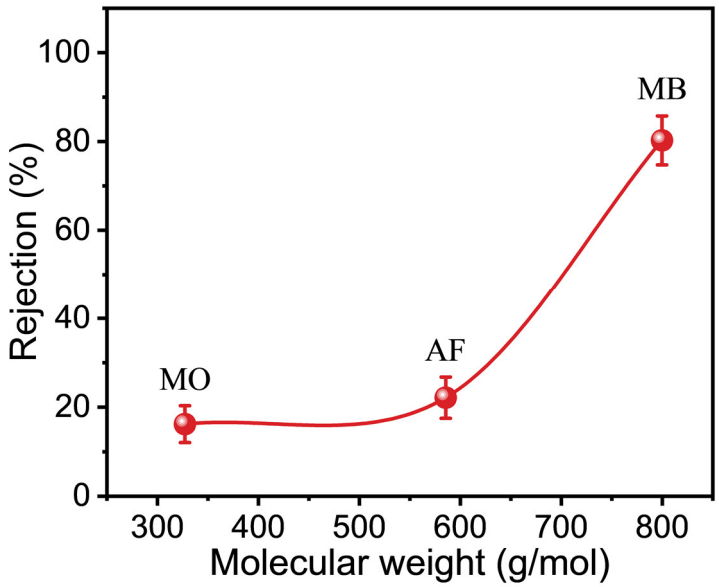

Figure 3.13 Negatively charged dyes rejection of 500 nm-thick pristine clay membranes in methanol and compared to Fe-clay membranes.

3.6 Conclusion

In conclusion, we have successfully developed Fe-clay nanolaminated membranes with exceptional structural stability and outstanding separation performance for both aqueous and organic solvent purification. By employing various cations to intercalate clay nanosheets, we demonstrated the crucial role of Fe^{3+} in maintaining interlayer space stability and enhancing the molecular sieving properties of the clay nanolaminates. The Fe^{3+} treated clay nanolaminated membranes exhibit excellent dye separation performance, surpassing the capabilities of current state-of-the-art membranes. This combined with their long-term operational stability make the Fe-clay membranes a remarkable candidate for practical applications in organic solvent filtration.

Moving forward, a more comprehensive understanding of the transport mechanisms within these membranes, as well as their behavior in different solvents, will be essential for further optimization and development. Additionally, exploring the potential of other intercalated cations or combinations of cations could lead to novel membrane properties and applications. Ultimately, this work paves the way for the practical implementation of nanolaminate clay-based membranes in various separation

processes and industrial settings.

3.7 Note

3.7.1 Comparison of the performance of the Fe-clay membranes with state-of-the-art membranes

Table 3.5 Comparison of dye separation performance of Fe-clay membrane with other 2D materials membranes and their hybrids in water under nanofiltration.

Membrane		Thickness	Solute	Solute MW (g/mol)	Concn. (ppm)	Water Permeance (LMHB)	Rejection (%)	Ref.
PEI-TA/PGA		460 nm	MO	327	100	41.8*	83	[56]
PEI-TA/PGA_{pre}		330 nm	MO	327		36.9*	96	
GO@nylon 6	GO@Nylon6-7	1.2 μm	MLB	320	100	32.3	78.23	[57]
			MO	327		33.2	86.47	
	GO@Nylon6-10	1.3 μm	MLB	320		11.9	88.65	
			MO	327		12.4	97.73	
	GO@Nylon6-13	1.5 μm	MLB	320		8.5	95.66	
			MO	327		8.9	99.82	
	GO@Nylon6-16	1.7 μm	MLB	320		3.6	96.29	
			MO	327		3.9	99.89	
SFGO-La^{3+}		70 nm	MO	327	10	32	96.5	[54]
			CV	408		24	98	
			AF	586		26.5	100	
			AR	1018		25	100	
			AB	1299		27.5	100	
GO/MXene		140 nm	MO	327	10	36	98	[55]
GO/MoS_2		4 μm	MLB	320	10	~10.2*	97.4	[58]
			MO	327			96.3	
			RhB	479			94.6	
			CR	697			99.6	
GO@Al-MOF		141 nm	MO	327	100	51.6*	87	[59]
			EBT	461			100	
			CR	697			100	
			MB	800			100	
			RB	1018			100	
GO/NH_2-Fe_3O_4		480 nm	MLB	320	100	57	70	[60]
			MO	327		70	75	
			CR	697		68	98	
GO/SiO_2	GO/S-SiO_2	1.4 μm	MO	327	10	72.8	99.3	[61]
	GO/M−SiO_2		MO	327		63.2	99.5	

	GO/L-SiO_2		MO	327		51.4	99.6	
c-GO@PSf/GO		20 nm	MLB	320	10	4*	>99	[62]
			MO	327			82.5	
			CR	697			>99	
			RG	1419			>99	
Calc-LDH		1 μm	MO	327	100	16	41	[63]
2D Cu-TCPP	VF-W	1170 nm	MO	327	20	16.5	24	[64]
	VF-F	530 nm	MO	327		4	75	
	EPD-F	200 nm	MO	327		11	42	
PSF/MXene	PSF0	106 μm	MO	327	100	1.8	97	[65]
	PSF1	115 μm	MO	327		2.1	94	
	PSF2	118 μm	MO	327		2.7	93	
	PSF3	125 μm	MO	327		3.2	92	
	PSF4	132 μm	MO	327		3.7	93.5	
Fe-Clay		~500 nm	MO	327	25	136.6	98.7	This work
			AF	586		132.1	100	
			MB	800		133.9	100	
			NP	979		129.3	100	

MO: methyl orange; MLB: methylene blue; CV: crystal violet; AF: acid fuchsin; AR: acid red 94; AB: alcian blue; RhB: rhodamine B; CR: congo red; EBT: Eriochrome Black T; MB: methyl blue; RB: rose bengal; RG: reactive green 19; MR: methyl red; NP: Nickel(II) phthalocyanine-tetrasulfonic acid.

*: it represents the pure water permeance.

Table 3.6 Comparison of dye separation performance of Fe-clay membrane against state-of-the-art membranes in methanol under nanofiltration.

Membrane		Thickness	Solute	Solute MW (g/mol)	Concn. (ppm)	Methanol Permeance (LMHB)	Rejection (%)	Ref.
Polyamide-CD/PAN membrane	Polyamide-CD (0.16)	~0.9 nm	MO	327	10-20	66	75	[66]
	Polyamide-CD (0.32)	~3.2 nm				47.6	83	
	Polyamide-CD (0.64)	~6.3 nm				17.6	88	
	Polyamide-CD (1.28)	~ 10.6 nm				2.45	92	
Polyamide-aligned macrocycles membrane	γ-CDA-TPC-0.1	~8.0 nm	MO	327	20	9.30	60	[67]
			SY	452			94.5	
	β-CDA-TPC-0.05	~5.5 nm	MO	327		9.84	81.3	
			SY	452			98.3	
	α-CDA-TPC-0.05	~10.0 nm	AZB	182		7.64	33.9	
			MO	327			93.0	
	α-CDA-TPC-0.1-Al	~14.0 nm	AZB	182		9.51	18.3	
			MO	327			91.3	
MPCM/PAN thin-film composite membranes	MPCM/PAN(2%, 10s)	3.5~10 nm	MO	327	10-20	22	83	[68]
			OG	452			96	
	MPCM/PAN(2%, 10min)		OG	452		9.3	98	
	MPCM/PAN(1%, 10s)		OG	452		39	91	
	MPCM/PAN(1%, 10min)		OG	452		21.3	93	
HLGO		8 nm	CG	249	200	6.8	100	[23]
			DR	314		6.6	100	
			MLB	320		6.3	100	
			CV	408		6.5	100	
			BB	826		6.6	100	
			RB	1018		7	100	
GO-Mg^{2+}		200 nm	CG	249	200	55	80	
			MLB	320		47	84	
			CV	408		47	88	
			RB	1018		41	94	
GO-Si2		180 nm	MO	327	100	290.1	52.7	[69]

SFGO-La^{3+}	70 nm	MO	327	10	~89	~44	[54]
		AF	586		97.39	95.03	
		AR	1018		106.82	95.73	
		AB	1299		97.4	>99.9	
LFGO-La^{3+}	70 nm	AF	586	10	33.72	97.5	
		AR	1018		40.32	99.13	
		AB	1299		34.14	>99.9	
GO/MXene	140 nm	MO	327	10	40	25	[55]
MXene $Ti_3C_2T_x$	320 nm	MO	327	10	3018	33	[29]
MXene $Ti_3C_2T_x$-NH_2	337 nm	MO	327		2500	73	
MXene $Ti_3C_2T_x$-$C_{12}H_{25}$	318 nm	MO	327		794	30	
BN	2 μm	AF	586	3	630	88.7	[70]
vermiculite (VMT) Membrane	15 nm	EB	961	20	30.1	99.7	[35]
F-VMT	NA	EB	961	20	490	99.7	
defect-sealed nanoporous graphene	on 8 μm PITEM supports	RB	1018	10	170.7	97.3	[71]
g-C_3N_4	1.1 μm	MO	327	10	500	50	[72]
g-C_3N_4–OH	1.1 μm	MO	327	10	750	60	
COF: TFP-DHF	61 nm	CR	696	10	76*	77	[73]
		RBL	922			95	
		V12	1344			99	
		RG	1419			100	
Fe-Clay	~500 nm	MO	327	25	167.1	96.79	This work
		AF	586		131.0	99.30	
		MB	800		134.4	99.96	

MO: methyl orange; SY: sunset yellow; AZB: azobenzene; OG: orange G; CG: chrysoidine G; DR: disperse red; MLB: methylene blue; CV: crystal violet; BB: brilliant blue; RB: rose bengal; AF: acid fuchsin; AR: acid red 94; AB: alcian blue; EB: Evans blue; CR: congo red; RBL: reactive black; V12: vitamin-B-12; RG: reactive green; MB: methyl blue.

*: it represents the pure methanol permeance.

3.8 Reference

1. Obotey Ezugbe, E. and S. Rathilal, *Membrane technologies in wastewater treatment: a review.* Membranes, 2020. **10**(5): p. 89.
2. Lim, Y.J., et al., *Seawater desalination by reverse osmosis: Current development and future challenges in membrane fabrication–A review.* Journal of Membrane Science, 2021. **629**: p. 119292.
3. Yang, Z., et al., *A review on reverse osmosis and nanofiltration membranes for water purification.* Polymers, 2019. **11**(8): p. 1252.
4. Bassyouni, M., et al., *A review of polymeric nanocomposite membranes for water purification.* Journal of Industrial and Engineering Chemistry, 2019. **73**: p. 19-46.
5. Marchetti, P., et al., *Molecular separation with organic solvent nanofiltration: a critical review.* Chemical reviews, 2014. **114**(21): p. 10735-10806.
6. Tandel, A.M., et al., *Designing organic solvent separation membranes: polymers, porous structures, 2D materials, and their combinations.* Materials Advances, 2021. **2**(14): p. 4574-4603.
7. Ali, S., et al., *Nanocomposite membranes for organic solvent nanofiltration: Recent advances, challenges, and prospects.* Chemosphere, 2022: p. 136329.
8. Shi, G.M., et al., *Recent progress of organic solvent nanofiltration membranes.* Progress in Polymer Science, 2021. **123**: p. 101470.
9. Wang, Z., et al., *Polymer membranes for organic solvent nanofiltration: Recent progress, challenges and perspectives.* Advanced Membranes, 2023. **3**: p. 100063.
10. Buonomenna, M. and J. Bae, *Organic solvent nanofiltration in pharmaceutical industry.* Separation & Purification Reviews, 2015. **44**(2): p. 157-182.
11. Werth, K., P. Kaupenjohann, and M. Skiborowski, *The potential of organic solvent nanofiltration processes for oleochemical industry.* Separation and purification technology, 2017. **182**: p. 185-196.
12. Lively, R.P. and D.S. Sholl, *From water to organics in membrane separations.* Nature materials, 2017. **16**(3): p. 276-279.
13. Fan, F.R., et al., *Emerging beyond-graphene elemental 2D materials for energy*

and catalysis applications. Chemical Society Reviews, 2021. **50**(19): p. 10983-11031.

14. Sangwan, V.K. and M.C. Hersam, *Electronic transport in two-dimensional materials.* Annual review of physical chemistry, 2018. **69**: p. 299-325.
15. Chen, X., et al., *The marriage of two-dimensional materials and phase change materials for energy storage, conversion and applications.* EnergyChem, 2022. **4**(2): p. 100071.
16. Liu, G., W. Jin, and N. Xu, *Two-dimensional-material membranes: a new family of high-performance separation membranes.* Angewandte Chemie International Edition, 2016. **55**(43): p. 13384-13397.
17. Liu, P., et al., *Two-dimensional material membranes for critical separations.* Inorganic Chemistry Frontiers, 2020. **7**(13): p. 2560-2581.
18. Cheng, L., et al., *Two-dimensional-material membranes: manipulating the transport pathway for molecular separation.* Accounts of Materials Research, 2021. **2**(2): p. 114-128.
19. Wang, S., et al., *Two-dimensional nanochannel membranes for molecular and ionic separations.* Chemical Society Reviews, 2020. **49**(4): p. 1071-1089.
20. Sun, M. and J. Li, *Graphene oxide membranes: Functional structures, preparation and environmental applications.* Nano Today, 2018. **20**: p. 121-137.
21. Yang, L., et al., *Recent advances in graphene oxide membranes for nanofiltration.* ACS Applied Nano Materials, 2022. **5**(3): p. 3121-3145.
22. An, Y.-C., et al., *A critical review on graphene oxide membrane for industrial wastewater treatment.* Environmental Research, 2023: p. 115409.
23. Yang, Q., et al., *Ultrathin graphene-based membrane with precise molecular sieving and ultrafast solvent permeation.* Nature materials, 2017. **16**(12): p. 1198-1202.
24. Nair, R., et al., *Unimpeded permeation of water through helium-leak–tight graphene-based membranes.* Science, 2012. **335**(6067): p. 442-444.
25. Sui, X., et al., *2D material based advanced membranes for separations in organic*

solvents. Small, 2020. **16**(50): p. 2003400.

26. Guo, B.-Y., et al., *MoS2 membranes for organic solvent nanofiltration: stability and structural control.* The Journal of Physical Chemistry Letters, 2019. **10**(16): p. 4609-4617.
27. Ran, J., et al., *Ultrathin lamellar MoS2 membranes for organic solvent nanofiltration.* Journal of Membrane Science, 2020. **602**: p. 117963.
28. Wang, J., et al., *A regularly channeled lamellar membrane for unparalleled water and organics permeation.* Angewandte Chemie International Edition, 2018. **57**(23): p. 6814-6818.
29. Wu, X., et al., *Elucidating ultrafast molecular permeation through well-defined 2D nanochannels of lamellar membranes.* Angewandte Chemie International Edition, 2019. **58**(51): p. 18524-18529.
30. Cai, X., et al., *Preparation of 2D material dispersions and their applications.* Chemical Society Reviews, 2018. **47**(16): p. 6224-6266.
31. Zheng, W. and L.Y.S. Lee, *Beyond sonication: Advanced exfoliation methods for scalable production of 2D materials.* Matter, 2022.
32. Shao, J.-J., et al., *Self-assembled two-dimensional nanofluidic proton channels with high thermal stability.* Nature communications, 2015. **6**(1): p. 7602.
33. Huang, K., et al., *Cation-controlled wetting properties of vermiculite membranes and its promise for fouling resistant oil–water separation.* Nature communications, 2020. **11**(1): p. 1097.
34. Li, M., et al., *Preparation and application of expanded and exfoliated vermiculite: A critical review.* Chemical Physics, 2021. **550**: p. 111313.
35. Tian, M., et al., *A two-dimensional lamellar vermiculite membrane for precise molecular separation and ion sieving.* ACS Sustainable Chemistry & Engineering, 2022. **10**(3): p. 1137-1148.
36. Chen, L., et al., *Ion sieving in graphene oxide membranes via cationic control of interlayer spacing.* Nature, 2017. **550**(7676): p. 380-383.
37. Ding, L., et al., *Effective ion sieving with Ti3C2T x MXene membranes for*

production of drinking water from seawater. Nature Sustainability, 2020. **3**(4): p. 296-302.

38. Mathieson, A.M. and G. Walker, *Crystal structure of magnesium-vermiculite.* American Mineralogist: Journal of Earth and Planetary Materials, 1954. **39**(3-4): p. 231-255.
39. Ries, L., et al., *Enhanced sieving from exfoliated MoS2 membranes via covalent functionalization.* Nature materials, 2019. **18**(10): p. 1112-1117.
40. Lu, X., et al., *Relating selectivity and separation performance of lamellar two-dimensional molybdenum disulfide (MoS2) membranes to nanosheet stacking behavior.* Environmental Science & Technology, 2020. **54**(15): p. 9640-9651.
41. Wang, W., et al., *High-surface-area functionalized nanolaminated membranes for energy-efficient nanofiltration and desalination in forward osmosis.* Nature Water, 2023. **1**(2): p. 187-197.
42. Abraham, J., et al., *Tunable sieving of ions using graphene oxide membranes.* Nature nanotechnology, 2017. **12**(6): p. 546-550.
43. Buekenhoudt, A., et al., *Unravelling the solvent flux behaviour of ceramic nanofiltration and ultrafiltration membranes.* Journal of membrane science, 2013. **439**: p. 36-47.
44. Wang, M., et al., *Anomalies of ionic/molecular transport in nano and sub-nano confinement.* Nano Letters, 2020. **20**(10): p. 6937-6946.
45. Aluru, N.R., et al., *Fluids and electrolytes under confinement in single-digit nanopores.* Chemical reviews, 2023. **123**(6): p. 2737-2831.
46. Karan, S., Z. Jiang, and A.G. Livingston, *Sub–10 nm polyamide nanofilms with ultrafast solvent transport for molecular separation.* Science, 2015. **348**(6241): p. 1347-1351.
47. Liu, R., et al., *Graphene oxide membrane for liquid phase organic molecular separation.* Carbon, 2014. **77**: p. 933-938.
48. Linstrom, P.J. and W.G. Mallard, *The NIST Chemistry WebBook: A chemical data resource on the internet.* Journal of Chemical & Engineering Data, 2001. **46**(5): p.

1059-1063.

49. Wu, H., et al., *Commensurate adsorption of hydrocarbons and alcohols in microporous metal organic frameworks.* Chemical Reviews, 2012. **112**(2): p. 836-868.
50. Hansen, C.M., *Hansen solubility parameters: a user's handbook*. 2007: CRC press.
51. Konios, D., et al., *Dispersion behaviour of graphene oxide and reduced graphene oxide.* Journal of colloid and interface science, 2014. **430**: p. 108-112.
52. Zeng, W., et al., *Solubility parameters*, in *Physical properties of polymers handbook*. 2007, Springer. p. 289-303.
53. Xie, L., et al., *Surface Charge Modification on 2D Nanofluidic Membrane for Regulating Ion Transport.* Advanced Functional Materials, 2023. **33**(4): p. 2208959.
54. Nie, L., et al., *Realizing small-flake graphene oxide membranes for ultrafast size-dependent organic solvent nanofiltration.* Science Advances, 2020. **6**(17): p. eaaz9184.
55. Wei, S., et al., *Two-dimensional graphene Oxide/MXene composite lamellar membranes for efficient solvent permeation and molecular separation.* Journal of Membrane Science, 2019. **582**: p. 414-422.
56. Cao, Y., et al., *A robust dually charged membrane prepared via catechol-amine chemistry for highly efficient dye/salt separation.* Journal of Membrane Science, 2021. **629**: p. 119287.
57. Chen, L., et al., *A large-area free-standing graphene oxide multilayer membrane with high stability for nanofiltration applications.* Chemical Engineering Journal, 2018. **345**: p. 536-544.
58. Zhang, P., et al., *Novel "loose" GO/MoS2 composites membranes with enhanced permeability for effective salts and dyes rejection at low pressure.* Journal of Membrane Science, 2019. **574**: p. 112-123.
59. Alemayehu, H.G., et al., *Highly stable membrane comprising MOF nanosheets and graphene oxide for ultra-permeable nanofiltration.* Journal of Membrane

Science, 2022. **652**: p. 120479.

60. Dong, L., et al., *NH2-Fe3O4-regulated graphene oxide membranes with well-defined laminar nanochannels for desalination of dye solutions.* Desalination, 2020. **476**: p. 114227.
61. Deng, H., et al., *Graphene oxide/silica composite nanofiltration membrane: Adjustment of the channel of water permeation.* Separation and Purification Technology, 2021. **278**: p. 119440.
62. Zhang, N., et al., *A composite membrane of cross-linked GO network semi-interpenetrating in polysulfone substrate for dye removal from water.* Journal of Membrane Science, 2020. **613**: p. 118456.
63. Huang, Z., et al., *Calcination of layered double hydroxide membrane with enhanced nanofiltration performance.* Journal of Industrial and Engineering Chemistry, 2020. **89**: p. 368-374.
64. Cai, J., et al., *Two-dimensional Cu-porphyrin nanosheet membranes for nanofiltration.* Nano Research, 2023. **16**(5): p. 6290-6297.
65. Dashtbozorg, A., et al., *High-performance and robust polysulfone nanocomposite membrane containing 2D functionalized MXene nanosheets for the nanofiltration of salt and dye solutions.* Desalination, 2022. **527**: p. 115600.
66. Huang, T., et al., *Ultrathin 2D-layered cyclodextrin membranes for high-performance organic solvent nanofiltration.* Advanced Functional Materials, 2020. **30**(4): p. 1906797.
67. Jiang, Z., et al., *Aligned macrocycle pores in ultrathin films for accurate molecular sieving.* Nature, 2022. **609**(7925): p. 58-64.
68. Huang, T., et al., *Molecularly-porous ultrathin membranes for highly selective organic solvent nanofiltration.* Nature Communications, 2020. **11**(1): p. 5882.
69. Wang, S., et al., *2D-dual-spacing channel membranes for high performance organic solvent nanofiltration.* Journal of Materials Chemistry A, 2019. **7**(19): p. 11673-11682.
70. Chen, C., et al., *Functionalized boron nitride membranes with ultrafast solvent*

transport performance for molecular separation. Nature communications, 2018. **9**(1): p. 1902.

71. Cheng, C., S.A. Iyengar, and R. Karnik, *Molecular size-dependent subcontinuum solvent permeation and ultrafast nanofiltration across nanoporous graphene membranes.* Nature Nanotechnology, 2021. **16**(9): p. 989-995.
72. Wu, X., et al., *Manipulating the cross-layer channels in gC 3 N 4 nanosheet membranes for enhanced molecular transport.* Journal of Materials Chemistry A, 2021. **9**(7): p. 4193-4202.
73. Shinde, D.B., et al., *Crystalline 2D covalent organic framework membranes for high-flux organic solvent nanofiltration.* Journal of the American Chemical Society, 2018. **140**(43): p. 14342-14349.

Chapter 4: Summary and perspectives

4.1 Summary

The journey of this thesis commenced with an exploration of the emergent field of 2D material membranes in Chapter 1. These unique membranes, characterized by their ultra-thin thickness, high mechanical strength, and versatile surface chemistry, have shown immense potential for a multitude of separation applications. The inherent flexibility of these 2D material membranes allows for tailoring properties such as nanopore architecture and microenvironments, enhancing their performance in specific applications. Yet, alongside these promising attributes, the chapter also drew attention to the significant challenges confronting the broader adoption of these materials, such as issues of long-term stability, scalability, and the development of more efficient, environmentally friendly fabrication methods.

In Chapter 2, the thesis delved into the realm of laminar membranes created from 2D nanosheets, with a specific focus on molybdenum disulfide (MoS_2) as a case study for successful desalination applications. The uniqueness of these membranes lies in their tunability, as evidenced by the ability to adjust capillary widths according to the nature of the functional groups attached to the MoS_2 nanosheets. Such a precise control over capillary dimensions and stacking order has yielded impressive results, particularly in terms of water permeation and salt rejection rates. This strategy highlights the significant potential of these membranes hold for energy-efficient desalination and nanofiltration applications.

Building upon the foundational insights offered in the first two chapters, Chapter 3 transitioned towards the application of 2D clay nanolaminated membranes for organic solvent nanofiltration (OSN). Initially, the clay-based membranes encountered stability issues in both water and solvents. However, these obstacles were overcome through the incorporation of mono and multivalent cations, particularly Fe^{3+}, resulting in substantial enhancements in both the stability and sieving capabilities of the membranes. The advancements in this area, combined with a deeper understanding of the membranes' transport mechanisms, have unlocked a new horizon of possibilities for these membranes in organic solvent filtration applications.

4.2 Perspectives

Moving forward, the field of 2D material membranes for separation technology presents numerous exciting research avenues. Among the key considerations for future work, the enhancement of long-term stability, scalability, and the development of sustainable fabrication methods for 2D material membranes stand out. This could entail a thorough investigation of novel fabrication techniques, an exploration into the potential of hybrid 2D material compositions, and the development of advanced anti-fouling strategies to enhance the practicality and longevity of these membranes.

Further in-depth investigations into the roles of different functional groups and cations in modifying the properties of 2D membranes are also needed. By identifying and utilizing the optimal combinations of these cations, it could be possible to engineer novel membranes with further enhanced performance and stability. Similarly, a detailed understanding of the transport mechanisms within these membranes and their behavior in different solvents can open the door for further optimization and fine-tuning of their properties.

Concerning the development of nanolaminated membranes, the prospect of fabricating larger-scale membranes that can maintain high performance and stability is an intriguing one. As these membranes edge closer to realistic applications, the development and implementation of comprehensive quality control and testing standards will also be crucial.

Regarding OSN, there is a clear opportunity for extensive research to exploit the full potential of 2D laminated clay membranes. In particular, exploring the potential of other intercalated cations or combinations of cations and understanding their interaction with different solvents could lead to the discovery of novel membrane properties and broaden the application range of these membranes.

In conclusion, the work presented in this thesis has not only offered valuable insights into the current state and potential of 2D material membranes in various separation technologies but has also laid a strong foundation for future research. As research in this vibrant field continues to break new ground, we can anticipate the

emergence of innovative materials, techniques, and strategies that will shape the future of this field. The evolution of these technologies holds immense promise not only for advancing scientific understanding but also for addressing some of the critical environmental and industrial challenges in a sustainable manner.